
Nonlinear Inverse Problems in Quantitative Phase Imaging

Thanh-an Michel Pham

Thèse N° 8941 (juin 2022)

*Thèse présentée à la faculté des sciences et techniques de l'ingénieur
pour l'obtention du grade de docteur ès sciences
et acceptée sur proposition du jury*

Prof. Christophe Moser, *président*
Prof. Michael Unser, *directeur de thèse*
Dr. Emmanuel Soubies, *co-directeur de thèse*
Prof. Laura Waller, *rapporteure*
Prof. George Barbastathis, *rapporteur*
Prof. Jean-Philippe Thiran, *rapporteur*

École polytechnique fédérale de Lausanne—2022

Cover design by Annette Unser
Printing and binding by Repro-EPFL
Typeset with L^AT_EX
Copyright © 2022 by Thanh-an Michel Pham
Available at <http://bigwww.epfl.ch/>

Abstract

The topic of this thesis is the development of new algorithmic reconstruction methods for quantitative phase imaging (QPI). In the past decade, advanced QPI has emerged as a valuable tool to study label-free biological samples and uncover their 3D structural information. This unique tool takes advantage of the scattering of light that results from the complex interplay between the incident electromagnetic wave and the specimen of interest. Yet, the reconstruction process presents numerous challenges in part due to the nonlinear nature of light scattering.

In this thesis, we investigate an accurate nonlinear wave-propagation model that relies on the Lippmann-Schwinger (LiSc) equation and apply it to 3D QPI within a variational framework. Our first contribution is a proper discretization of LiSc and a computationally efficient implementation of the nonlinear model.

Using our novel forward model, we formulate an inverse-scattering problem within a modern variational framework and solve it to recover the 3D refractive-index (RI) map of a sample when the measurements are complex-valued. In such a setting, the sample is probed with a series of tilted incident waves, while the complex-valued waves are recorded for each illumination. Our algorithmic reconstruction involves a nontrivial proximal gradient-based iterative scheme that requires the Jacobian matrix of the nonlinear operator, for which we are able to derive an explicit expression. By accounting for multiple scattering and adding suitable prior knowledge, our results show that we significantly improve the quality of reconstruction over the state of the art.

We then adapt our LiSc model to intensity-only measurements, which has the advantage of simplifying the acquisition setup. We solve this harder inverse problem by leveraging recent advances in proximal algorithms. Our method obtains RI maps with a quality similar to that obtained from complex measurements.

Finally, we propose an extension of single-molecule localization microscopy. This modality delivers nanoscale resolution by sequentially activating a subset of fluorescent labels and by extracting their superresolved position. The emission patterns of each label can be distorted by the sample, which reduces the localization accuracy if not accounted for. Here, we exploit those sample-induced aberrations to recover the RI map. We propose an optimization framework in which we reconstruct the RI map using LiSc and optimize the label positions in a joint fashion. Our results show that we effectively recover the RI map of the sample and further improve the localization.

Keywords: Quantitative phase imaging, nonlinear inverse problem, optical diffraction tomography, Lippmann-Schwinger equation, computational microscopy, single-molecule localization microscopy

Résumé

Le sujet de cette thèse est le développement de nouvelles méthodes de reconstruction algorithmique pour l'imagerie quantitative de phase (IQP). Au cours de la dernière décennie, IQP s'est imposée comme un précieux outil pour étudier des spécimens biologiques sans marqueur et découvrir leurs informations structurales tridimensionnelles (3D). Cet outil unique exploite la dispersion de la lumière qui résulte de l'interaction complexe entre l'onde électromagnétique incidente et le spécimen étudié. Cependant, le processus de reconstruction présente de nombreux défis, notamment en raison de la nature non-linéaire de la dispersion de la lumière.

Dans cette thèse, nous étudions un modèle non-linéaire de propagation des ondes de haute fidélité qui repose sur l'équation de Lippmann-Schwinger (LiSc) et nous l'appliquons à l'IQP 3D dans un cadre variationnel. Notre première contribution est une discrétisation appropriée de LiSc et une implémentation efficace du modèle non-linéaire.

à l'aide de notre nouveau modèle physique, nous formulons un problème de dispersion inverse dans un cadre variationnel moderne et le résolvons pour reconstruire le volume d'indice de réfraction (IR) 3D d'un spécimen lorsque les mesures sont à valeur complexe. Dans un tel contexte, le spécimen est sondé avec une succession d'ondes incidentes à orientations variées, tandis que les ondes à valeur complexe sont mesurées pour chaque illumination. Notre reconstruction algorithmique implique un schéma itératif non trivial basé sur le gradient proximal qui nécessite la matrice jacobienne de l'opérateur non-linéaire, dont nous sommes capables d'en dériver une expression explicite. en tenant compte de la dispersion multiple et en ajoutant des connaissances préalables appropriées, nos résultats montrent que nous améliorons considérablement la qualité de la reconstruction par rapport à l'état de l'art.

Nous adaptons ensuite notre modèle LiSc aux mesures d'intensité uniquement, ce qui présente l'avantage de simplifier la configuration du système d'acquisition. Nous résolvons ce problème inverse plus difficile en tirant parti des progrès récents des algorithmes proximaux. Notre méthode permet d'obtenir des volumes d'IR d'une qualité similaire à celle obtenue à partir de mesures complexes.

Enfin, nous proposons une extension de la microscopie de localisation de molécules isolées. Cette modalité permet d'obtenir une résolution à l'échelle nanométrique en activant séquentiellement un sous-ensemble de marqueurs fluorescents et en extrayant leur position superrésolue. Les patterns d'émission de chaque marqueur peuvent être déformés par le spécimen, ce qui réduit la précision de la localisation. Ici, nous exploitons ces aberrations induites par le spécimen pour récupérer le volume d'IR. Nous proposons un schéma d'optimisation dans lequel nous reconstruisons le volume d'IR en utilisant LiSc et optimisons la position des marqueurs de manière simultanée. Nos résultats montrent que nous pouvons reconstruire le volume d'IR du spécimen et que nous améliorons la localisation.

Mots-clés : Imagerie quantitative de phase, problème inverse non-linéaire, tomographie par diffraction optique, équation de Lippmann-Schwinger, microscopie computationnelle, microscopie à localisation de molécules isolées.

Sometimes science is more art than science.

Rick Sanchez

À mes parents, mon frère et Chi-Vinh.

Acknowledgement

This thesis is the materialization of five years of hard work. All along these years, many people have played a key role in shaping the researcher I have become. First of all, Prof. Michael Unser and Dr. Emmanuel Soubies were the best advisors I could have dreamed. They trusted me enough to give me the freedom I wanted and the advices I needed. They taught me many of the nitty-gritty details that research requires. Manu is one of the greatest and nicest researcher I know. He had this ability to conduct research on nearly any subject in the lab. He could endure my (researcher) flaws and knew how to cheer me up when my mood was fluctuating.

This thesis would have made no sense without the fruitful collaboration I had with the Optics laboratory; in particular, Prof. Demetri Psaltis, Dr. Alexandre Goy, Dr. Joowon Lim, and Dr. Ahmed Ayoub. They played a key role in the reconstruction of real data and in my understanding of optics. I am sincerely grateful for the mentoring in optics of Dr. Ferréol Soulez as well. Then, I would like to thank the Jury members for my PhD oral examination: Prof. Christophe Moser, Prof. Laura Waller, Prof. George Barbastathis, and Prof. Jean-Philippe Thiran. I am flattered that they accepted to be part of this journey.

I am grateful to Prof. Mathews Jacob who gave me a first taste in research with my Master thesis on SMLM. Coincidentally, Dr. Daniel Sage was also working on this subject and offered me an internship¹ within the biomedical imaging group (BIG), which opened the door to a PhD. Since then, Daniel and I have shared at least 200 coffees over the 5 years; I enjoyed all our talks and support he gave me. The dark humor of Dr. Philippe Thévenaz occurred at the most unexpected moments. I am very grateful for these laughable moments and for his papers proofreading. All

¹unpaid

these years were smoothly administrated thanks to Claudia Gasparini and I have kind thoughts for her dog Chippie—she will be missed.

My first office mates Kyong and Harshit were a perfect match. In particular, I could fully express my sarcasm with Harshit. Shayan and Thomas are my thesis mates, and we could count on each other to complain about our respective thesis. This was precious, especially in the last months of the thesis. I could appreciate the extra-work activities with Harshit and Shayan, punctuated by many random thoughts and behaviors. I loved my interactions with Quentin Denoyelle, mainly at la Jetée and not research-related, because I couldn't understand what he was doing (it did concern an idea of certificate). One conference I loved was ISBI at Venice, probably because I could enjoy lots of fun with Laurene and Anaïs (and Manu). Since then, I loved our interactions. Ramens with Laurene remain plain joy. I wish a great future to Mehrsa and hope that the motto “nothing matters” won't influence too much her research. Jonathan Dong helped me at important times toward the end of my thesis, and our jam sessions are always refreshing moments. Further, there are other collaborations that ended up with friendship and soon-to-be incredible publications. I was lucky enough to cross the path of Dr. Nathalie Brandenburg, Camilla Ceroni, and Dr. Juliette Griffié.

I would like to thank Aleix, a great guy who just arrived in my office. Beyond his help for my English and research, he made working days laughable again. My friendship with Pakshal is valuable at so many levels. I could trust him unconditionally for Image Processing courses, Indian foods, the organization of a few lab outings, and proofreading anything. He could also bear my complaints all along these years. We watched many football games at McCarthy's, and even the seminal game of Lausanne versus Stade Nyonnais. Special mentions to the two Spanish visitors we had: Carlos and Esti. In a very short time, I could enjoy their way of life and can't wait to visit them in Spain or neighboring countries. Finally, my thesis experience would not have been that great if it was not for the past and current members of the lab.

Outside the lab, Nicolas was a support for many of my complaints—a recurring theme—and I believe vice-versa) and our whining was a pleasure every time. We shared enjoyable vacations with Jenifer Wang as well, another friend I am glad to have. The so-called Rolex group gathers most of the longest friendships I have. I could name them all, but I am lazy. They do not need that to know how much I value our friendship. More recently, I loved my outing and trips with Nat and Fanny, so many random things happened. Special mention to Alexis and Léon, two

friends who have played a major role in my life and I will be indebted to them for eternity.

I would like to thank the Dang family, which includes all the uncles, aunts, cousins, and little cousins. All these cheerful celebrations were always refreshing. My parents who provided unconditional support and food and my brother who, by the way, drew the cover of this thesis were solid foundations to live a peaceful PhD.

Notations

Scalars and continuously-defined functions are denoted by italic letters (*e.g.*, $\eta \in \mathbb{R}$, $g \in L_2(\mathbb{R})$). The complex conjugate of $v \in \mathbb{C}$ is denoted by v^* . Vectors and matrices are denoted by bold lowercase and bold uppercase letters, respectively (*e.g.*, $\mathbf{f} \in \mathbb{R}^N$, $\mathbf{G} \in \mathbb{C}^{N \times N}$). For a vector $\mathbf{f} \in \mathbb{R}^N$, $\|\mathbf{f}\|$ stands for its ℓ_2 -norm. Other p -norms will be specified with an index (*i.e.*, $\|\cdot\|_p$). The n th element of a vector is denoted as $f[n]$ or f_n . Similarly, the n th column of a matrix $\mathbf{X} \in \mathbb{R}^{M \times N}$ is denoted as \mathbf{x}_n or $[\mathbf{X}]_n$. The notation \mathbf{G}^H refers to the conjugate transpose of the matrix $\mathbf{G} \in \mathbb{C}^{N \times N}$.

We denote by \mathbf{F} the discrete Fourier transform (DFT) defined in 1D by $(\mathbf{F}\mathbf{v})[k] = \sum_{n=-N/2+1}^{N/2} \mathbf{v}[n]e^{-\frac{2j\pi}{N}nk}$ (The higher-dimension DFT follows by recursive application of the 1D DFT along each dimension). The notations \hat{f} and $\hat{\mathbf{f}}$ refer to the continuous Fourier transform of f and the discrete Fourier transform of \mathbf{f} , respectively. Alternatively, $\mathcal{F}\{\cdot\}$ and $\mathcal{F}^{-1}\{\cdot\}$ denote the continuous Fourier transform and its inverse, respectively.

The reflection operator of a vector is denoted as \mathbf{f}^\vee . The matrix $\mathbf{I}_N \in \mathbb{R}^{N \times N}$ is the identity matrix and $\mathbf{diag}(\mathbf{f}) \in \mathbb{R}^{N \times N}$ is a diagonal matrix formed out of the entries of $\mathbf{f} \in \mathbb{R}^N$. The notation $\mathbf{1}_M = (1, 1, \dots, 1) \in \mathbb{R}^M$ stands for an M -length vector of ones. Similarly, $\mathbf{0}_M$ denotes a vector of M zeros.

Finally, $*$, \odot , and \oslash stand for discrete convolution, Hadamard product and pointwise division, respectively, and $\llbracket 1; N \rrbracket := [1 \dots N]$.

Abbreviations

QPI	quantitative phase imaging
3D	three-dimensional
RI	refractive index
ODT	optical diffraction tomography
LiSc	Lippmann-Schwinger
LSm	Lippmann-Schwinger based model
SMLM	single-molecule localization microscopy
FRC	Fourier ring-correlation
DFT	discrete Fourier transform
BPM	beam propagation method
IBA	iterative Born approximation
SSNP	split-step non-paraxial method
MLB	multi-layer Born model
SEAGLE	series expansion with accelerated gradient descent on Lippmann-Schwinger equation
2D	two-dimensional
DHM	digital holography microscopy
FP	Fourier ptychography
DDA	discrete dipole approximation
GS	Gerchberg-Saxton
CG	conjugate-gradient method
BiCG	biconjugate-gradient stabilized method
NAGD	Nesterov accelerated gradient descent

TV	total variation seminorm
HS	Hessian-Schatten seminorm
FBS	forward-backward splitting
SNR	signal-to-noise ratio
ADMM	alternating direction method of multipliers
LFR	light-field refocusing
SSIM	structural similarity index measure
RMSE	root-mean-square error
PUMA	phase unwrapping max-flow/min-cut
IRTV	iteratively reweighted total variation
CNN	convolutional neural network
PUDIP	phase unwrapping with deep image prior
GA	Goldstein's algorithm
LS	Least-squares algorithm
RSNR	regressed signal-to-noise ratio
SLM	spatial light modulator
MSE	mean-square error
RMSMD	root-mean-square minimum distance

Contents

Abstract	i
Résumé	iii
Acknowledgement	ix
Notations	xiii
Abbreviations	xv
List of Figures	xxiii
List of Tables	xxvii
Introduction	1
1 Physics of Wave Propagation: Let There Be Light Scattering	9
1.1 Theory of Scalar Diffraction: Continuous-Domain Formulation . . .	10
1.2 Numerical Models for Wave Propagation	12
1.2.1 Linear Models	12
1.2.2 Nonlinear Models	14
1.3 Summary	16
2 Quantitative Phase Imaging (QPI)	17
2.1 Two-dimensional (2D) QPI: All You Need Is Phase	18

2.1.1	Digital Holography Microscopy (DHM)	18
2.1.2	2D Fourier Ptychography (FP)	19
2.2	Three-dimensional (3D) QPI	20
2.2.1	Reconstruction from Complex Measurements	20
2.2.2	Reconstruction from Intensity-only Measurements	21
2.3	Variational Approaches for Optical Diffraction Tomography (ODT)	22
2.3.1	Limited Angles of Illuminations: Missing-Cone Problem	22
2.4	Summary	23
3	Accurate Discretization of the Lippmann-Schwinger (LiSc) Equation	27
3.1	Introduction	27
3.2	Contributions	27
3.3	Continuous-Domain Formulation	28
3.4	Discrete Formulation	28
3.5	Green's Function Discretization Inside the Support	29
3.6	Memory Savings	32
3.7	Comparison of Models Accuracy	33
3.8	Solvers for LiSc-based Model	35
3.9	Green's Function Discretization Outside the Support	36
3.10	Summary	37
4	ODT from Complex Measurements	39
4.1	Introduction	39
4.2	Challenges in 3D ODT	39
4.3	Contributions	40
4.4	Accurate and Efficient Implementation of the Forward Model	41
4.4.1	Discrete Formulation	42
4.4.2	Free-Space Propagation and Pupil Function	44
4.4.3	Computation of the 3D Incident Field	44
4.5	Reconstruction Framework	46
4.5.1	Problem Formulation	46
4.5.2	Optimization	47
4.5.3	Efficient Computation of the Gradient	48
4.6	Results for 3D Data	56

4.6.1	Simulated Data	57
4.6.2	Experimental Data	59
4.7	Adaptive Regularization with Dictionary Learning	60
4.8	Summary	67
5	ODT from Intensity-only Measurements	69
5.1	Introduction	69
5.2	Contributions	69
5.3	Unified Regularized Reconstruction Framework	70
5.3.1	Problem Formulation	70
5.3.2	Optimization with the Alternating Direction Method of Multipliers (ADMM)	70
5.4	Results for 2D Data	74
5.4.1	Simulated Data	74
5.4.2	Experimental Data	77
5.4.3	Discussion	78
5.5	Reconstruction Framework Revisited	81
5.5.1	Optimization for 3D Data	81
5.6	Results for 3D Data	82
5.6.1	Simulated Data	84
5.6.2	Experimental Data	84
5.6.3	Discussion	84
5.7	Summary	86
6	Single-Molecule Localization Microscopy (SMLM) Meets ODT	87
6.1	Introduction	87
6.2	Context	88
6.3	Contributions	89
6.4	Image-Formation Model	89
6.4.1	SMLM: Perspective from ODT	89
6.4.2	Discrete Forward Model	91
6.5	Joint Recovery of the Molecule Localization and Refractive Indices (RI)	92
6.5.1	Joint-Optimization Framework	92
6.5.2	Update of Molecule Amplitudes and Positions	93
6.5.3	Update of the RI	96
6.5.4	Initialization Strategies	96

6.6	Results on Simulated Data	98
6.6.1	Simulation Setting	98
6.6.2	Metrics and Visualization	100
6.6.3	Results	102
6.7	Summary	109
7	Phase Unwrapping with Deep Image Prior (PUDIP)	111
7.1	Introduction	111
7.2	Context	112
7.2.1	Classical Methods	112
7.2.2	Deep-Learning-Based Approaches	113
7.3	Contributions	114
7.4	Problem Formulation	116
7.5	Phase Unwrapping with Deep Image Prior	118
7.5.1	Architecture	118
7.5.2	Optimization Strategy	119
7.5.3	Parameter Setting	119
7.6	Results On Simulated Data	120
7.6.1	Baseline Methods	120
7.6.2	Quantitative Evaluation	122
7.6.3	Simulated Phase Images of Organoid-Like Sample	123
7.6.4	Phase Unwrapping of Artificial Images	124
7.6.5	Phase Unwrapping in Presence of Structured Noise	126
7.7	Results on Experimental Data	128
7.7.1	Experimental Setup	130
7.7.2	Post-Processing of the Unwrapped Phase	130
7.7.3	Phase Unwrapping of Organoids	130
7.7.4	Phase Unwrapping of Time-Lapse Measurements	134
7.7.5	Segmentation of Time-Lapse Measurements	134
7.8	Summary	135
8	Metrics for ODT and SMLM	137
8.1	Introduction	137
8.2	Contributions	137
8.3	Assessment Tool for ODT using Structured Illumination	138
8.3.1	Context	138

8.3.2	Proposed Metric	139
8.3.3	Materials and Reconstruction Methods	141
8.3.4	Assessment Results	142
8.3.5	Discussion	143
8.4	Optimal-Transport-Based Metric For SMLM	146
8.4.1	Context	146
8.4.2	Flat Metric for SMLM	148
8.4.3	Results on Simulated Data	151
8.4.4	Discussion	154
8.5	Closed-Form Expression of the Fourier-Ring Correlation (FRC) for SMLM	156
8.5.1	Context	156
8.5.2	Notations and Definitions	156
8.5.3	Conventional FRC Computation in SMLM	157
8.5.4	Closed-Form Expression of The FRC in Continuous Domain	158
8.5.5	Results on Simulated Data	160
8.5.6	Discussion	163
8.6	Summary	164
9	Conclusion	165
A	Appendices	169
A.1	Short Remark on the GlobalBioIm Library	169
A.2	Proximity Operators	169
A.2.1	Proximity Operators via ADMM	170
A.2.2	Proximity Operators via the Fast Gradient-Projection (FGP) Method	172
A.3	Proofs for Chapter 3	172
A.3.1	Preliminary Lemmas	172
A.3.2	Proof of Theorem 3.5.1	175
A.3.3	Proof of Proposition 3.6.1	179
A.4	Experimental Setup	180
A.5	Supplementary Materials for Chapter 7	181
A.5.1	Architecture of the Generative Network	181
A.5.2	Stability of PUDIP	183
A.5.3	Training Dataset of PhaseNet	183

- A.5.4 Simulation Setup 183
- A.5.5 Phase Unwrapping of Simulated Data 185
- A.5.6 Experimental Data 189
- A.5.7 Reconstructions by Goldstein’s Algorithm and
PhaseNet 189

- Bibliography** **189**

- Curriculum Vitæ** **227**

List of Figures

1	Roadmap of the Thesis	8
1.1	Scheme of Wave Propagation in an Inhomogeneous Medium	10
2.1	Principle of Off-Axis Digital Holography Microscopy	19
2.2	Cone of Illuminations	23
3.1	Illustration of the Equivalence Between the Green's Function and its Truncated Version on Ω	30
3.2	Relative Error of the Proposed Discretization <i>vs.</i> a Naive Discretization of the Green's Function	32
3.3	Simulated Scattering of a Monochromatic Wave by a Bead	33
3.4	Forward-Model Solution for a Strongly-Scattering Bead using Different Solvers	34
3.5	Numbers of Iterations to Converge for Different Solvers	35
4.1	Principle of Optical Diffraction Tomography	42
4.2	Propagation of the Incident Field	44
4.3	Memory Requirements for Different Solvers	52
4.4	Shepp-Logan Phantom with Refractive Indices	53
4.5	Reconstructions Obtained by the Proposed Method and by SEAGLE for the Shepp-Logan Phantom	55
4.6	Reconstructions Obtained by the Proposed Method and by SEAGLE for the Institut Fresnel's Database	56

4.7	Refractive-Index Reconstructions of the Simulated Red Blood Cells by Rytov, the Beam Propagation Method, and the Proposed Method	58
4.8	Refractive-Index Reconstructions of the Yeast Cell by Rytov, Beam Propagation Method, and the Proposed Method	59
4.9	Iso-Surface Color Renderings of the Refractive-Index Reconstructions of the Yeast Cell	61
4.10	TV-Regularized Solutions of the Yeast Cell with Various Regularization Parameters	65
4.11	Dictionary Learnt from Lateral Planes of a TV-Regularized Solution	65
4.12	Yeast Reconstructions with the Adaptive Regularization	66
5.1	Setup of Optical-Diffraction Tomography from Intensity-only Measurements	71
5.2	Reconstructed Refractive-Index Maps of Simulated Samples	76
5.3	Acquisition Setup for the Institut Fresnel’s Dataset	77
5.4	Permittivity Reconstruction of the Institut Fresnel’s Dataset using the Proposed Framework	79
5.5	Permittivity Reconstructions of the Institut Fresnel’s Dataset with a Limited Number of Measurements.	80
5.6	Refractive-Index Reconstructions of the Simulated Red Blood Cells (Intensity-only Measurements)	83
5.7	Refractive-Index Reconstructions of the Yeast Cell (Intensity-only Measurements)	85
6.1	Scheme of Biplane Single-Molecule Localization Microscopy	90
6.2	Simulation Setup of Single-Molecule Localization Microscopy from Optical-Diffraction Tomography Perspective	99
6.3	Reconstructions of the Refractive-Index Map from Single-Molecule Localization Microscopy Measurements	101
6.4	Observable Region of the Sample	102
6.5	Rendering of Localized Molecules (Y-Projection)	103
6.6	Reconstructions of the Refractive-Index Map with Different Fluorophore Distributions	106
6.7	Reconstructions of the Refractive-Index Map with Different Noise Levels	107

6.8	Box Plots of the Localization and Amplitude Error for Different Noise Levels	108
7.1	Example of Phase Image of Organoids	113
7.2	Schematic Diagram of the Proposed Phase Unwrapping with Deep Image Prior	115
7.3	Unwrapped Phase Images of Two Simulated Samples	122
7.4	Organoid-like Reconstructions	125
7.5	Unwrapped Phase Images for the Training Dataset of PhaseNet	128
7.6	Unwrapped Phase Images for Samples with Speckle Noise	129
7.7	Reconstructed Phase Images of Organoids	131
7.8	Time-Lapse Reconstructions of Phase Images of Organoids	132
7.9	Segmentation of Time-Lapse Reconstructions of Phase Images of Organoids	133
8.1	Overall Scheme of the Proposed Metric for Optical Diffraction Tomography	140
8.2	Unwrapped Phase Images of Biological Samples for Normal Incidence	141
8.3	3D Refractive-Index Reconstructions of Biological Samples by Radon, Born, and Rytov Methods	143
8.4	Wrapped Phase Images of Einstein/USAF Chart after Propagating through Biological Samples	144
8.5	Retrieved Projected Fields using Radon, Born, and Rytov Methods	145
8.6	Proposed Flat Metric <i>vs.</i> Efficiency	146
8.7	Interpretation of Flat Metric with Two Discrete Measures	149
8.8	Illustration of How Flat Metric is Computed	153
8.9	Efficiency and Root-Mean-Square Minimum Distance on Single-Molecule Localization Microscopy 2016 Challenge	154
8.10	Closed-Form <i>vs.</i> Discrete Fourier-Ring Correlation	162
8.11	Relative Discrepancy Between Discrete and Closed-Form Fourier-Ring Correlation	163
A.1	Experimental Tomographic Setup	180
A.2	Architecture of the Neural Network for Phase Unwrapping with Deep Image Prior	182
A.3	Loss Function / Signal-to-Noise Ratio with Respect to Iterations	183

A.4	Examples of the Training Dataset of PhaseNet	184
A.5	Organoid-like Reconstructions (Second Example)	186
A.6	Organoid-like Reconstructions (Third Example)	187
A.7	Reconstructed Unwrapped-Phase Images of Simulated Samples with Diverse Cropping Angles	188
A.8	Reconstructed Unwrapped-Phase Images of Simulated Samples with Diverse Maximal Values	190
A.9	Unwrapped-Phase Images of Simulated Samples with Diverse Random Distributions (First Batch)	191
A.10	Unwrapped-Phase Images of Simulated Samples with Diverse Random Distributions (Second Batch)	192
A.11	Unwrapped-Phase Images of Simulated Samples with Diverse Random Distributions (Third Batch)	193
A.12	Unwrapped-Phase Images of Simulated Samples with Diverse Random Distributions (Fourth Batch)	194
A.13	Reconstructions of Experimental Data Obtained by Goldstein’s Algorithm and PhaseNet	195
A.14	Time-Lapse Reconstructions for Supplementary Real Data (First Batch)	196
A.15	Time-Lapse Reconstructions for Supplementary Real Data (Second Batch)	197
A.16	Time-Lapse Reconstructions for Supplementary Real Data (Third Batch)	198
A.17	Time-Lapse Reconstructions by PhaseNet for all Real Data and Corresponding Segmentation	199

List of Tables

2.1	Summary of Existing Reconstruction Algorithms	25
4.1	Proposed Method <i>vs.</i> SEAGLE in Terms of Running Time and Memory Consumption	54
4.2	Relative Error of the Refractive-Index Reconstructions of Simulated Red Blood Cells by Rytov, the Beam Propagation Method, and the Proposed Method	57
5.1	Reconstruction Performance of the Unified Regularized Reconstruction Framework	75
5.2	Relative Error of the Refractive-Index Reconstructions of Red Blood Cells (Intensity-only Measurements)	84
6.1	Root-Mean-Square Error for the Estimated Positions and Amplitudes	104
6.2	Root-Mean-Square Error of the Estimated Positions and Amplitudes for Different Fluorophore Distributions	105
7.1	Baseline Methods for Phase Unwrapping	121
7.2	Quantitative Comparison for Simulated Ellipses with Varying Cropping Angles	123
7.3	Quantitative Comparison for Ellipses with Varying Maximum Phase Values	124
7.4	Quantitative Comparison for the Training Dataset of PhaseNet . . .	127
7.5	Quantitative Comparison for Dataset with Speckle Noise	127

8.1 Proposed Metric for Diverse Reconstruction Methods 145
8.2 Running Time to Compute the Closed-Form Fourier-Ring Correlation 161

Introduction

Computational microscopy is a research field at the intersection of optics and computer science. It tightly integrates the design of acquisition apparatus with algorithmic reconstructions to reveal otherwise-inaccessible information. By relying on such synergy, quantitative phase imaging (QPI) uncovers the three-dimensional (3D) structural information of label-free biological samples. The topic of this thesis is the development of new algorithmic reconstruction methods for QPI. In this introduction, we first give an overview of the scientific context in which this thesis takes place and we then summarize our contributions.

Background

Optical microscopes are essential tools for observing objects that are too small to be seen by the naked eye. Since their rise in the late 19th century, these instruments have played a central role in scientific discoveries with a tremendous impact on our understanding of diseases, and are now commonly used in medicine and biology.

These apparatus generate magnified images by illuminating objects with visible light and by using a system of lenses. There are two main categories: incoherent and coherent microscopes. Incoherent microscopy relies on fluorescent emitters to generate images. The ability to label specific structures makes it the main imaging tool for cell biology, but the usage of exogenous agents and intense illuminations can alter the physiology of the specimens. On the other hand, coherent microscopy obtains images by collecting the light shone on the sample, which makes it a *label-free* microscopy. In the earliest coherent techniques, image contrast arose from the absorption of light by the sample. However, most biological cells and tissues are

transparent in the sense that they do not absorb light significantly and thus exhibit very low contrast, *i.e.*, their structures show little difference from the background.

Transparent objects were rendered visible only after the pivotal contribution of Zernike in the 1940s [3]. Zernike’s phase-contrast microscope generates images from light scattering. Instead of absorbing light, structures in biological specimens recess the speed of light unevenly, which causes light scattering. Therefore, contrast stems from the refractive index (RI) inhomogeneity in the specimen, as RI of a material affects the speed of light through the material. Awarded the Nobel Prize in 1953 for his invention, Zernike may not have anticipated that phase-contrast microscopy would be the precursor of the active research field of QPI.

QPI encompasses a family of coherent microscopes that extracts *quantitative* information about the sample from light scattering, and has seen exciting applications in neuroscience and in biomedical studies [4, 5]. It has the ability to reveal nanoscale features of transparent samples in two or three dimensions [4], which makes it an appealing and complementary approach to fluorescence imaging modalities [6]. Further, in QPI, samples can be studied over an arbitrary period of time without the limitations of photobleaching and phototoxicity. By varying the characteristics of the illuminations, optical diffraction tomography (ODT)—a subfield of QPI—even uncovers the 3D RI maps of samples from a collection of 2D complex-valued measurements.² These 3D RI maps are algorithmically reconstructed by resolving an inverse-scattering problem [10, 11], which requires numerical modelling of the acquisition process. This essentially involves models of light scattering (Chapter 1).

Early works deployed simplified physical models in the search for computational efficiency [10–13], which led to a desirable linear relation between the quantity of interest and the measurements. However, these models are approximative and thus cannot achieve accurate reconstructions of more strongly scattering samples (*e.g.*, thicker).

More recent works circumvented this limitation by partially accounting for the nonlinear nature of light scattering [14, 15]; more specifically, for multiple-scattering events. RI maps reconstructed from these nonlinear models exhibited remarkable improvements over the ones obtained from linear models. These results showed

² In ODT, 2D complex measurements are acquired by interferometric apparatus such as digital holography microscopy, which requires a careful design of the imaging system. Alternatively, ODT from intensity-only measurements has the advantage of simplifying the acquisition apparatus [7–9]. However, this simplification makes the corresponding inverse-scattering problem more challenging (Chapter 2).

that, although these nonlinear models come at the cost of a computational burden, they can dramatically improve the quality of reconstruction in QPI. However, the existing methods do not capture all the multiple-scattering events or reflections, which hinders the imaging of even more strongly-scattering samples. This calls for more accurate models to achieve higher quality in such configurations.

Another challenge in ODT is ill-posedness—a common issue in inverse problems—in the sense that there exist several solutions (*i.e.*, RI maps) that produce similar measurements. The effects of such ill-posedness are exacerbated in ODT by the so-called missing-cone problem, which results in an axial resolution that is worse than the lateral resolution (Chapter 2). To circumvent ill-posedness, the standard practice is to promote solutions with desirable properties by regularizing the RI map. This strategy has been deployed for QPI with classical regularization schemes [14, 16, 17], but the particularity of the missing-cone problem offers a unique opportunity to design dedicated and better-performing regularization techniques.

Contributions

This thesis contributes to the field of QPI at different levels. A central theme is the quest for higher quality of reconstructions and efficient implementation of the deployed methods. To achieve this objective, we develop more accurate models of the acquisition process and efficient reconstruction algorithms including novel learning-based regularization schemes. We consistently formulate our inverse problems within a variational framework. By doing so, we are able to leverage strong commonalities between our works, at the mathematical and implementation levels.

The roadmap of the thesis is displayed in Fig. 1. We hereafter summarize our contributions and refer to the relevant chapters and related publications.

Accurate Discretization of the Lippmann-Schwinger (LiSc) Equation (Chapter 3)

Under the theory of scalar diffraction, the LiSc equation governs light scattering. We properly discretize the LiSc equation and propose a computationally efficient implementation of the obtained nonlinear LiSc based model (LSm). Our method effectively achieves higher accuracy than existing models while mitigating the computational burden.

Related Publications

E. Soubies, T.-a. Pham, and M. Unser, “Efficient inversion of multiple-scattering model for optical diffraction tomography”, *Optics express*, vol. 25, no. 18, pp. 21 786–21 800, 2017. DOI: 10.1364/oe.25.021786

T.-a. Pham, E. Soubies, A. Ayoub, J. Lim, D. Psaltis, and M. Unser, “Three-dimensional optical diffraction tomography with Lippmann-Schwinger model”, *IEEE transactions on computational imaging*, vol. 6, pp. 727–738, 2020. DOI: 10.1109/tci.2020.2969070

ODT from Complex Measurements (Chapter 4)

Using our novel forward model, we formulate an inverse-scattering problem within a modern variational framework and solve it to recover the 3D RI map of the sample when the measurements are complex-valued. Our algorithmic reconstruction involves a nontrivial proximal gradient-based iterative scheme that requires the Jacobian matrix of the nonlinear operator, for which we are able to derive an explicit expression. By accounting for multiple scattering and adding suitable prior knowledge, we significantly improve the quality of reconstruction over the state of the art.

Further, we develop a novel adaptive regularization scheme that mitigates the effects of the missing-cone problem [20]. Our dictionary-learning-based approach learns 2D features of the lateral planes from the specimen and promotes such features on all the planes.

Related Publications

E. Soubies, T.-a. Pham, and M. Unser, “Efficient inversion of multiple-scattering model for optical diffraction tomography”, *Optics express*, vol. 25, no. 18, pp. 21 786–21 800, 2017. DOI: 10.1364/oe.25.021786

T.-a. Pham, E. Soubies, A. Ayoub, J. Lim, D. Psaltis, and M. Unser, “Three-dimensional optical diffraction tomography with Lippmann-Schwinger model”, *IEEE transactions on computational imaging*, vol. 6, pp. 727–738, 2020. DOI: 10.1109/tci.2020.2969070

T.-a. Pham, E. Soubies, A. Ayoub, D. Psaltis, and M. Unser, “Adaptive regularization for three-dimensional optical diffraction tomography”, in *Proceedings of the seventeenth IEEE international symposium on biomedical imaging (ISBI’20)*, Iowa City IA, USA, 2020, pp. 182–186

ODT from Intensity-only Measurements (Chapter 5)

We propose a versatile reconstruction framework to tackle the corresponding inverse-scattering problem with any physical model. We split the optimization task in a way that decouples the complex-field-based reconstruction from the phase retrieval. This allows us to take advantage of our previous contributions and of proximity operators for phase retrieval [21]. In our experiments, we reconstruct RI maps from intensity-only measurements with quality similar to the ones recovered from complex measurements. This shows that, in some settings, intensity information is sufficient for recovering RI maps.

Related Publications

T.-a. Pham, E. Soubies, A. Goy, J. Lim, F. Soulez, D. Psaltis, and M. Unser, “Versatile reconstruction framework for diffraction tomography with intensity measurements and multiple scattering”, *Optics express*, vol. 26, no. 3, pp. 2749–2763, 2018. DOI: 10.1364/oe.26.002749

T.-a. Pham, E. Soubies, J. Lim, A. Goy, F. Soulez, D. Psaltis, and M. Unser, “Phaseless diffraction tomography with regularized beam propagation”, in *Proceedings of the fifteenth IEEE international symposium on biomedical imaging: From nano to macro (ISBI’18)*, Washington DC, USA, 2018, pp. 1268–1271

Single-Molecule Localization Microscopy (SMLM) Meets ODT (Chapter 6)

SMLM is an incoherent microscopy technique that delivers nanoscale resolution by sequentially activating a subset of fluorescent labels and by extracting their superresolved position algorithmically. The emission patterns of each label can be distorted by the sample, which reduces the localization accuracy if not accounted for. Here, we exploit those sample-induced aberrations to recover the RI map. We propose an optimization framework in which we reconstruct the RI map using LSm and optimize the label positions in a joint fashion. In our numerical experiments, we effectively recover the RI map of the sample and further improve the localization—the primary objective of SMLM. Our results lay the foundation of an exciting and novel extension of SMLM.

Related Publications

T.-a. Pham, E. Soubies, F. Soulez, and M. Unser, “Optical diffraction tomography from single-molecule localization microscopy”, *Optics communications*, vol. 499, p. 127 290, 2021. DOI: 10.1016/j.optcom.2021.127290

T.-a. Pham, E. Soubies, F. Soulez, and M. Unser, “Diffraction tomography from single-molecule localization microscopy: Numerical feasibility”, *IEEE international symposium on biomedical imaging*, 2021

Phase Unwrapping with Deep Image Prior (PUDIP) (Chapter 7)

When acquired by an interferometric setup, the phase of 2D complex measurements is wrapped (*i.e.*, modulo 2π). In ODT from complex measurements, we usually have to unwrap such 2D phase images from their wrapped counterparts. To tackle challenging cases such as phase images of organoids, we propose an untrained deep-learning-based method, which incorporates an explicit feedback mechanism. Our comparisons show that our method significantly outperforms the state of the art. While unwrapping challenging 2D phase images has its own merits, this approach also paves the way for ODT for large samples (*e.g.*, organoids) with higher reliability.

Related Publication

F. Yang, T.-A. Pham, N. Brandenberg, M. P. Lutolf, J. Ma, and M. Unser, “Robust Phase Unwrapping via Deep Image Prior for Quantitative Phase Imaging”, *IEEE transactions on image processing*, vol. 30, pp. 7025–7037, 2021. DOI: 10.1109/tip.2021.3099956

Metrics for ODT and SMLM (Chapter 8)

In this chapter, our first contribution is a metric with no ground-truth requirement for ODT reconstructions, which could be of use for biological samples. Then, we leverage the unique features of SMLM (*i.e.*, list of estimated positions, image rendering) to investigate metrics from new perspectives. Building upon a broad benchmarking of localization software packages [27], we propose a novel optimal-transport-based metric for SMLM which captures both detection and localization performance and relies on solid mathematical foundations. Finally, we derive a

closed-form expression of the Fourier ring-correlation (FRC) for the particular case of SMLM, which allows us to investigate the classical way of computing FRC (*i.e.*, SMLM image rendering and discrete Fourier transform (DFT)).

Related Publications

A. B. Ayoub, T.-A. Pham, J. Lim, M. Unser, and D. Psaltis, “A method for assessing the fidelity of optical diffraction tomography reconstruction methods using structured illumination”, *Optics communications*, p. 124486, 2019. DOI: 10.1016/j.optcom.2019.124486

Q. Denoyelle, T.-a. Pham, P. del Aguila Pla, D. Sage, and M. Unser, “Optimal-transport-based metric for SMLM”, in *Proceedings of the eighteenth IEEE international symposium on biomedical imaging (ISBI’21)*, Nice, French Republic, 2021, pp. 797–801

T.-a. Pham, E. Soubies, D. Sage, and M. Unser, “Closed-form expression of the Fourier ring-correlation for single-molecule localization microscopy”, in *Proceedings of the sixteenth IEEE international symposium on biomedical imaging: From nano to macro (ISBI’19)*, Venice, Italian Republic, 2019, pp. 321–324

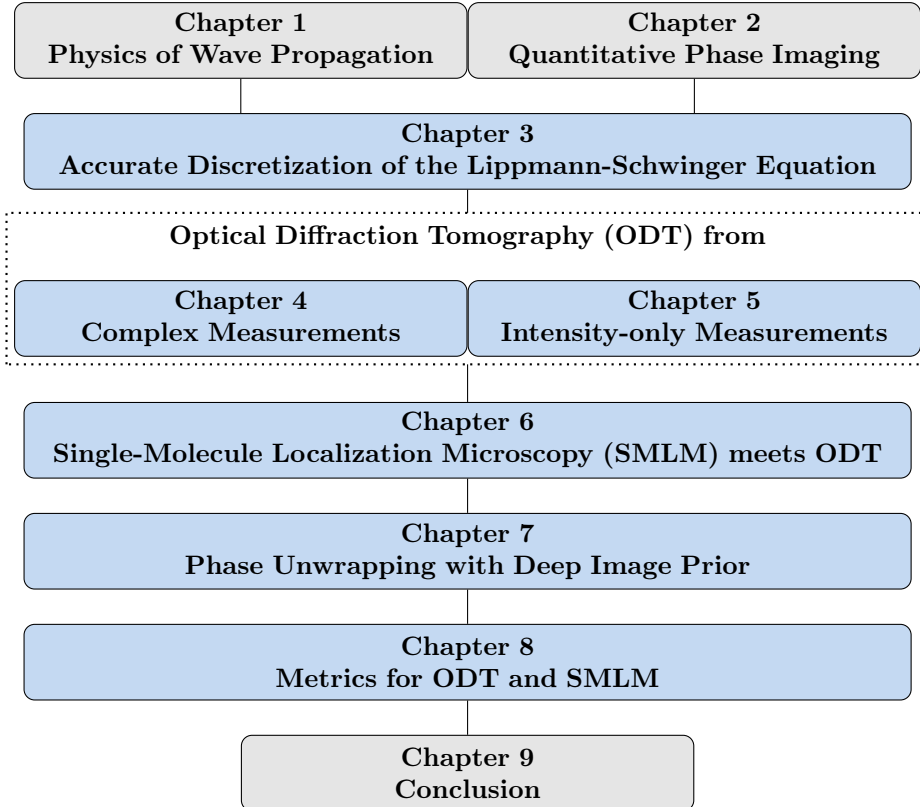


Figure 1: Roadmap of the thesis.

Chapter 1

Physics of Wave Propagation: Let There Be Light Scattering

Light scattering plays a key role in QPI. This physical phenomenon is governed by the Maxwell equations, which describe light as vectorial electromagnetic fields. The theory of scalar diffraction has the tremendous advantage of simplifying such vectorial fields to complex scalar fields. Although scalar fields do not provide an exact description of light scattering in an inhomogeneous medium, this framework remains an excellent approximation [31], and this thesis is developed within this framework.¹

In this chapter, we describe the underlying mathematics of light scattering. In Section 1.1, we start from the wave equation and derive the equations that dictate light scattering. In Section 1.2, we present existing numerical models which are derived from these equations.

¹ It is noteworthy that there exist methods that account for the vectorial nature of light, such as the finite difference time domain [32] or the discrete dipole approximation [33], but at the cost of a higher computational burden.

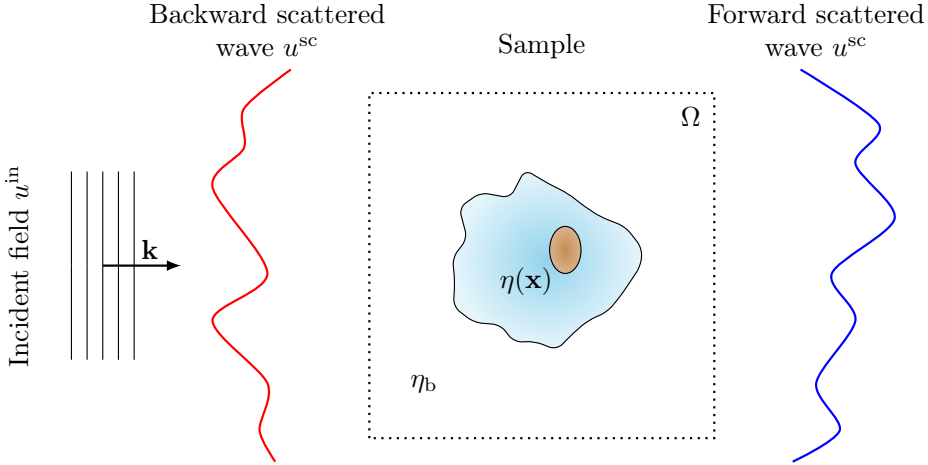


Figure 1.1: A sample of RI $\eta(\mathbf{x})$ is immersed in a medium of index η_b and illuminated by an incident plane wave (wave vector \mathbf{k}). The interaction of the wave with the object produces forward and backward scattered waves.

1.1 Theory of Scalar Diffraction: Continuous-Domain Formulation

Let us consider an unknown object of RI $\eta : \Omega \rightarrow \mathbb{R}$ that lies in the region $\Omega \subseteq \mathbb{R}^D$ ($D \in \{2, 3\}$) within a medium of RI $\eta_b \in \mathbb{R}$, as depicted in Fig. 1.1. This sample is illuminated by the incident plane wave

$$u^{\text{in}}(\mathbf{x}, t) = \text{Re} \left(u_0 e^{j\{\mathbf{k}, \mathbf{x}\} - j\omega t} \right), \quad (1.1)$$

where the wave vector $\mathbf{k} \in \mathbb{R}^D$ specifies the direction of the wave propagation, $\omega \in \mathbb{R}$ denotes its angular frequency, and $u_0 \in \mathbb{C}$ defines its complex envelope (amplitude). The resulting total electric field $u(\mathbf{x}, t)$ satisfies the wave equation

$$\Delta u(\mathbf{x}, t) - \frac{\eta^2(\mathbf{x})}{c^2} \frac{\partial^2 u}{\partial t^2}(\mathbf{x}, t) = 0, \quad (1.2)$$

where $\Delta = \sum_{d=1}^D \frac{\partial^2}{\partial x_d^2}$ is the Laplacian operator and $c \simeq 3 \times 10^8 \text{m/s}$ is the speed of light in free space. By substituting $u(\mathbf{x}, t) = \text{Re}(u(\mathbf{x})e^{-j\omega t})$ into (1.2), where $u(\mathbf{x})$ is the complex amplitude of $u(\mathbf{x}, t)$, we obtain the inhomogeneous Helmholtz equation

$$\Delta u(\mathbf{x}) + k_0^2 \eta^2(\mathbf{x})u(\mathbf{x}) = 0, \quad (1.3)$$

where $k_0 = \omega/c$ is the propagating constant in free space. The total field $u(\mathbf{x})$ is the sum of the scattered field $u^{\text{sc}}(\mathbf{x})$ and the incident field $u^{\text{in}}(\mathbf{x})$, which is itself a solution of the homogeneous Helmholtz equation $\Delta u^{\text{in}}(\mathbf{x}) + k_b^2 u^{\text{in}}(\mathbf{x}) = 0$, where $k_b = k_0 \eta_b$. Accordingly, (1.3) can be rewritten as [12]

$$\Delta u^{\text{sc}}(\mathbf{x}) + k_b^2 u^{\text{sc}}(\mathbf{x}) = -f(\mathbf{x})u(\mathbf{x}), \quad (1.4)$$

where $f(\mathbf{x}) = k_0^2(\eta^2(\mathbf{x}) - \eta_b^2)$ defines the scattering potential function. It follows that

$$u^{\text{sc}}(\mathbf{x}) = \int_{\Omega} g(\mathbf{x} - \mathbf{x}')f(\mathbf{x}')u(\mathbf{x}') d\mathbf{x}', \quad (1.5)$$

where $g(\mathbf{x})$ is the Green's function of the shift-invariant differential operator $(\Delta + k_b^2 \mathbf{I})$, where \mathbf{I} is the identity operator. Specifically, g verifies $\Delta g(\mathbf{x}) + k_b^2 g(\mathbf{x}) = -\delta(\mathbf{x})$, where δ is the Dirac distribution and the minus sign is a convention used in physics. Under Sommerfeld's radiation condition, $g(\mathbf{x})$ is given by [34, and references therein]

$$g(\mathbf{x}) = \begin{cases} \frac{j}{4} H_0^{(1)}(k_b \|\mathbf{x}\|), & D = 2, \\ \frac{1}{4\pi} \frac{e^{jk_b \|\mathbf{x}\|}}{\|\mathbf{x}\|}, & D = 3. \end{cases} \quad (1.6)$$

There, $H_0^{(1)}$ is the Hankel function of the first kind. Finally, the total field $u(\mathbf{x})$ is governed by the LiSc equation—an integral formulation of the Helmholtz equation

$$u(\mathbf{x}) = u^{\text{in}}(\mathbf{x}) + \int_{\Omega} g(\mathbf{x} - \mathbf{x}')f(\mathbf{x}')u(\mathbf{x}') d\mathbf{x}'. \quad (1.7)$$

In the next section, we present several approximations of (1.3) or (1.7) that have been introduced in the literature.

1.2 Numerical Models for Wave Propagation

Pioneering works developed simplified models which we denote as linear models, because they yield a linear relation between the RI / scattering potential and the total field. More recent studies investigated nonlinear models of wave propagation. Although these models are computationally more expensive than the linear ones, they exhibit a higher accuracy. Here, we briefly describe several models, with no consideration for their respective validity. More complete descriptions can be found in [14, 15, 35–39]. Without loss of generality and to simplify the presentation, we consider that $D = 3$ and $\Omega = [-L/2, L/2]^3$ for $L > 0$.

1.2.1 Linear Models

Radon Approximation (X-Ray Transform)

The Radon approximation [35] only accounts for the phase delay of the incident field that is induced by the scattering potential. Without loss of generality, we consider that the incident field is a plane wave propagating along the x_3 -axis (*i.e.*, $\mathbf{k} = (0, 0, k_b)$). We first denote the total field by

$$u(\mathbf{x}) = a(\mathbf{x})e^{jk_b x_3}, \quad (1.8)$$

where one can interpret (1.8) as a plane wave propagating along x_3 , modulated by the complex envelope $a : \mathbb{R}^3 \rightarrow \mathbb{C}$ [14]. Observing that $k_0^2 \eta^2(\mathbf{x}) = f(\mathbf{x}) + k_b^2$, (1.3) reads as

$$\Delta_{\perp} u(\mathbf{x}) + \frac{\partial^2}{\partial x_3^2} u(\mathbf{x}) + (f(\mathbf{x}) + k_b^2)u(\mathbf{x}) = 0, \quad (1.9)$$

where we explicitly write the Laplacian operators along the x_3 direction and along the transverse directions $\Delta_{\perp} = \frac{\partial^2}{\partial x_1^2} + \frac{\partial^2}{\partial x_2^2}$. Separately, we have

$$\begin{aligned} \frac{\partial^2}{\partial x_3^2} a(\mathbf{x})e^{jk_b x_3} &= \frac{\partial}{\partial x_3} \left(\frac{\partial a(\mathbf{x})}{\partial x_3} e^{jk_b x_3} + a(\mathbf{x})jk_b e^{jk_b x_3} \right) \\ &= e^{jk_b x_3} \left(\frac{\partial^2 a(\mathbf{x})}{\partial x_3^2} + 2jk_b \frac{\partial a(\mathbf{x})}{\partial x_3} - k_b^2 a(\mathbf{x}) \right). \end{aligned} \quad (1.10)$$

By using (1.10) and substituting (1.8) into (1.9), we obtain

$$e^{jk_b x_3} \left(\Delta_{\perp} + \frac{\partial^2}{\partial x_3^2} + 2jk_b \frac{\partial}{\partial x_3} + f(\mathbf{x})\mathbb{I} \right) a(\mathbf{x}) = 0. \quad (1.11)$$

The Radon approximation involves two simplifications. The first is the slowly-varying envelope approximation [31, 40], which allows us to suppress the second derivative of a with respect to x_3 , if $|\frac{\partial^2}{\partial x_3^2} a| \ll |k_b \frac{\partial}{\partial x_3}|$. In the second simplification, the diffraction part is assumed to be negligible, *i.e.*, the transverse Laplacian operator Δ_\perp is suppressed. Then, (1.11) reads as

$$\frac{\partial a(\mathbf{x})}{\partial x_3} = \frac{j}{2k_b} f(\mathbf{x})a(\mathbf{x}). \quad (1.12)$$

The solution of (1.12) yields the Radon approximation

$$a(\mathbf{x}) = a_0 e^{\frac{j}{2k_b} \int_{-L/2}^{x_3} f(x_1, x_2, x'_3) dx'_3}, \quad (1.13)$$

where $a_0 = a(x_1, x_2, -L/2) = u^{\text{in}}(x_1, x_2, -L/2)$. In (1.13), we see that the phase of the total field $u(x_1, x_2, L/2) = a_0 e^{\frac{j}{2k_b} \int_{-L/2}^{L/2} f(x_1, x_2, x'_3) dx'_3} e^{jk_b L/2}$ is effectively proportional to the line integral of the scattering potential along the direction of the plane wave propagation.²

Born Approximation

Born approximation [12, 42] assumes that the sample is weakly scattering and simplifies (1.7) to

$$u(\mathbf{x}) = u^{\text{in}}(\mathbf{x}) + \int_{\Omega} g(\mathbf{x} - \mathbf{x}') f(\mathbf{x}') u^{\text{in}}(\mathbf{x}') d\mathbf{x}', \quad (1.14)$$

where $u \approx u^{\text{in}}$ in the integral of (1.7). Now we see that the total field is linearly dependent on the scattering potential. The (first-order) Born approximation only accounts for single-scattering events.

² In 2D, the Radon and X-ray transforms are equivalent. In 3D, the Radon transform integrates along 2D planes while the X-ray transform integrates along lines [41].

1.2.2 Nonlinear Models

Rytov Approximation

We refer the reader to [36] for a complete derivation of the Rytov approximation. Here, we report the relation between the total field and the scattering potential

$$u(\mathbf{x}) = u^{\text{in}}(\mathbf{x}) + \exp\left(\frac{\int_{\Omega} g(\mathbf{x} - \mathbf{x}')f(\mathbf{x}')u^{\text{in}}(\mathbf{x}') d\mathbf{x}'}{u^{\text{in}}(\mathbf{x})}\right). \quad (1.15)$$

Note that this (first-order) Rytov approximation only accounts for single-scattering events.

Beam-Propagation Method (BPM)

In 3D, BPM [14, 43], also known as the multislice model [7, 9, 44, 45], propagates the wave field along the direction x_3 in a slice-by-slice manner. The 2D slice of the total field $u(\cdot, \cdot, x_3 + \delta x_3)$ is obtained from $u(\cdot, \cdot, x_3)$ by computing

$$u(x_1, x_2, x_3 + \delta x_3) = e^{jk_0 n(\mathbf{x})\delta x_3} \times \mathcal{F}^{-1} \left\{ \mathcal{F}\{a(\cdot, \cdot, x_3)\} \times e^{-j \frac{\omega_{x_1}^2 + \omega_{x_2}^2}{\sqrt{k_b^2 - \omega_{x_1}^2 - \omega_{x_2}^2}} \delta x_3} \right\}. \quad (1.16)$$

We see that BPM alternates between diffraction and refraction steps and, by construction, ignores reflections.

Iterative Born Approximation (IBA)

IBA [15, 46] improves upon the first-order Born approximation by partially capturing multiple-scattering events. IBA considers the K -term recursive model

$$u^k(\mathbf{x}) = u^{\text{in}}(\mathbf{x}) + \int_{\Omega} g(\mathbf{x} - \mathbf{x}')f(\mathbf{x}')u^{k-1}(\mathbf{x}') d\mathbf{x}', \quad (1.17)$$

where $u^0 = 0$ and $k = 1, \dots, K$. Note that this iterative scheme can diverge for samples with large RI [15].

Split-Step Non-Paraxial Method (SSNP)

SSNP significantly improves upon BPM by propagating the derivative of the field as well. We refer the reader to [37, 47, 48] for a detailed description of the method.

Multi-Layer Born Model (MLB)

MLB significantly outperforms BPM by modeling the refraction step more accurately [38], while conserving the fast computation of BPM. We can interpret the refraction step of BPM as a simple Radon approximation; in MLB, the authors adopted the first-order Born approximation instead. More precisely, the total field at each 2D slice acts as the incident field of the next slice (see (1.14)). Further, they also derive a similar model which is compatible with a reflective imaging system.

Modified Born Series

In [49–51], the authors improve upon IBA by adopting a modified Green’s function in the recursive formula. This makes the convergence conditions much less stringent while conserving the fast computation of IBA. This model accounts for multiple-scattering events as well as reflections.

Series Expansion with Accelerated Gradient Descent on Lippmann-Schwinger Equation (SEAGLE)

In [52], the authors numerically solve (1.7) to compute the total field, which accounts for multiple-scattering events as well as reflections. We will provide a more detailed description in Chapter 3.

Machine Learning Regularized Solution of the Lippmann-Schwinger Equation

In [53], the authors solve (1.7) by using a recurrent neural network with long short-term memory. Once trained, the network surprisingly generalizes well to scattering potentials that differ from the training set.

1.3 Summary

In this chapter, we introduced the Helmholtz and LiSc equations that govern the physics of light scattering in an inhomogeneous medium. Under diverse assumptions, many approximate models can be derived from these equations. In general, a more accurate model comes at the price of a higher computational cost. In the next chapter, we will give an overview of QPI. We will see that numerical light scattering models play a key role in QPI; in particular, their accuracy is crucial to the quality of the recovered volumes.

Chapter 2

Quantitative Phase Imaging (QPI)

QPI encompasses a large family of label-free microscopes. They have emerged as valuable tools for recovering structural information about cells and tissues. This unique ability makes QPI a complementary method to fluorescence microscopy, while exhibiting reduced phototoxicity and no photobleaching. In the past decades, several QPI modalities were developed, going from two-dimensional (2D) to 3D imaging, with the more recent variants relying on algorithmic reconstructions. By illuminating the sample with light, QPI modalities have the ability to reveal structural information without any label. At the heart of this unique feature lies the complex physics of light scattering which was detailed in Chapter 1. For most biological specimens, incident light as a complex scalar field will mainly undergo phase change by the RI inhomogeneity of the sample.

In this chapter, we give an overview of QPI modalities with a particular emphasis on light-scattering models. We then present a reconstruction framework that is commonly used in QPI.

2.1 Two-dimensional (2D) QPI: All You Need Is Phase

2D QPI modalities obtain images that represent quantitative maps of the specimen-induced phase delays [54].¹ Since microscope objectives can only record intensities of wave fields, several techniques have been developed in the past decades to measure phase images [4]. Here, we briefly present the main modalities in 2D QPI. Note that there exist a plethora of other variants that are well described in [4, 55–58].

2.1.1 Digital Holography Microscopy (DHM)

The working principle of DHM stems from the seminal work of Gabor [59], which exploits interference between the incident and total fields. DHM splits the incident field into an object beam that illuminates the sample and a reference beam [60]. After its propagation through the sample, the first beam is distorted by the sample, thus introducing phase delays. By contrast, the reference beam has a controlled phase perturbation. Both beams are then rejoined by a beam splitter to interfere and the resulting hologram is recorded by the imaging system. To understand the rationale behind this technique, consider the recorded hologram with the incident field $u^{\text{in}} : \mathbb{R}^2 \rightarrow \mathbb{C}$

$$\begin{aligned}
 I(y_1, y_2) &= |u(y_1, y_2) + u^{\text{in}}(y_1, y_2)e^{j\beta(y_1, y_2)}|^2 \\
 &= |u(y_1, y_2)|^2 + |u^{\text{in}}(y_1, y_2)|^2 + 2\langle u(y_1, y_2), u^{\text{in}}(y_1, y_2)e^{j\beta(y_1, y_2)} \rangle \\
 &= |u(y_1, y_2)|^2 + |u^{\text{in}}(y_1, y_2)|^2 \\
 &\quad + 2|u(y_1, y_2)||u^{\text{in}}(y_1, y_2)|\cos(\beta(y_1, y_2) - \phi(y_1, y_2)), \quad (2.1)
 \end{aligned}$$

where $\beta : \mathbb{R}^2 \rightarrow \mathbb{R}$ is the controlled phase perturbation, and, $u : \mathbb{R}^2 \rightarrow \mathbb{C}$ and $\phi : \mathbb{R}^2 \rightarrow \mathbb{R}$ denote the total field and its phase, respectively. Here, the quantity of interest is the cross-term that contains the phase information. Phase-shifting interferometry acquires M intensity measurements with incremented phase delays which are spatially constant in the incident field (*i.e.*, $\beta(y_1, y_2) = \beta_m$, for $m = 1, \dots, M$). Generally, ϕ is determined from four intensity measurements using $\beta_m =$

¹ From another perspective, the Radon approximation applies here (Chapter 1).

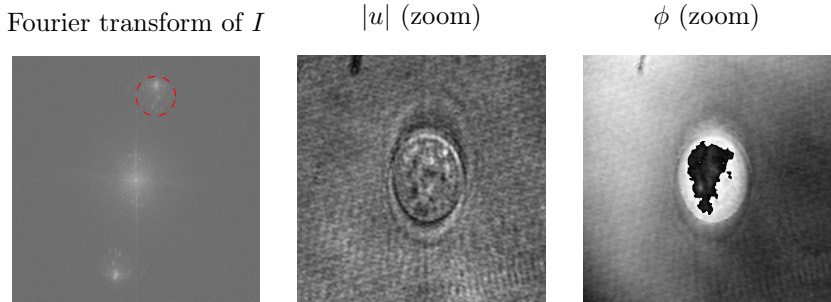


Figure 2.1: Principle of off-axis DHM. Left: Fourier transform of the acquired intensity image ($\log(1 + |\hat{I}|)$). The circle indicates the filter that allows extraction of the complex field. Middle and Right: Amplitude and phase image, respectively.

$\{0, \pi/2, 3\pi/2, \pi\}$ [61] and is given by

$$\phi(y_1, y_2) = \arctan \left(\frac{I_{3\pi/2}(y_1, y_2) - I_{\pi/2}(y_1, y_2)}{I_0(y_1, y_2) - I_\pi(y_1, y_2)} \right). \quad (2.2)$$

Alternatively, off-axis interferometry circumvents the need for several intensity measurements by adding a spatially-varying phase perturbation $\beta(y_1, y_2) = \alpha_1 y_1 + \alpha_2 y_2$ [62] instead. By doing so, the cross-term is modulated, which shifts the quantity of interest in the Fourier domain. Then, a simple filtering allows the recovery of the complex total field (*i.e.*, in the Fourier domain, the filter is a disk shifted according to $\beta(y_1, y_2)$). We display in Fig. 2.1 the different steps in off-axis DHM.

2.1.2 2D Fourier Ptychography (FP)

2D FP is another popular approach to recover phase images [63–67]. FP relies on varying the illumination angles of the incident field and algorithmically reconstructs a phase image from multiple intensity measurements. In 2D FP, reconstruction methods assume that the sample is thin (*i.e.*, 2D) and establish a direct mapping

between the intensity measurements and the Fourier transform of the phase image. For further details, we refer the reader to the excellent review [55].

2.2 Three-dimensional (3D) QPI

Advanced QPI modalities reveal 3D structural information using a series of 2D measurements [68]. Similar to 2D FP, algorithmic reconstructions exploit the angular diversity of the illuminations to get 3D RI maps (or equivalently scattering-potentials maps). RI maps are an intrinsic property of the samples from which other biologically relevant quantities can be derived [69]. We will see that there exist many variants within this very rich family of tomographic imaging systems. We draw a distinction between the class of 2D measurements used to reconstruct the RI map: complex or intensity-only measurements. In the first category, the imaging modality is usually referred to as ODT. The measurements are acquired with an interferometric apparatus (*e.g.*, DHM). In the second category, 3D FP [7] or intensity diffraction tomography [8] rely on intensity-only measurements, which has the advantage of simplifying the acquisition apparatus. LED array is a popular illumination system, although other alternatives exist [70]. In this thesis, we abusively refer to both categories as ODT from complex or intensity-only measurements.

2.2.1 Reconstruction from Complex Measurements

In the early works [10, 11], RI reconstruction is performed using a suitable variant of the filtered back-projection algorithm (FBP) [88]. This kind of approach is computationally efficient, but the underlying model ignores the effect of diffraction. Under the assumption that the scattered field is weak compared to the incident one, improved methods rely on the first Born model [12, 71], the first Rytov model [13, 73], or other more advanced variants [89, 90] (Chapter 1). All are approximations of the LiSc equation. Such simplifications lead to computationally-efficient back-propagation algorithms for reconstructing RI maps. Similar to FBP, these algorithms draw a direct mapping between quantities derived from the measurements and the 3D Fourier transform of the RI maps [12, 13, 36]. The main difference is that the Born model works directly with the scattered field, whereas the Rytov model uses the unwrapped phase of the measurements—an inverse problem which we will detail in Chapter 7. Several studies have shown that the Rytov model yields

more accurate reconstructions than the Born model [16, 73, 91]. Yet, the validity of these linear models is mainly restricted to weakly scattering samples.

To overcome this limitation, nonlinear models that account for multiple scattering have been proposed, such as BPM [14, 87], the contrast source-inversion method [92, 93], hybrid methods [84, 94], the conjugate-gradient method [79, 80, 83], the IBA [15], or an improved version [51]. Finally, within a regularized variational approach, iterative forward models that solve the LiSc equation have been recently used in [18, 52, 84]. Note that this is also closely related to the discrete dipole approximation (DDA) and the methods of moments mainly used in microwave imaging [33], although recent works applied DDA to a vectorial imaging system [84]. The reader can refer to [68] for a review on ODT reconstruction methods for bioimaging.

2.2.2 Reconstruction from Intensity-only Measurements

The more challenging problem of reconstructing 3D RI maps from intensity-only measurements was recently addressed in the context of FP, although related methods were previously proposed in other domains [72, 74, 75, 78, 81, 82, 85, 86, 95, 96]. In 3D FP, the acquisition procedure is similar to 2D FP, but algorithmic reconstructions account for the three dimensionality of the sample instead [7, 77, 97]. The conventional reconstruction scheme consists of alternating between recovering the measurement phase and reconstructing the RI of the sample. The phase retrieval is generally performed with the Gerchberg-Saxton (GS) projection operator [98], while the RI reconstruction step is essentially the same as in ODT (intensity and phase). Over the years, the forward models have evolved from “linear” [63, 97]² to nonlinear [7, 9, 38, 45, 51, 77]. For more details, we refer the reader to [99]. In Table 2.1, we have compiled a (non-exhaustive) list of reconstruction methods for both holographic (*i.e.*, intensity and phase) and intensity-only measurements; note that we also refer to the relevant chapters of this thesis in the table.

² To be accurate, the actual forward model includes a squared magnitude, which is nonlinear *per se*. Here, “linear” solely refers to the underlying light-scattering model.

2.3 Variational Approaches for Optical Diffraction Tomography (ODT)

In the variational framework, we estimate the quantity of interest (*e.g.*, scattering potential $\mathbf{f} \in \mathbb{R}^N$) from the measurements $\{\mathbf{y}_q \in \mathbb{R}^M\}_{q \in [1 \dots Q]}$ by solving the optimization problem

$$\hat{\mathbf{f}} \in \left\{ \arg \min_{\mathbf{f} \in B} \sum_{q=1}^Q \mathcal{D}(\mathbf{H}_q(\mathbf{f}), \mathbf{y}_q) + \tau \mathcal{R}(\mathbf{L}\mathbf{f}) \right\}. \quad (2.3)$$

The operator $\mathbf{H}_q : \mathbb{R}^N \rightarrow \mathbb{R}^M$ for $q = 1, \dots, Q$ models the acquisition of measurements, which, in ODT, involves numerical models for wave propagation (Chapter 1). The functional $\mathcal{D} : \mathbb{R}^M \times \mathbb{R}^M \rightarrow \mathbb{R}_{\geq 0}$ measures the fidelity of the model to the data. The regularization term $\mathcal{R} : \mathbb{R}^{S \times S'} \rightarrow \mathbb{R}_{\geq 0}$ promotes solutions with suitable properties. For instance, $\mathcal{R} = \|\cdot\|_1$ promotes the sparsity of the quantity $\mathbf{L}\mathbf{f}$, where $\mathbf{L} : \mathbb{R}^N \rightarrow \mathbb{R}^{S \times S'}$ is a linear operator (*e.g.*, the identity, gradient, or Hessian operator). The scalar $\tau > 0$ is a tradeoff parameter that balances the effect of these two terms. The set B represents physical constraints on the scattering potential (*e.g.*, nonnegativity constraint $B = \mathbb{R}_{\geq 0}^N$).

From a Bayesian point of view, we can relate \mathcal{D} to the log-likelihood of the noise distribution. Because the number of measurements M is much smaller than the number of unknowns N , the data-fidelity term \mathcal{D} does not generally admit a unique global minimizer. The regularization term $\mathcal{R}(\mathbf{L}\cdot)$ and the set B should thus be chosen in order to discriminate between candidate solutions using the knowledge that one has on the observed sample.

2.3.1 Limited Angles of Illuminations: Missing-Cone Problem

In general, the illumination angles are limited to a cone due to the numerical aperture of objective lenses (Fig. 2.2). This restriction has strong implications on the quality of recovered RI maps, which is usually referred to as the missing-cone problem. This generates anisotropic artifacts, which effects are more prominent along the axial direction (*i.e.*, the axis of the cone). Put simply, the lateral resolution is better than its axial resolution. To circumvent this issue, reconstruction methods

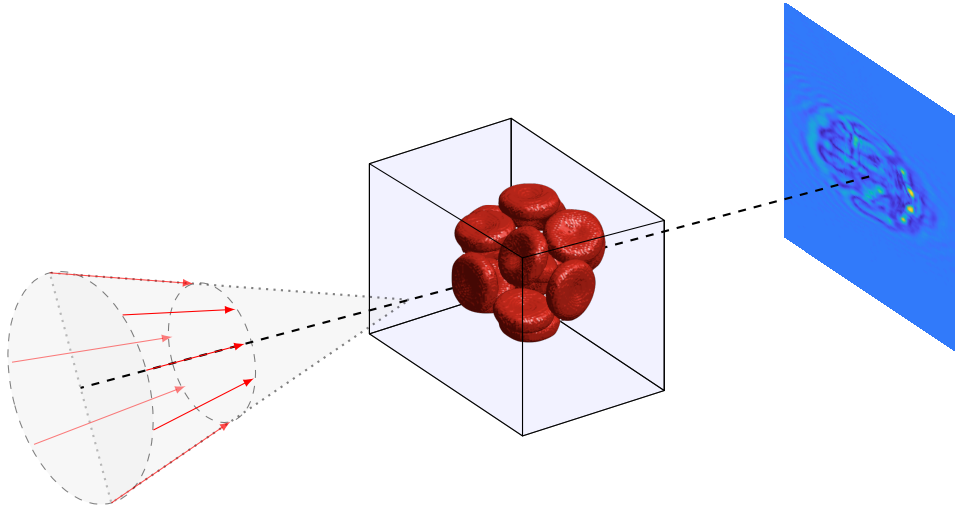


Figure 2.2: Cone of illuminations. The arrows represent the direction of propagation of the illuminations which are limited to a cone around the optical axis.

usually rely on regularization to fill the missing axial information; this strategy was shown to significantly improve the quality of the reconstruction [16, 73]. More recently, deep-learning methods were designed for that specific problem [100–103].

It is noteworthy that there exist other imaging systems which circumvent such issues by rotating the sample instead of (or in addition to) varying the illumination angles [68, 104–106].

2.4 Summary

In this chapter, we presented the basics of QPI and its numerous 2D and 3D variants. To recover 3D RI maps of the sample, ODT—a subfield of QPI—usually relies on solving an optimization problem. We described the mathematical formal-

ism which underlies such variational approaches. We also characterized a common issue met in 3D QPI: the missing-cone problem. Stemming from the design of imaging systems, this problem generates artifacts which are more prominent along the optical axis. This chapter allows us to emphasize the determining role of two elements: the forward model \mathbf{H} which simulates light scattering and the regularization term \mathcal{R} that imposes some prior knowledge on the reconstructed volume. Higher accuracy of \mathbf{H} usually improves the quality of reconstruction and the prior knowledge alleviates the negative effects of the missing-cone problem and other mismatches.

In the next chapters, we will present our contributions on new algorithmic reconstruction methods for ODT. We start in the following chapter with an accurate nonlinear physical model based on the LiSc equation, and our tricks to alleviate the inherent computational burden.

Table 2.1: Summary of existing RI reconstruction algorithms from holographic (*i.e.*, complex) or intensity-only measurements. Ref.: Reference. Algo.: Algorithm. Reg.: Regularization. M.: Modified. §: Chapter. IBA: iterative Born approximation. BPM: Beam-propagation method. MLB: Multi-layer Born. LSm: Lippmann-Schwinger (equation). SSNP: Split-step non-paraxial method. PO: Proximity operator. GS: Gerchberg-Saxton (projection operator). E.: Embedded. HS: Hessian-Schatten norm. TV: Total-variation constraint. *a.h.*: *ad hoc*. 3PIE: Ptychographical iterative engine. GD: Gradient descent. FBS: Forward-backward splitting. iter: Iterative. ADMM: Alternating direction method of multipliers.

Complex measurements				Intensity-only measurements				
Ref.	Model	Algo.	Reg.	Ref.	Model	Phase	RI	Reg.
[10, 11]	FBP	direct	–	[63–67, 72]	Born	GS	direct	–
[12, 71]	Born	direct	–	[74, 75]	Rytov	E	iter	–
[13, 73]	Rytov	direct	–	[76]	Born	GS	iter	TV
[16]	Rytov	iter	TV	[45, 77]	BPM	GS	3PIE	–
[79, 80]	LiSc	iter	–	[7, 78]	BPM	GS / E	FBS	<i>a.h.</i>
[83, 84]	LiSc	iter	<i>a.h.</i>	[81, 82]	LiSc	E / <i>a.h.</i>	iter	–
[14, 87]	BPM	FBS	TV	[85, 86]	LiSc	E	iter	<i>a.h.</i>
[15]	IBA	FBS	TV	[9]	BPM	GS / E	FBS	TV
[37]	SSNP	FBS	TV	[38]	MLB	E	FBS	TV
[51]	M. IBA	FBS	TV					
[52], §4	LiSc	FBS	TV/HS	§5	Any	PO	ADMM	TV

Chapter 3

Accurate Discretization of the Lippmann-Schwinger (LiSc) Equation

3.1 Introduction

In this chapter, we propose an accurate and efficient model for wave propagation that is based on the LiSc equation and accounts for multiple-scattering events (both reflection and transmission).¹

3.2 Contributions

Our contributions are twofold. First, we properly discretize the LiSc equation to obtain a linear system; second, we devise efficient numerical to solve this linear system. In particular, we efficiently handle the singularity of the Green's function with the help of a truncation trick and a memory-saving strategy described in Sections 3.5 and 3.6, respectively. In Section 3.7, we compare the accuracy of

¹ The content of this chapter is based on [18, 19].

the proposed model with other models for wave propagation. In Section 3.8, we compare different algorithms for solving the obtained linear system.

3.3 Continuous-Domain Formulation

Here, we briefly recall the 3D continuous-domain formulation for the sake of completeness (Chapter 1). Let $\eta : \Omega \rightarrow \mathbb{R}$ denotes the continuously-defined RI of a sample whose support is assumed to be included in the region of interest $\Omega \subset \mathbb{R}^3$. Without loss of generality and to simplify the presentation, let us consider that $\Omega = [-L/2, L/2]^3$ for $L > 0$. The interaction of the sample with a monochromatic incident field $u^{\text{in}} : \mathbb{R}^3 \rightarrow \mathbb{C}$ of wavelength λ produces a scattered field $u^{\text{sc}} : \mathbb{R}^3 \rightarrow \mathbb{C}$. The resulting total field $u = u^{\text{sc}} + u^{\text{in}}$ is governed by the LiSc equation

$$u(\mathbf{x}) = u^{\text{in}}(\mathbf{x}) + \int_{\Omega} g(\mathbf{x} - \mathbf{z}) f(\mathbf{z}) u(\mathbf{z}) d\mathbf{z}, \quad (3.1)$$

where $f(\mathbf{x}) = k_{\text{b}}^2 (\eta(\mathbf{x})^2 / \eta_{\text{b}}^2 - 1)$ is the scattering potential. Here, $k_{\text{b}} = 2\pi\eta_{\text{b}}/\lambda$ is the wavenumber in the surrounding medium and η_{b} the corresponding RI. Finally, $g : \mathbb{R}^3 \rightarrow \mathbb{C}$ is the free-space Green's function which, under Sommerfeld's radiation condition, is given by [34]

$$g(\mathbf{x}) = \frac{\exp(jk_{\text{b}}\|\mathbf{x}\|)}{4\pi\|\mathbf{x}\|}. \quad (3.2)$$

3.4 Discrete Formulation

Let us discretize Ω into $N = n^3$ voxels.² Then, the computation of the total field $\mathbf{u}^{\text{sc}} \in \mathbb{C}^N$ in the volume is given by [18, 52, 107]

$$\mathbf{u} = (\mathbf{I} - \mathbf{G} \mathbf{diag}(\mathbf{f}))^{-1} \mathbf{u}^{\text{in}} \quad (3.3)$$

where $\mathbf{I} \in \mathbb{R}^{N \times N}$ is the identity matrix, $\mathbf{diag}(\mathbf{f}) \in \mathbb{R}^{N \times N}$ is a diagonal matrix formed out of the entries of \mathbf{f} , and $\mathbf{f} \in \mathbb{R}^N$, $\mathbf{u}^{\text{in}} \in \mathbb{C}^N$, and $\mathbf{u} \in \mathbb{C}^N$ are sampled version of f , u^{in} , and u within Ω , respectively. The matrix $\mathbf{G} \in \mathbb{C}^{N \times N}$ is the discrete counterpart of the continuous convolution with the Green's function in (3.1).

² The generalization to the case where there is a different number of points in each dimension is straightforward.

One will have noticed that (3.3) requires the resolution of a linear system. This can be efficiently performed using a conjugate-gradient method [18] (CG) or a biconjugate-gradient stabilized method [108] (BiCG) as we shall see. Needless to say, the matrices \mathbf{G} and \mathbf{P} are never explicitly built. Instead, we exploit the fact that the application of the corresponding linear operators can be efficiently performed using the fast Fourier transform (FFT). It is worthy to mention that we assume that the incident field is perfectly known within Ω in this chapter.

3.5 Green's Function Discretization Inside the Support

Because of the singularity of the Green's function (3.2) as well as of its Fourier transform (*i.e.*, $\hat{g}(\boldsymbol{\omega}) = 1/(k_b^2 - \|\boldsymbol{\omega}\|^2)$ with $\boldsymbol{\omega} \in \mathbb{R}^3$), \mathbf{G} in (3.3) cannot be defined through a naive discretization of g . In this section, we describe how \mathbf{G} has to be defined in order to minimize the approximation error with respect to the continuous model (3.1).

First, let us recall that we aim at computing the total field u only inside Ω and that the support of f is itself assumed to be included in Ω . Hence, (3.1) can be equivalently written as, $\forall \mathbf{x} \in \Omega$,

$$u(\mathbf{x}) = u^{\text{in}}(\mathbf{x}) + \int_{\Omega} g_t(\mathbf{x} - \mathbf{z}) f(\mathbf{z}) u(\mathbf{z}) d\mathbf{z}, \quad (3.4)$$

where g_t is a truncated version of the Green's function. More precisely, g_t is defined by

$$g_t(\mathbf{x}) = \text{rect}\left(\frac{\|\mathbf{x}\|}{2\sqrt{3}L}\right) g(\mathbf{x}), \quad (3.5)$$

where $\text{rect}(x) = \{1, |x| \leq 1/2; 0, \text{ otherwise}\}$. With this definition, one easily gets the equivalence between (3.1) and (3.4), as illustrated in Fig. 3.1.

To the best of our knowledge, this observation has to be attributed to Vainikko [109] but has then been revitalized by Vico *et al.* [110]. It is essential to a proper discretization of the LiSc equation (3.1). Specifically, we have that

$$\hat{g}_t(\boldsymbol{\omega}) = \frac{1}{\|\boldsymbol{\omega}\|^2 - k_b^2} \left(1 - e^{i\sqrt{3}Lk_b} (\cos(\sqrt{3}L\|\boldsymbol{\omega}\|) + jk_b\sqrt{3}L \text{sinc}(\sqrt{3}L\|\boldsymbol{\omega}\|)) \right) \quad (3.6)$$

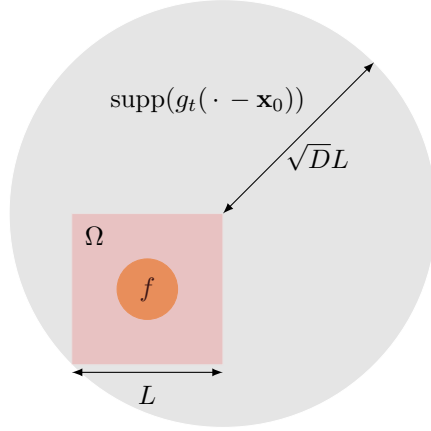


Figure 3.1: Illustration in dimension two (*i.e.*, $D = 2$) of the equivalence between (3.1) and (3.4). $g_t(\cdot - \mathbf{x}_0)$ denotes g_t shifted by $\mathbf{x}_0 = (L/2, L/2)$.

for $\|\boldsymbol{\omega}\| \neq k_b$, which can be extended by continuity as

$$\hat{g}_t(\boldsymbol{\omega}) = j \left(\frac{\sqrt{3}L}{2k_b} - \frac{e^{j\sqrt{3}Lk_b}}{2k_b^2} \sin(\sqrt{3}Lk_b) \right) \quad (3.7)$$

when $\|\boldsymbol{\omega}\| = k_b$. The practical outcome is that (3.4) can now be discretized in the Fourier domain since \hat{g}_t is a smooth function.

We now show how $g_t * v$, for $v \in L_2(\mathbb{R}^3)$, can be numerically evaluated using FFTs and we provide error bounds on the approximation. The proof is provided in Appendix A.3.2.

Theorem 3.5.1. *Let $v \in L_2([-\frac{L}{2}, \frac{L}{2}]^3)$ and $\mathbf{v} \in \mathbb{C}^N$ be the sampled version of v using $n > k_b L / \pi$ sampling points in each dimension ($N = n^3$). Let \mathbf{v}_p be the p -times zero-padded version of \mathbf{v} . Define $h = L/n$ and $\delta = 2\pi/(Lp)$. Then, considering a trapezoidal quadrature rule for (3.4), we get that $\forall \mathbf{k} \in \llbracket \frac{-n}{2} + 1; \frac{n}{2} \rrbracket^3$*

$$(\mathbf{G}\mathbf{v})[\mathbf{k}] = (\mathbf{F}^{-1}(\hat{\mathbf{g}}_t \odot \hat{\mathbf{v}}_p))[\mathbf{k}], \quad (3.8)$$

where $\widehat{\mathbf{g}}_{\mathbf{t}} = (\widehat{g}_{\mathbf{t}}(\delta\mathbf{q}))_{\mathbf{q} \in \llbracket \frac{-np}{2} + 1; \frac{np}{2} \rrbracket^3}$ and $\widehat{\mathbf{v}}_p = \mathbf{F}\mathbf{v}_p$.

Moreover, if v has $(q-1)$ continuous derivatives for $q \geq 3$ and a q th derivative of bounded variations, we have the error bound

$$|(g_{\mathbf{t}} * v)(h\mathbf{k}) - (\mathbf{G}\mathbf{v})[\mathbf{k}]| \leq \frac{C^{\text{tr}}}{n^q} + \frac{C^{\text{al}}}{n^{q-2}} + \frac{C^{\text{tp}}}{p^2}, \quad (3.9)$$

where C^{al} , C^{tr} , and C^{tp} are positive constants that are associated to the errors due to the aliasing in \mathbf{v} , the truncation of the Fourier integral, and the trapezoidal quadrature rule used to approximate this integral, respectively.

Remark 3.5.1. Equation (3.8) is hiding a cropping operation. Indeed, the result of $\mathbf{F}^{-1}(\widehat{\mathbf{g}}_{\mathbf{t}} \odot \widehat{\mathbf{v}}_p)$ is defined on the grid $\llbracket \frac{-np}{2} + 1; \frac{np}{2} \rrbracket^3$ but we only retain the elements that belong to $\llbracket \frac{-n}{2} + 1; \frac{n}{2} \rrbracket^3$.

Remark 3.5.2. The assumption that $n > k_{\text{b}}L/\pi \Leftrightarrow k_{\text{b}} < \pi/h$ ensures that the “peaks” of $|\widehat{g}_{\mathbf{t}}(\boldsymbol{\omega})|$ for $\|\boldsymbol{\omega}\| = k_{\text{b}}$ are included in the frequency domain associated to the DFT (i.e., $[-\pi/h, \pi/h]^3$). This is a natural and minimal requirement to reduce the approximation error.

From Theorem 3.5.1, one sees that the number of sampling points n controls both the aliasing error and the error due to the truncation of the Fourier integral. It is noteworthy that these bounds decrease with the smoothness of v (i.e., q). On the other hand, the padding factor p controls the error that results from the trapezoidal quadrature rule.

Remark 3.5.3. A simple argument suggests that the padding factor should be at least $p = 4$ to properly capture the oscillations of $\widehat{g}_{\mathbf{t}}$. Indeed, in the spatial domain, the diameter of the support of $g_{\mathbf{t}}$ is $2\sqrt{3}L \approx 3.4L$. Hence, in order to satisfy the Shannon-Nyquist criterion, the considered spatial domain should be at least of size $4L$, which corresponds to a padding factor $p = 4$.

To assess the accuracy of the implementation of \mathbf{G} provided by Theorem 3.5.1, we consider the convolution of the Green's function with a 3D Gaussian source $v(\mathbf{x}) = \exp(-\|\mathbf{x}\|^2/(2\sigma^2))/(\sigma^3(2\pi)^{\frac{3}{2}})$. For this particular setting, an analytical expression of $g * v$ is known [110]. In Fig. 3.2, we report the relative error

$$\epsilon_{\text{rel}} = \frac{\|\mathbf{v}_{\text{exact}} - \mathbf{G}\mathbf{v}\|}{\|\mathbf{v}_{\text{exact}}\|}, \quad (3.10)$$

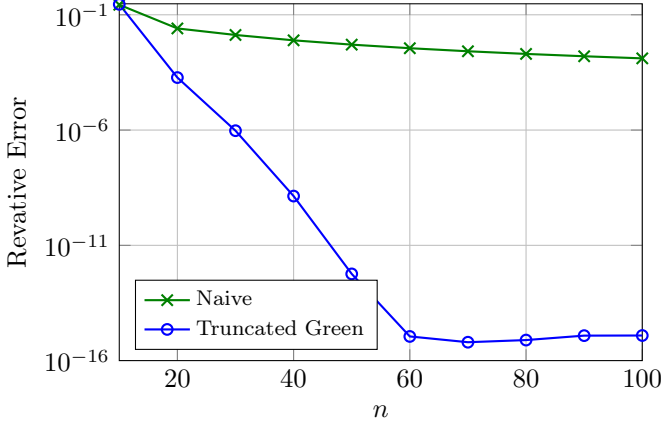


Figure 3.2: Relative error (3.10) as a function of the number of discretization points n per side of Ω . The truncated Green’s function approach is compared to a naive discretization of the Green’s function in the spatial domain. The standard deviation of the Gaussian source is set to $\sigma = 0.4$, the size of the domain $L = 1$, and the wavenumber $k_b = 1.5$. For the truncated Green’s function approach, we set $p = 4$.

where $\mathbf{v}_{\text{exact}} = ((g * v)[h\mathbf{k}])_{\mathbf{k} \in [-\frac{n}{2}+1; \frac{n}{2}]^3}$ contains the samples of the analytical solution. We compare the proposed discretization (Theorem 3.5.1) with a naive discretization of g in the spatial domain (by “cropping” the singularity). Clearly, the truncated Green’s function approach is by far superior to a naive discretization of g in the spatial domain.

3.6 Memory Savings

According to Theorem 3.5.1, an accurate computation of the field inside Ω requires one to zero-pad the volume \mathbf{v} . From Remark 3.5.3, we should set at least $p = 4$. This can lead to severe computational and memory issues for the reconstruction of large 3D volumes. Fortunately, as mentioned in [110], this computation can be

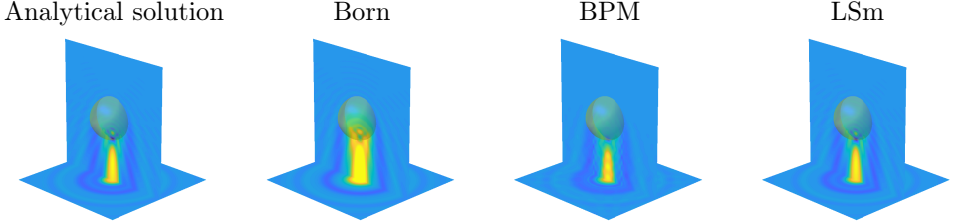


Figure 3.3: Simulated scattering of a monochromatic wave ($\lambda = 532\text{nm}$) by a bead embedded in water ($\eta_b = 1.3388$). The bead has a diameter of 3λ and a RI of 1.4388. The reported total fields are obtained through the analytical solution, the Born model, and the proposed model for $p = 4$ and $h = \lambda/16$ (i.e., $n = 144$).

reformulated as a discrete convolution with a modified kernel that only involves the twofold padding $p = 2$. We summarize this result in Proposition 3.6.1 and provide a detailed proof in Appendix A.3.3. Moreover, we provide an expression of the modified kernel that reveals how one can build it directly on the grid $[-n + 1; n]^3$.

Proposition 3.6.1. *Let $p \in 2\mathbb{N} \setminus \{0\}$. Then, $\forall \mathbf{k} \in [-\frac{n}{2} + 1; \frac{n}{2}]^3$, we have that*

$$(\mathbf{F}^{-1}(\widehat{\mathbf{g}}_t \odot \widehat{\mathbf{v}}_p))[\mathbf{k}] = (\mathbf{F}^{-1}(\widehat{\mathbf{g}}_t^p \odot \widehat{\mathbf{v}}_2))[\mathbf{k}], \quad (3.11)$$

where \mathbf{v}_2 is a twofold zero-padded version of \mathbf{v} , and $\widehat{\mathbf{g}}_t^p$ is the modified kernel

$$\widehat{\mathbf{g}}_t^p[\mathbf{k}] = \frac{8}{p^3} \sum_{\mathbf{s} \in [0; \frac{p}{2} - 1]^3} \mathbf{F}^{-1}(\widehat{\mathbf{g}}_t[\frac{p}{2} \cdot - \mathbf{s}])[\mathbf{k}] e^{\frac{-2j\pi}{np} \mathbf{k}^T \mathbf{s}}, \quad (3.12)$$

3.7 Comparison of Models Accuracy

To conclude these comparisons, we compare the accuracy of the LiSc-based model (LSm) with the popular Born approximation and BPM. To that end, we consider the interaction of a plane wave with a bead since an analytical expression of the

total field is known for this setting [111]. The total fields computed by the three approaches are displayed in Fig. 3.3. In addition, we provide the theoretical total field. One can appreciate the gain in accuracy that the proposed method brings over the standard approximations used in ODT.

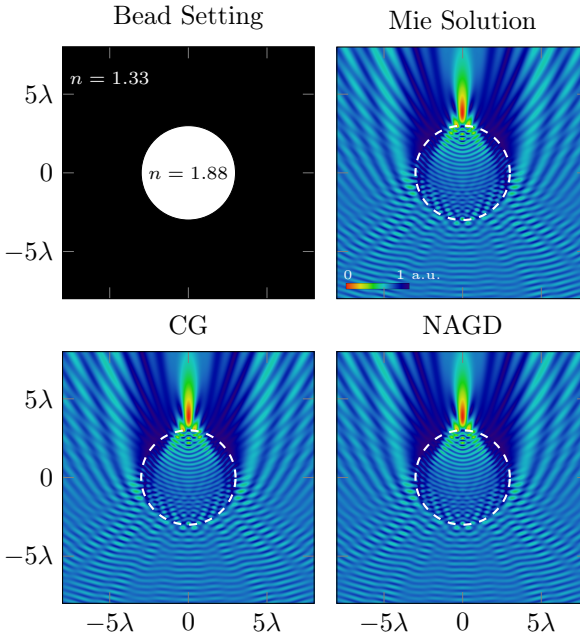


Figure 3.4: Forward-model solution for a bead with radius 3λ and a contrast of 1 using CG (bottom-left) and NAGD (bottom-right), as well as the Mie solution (top-right). The setting used for this experiment is presented in the top-left panel. The colormap is the same for each figure.

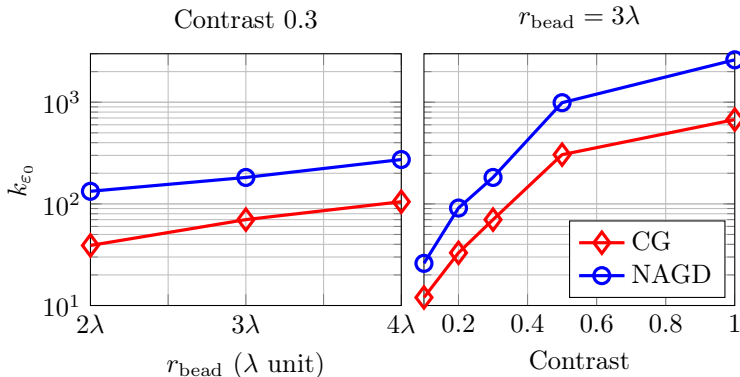


Figure 3.5: Evolution of the number of iterations k_{ϵ_0} needed to let the relative error (3.13) fall below $\epsilon_0 = 10^{-2}$ as function of bead radius (left) and bead contrast (right).

3.8 Solvers for LiSc-based Model

There exist many quadratic optimization algorithms to solve (3.3) [112]. Liu *et al* [52, 107] used the Nesterov accelerated gradient descent (NAGD), which allowed them to auto-differentiate through the steps of the solver (as we shall see in Chapter 4). In a non-optical regime, several works suggested that Krylov-based methods [112] were suitable alternatives [84, 113, 114], such as the CG [115]. We now provide numerical evidence that GC is more efficient than NAGD for solving (3.3). To this end, we consider a 2D circular object (bead) of radius r_{bead} and RI n_{bead} immersed into water ($n_b = 1.333$), as presented in Fig. 3.4 (top-left). In such a situation, an analytic expression of the total field is provided by the Mie theory [111, 116]. Hence, at each iteration k , we compute the relative error ϵ_k of the current estimate \mathbf{u}^k to the Mie solution \mathbf{u}_{Mie} as

$$\epsilon_k = \frac{\|\mathbf{u}^k - \mathbf{u}_{\text{Mie}}\|^2}{\|\mathbf{u}_{\text{Mie}}\|^2}. \quad (3.13)$$

In our experiment, the bead is impinged by a plane wave of wavelength $\lambda = 406$ nm. The region of interest is square with a side length of 16λ (see top-left panel of Fig. 3.4). It is sampled using 1,024 points along each side. We used a fine grid in order to limit the impact of numerical errors related to discretization. The wave source corresponds to the bottom border of this region. Then, as in [52, 107], we refer to the RI n_{bead} by its contrast with respect to the background medium, defined as $\max(|\mathbf{f}|)/(k_0^2 n_b^2)$. We show in Fig. 3.5 the evolution of k_{ε_0} , which is the number of iterations needed to let the relative error (3.13) fall below $\varepsilon_0 = 10^{-2}$. One can observe that CG is much more efficient than NAGD, in particular for large contrasts. Our comparison in terms of a number of iterations is fair because the computational cost of one iteration is the same for both algorithms. Note that the descent step of NAGD was adapted during the iterations following the same rule as in [52, 107].

Finally, the solution obtained with the two algorithms for $r_{\text{bead}} = 3\lambda$ and a contrast of 1 are shown in Fig. 3.4. The analytic Mie solution is also provided for comparison. From these figures, one can appreciate the high accuracy obtained by solving (3.3), as first demonstrated in [52, 107].

3.9 Green's Function Discretization Outside the Support

As we will see in the next chapters, we are also interested in evaluating the total field outside of Ω at M points, which involves another discretization of the Green's function $\tilde{\mathbf{G}} \in \mathbb{C}^{M \times N}$. In that case, we do not need to evaluate the Green's function at its singularity. In 2D settings, $\tilde{\mathbf{G}} \in \mathbb{C}^{M \times N}$ is sometimes accessible explicitly [18, 52, 117]. By contrast, the scale of 3D settings prevents this approach. Fortunately, we are interested in particular 3D settings in which the M points lie on a regular grid embedded in a plane Γ . By exploiting such planarity, we can significantly reduce the memory and the computational burden of the evaluation of $\tilde{\mathbf{G}}\mathbf{v}$.

Let $x_\Gamma > 0$ be the axial position of the plane of interest Γ (*i.e.*, $\forall \mathbf{x} \in \Gamma$, $x_3 = x_\Gamma$). Then, letting $v = f \cdot u$ and expressing the integral in (3.1) using a

numerical quadrature along the third dimension, we get, $\forall \mathbf{x} = (x_1, x_2, x_\Gamma) \in \Gamma$,

$$(g * v)(\mathbf{x}) = \sum_{k=-\frac{n}{2}+1}^{\frac{n}{2}} h \int_{[-\frac{L}{2}, \frac{L}{2}]^2} g(\mathbf{x} - \mathbf{z}_k) v(\mathbf{z}_k) dz_{k_1} dz_{k_2}, \quad (3.14)$$

where $\mathbf{z}_k = (z_{k_1}, z_{k_2}, kh)$.

From (3.14), $g * v$ is computed as a sum of 2D aperiodic convolutions. Considering that the sampling step at the plane Γ is identical to that of the volume Ω , the 2D convolutions in (3.14) is evaluated in the same way as described in Theorem 3.5.1. This strategy reduces the computational complexity of the application of $\tilde{\mathbf{G}}$ to $\mathcal{O}(nM \log(M))$. Note that, if the sampling step at the plane is q times that of the volume (*i.e.*, $h' = qh$, $q \in \mathbb{N}$), one can simply downsample the result of the above procedure by q .

3.10 Summary

In this chapter, we presented a model to simulate wave propagation that accounts for multiple-scattering events. We properly discretized the LiSc equation and assessed the accuracy and numerical efficiency of the obtained model. Our comparisons show that the proposed model (LSm) achieves high accuracy while mitigating the computational burden.

Now that we are equipped with our accurate and efficient physical model, we will tackle the challenging case of inverse-scattering problems in the next chapter.

Chapter 4

ODT from Complex Measurements

4.1 Introduction

In this chapter, we present a reconstruction framework for ODT from complex measurements using our LiSc based model (LSm, see Chapter 3).¹ We recall that, in ODT, the acquisition setup sequentially illuminates the sample from different angles. For each illumination, the outgoing complex total field (*i.e.*, the scattered field) is recorded by a DHM [60, 118]. Then, from this set of measurements, one reconstructs a 3D RI map by solving an inverse-scattering problem. To understand better the contributions of this chapter, we first present the challenges one typically faces in 3D ODT.

4.2 Challenges in 3D ODT

So far, the use of the more sophisticated LiSc based models and DDA² has been mostly limited to microwave imaging [79, 119, 120] (see also the numerous references

¹ The content of this chapter is based on [18–20].

² The DDA is a model that accounts for polarization—the vectorial nature of light.

listed in [121]). Although led by the same underlying physics, ODT differs from microwave imaging on several aspects that further increases the difficulty of the reconstruction problem.

- The direction of propagation of the incident wave is restricted to a small cone around the optical axis (Fig. 4.1), resulting in the well-known missing-cone problem [16] (Chapter 2).
- In typical ODT applications such as biology, the size of the sample is significantly larger (*e.g.*, $100\times$) than the wavelength of the incident wave. This requires a fine discretization that entails very large memory requirements.
- The large size of the detector leads to numerical challenges for the computation of the far-field.
- The benefit of a theoretical expression of the incident wave field, as used in microwave imaging [121], is made unlikely in ODT due to unknown distortions that are inherent to the system.

These challenges have hindered the adoption of sophisticated models in ODT, with notable exceptions [84, 122] that focused on the reflective mode and considered relatively simple non-biological samples.

4.3 Contributions

This chapter builds upon the prior works [18, 52, 117] that are dedicated to the resolution of the 2D inverse scattering problem using an LiSc-based model. We extend these works to the 3D ODT problem. Our main contribution is the development of an accurate and efficient implementation of the forward model in 3D. This is crucial to obtain good reconstructions while keeping the computational burden of the method reasonable for large-scale volumes. More precisely, we provide a description on how to implement a LiSc-based model for inverse scattering by tackling these challenging difficulties. These contributions complete the ones of Chapter 3—a detailed description of the discretization of the Green’s function (inside and outside Ω).

- *Estimation of the incident field (Section 4.4.3).* We build the volume of the incident field by numerical propagation of a real acquisition of it at the detector plane. In particular, we propose a strategy that results in significantly reduced numerical errors.
- *Efficient computation of the gradient (Section 4.5.3).* We rely on a gradient-based optimization scheme to reconstruct the RI map, which requires the Jacobian matrix of our nonlinear physical model. We derive an explicit expression of the Jacobian matrix and this allows us to reduce the memory and computational burdens.

Finally, to deal with the missing-cone problem, we deploy a regularized variational reconstruction approach (Section 4.5). In Section 4.6, we present reconstructions of biological samples for both simulated and real data, and compare them to those from baselines methods. Further, in Section 4.7, we propose a novel regularization scheme designed to mitigate the missing-cone problem.

4.4 Accurate and Efficient Implementation of the Forward Model

For the sake of completeness, we briefly recall the LiSc equation in the continuous domain. Let $\eta : \Omega \rightarrow \mathbb{R}$ denotes the continuously-defined RI of a sample whose support is assumed to be included in the region of interest $\Omega \subset \mathbb{R}^3$. Let us consider that $\Omega = [-L/2, L/2]^3$ for $L > 0$. The interaction of the sample with a monochromatic incident field $u^{\text{in}} : \mathbb{R}^3 \rightarrow \mathbb{C}$ of wavelength λ produces a scattered field $u^{\text{sc}} : \mathbb{R}^3 \rightarrow \mathbb{C}$. The resulting total field $u = u^{\text{sc}} + u^{\text{in}}$ is governed by the LiSc equation

$$u(\mathbf{x}) = u^{\text{in}}(\mathbf{x}) + \int_{\Omega} g(\mathbf{x} - \mathbf{z})f(\mathbf{z})u(\mathbf{z}) \, d\mathbf{z}, \quad (4.1)$$

where $f(\mathbf{x}) = k_{\text{b}}^2 (\eta(\mathbf{x})^2/\eta_{\text{b}}^2 - 1)$ is the scattering potential. Here, $k_{\text{b}} = 2\pi\eta_{\text{b}}/\lambda$ is the wavenumber in the surrounding medium and η_{b} the corresponding RI. Finally, $g : \mathbb{R}^3 \rightarrow \mathbb{C}$ is the free-space Green's function which, under Sommerfeld's radiation condition, is given by [34]

$$g(\mathbf{x}) = \frac{\exp(jk_{\text{b}}\|\mathbf{x}\|)}{4\pi\|\mathbf{x}\|}. \quad (4.2)$$

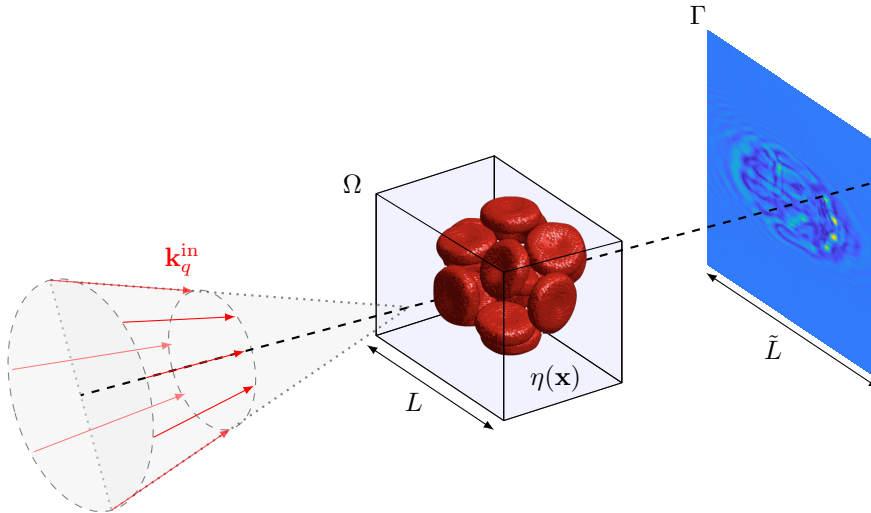


Figure 4.1: Principle of ODT. The arrows represent the wave vectors $\{\mathbf{k}_q^{\text{in}}\}_{q=1}^Q \in \mathbb{R}^3$ of the Q incident plane waves $\{u_q^{\text{in}}\}_{q=1}^Q$ which are limited to a cone around the optical axis.

Equation (4.1) completely characterizes the image formation model in ODT. Using an interferometric setup, the total field u is recorded at the measurement plane $\Gamma = [-\tilde{L}/2, \tilde{L}/2]^2$, $\tilde{L} \geq L$, of the camera. This measurement plane lies outside Ω at a distance denoted by $x_\Gamma > 0$. Finally, we denote by $M = m^2$ the number of pixels of the detector.

4.4.1 Discrete Formulation

To numerically solve the ODT inverse problem, (4.1) has to be properly discretized. To do so, we first discretize Ω into $N = n^3$ voxels.³ Then, the computation of the

³ The generalization to the case where there is a different number of points in each dimension is straightforward.

scattered field $\mathbf{y}^{\text{sc}} \in \mathbb{C}^M$ at the camera plane Γ follows a two-step process [18, 52],

$$\mathbf{u} = (\mathbf{I} - \mathbf{G} \text{diag}(\mathbf{f}))^{-1} \mathbf{u}^{\text{in}} \quad (4.3)$$

$$\mathbf{y}^{\text{sc}} = \mathbf{P} \tilde{\mathbf{G}} \text{diag}(\mathbf{f}) \mathbf{u}, \quad (4.4)$$

where $\mathbf{I} \in \mathbb{R}^{N \times N}$ is the identity matrix, $\text{diag}(\mathbf{f}) \in \mathbb{R}^{N \times N}$ is a diagonal matrix formed out of the entries of \mathbf{f} , and $\mathbf{f} \in \mathbb{R}^N$, $\mathbf{u}^{\text{in}} \in \mathbb{C}^N$, and $\mathbf{u} \in \mathbb{C}^N$ are sampled version of f , u^{in} , and u within Ω , respectively. The matrix $\mathbf{G} \in \mathbb{C}^{N \times N}$ is the discrete counterpart of the continuous convolution with the Green's function in (4.1) (Section 3.5). Similarly, $\tilde{\mathbf{G}} \in \mathbb{C}^{M \times N}$ is a matrix that, given \mathbf{u} and \mathbf{f} inside Ω , gives the scattered field at the measurement plane Γ (Section 3.9). Finally, $\mathbf{P} \in \mathbb{C}^{M \times M}$ models the effect of the pupil function of the microscope and can also encode the contribution of a free-space propagation to account for an optical refocus of the measurements.

As discussed in Chapter 3, (4.3) requires the resolution of a linear system, which we perform efficiently using BiCG [108]. Yet, (4.3) carries the main computational complexity of the forward process (4.3)-(4.4). To obtain the scattered field at the camera plane Γ , a naive approach would be to compute the total field \mathbf{u} in (4.3) on a large region that includes Γ . Here, the introduction of $\tilde{\mathbf{G}}$ allows one to restrict the computation of \mathbf{u} to the smaller region Ω as soon as it fully contains the support of the sample [18, 52]. This significantly reduces the computational burden of the forward process.

The first step (4.3) actually corresponds to compute the (discrete) total field in Ω , which was thoroughly described in Chapter 3. Notably, we dealt with the singularity of the Green's function g via a simple yet elegant truncation trick. The second step (4.4) involves the discretization of the Green's function for the measurements $\tilde{\mathbf{G}}$ and requires us to model the pupil function. The discretization of the Green's function for the measurements is addressed in Section 3.9. Here, the plane of interest is simply the camera plane with M voxels. In addition, the acquisition setup for real data provides only 2D measurements of the incident field at the focal plane. However, LSm needs a 3D incident field. We will now describe efficient and accurate methods to tackle those problems.

4.4.2 Free-Space Propagation and Pupil Function

The last matrix to describe in (4.4) is \mathbf{P} . It models the lowpass filtering behavior of the microscope and can also be used to perform a free-space propagation of the field. For instance, this is required for the acquisition setup described in Section 4.6.2. Hence, \mathbf{P} corresponds to the discrete convolution operator associated to the continuously defined kernel $p \in L_2(\mathbb{R}^2)$ that depends on the point-spread function (PSF) of the system as well as the considered propagation kernel. Although the output of $\tilde{\mathbf{G}}$ (scattered field on Γ) is not compactly supported, it enjoys fast decay, which allows us to apply \mathbf{P} via a FFT with suitable padding.

4.4.3 Computation of the 3D Incident Field

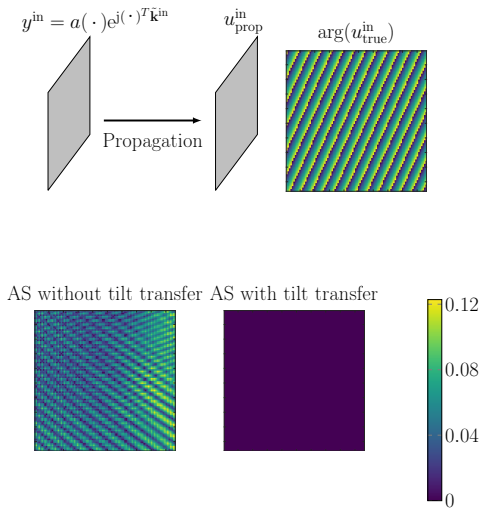


Figure 4.2: Propagation of the incident field. Top: Scheme of the numerical experiment (left) and phase ($\arg(\cdot)$) of the expected propagated field (right). Bottom: Error map $|u_{\text{true}}^{\text{in}} - u_{\text{prop}}^{\text{in}}|$ of the angular spectrum (AS) method [31] without and with tilt transfer (left and right respectively).

The evaluation of the forward model (4.3) and (4.4) at a given point $\mathbf{f} \in \mathbb{R}^N$ requires the knowledge of the 3D incident field $\mathbf{u}^{\text{in}} \in \mathbb{C}^N$. In real data, we only acquire a 2D measurement of each incident field. Here, we propose to build this volume through the free-space propagation of the 2D measurement $\mathbf{y}^{\text{in}} \in \mathbb{C}^M$ of this field at the detector plane Γ . This is possible as the area of Γ is assumed to be larger than that of a face of the volume Ω since $L \leq \tilde{L}$.

Let us denote by $y^{\text{in}} : \Gamma \rightarrow \mathbb{C}$ the continuous version of \mathbf{y}^{in} to simplify the presentation. Then, we get from the angular spectrum method [31] that, $\forall \mathbf{x} = (x_1, x_2, x_3) \in \Omega$,

$$u^{\text{in}}(\mathbf{x}) = (p_{x_3} * y^{\text{in}})(x_1, x_2). \quad (4.5)$$

There, p_{x_3} is the propagation kernel that is defined in the Fourier domain by

$$\hat{p}_z(\boldsymbol{\omega}) = \exp\left(-j(x_\Gamma - z)\sqrt{k_b - (\omega_1^2 + \omega_2^2)}\right), \quad (4.6)$$

where x_Γ denotes the position of the measurement plane Γ .

Because both the propagation kernel and the measured incident field are not compactly supported, a naive computation of the aperiodic convolution in (4.5) would introduce significant errors within the estimated volume u^{in} . The difficulty lies in the way of properly extending the measured field y^{in} outside Γ to ensure that the result of the convolution inside Ω is valid. For instance, a zero padding or a simple periodization are not satisfactory as they would introduce large discontinuities in the amplitude and/or the phase of y^{in} .

Instead, let us inject in (4.5) the expression of $y^{\text{in}}(\mathbf{x}) = a(\mathbf{x}) \exp(j\mathbf{x}^T \tilde{\mathbf{k}}^{\text{in}})$, where $a : \Gamma \rightarrow \mathbb{C}$ is the complex amplitude of the field and $\tilde{\mathbf{k}}^{\text{in}} = (k_1^{\text{in}}, k_2^{\text{in}})$ corresponds to the restriction of the wave vector $\mathbf{k}^{\text{in}} \in \mathbb{R}^3$ to its first two components, leading to

$$\begin{aligned} u^{\text{in}}(\mathbf{x}) &= \left(p_{x_3} * a(\cdot) e^{j(\cdot)^T \tilde{\mathbf{k}}^{\text{in}}}\right)(\tilde{\mathbf{x}}) \\ &= \frac{1}{(2\pi)^2} \int_{\mathbb{R}^2} \widehat{p}_{x_3}(\boldsymbol{\omega}) \hat{a}(\boldsymbol{\omega} - \tilde{\mathbf{k}}^{\text{in}}) e^{j\boldsymbol{\omega}^T \tilde{\mathbf{x}}} d\boldsymbol{\omega} \\ &= \frac{e^{j\tilde{\mathbf{x}}^T \tilde{\mathbf{k}}^{\text{in}}}}{(2\pi)^2} \int_{\mathbb{R}^2} \widehat{p}_{x_3}(\boldsymbol{\omega} + \tilde{\mathbf{k}}^{\text{in}}) \hat{a}(\boldsymbol{\omega}) e^{j\boldsymbol{\omega}^T \tilde{\mathbf{x}}} d\boldsymbol{\omega} \\ &= e^{j\tilde{\mathbf{x}}^T \tilde{\mathbf{k}}^{\text{in}}} \left(a * p_{x_3}(\cdot) e^{-j(\cdot)^T \tilde{\mathbf{k}}^{\text{in}}}\right)(\tilde{\mathbf{x}}), \end{aligned} \quad (4.7)$$

with $\tilde{\mathbf{x}} = (x_1, x_2)$ and $\boldsymbol{\omega} = (\omega_1, \omega_2) \in \mathbb{R}^2$. Hence, (4.5) can be equivalently expressed as a 2D aperiodic convolution of the complex amplitude a with the kernel $p_{x_3}(\cdot)e^{-j(\cdot)^T \tilde{\mathbf{k}}^{\text{in}}}$, followed by a modulation in the space domain. This approach is called tilt transfer because the shift of y^{in} in the Fourier domain is transferred to the propagation kernel [123, 124]. The advantage of this formulation is that, by contrast to y^{in} , the complex amplitude a is not far from a constant signal, up to some noise and optical aberrations. Hence, we compute (4.7) using a periodic convolution with minor discretization artifacts.

The advantage of this approach is illustrated in Fig. 4.2 where we propagate a slice of an ideal tilted plane wave y^{in} using the angular spectrum method with and without tilt transfer. The difference between the expected incident field $u_{\text{true}}^{\text{in}}$ and the propagated field $u_{\text{prop}}^{\text{in}}$ is depicted in the bottom panel. Clearly, the tilt transfer allows one to significantly reduce the discretization errors and attenuate the aliasing artifacts.

4.5 Reconstruction Framework

4.5.1 Problem Formulation

Following the formulation in Section 2.3, we adopt a standard variational approach to recover the scattering potential \mathbf{f} from the Q scattered fields $\{\mathbf{y}_q^{\text{sc}}\}_{q=1}^Q$ that are recorded when the sample is impinged with the incident fields $\{\mathbf{u}_q^{\text{in}}\}_{q=1}^Q$. Specifically, the reconstructed \mathbf{f}^* is specified as

$$\mathbf{f}^* \in \left\{ \arg \min_{\mathbf{f} \in \mathbb{R}^N} \left(\sum_{q=1}^Q \frac{1}{2\|\mathbf{y}_q^{\text{sc}}\|^2} \|\mathbf{H}_q(\mathbf{f}) - \mathbf{y}_q^{\text{sc}}\|^2 + \tau \mathcal{R}(\mathbf{L}\mathbf{f}) + i_{\geq 0}(\mathbf{f}) \right) \right\}. \quad (4.8)$$

In (4.8), $\mathbf{H}_q : \mathbb{R}^N \rightarrow \mathbb{C}^M$ denotes the forward model described by (4.3) and (4.4) for the q th incident wave \mathbf{u}_q^{in} . Let us recall that $\mathcal{R} : \mathbb{R}^{S \times S'} \rightarrow \mathbb{R}_{\geq 0}$ is a regularization functional, $\mathbf{L} : \mathbb{R}^N \rightarrow \mathbb{R}^{S \times S'}$ is a linear operator, and $\tau > 0$ balances between data fidelity and regularization. The term $i_{\geq 0}(\mathbf{f}) = \{0, \mathbf{f} \in (\mathbb{R}_{\geq 0})^N; +\infty, \text{ otherwise}\}$ is a nonnegativity constraint that is suitable for our applications. For other applications that involve inverse scattering, this term is modified to constrain the scattering potential to a given range of values. Such priors have been shown to significantly

Algorithm 1 Accelerated FBS [127, 128] for solving (4.8)

Require: $\mathbf{f}^0 \in \mathbb{R}^N$, $(\gamma_t > 0)_{t \in \mathbb{N} \setminus \{0\}}$

- 1: $\mathbf{v}^1 = \mathbf{f}^0$
- 2: $\alpha_1 = 1$
- 3: $t = 1$
- 4: **while** (not converged) **do**
- 5: Select a subset $\mathcal{Q} \subset [1 \dots Q]$
- 6: $\mathbf{d}^t = \sum_{q \in \mathcal{Q}} \frac{1}{\|\mathbf{y}_q^{\text{sc}}\|^2} \text{Re} \left(\mathbf{J}_{\mathbf{H}_q}^* (\mathbf{f}^t) (\mathbf{H}_q (\mathbf{f}^t) - \mathbf{y}_q^{\text{sc}}) \right)$
- 7: $\mathbf{f}^t = \text{prox}_{\gamma_t \tau \mathcal{R}(\mathbf{L} \cdot) + i_{\geq 0}} (\mathbf{v}^t - \gamma_t \mathbf{d}^t)$
- 8: $\alpha_{t+1} \leftarrow \frac{1 + \sqrt{1 + 4\alpha_t^2}}{2}$
- 9: $\mathbf{v}^{t+1} = \mathbf{f}^t + \left(\frac{\alpha_t - 1}{\alpha_{t+1}} \right) (\mathbf{f}^t - \mathbf{f}^{t-1})$
- 10: $t \leftarrow t + 1$
- 11: **end while**
- 12: **return** \mathbf{f}^t

improve the quality of the reconstruction [16, 73]. Finally, we consider as regularizer $\mathcal{R}(\mathbf{L} \cdot)$ either the total-variation seminorm (TV) [125] or the Hessian-Schatten seminorm (HS) [126]. It is noteworthy to mention that we proposed other alternatives well suited for ODT. In Section 4.7, we describe an adaptive regularization based on convolutional dictionary learning.

4.5.2 Optimization

Following [18, 52, 117], we deploy an accelerated forward-backward splitting (FBS) algorithm [127, 128] to solve the optimization problem (4.8). The iterates are summarized in Algorithm 1, with some further details below.

- We implemented a stochastic-gradient version of the algorithm by selecting a subset of of the measurements $\{\mathbf{y}_q^{\text{sc}}\}_{q=1}^Q$ at each iteration (Line 5). This allows us to reduce the computational burden of the method.
- Line 6 corresponds to the evaluation of the gradient of $\frac{1}{2\|\mathbf{y}_q^{\text{sc}}\|^2} \sum_{q \in \mathcal{Q}} \|\mathbf{H}_q(\cdot) -$

$\mathbf{y}_q^{\text{sc}}\|^2$. We provide its expression in the Section 4.5.3. We will discuss different strategies about its computation as well.

- For both the TV and HS regularizers, no known closed-form expression exists for the proximity operator of $\gamma_k \tau \mathcal{R}(\mathbf{L} \cdot) + i_{\geq 0}$ (Line 7). However, there exist efficient algorithms to evaluate them. Specifically, we use the fast gradient-projection method for TV [129] and its extension to the HS regularizer [126] (A.2.2).
- We set the sequence of step sizes to $\gamma_k = \gamma_0 / \sqrt{k}$ for $\gamma_0 > 0$. This is standard and ensures the convergence of incremental proximal-gradient methods [130].

The whole reconstruction pipeline is implemented within the framework of the GlobalBioIm library [131] and is available online (Appendix A.1).

4.5.3 Efficient Computation of the Gradient

Proposed Methodology

Let us first denote $\mathcal{E}_q(\mathbf{f}) = \mathcal{D}(\mathbf{H}_q(\mathbf{f}), \mathbf{y}_q^{\text{sc}})$ and the data-fidelity term in (4.8) as

$$\begin{aligned} \mathcal{E}_{\text{tot}}(\mathbf{f}) &= \sum_{q \in \mathcal{Q}} \mathcal{E}_q(\mathbf{f}) \\ &= \sum_{q \in \mathcal{Q}} \frac{1}{2 \|\mathbf{y}_q^{\text{sc}}\|^2} \|\mathbf{H}_q(\mathbf{f}) - \mathbf{y}_q^{\text{sc}}\|^2. \end{aligned} \quad (4.9)$$

The gradient of \mathcal{E}_{tot} is given by

$$\nabla \mathcal{E}_{\text{tot}}(\mathbf{f}) = \sum_{q \in \mathcal{Q}} \nabla \mathcal{E}_q(\mathbf{f}), \quad (4.10)$$

with

$$\nabla \mathcal{E}_q(\mathbf{f}) = \frac{1}{\|\mathbf{y}_q^{\text{sc}}\|^2} \text{Re} \left(\mathbf{J}_{h_q}^H(\mathbf{f}) \tilde{\mathbf{G}}^H (\tilde{\mathbf{G}} \text{diag}(\mathbf{f}) \mathbf{u}_q(\mathbf{f}) - \mathbf{y}_q^{\text{sc}}) \right), \quad (4.11)$$

where $\mathbf{J}_{h_q}(\mathbf{f})$ denotes the Jacobian matrix of

$$h_q : \mathbf{f} \mapsto \text{diag}(\mathbf{f}) \mathbf{u}_q(\mathbf{f}). \quad (4.12)$$

The computation of $\mathbf{J}_{h_q}^H(\mathbf{f})$, required in (4.10), is challenging. The existence of a closed-form solution is made unlikely by the fact that the forward model in (4.3) itself requires one to invert an operator. We distinguish two distinct strategies.

1. SEAGLE [52]: Build an error-backpropagation rule from the NAGD algorithm used to compute the forward model (4.3).
2. Ours: Derive an explicit expression of $\mathbf{J}_{h_q}(\mathbf{f})$, as given below (Proposition 4.5.1).

The error-backpropagation strategy used in SEAGLE to compute $\mathbf{J}_{h_q}^H(\mathbf{f})$ implies that one must store all the forward iterates. This consumes memory resources and compromises the deployment of the method for large 3D data. Instead, Proposition 4.5.1 reveals that its computation requires one to invert the operator $(\mathbf{I} - \mathbf{diag}(\mathbf{f})\mathbf{G}^H)$. This operator has the same form (and size) that the operator we invert within the forward computation in (4.3) and both can be computed in a similar way, using an iterative algorithm. Moreover, it allows us to decouple the forward and gradient computation in Algorithm 1, which has the two following advantages:

- choice of any iterative algorithm for computing (4.3), and computing $\mathbf{J}_{h_q}^H(\mathbf{f})$.
- reduction of the memory consumption (no needs for storing forward iterates).

Proposition 4.5.1. *The Jacobian matrix of the function h_q in (4.12) is given by*

$$\mathbf{J}_{h_q}(\mathbf{f}) = (\mathbf{I} + \mathbf{diag}(\mathbf{f})(\mathbf{I} - \mathbf{G} \mathbf{diag}(\mathbf{f}))^{-1} \mathbf{G}) \mathbf{diag}(\mathbf{u}_q(\mathbf{f})). \quad (4.13)$$

Proof. We use the Gâteaux derivative in the direction $\mathbf{v} \in \mathbb{R}^N$ given by

$$\begin{aligned} dh_q(\mathbf{f}; \mathbf{v}) &= \lim_{\varepsilon \rightarrow 0} \frac{\mathbf{diag}(\mathbf{f} + \varepsilon \mathbf{v}) \mathbf{u}_q(\mathbf{f} + \varepsilon \mathbf{v}) - \mathbf{diag}(\mathbf{f}) \mathbf{u}_q(\mathbf{f})}{\varepsilon} \\ &= \mathbf{diag}(\mathbf{u}_q(\mathbf{f})) \mathbf{v} + \lim_{\varepsilon \rightarrow 0} \mathbf{diag}(\mathbf{f}) \frac{\mathbf{u}_q(\mathbf{f} + \varepsilon \mathbf{v}) - \mathbf{u}_q(\mathbf{f})}{\varepsilon}. \end{aligned} \quad (4.14)$$

Then, from (4.3), we get that

$$\begin{aligned} \mathbf{u}_q^{\text{in}} &= (\mathbf{I} - \mathbf{G} \mathbf{diag}(\mathbf{f} + \varepsilon \mathbf{v})) \mathbf{u}_q(\mathbf{f} + \varepsilon \mathbf{v}) \\ &= (\mathbf{I} - \mathbf{G} \mathbf{diag}(\mathbf{f})) \mathbf{u}_q(\mathbf{f} + \varepsilon \mathbf{v}) - \varepsilon \mathbf{G} \mathbf{diag}(\mathbf{v}) \mathbf{u}_q(\mathbf{f} + \varepsilon \mathbf{v}) \end{aligned} \quad (4.15)$$

and

$$(\mathbf{I} - \mathbf{G} \text{diag}(\mathbf{f}))\mathbf{u}_q(\mathbf{f}) = \mathbf{u}_q^{\text{in}}. \quad (4.16)$$

Combining (4.15) and (4.16), we obtain that

$$(\mathbf{I} - \mathbf{G} \text{diag}(\mathbf{f}))(\mathbf{u}_q(\mathbf{f} + \varepsilon\mathbf{v}) - \mathbf{u}_q(\mathbf{f})) = \varepsilon\mathbf{G} \text{diag}(\mathbf{v})\mathbf{u}_q(\mathbf{f} + \varepsilon\mathbf{v}). \quad (4.17)$$

Finally, we get that

$$dh_q(\mathbf{f}; \mathbf{v}) = (\mathbf{I} + \text{diag}(\mathbf{f})(\mathbf{I} - \mathbf{G} \text{diag}(\mathbf{f}))^{-1}\mathbf{G}) \text{diag}(\mathbf{u}_q(\mathbf{f}))\mathbf{v} \quad (4.18)$$

and, thus, that

$$\mathbf{J}_{h_q}(\mathbf{f}) = (\mathbf{I} + \text{diag}(\mathbf{f})(\mathbf{I} - \mathbf{G} \text{diag}(\mathbf{f}))^{-1}\mathbf{G}) \text{diag}(\mathbf{u}_q(\mathbf{f})), \quad (4.19)$$

which completes the proof. \square

Numerical Validation

This section is devoted to simulated numerical experiments that illustrate the two main advantages of the proposed method over SEAGLE, which consist in a reduced computational cost and a reduced memory consumption. Both algorithms share the implementation of the overall FISTA algorithm as well as inner procedures such as the computation of the proximity operator of the regularization term (Appendix A.2). The only difference between the two methods resides in the computation of the forward model in (4.3) and $\mathbf{J}_{h_q}^H(\mathbf{f})$. For SEAGLE, this is performed using the NAGD algorithm (Section 3.7) and an error-backpropagation strategy. For our method, (4.3) and $\mathbf{J}_{h_q}^H(\mathbf{f})$ are computed using the CG algorithm, in accordance with Proposition 4.5.1. Note that no parallelization is used. Reconstructions are performed with MATLAB 9.1 (The MathWorks Inc., Natick, MA, 2000) on a PowerEdge T430 Dell computer (Intel Xeon E5-2620 v3).

Memory Requirement Here, we elaborate on the memory consumption of the proposed method in comparison with SEAGLE. First, let us state that gradient based methods, such as NAGD or CG, have similar memory requirements. It corresponds roughly to three times the size of the optimization variable which is the part that is common to both algorithms. The additional memory requirement that

is specific to SEAGLE relies only on the storage of the NAGD iterates during the forward computation. Suppose that $K_{\text{NAGD}} \in \mathbb{N}$ iterations are necessary to compute the forward model with (4.3) and that the region Ω is sampled over $N \in \mathbb{N}$ pixels (voxels, in 3D). Since the total field $\mathbf{u}_q(\mathbf{f})$ computed by NAGD is complex-valued, each pixel is represented with 16 bytes (double precision for accurate computations). Hence, the difference of memory consumption between SEAGLE and our method is

$$\Delta_{\text{Mem}} = N \times K_{\text{NAGD}} \times 16 \text{ [bytes]}, \quad (4.20)$$

which corresponds to the storage of the K_{NAGD} intermediate iterates of NAGD. Here, we assumed that $\nabla \mathcal{E}_{\text{tot}}$ was computed by sequentially adding the partial gradients $\nabla \mathcal{E}_q$ associated to the Q incident fields. Hence, once the partial gradient associated to one incident angle is computed by successively applying the forward model (NAGD) and the error-backpropagation procedure, the memory used to store the intermediate iterates can be recycled to compute the partial gradient associated to the next incident angle.

To speedup the process, these computations can easily be parallelized by performing the computation for each illumination on a separate thread. Here, the memory requirement would be multiplied by the number $N_{\text{Threads}} \in \mathbb{N}$ of threads, so that

$$\Delta_{\text{Mem}} = N \times K_{\text{NAGD}} \times N_{\text{Threads}} \times 16 \text{ [bytes]}. \quad (4.21)$$

Indeed, since the threads of a single computer share memory, computing N_{Threads} partial gradients in parallel requires N_{Threads} times more memory.

For illustration, we give in Fig. 4.3 the evolution of Δ_{Mem} as a function of N for different values of K_{NAGD} and N_{Threads} . One can see with the vertical dashed lines that, for 3D volumes, the memory used by SEAGLE quickly reaches several tens of Megabytes, even for small volumes (*e.g.*, $128 \times 128 \times 128$), to hundreds of Gigabytes for the larger volumes that are typical of microscopy (*e.g.*, $512 \times 512 \times 256$). This shows the limitation of SEAGLE for 3D reconstruction in the presence of a shortage of memory resources and reinforces the interest of the proposed alternative.

Reconstructions of RI—Simulated Data Here, we reconstruct RI maps on simulated data to illustrate the advantages of the proposed method.

Simulation Settings: The Shepp-Logan phantom of Fig. 4.4 has the contrast $\max(|\mathbf{f}|) / (k_{\text{b}}^2) = 0.2$. It is immersed into water ($\eta_{\text{b}} = 1.333$). The wavelength of the incident plane waves is $\lambda = 406$ nm. We consider thirty-one incident angles,

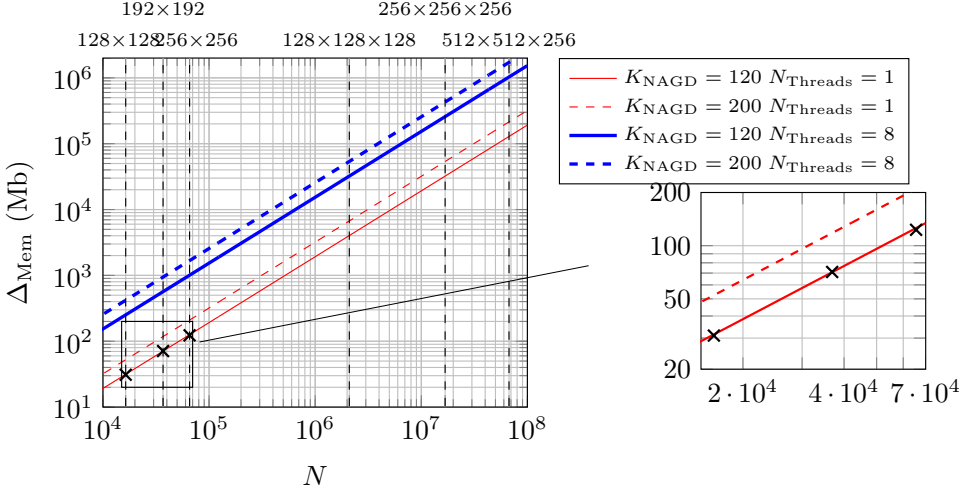


Figure 4.3: Predicted evolution of Δ_{Mem} as function of the number N of points for two values of K_{NAGD} and N_{Threads} . The vertical dashed lines give examples of 2D and 3D volumes for a range of values of N . Finally, the three crosses correspond to values of Δ_{Mem} measured experimentally.

from -60° to $+60^\circ$. The sources are placed at the bottom side of the sample, at a distance of 16.5λ from its center. Moreover, we consider two detectors placed on both top and bottom sides of the object, also at a distance of 16.5λ from its center. Hence, the overall region is a square of length 33λ per side. Data are simulated using a fine discretization of this region, with a (1024×1024) grid that leads to square pixels of surface $(3.223 \cdot 10^{-2}\lambda)^2$. We used a large number of CG iterations to get an accurate simulation. Then, the measurements were extracted from the first and last rows of each total field associated to the incident fields. This lead to a total of $(31 \times 2 \times 1024)$ measurements. Finally, we defined three ODT problems by downsizing (using averaging) the $(31 \times 2 \times 1024)$ measurements to grids with size of $(31 \times 2 \times 512)$, $(31 \times 2 \times 384)$, and $(31 \times 2 \times 256)$.

This setting corresponds to an ill-posed and highly scattering situation. Moreover, the detector length is only two times larger than the object, which results

in a loss of information for large incident angles. This makes the resulting inverse problem challenging.

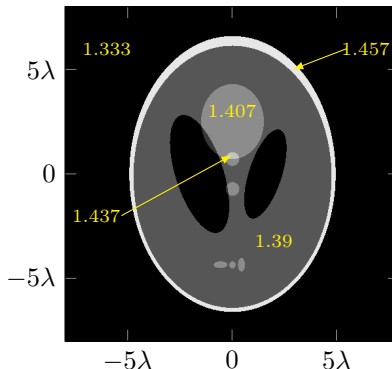


Figure 4.4: Shepp-Logan phantom and RI of the gray levels. The contrast is 20%.

Algorithm Parameters: For each simulated OTD problem, we considered a square region of interest Ω with sides half the sources–detector distance. That corresponds to images of size (256×256) with pixels of area $(6.445 \cdot 10^{-2}\lambda)^2$, (192×192) with pixels of area $(8.839 \cdot 10^{-2}\lambda)^2$, and (128×128) with pixels of area $(1.289 \cdot 10^{-1}\lambda)^2$. The support of the phantom is fully contained in Ω .

Then, to compute the gradient (stochastic-gradient strategy), we selected eight angles over the thirty-one that were available and changed this selection at each iteration.

The NAGD or CG forward algorithms are stopped either after hundred-twenty iterations or when the relative error between two iterates is below 10^{-4} . Finally, two-hundred iterations of FISTA are performed with a descent step fixed empirically to $\gamma = 5 \cdot 10^{-3}$. We used the regularization parameter $\tau = 3.3 \cdot 10^{-2}$.

Metrics: We compared the two methods in terms of running time and memory consumption, as measured by the peak memory (maximum allocated memory) reached by each algorithm during execution. The outcome is reported in Table 4.1. Once again, due to the use of our inverse-problem library [131], the comparison of the two methods is fair because their implementations differ only by the forward

algorithm and by the computation of $\mathbf{J}_{h_q}^H(\mathbf{f})$. Moreover, CG and NAGD are implemented in the same fashion since they inherit the same optimization class of our inverse-problem library *GlobalBioIm*. Finally, we also provide the signal-to-noise ratio (SNR) of the reconstructed RI and observe that the computational gain comes at no cost in quality.

Table 4.1: Proposed method *vs.* SEAGLE [52, 107] in terms of running time and memory consumption. The reconstructed RI maps are presented in Fig. 4.5.

ROI Ω size	(128×128)		(192×192)		(256×256)	
	Ours	[52]	Ours	[52]	Ours	[52]
Time (min)	9	35	12	72	19	110
Memory (Mb)	138	169	224	295	337	460
SNR (dB)	43.96	43.76	45.44	45.48	46.96	46.99

Reconstructions of RI—2D Experimental Data We further evaluated our method using the *FoamDielExt* target (TM polarisation) of the Institut Fresnel’s public database [132]. The data were collected for the 2D inhomogeneous sample depicted in the left panel of Fig. 4.6. The permittivity of the ground truth was measured experimentally and is subject to uncertainties [132]. The object is fully contained in a square region of length 15 cm per side, which we discretize using a 256×256 grid. Sensors were distributed circularly around the object, at a distance of 1.67 m from its center, and with a step of 1° . Eight sources, uniformly distributed around the object, were sequentially activated. For each activated source, the sensors closer than 60° from the source were excluded. Thus, 241 detectors among the 360 available were used for each source. Frequencies from 2 to 10 GHz with a step of 1 GHz are available in the database but we used only the 3 GHz measurements (*i.e.*, $\lambda = 10$ cm).

The NAGD or CG forward algorithms are stopped either after two-hundred iterations or when the relative error between two iterates is below 10^{-6} . Hundred iterations of FISTA are performed with a descent step $\gamma = 5 \cdot 10^{-3}$. We used the regularization parameter $\tau = 1.6 \cdot 10^{-2}$.

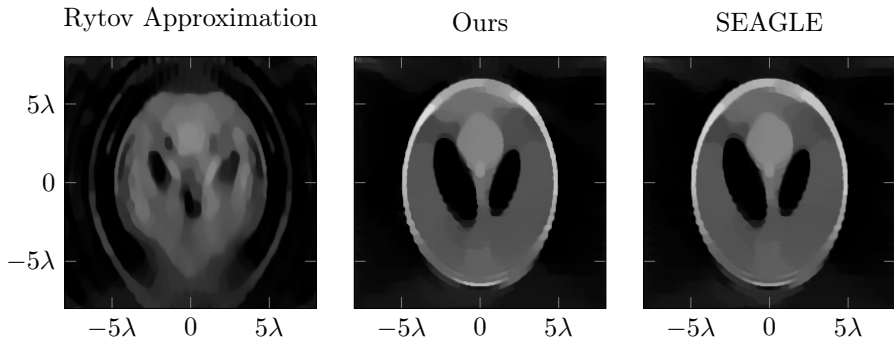


Figure 4.5: Reconstructions obtained by the proposed method and by SEAGLE for the (256×256) ODT problem with $\tau = 3.3 \cdot 10^{-2}$. The colormap is identical to that of Fig. 4.4. For comparison, we provide the TV-regularized Rytov reconstruction with $\tau = 3 \cdot 10^{-3}$.

Discussion Our proposed alternative to SEAGLE allows us to reduce both time and memory. Moreover, we have measured the peak memory difference Δ_{Mem} between the two methods and superimposed it on the predictions of Fig. 4.3 where the adequacy between the theoretical curves and the measured points is remarkable. Hence, although our experiments are restricted to 2D data, where the gap between the two algorithms is moderate, the evolution of Δ_{Mem} for 3D data can be extrapolated from Fig. 4.3. This shows the relevance of our method when size increases.

The SNR values given in Table 4.1 as well as the reconstructions presented in Fig. 4.5 suggest that the two methods perform similarly in terms of quality. This is not surprising since the overall algorithm is the same, the differences residing merely in the computation of the forward model in (4.3) and the Jacobian $\mathbf{J}_{h_q}(\mathbf{f})$. Moreover, one can observe that the quality of reconstruction decreases when the discretization grid becomes coarser. Indeed, the model is insufficiently accurate when the discretization is too poor. For instance, in the case of the (128×128) grid, one wavelength unit is discretized using eight pixels, which is clearly detrimental to the accuracy of the forward model.

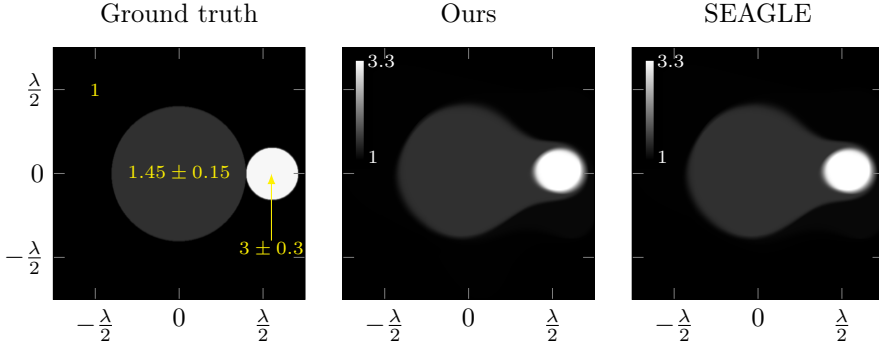


Figure 4.6: Reconstructions (permittivity) obtained by the proposed method and by SEAGLE for the *FoamDieExt* target of the Institut Fresnel’s database [132] with $\tau = 1.6 \cdot 10^{-2}$. The SNR values (computed from the experimentally measured permittivity of the ground truth) are 25.13 dB (Ours) and 25.15 dB (SEAGLE) while the computing times are respectively of 6 min and 93 min.

Reconstructions for the (256×256) problem are presented in Fig. 4.5 for completeness. Besides the difficulty of the considered scenario, the two methods are able to retrieve most details of the object in comparison with the Rytov approximation. Artifacts are mainly due to the missing-cone problem and to the limited length of the detector. This corroborates the findings of [52].

We further validate our method on real data. In Fig. 4.6, we see that both methods provide good reconstructions that are essentially indistinguishable (also SNR values provided in the caption of the figure). This corroborates the simulated numerical experiments of Section 4.5.3. The main point here is that, for this setting, the proposed method was 15 times faster than SEAGLE.

4.6 Results for 3D Data

In this section, we validate our computational pipeline on 3D simulated data (Section 4.6.1). Then, we deploy the proposed approach on real data (Section 4.6.1).

Table 4.2: Relative error of the RI RBCs reconstructions.

Method	Rytov	BPM	LSm
$\frac{\ \hat{\eta} - \eta_{\text{gt}}\ ^2}{\ \eta_{\text{gt}}\ ^2}$	1.8231×10^{-4}	2.4585×10^{-5}	9.0120×10^{-6}

For both cases, we provide comparison with existing algorithms.

4.6.1 Simulated Data

Simulation Setting

We simulated red blood cells (RBCs) with a maximal RI of 1.05 (Fig. 4.7 top row) [37]. This sample is immersed in air ($\eta_b = 1$) and is illuminated by tilted plane waves with wavelength $\lambda = 600\text{nm}$. To simulate the ODT measurements, we used the DDA on a grid with a resolution of 50nm. To probe the sample, we generated 40 views within a cone of illumination whose half-angle is 45° . This corresponds to severely restricted angles of view and makes the reconstruction problem very challenging. Each view has 512^2 measurements (resolution of 150nm). Finally, we have simulated, independently for each view, an acquisition of the incident field on Γ .

Comparisons

We compare our LSm reconstruction method with the direct back-propagation algorithm that is based on the Rytov model. In addition, we do compare it to BPM. For each iterative method (BPM and ours), we used TV regularization together with a nonnegativity constraint. Finally, the regularization parameter $\tau > 0$ was optimized through grid search in each scenario to maximize the performance with respect to the ground truth. BPM took about 31 seconds per iteration (proximity operator of TV included) for a reconstruction size of $512 \times 512 \times 150$ (200 iterations). The proposed method took about 112 seconds per iteration (proximity operator of TV included) for a reconstruction size of $144 \times 144 \times 144$ (300 iterations).

In Fig. 4.7, one observes that our method faithfully recovers RBCs at several orientations. In comparison with the considered baselines, we observe that LSm allows to recover more accurately the RBCs shape (and RI) as pointed out by the

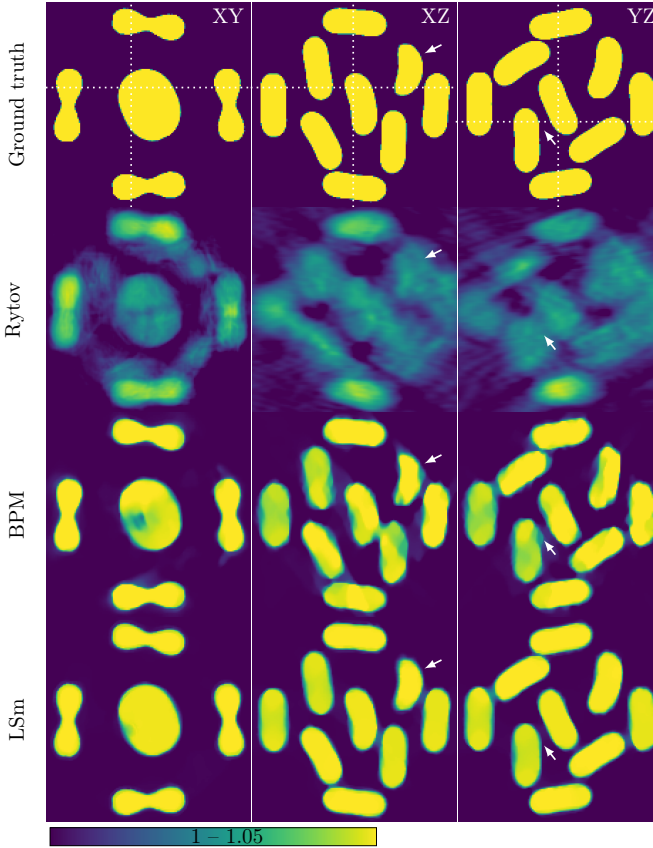


Figure 4.7: RI reconstructions of the simulated RBCs by Rytov, BPM, and the proposed method (LSm).

white arrows. In Table 4.2, we present the relative error of the RBCs reconstructions. As expected, the more sophisticated LSm obtains the lowest relative error.

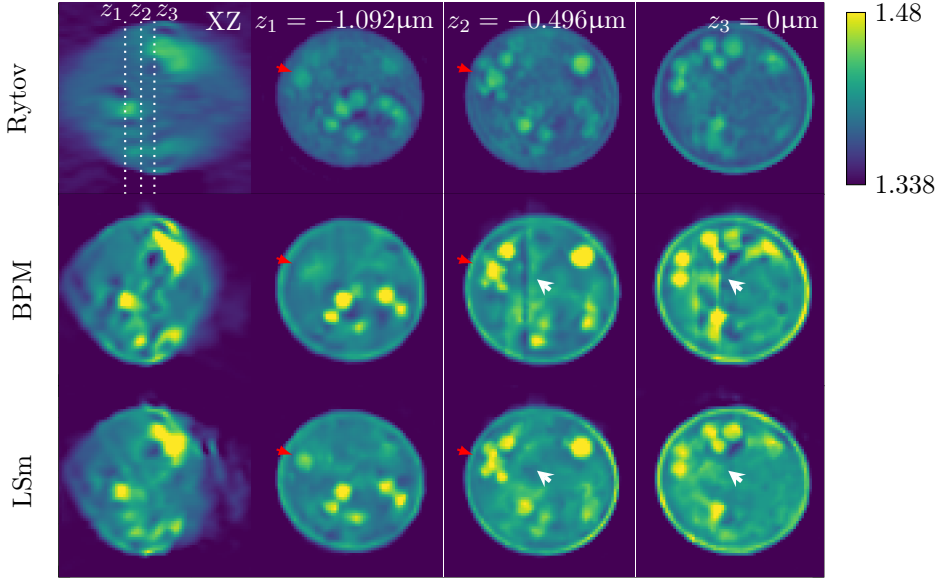


Figure 4.8: RI reconstructions of the yeast cell with Rytov, BPM, and the proposed method (LSm). The first column corresponds to the central XZ slice of the sample. Then, from left to right: XY slices at depths $z_1 = -1.092\mu m$, $z_2 = -0.496\mu m$, and $z_3 = 0\mu m$.

4.6.2 Experimental Data

Acquisition Setup

We acquired real data using the experimental tomographic setup described in [28] (Appendix A.4). The sample is a yeast cell immersed in water ($n_b = 1.338$) and is illuminated by tilted incident waves with wavelength $\lambda = 532\text{nm}$. As in our simulation setup, we acquired 61 views within a cone of illumination whose half-angle is 35° . The measurements lie on a plane that is centered and perpendicular to the optical axis. The complex fields with and without the sample were acquired

for each view, thus providing the total and incident field, respectively. The pixel size is 99nm.

The reconstructions are performed on a grid of the same resolution than that of the measurements. We used the HS regularization as we found it more suitable for this type of sample. Finally, we model \mathbf{P} as the composition of a linear filtering by an ideal pupil function (binary disk in Fourier domain with radius $2NA/\lambda$, $NA = 1.45$) and a free-space propagation to the center of the sample. BPM took about 33 seconds per iteration (proximity operator of the HS included) for a reconstruction size of $150 \times 150 \times 100$ (200 iterations). The proposed method took about 38 seconds per iteration (proximity operator of the HS included) for a reconstruction size of $96 \times 96 \times 96$ (200 iterations).

Reconstruction Results

The reconstructed volumes obtained with the Rytov method, the BPM, and the proposed approach are presented in Fig. 4.8. Once again, nonlinear models clearly outperform the (linear) Rytov reconstruction. Moreover, the reconstruction of the RI obtained by LSm does not suffer from the artefacts indicated in BPM slices z_2, z_3 with thick white arrows. Also, the areas with higher RI are better resolved (z_1, z_2 , thin red arrows) when LSm is deployed. Finally, one can appreciate in Fig. 4.9 that the inner areas with higher RI (green) are more resolved for LSm than for BPM.

4.7 Adaptive Regularization with Dictionary Learning

As we could see in the previous sections, the missing-cone problem yields artifacts which are more prominent along the optical axis (Chapter 2), which can be circumvented by regularization [14, 16, 73]. However, these regularization approaches do not take into account the anisotropic resolution of ODT.

In this section, we propose to go one step further and leverage such anisotropy to improve the quality of the reconstructions. Our motivation is to learn highly resolved features from lateral planes and use them to enhance the quality in the axial direction. Hence, inspired by the strategy proposed by Soulez [133] for the deconvolution of fluorescent microscopic images, we deploy a dictionary-based regularizer that is learnt from the lateral planes of an initial reconstructed volume.

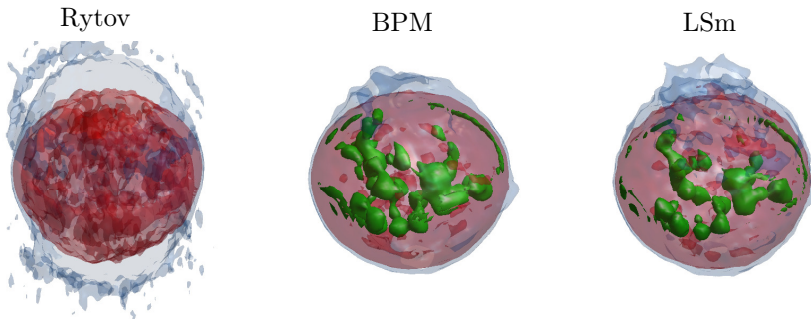


Figure 4.9: Iso-surface color renderings of the RI reconstructions of the yeast. The isovalues are 1.35, 1.38, and 1.46 for the blue, red, and green color channels, respectively.

Three-step reconstruction

In the spirit of [133], we designed a three-step reconstruction scheme.

1. TV-regularized reconstruction.
2. Dictionary learning (DL) from lateral planes.
3. Final reconstruction using the learnt dictionary.

TV-Regularized Reconstruction The first step consists in solving the non-negative TV-regularized problem

$$\mathbf{f}^{\text{TV}} \in \left\{ \arg \min_{\mathbf{f} \in \mathbb{R}_{\geq 0}^N} \left(\sum_{q=1}^Q \|\mathbf{H}_q(\mathbf{f}) - \mathbf{y}_q^{\text{sc}}\|_2^2 + \tau_{\text{TV}} \|\mathbf{f}\|_{\text{TV}} \right) \right\}, \quad (4.22)$$

where $\mathbf{H}_q : \mathbb{C}^N \mapsto \mathbb{C}^M$ denotes the two-step forward model described by (4.3) and (4.4) for the q th incident wave \mathbf{u}_q^{in} , $\|\cdot\|_{\text{TV}} = \|\nabla \cdot\|_{2,1}$ is TV (Section 2.3), and $\tau_{\text{TV}} > 0$ is the regularization parameter which balances between the data-fidelity term and the TV term. As done previously, we deploy FBS, implemented using the GlobalBioIm library [131] (Appendix A.1), to obtain \mathbf{f}^{TV} .

DL from Lateral Planes Given the nonnegative TV solution \mathbf{f}^{TV} , our goal is to learn a dictionary $\mathbf{D} \in \mathbb{R}^{N_p \times K}$ formed out of K atoms of size $N_p < N$ such that \mathbf{f}^{TV} can be represented as

$$\mathbf{f}^{\text{TV}} = \sum_{p=1}^{P_{\text{XY}}} (\mathbf{R}_p^{\text{XY}})^T \mathbf{D} \boldsymbol{\alpha}_p, \quad (4.23)$$

where $\mathbf{R}_p^{\text{XY}} : \mathbb{R}^N \rightarrow \mathbb{R}^{N_p}$ is an operator that extracts a 2D patch of size N_p centered on the p th element of the input vector (its adjoint inserts the patch at the p th position), P_{XY} denotes the number of patches, and $\{\boldsymbol{\alpha}_p \in \mathbb{R}^K\}_{p=1}^{P_{\text{XY}}}$ are sparse vectors. The superscript XY in \mathbf{R}^{XY} denotes the fact that the operation only extracts 2D patches from lateral planes.

We formulate the DL problem as

$$\{\widehat{\mathbf{D}}, \widehat{\boldsymbol{\alpha}}_p\} \in \left\{ \arg \min_{\substack{\mathbf{D} \in \mathbb{R}^{N_p \times K} \\ \boldsymbol{\alpha}_p \in \mathbb{R}^K}} \left(\left\| \sum_{p=1}^{P_{\text{XY}}} (\mathbf{R}_p^{\text{XY}})^T \mathbf{D} \boldsymbol{\alpha}_p - \mathbf{f}^{\text{TV}} \right\|_2^2 + \tau_{\text{DL}} \sum_{p=1}^{P_{\text{XY}}} \|\boldsymbol{\alpha}_p\|_1 \right) \right\}, \quad (4.24)$$

where $\tau_{\text{DL}} > 0$ controls the sparsity level.

Our formulation is fundamentally different from the pioneering approaches [134, 135] where the solution was such that each extracted patch had a sparse representation in \mathbf{D} . Our representation $\mathbf{f} = \sum_{p=1}^{P_{\text{XY}}} (\mathbf{R}_p^{\text{XY}})^T \mathbf{D} \boldsymbol{\alpha}_p$ is related to convolutional dictionary learning (CDL) [136–138], as shown by Pappas *et al.* [139, 140]. As opposed to traditional DL, CDL accounts for global information in the image such as shift invariance. Hence, (4.25) not only enjoys the global sparse representation of CDL but also benefits from the local (patch-based) processing of DL [139, 140].

By introducing the auxiliary variable $\mathbf{s}_p = \mathbf{D} \boldsymbol{\alpha}_p$ in (4.24), we can deploy the alternating-direction method of multipliers (ADMM) to minimize the augmented-Lagrangian functional

$$\mathcal{L}(\widehat{\mathbf{D}}, \widehat{\boldsymbol{\alpha}}_p, \widehat{\mathbf{s}}_p, \widehat{\mathbf{w}}_p) = \left\| \sum_{p=1}^{P_{\text{XY}}} (\mathbf{R}_p^{\text{XY}})^T \mathbf{s}_p - \mathbf{f}^{\text{TV}} \right\|_2^2 + \sum_{p=1}^{P_{\text{XY}}} \frac{\rho}{2} \left\| \mathbf{s}_p - \mathbf{D} \boldsymbol{\alpha}_p + \frac{\mathbf{w}_p}{\rho} \right\|_2^2 + \tau_{\text{DL}} \|\boldsymbol{\alpha}_p\|_1, \quad (4.25)$$

Algorithm 2 Proposed algorithm to solve (4.26)

Require: $\mathbf{y} \in \mathbb{C}^{MQ}$, $\mathbf{f}^0 \in \mathbb{C}^N$, $\widehat{\mathbf{D}} \in \mathbb{R}^{N_p \times K}$, $\gamma > 0, \tau_{\text{sc}} > 0$

- 1: Define $\mathcal{F} = \sum_{q=1}^Q \|\mathbf{H}_q(\mathbf{R}^T \cdot) - \mathbf{y}_q^{\text{sc}}\|_2^2 + \mathcal{R}_{\text{pos}}(\mathbf{R}^T \cdot)$
- 2: $\mathbf{s}^0 = \frac{1}{n^2} \mathbf{R} \mathbf{f}^0$
- 3: $t = 1$
- 4: **while** (not converged) **do**
- 5: $\mathbf{z}^t = \mathbf{s}^t - \gamma \nabla \mathcal{F}(\mathbf{s}^t)$
- 6: $\mathbf{s}_p^{t+1} = \mathcal{C}_{\tau_{\text{sc}}, \widehat{\mathbf{D}}}(\mathbf{z}_p^t), \quad \forall p \in \{1, \dots, P\}$
- 7: $t \leftarrow t + 1$
- 8: **end while**
- 9: **return** $\mathbf{f}^* = \mathbf{R}^T \mathbf{s}^{t-1}$

where $\{\mathbf{w}_p \in \mathbb{R}^{N_p}\}_{p=1}^{P_{\text{XY}}}$ are the dual variables and $\rho > 0$ is the Lagrangian multiplier. Using the CDL terminology [140], the auxiliary variable \mathbf{s}_p is referred to as the *p*th slice. The ADMM is implemented using the SPAM toolbox.⁴ [141]

Final Reconstruction Using the Learnt Dictionary Equipped with the dictionary $\widehat{\mathbf{D}} \in \mathbb{R}^{N_p \times K}$ learnt from lateral planes in Section 4.7, we now consider the optimization problem

$$\left\{ \begin{array}{l} \mathbf{f}^* = \mathbf{R}^T \mathbf{s}^*, \\ \mathbf{s}^* \in \left\{ \arg \min_{\mathbf{s} \in \mathbb{R}^{N_p P}} \left(\sum_{q=1}^Q \|\mathbf{H}_q(\mathbf{R}^T \mathbf{s}) - \mathbf{y}_q^{\text{sc}}\|_2^2 + \mathcal{R}_{\text{pos}}(\mathbf{R}^T \mathbf{s}) + \mathcal{R}_{\widehat{\mathbf{D}}}(\mathbf{s}) \right) \right\}, \end{array} \right\}, \quad (4.26)$$

where $\mathbf{s} = [\mathbf{s}_1^T \dots \mathbf{s}_P^T]^T \in \mathbb{R}^{N_p P}$ is the concatenation of all the slices, $P = P_{\text{XY}} + P_{\text{XZ}} + P_{\text{YZ}}$ is the total number of slices, and $\mathbf{R} = [\mathbf{R}_{\text{XY}}^T \ \mathbf{R}_{\text{XZ}}^T \ \mathbf{R}_{\text{YZ}}^T]^T \in \mathbb{R}^{N_p P \times N}$ with \mathbf{R}_{XZ} (\mathbf{R}_{YZ}) the counterpart of \mathbf{R}_{XY} for the XZ (YZ, respectively) sections of the volume. We use the differentiable functional $\mathcal{R}_{\text{pos}} : \mathbb{R}^N \rightarrow \mathbb{R}$

$$\mathcal{R}_{\text{pos}}(\mathbf{f}) = \sum_{n=1}^N \frac{\lambda_{\text{pos}}}{\mu} \log(\exp(-\mu f_n) + 1) \quad (4.27)$$

⁴ <http://spams-devel.gforge.inria.fr/>

to favor nonnegative solutions. Here, $\lambda_{\text{pos}} > 0$ is a weighting factor and $\mu > 0$ shapes the tolerance to negative values. Finally, the functional $\mathcal{R}_{\hat{\mathbf{D}}} : \mathbb{R}^{N_p P} \rightarrow \mathbb{R}$ in (4.26) is a regularization term designed to enforce the slices \mathbf{s}_p to have a sparse representation in $\hat{\mathbf{D}}$. Denoting $\mathcal{F} = \sum_{q=1}^Q \|\mathbf{H}_q(\mathbf{R}^T \cdot) - \mathbf{y}_q^{\text{sc}}\|_2^2 + \mathcal{R}_{\text{pos}}(\mathbf{R}^T \cdot)$, we can deploy the FBS algorithm whose iterates are given by

$$\mathbf{s}^{t+1} = \text{prox}_{\gamma \mathcal{R}_{\hat{\mathbf{D}}}}(\mathbf{s}^t - \gamma \nabla \mathcal{F}(\mathbf{s}^t)), \quad (4.28)$$

where $\gamma > 0$ is a descent parameter and $\text{prox}_{\gamma \mathcal{R}_{\hat{\mathbf{D}}}}$ denotes the proximity operator of the functional $\mathcal{R}_{\hat{\mathbf{D}}}$. Here, we follow the plug-and-play prior philosophy [142–144] and replace $\text{prox}_{\gamma \mathcal{R}_{\hat{\mathbf{D}}}}$ in (4.28) by the “denoising” operator

$$\begin{aligned} \mathcal{C}_{\tau_{\text{sc}}, \hat{\mathbf{D}}} : \mathbb{R}^{N_p} &\longrightarrow \mathbb{R}^{N_p} \\ \mathbf{s} &\longmapsto \hat{\mathbf{D}} \boldsymbol{\alpha}^*, \end{aligned} \quad (4.29)$$

where $\tau_{\text{sc}} > 0$, and

$$\boldsymbol{\alpha}^* \in \left\{ \arg \min_{\boldsymbol{\alpha} \in \mathbb{R}^K} \left(\frac{1}{2} \|\mathbf{s} - \hat{\mathbf{D}} \boldsymbol{\alpha}\|_2^2 + \tau_{\text{sc}} \|\boldsymbol{\alpha}\|_1 \right) \right\}. \quad (4.30)$$

Numerous solvers exist to solve (4.30) [135, 145]. Again, we use the GlobalBioIm library together with the SPAMS toolbox for this step. Finally, we summarize the complete reconstruction scheme of this section in Algorithm 2.

Results

We validate our method on the yeast cell shown in Fig. 4.8 and used the same setting described in Section 4.6.2. In particular, the size of the reconstructed volume is $(96 \times 96 \times 96)$ with a sampling step of 99.3nm (9.53 μm in each dimension).

TV-Regularized Reconstruction We first reconstructed the sample using the method described in [18] by minimizing (4.22). The initial guess was the solution provided by the Rytov model [13]. We used diverse regularization parameters τ_{TV} for TV (Fig. 4.10). When the regularization is weak, artifacts due to model mismatch are hindering the quality of reconstruction. On the contrary, over-regularization results in cartoon-like solutions.

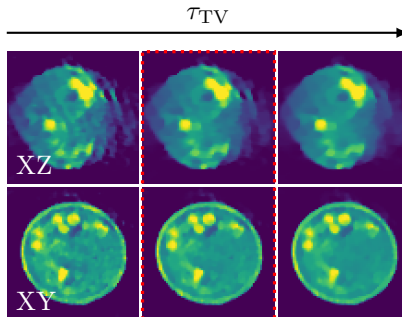


Figure 4.10: TV-regularized solutions obtained with regularization parameters $\tau_{\text{TV}} = \{0.15, 0.3, 0.5\}/96^3$ (from left to right, respectively).

Learning the Dictionary We learned the dictionary by minimizing (4.25). We used patches of size (8×8) ($N_p = 64$) and $K = 64$ atoms. We set $\tau_{\text{DL}} = 1/\sqrt{8}$ and $\rho = 0.5 \max(\mathbf{f}^{\text{TV}})N_p^2$. The learnt atoms of the dictionary $\hat{\mathbf{D}}$ are shown in Fig. 4.11.

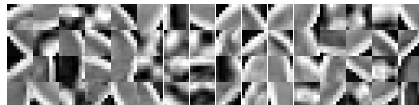


Figure 4.11: Dictionary $\hat{\mathbf{D}}$ learnt from lateral planes of the TV regularized solution (\mathbf{f}^{TV} , dotted rectangle in Fig. 4.10).

Final Reconstruction We solved the optimization problem (4.26) and encouraged the nonnegativity of the solution with $\lambda_{\text{pos}} = 1/96^3$ and $\mu = 5$ in (4.27). The initial guess was \mathbf{f}^{TV} . The denoising operator (4.29)–(4.30) was used with regularization parameter $\tau_{\text{sc}} = 10^{-4}$.

We observe that the Rytov-based solution suffers from the missing-cone problem whereas the regularized solutions (*i.e.*, TV and the proposed one) mitigate

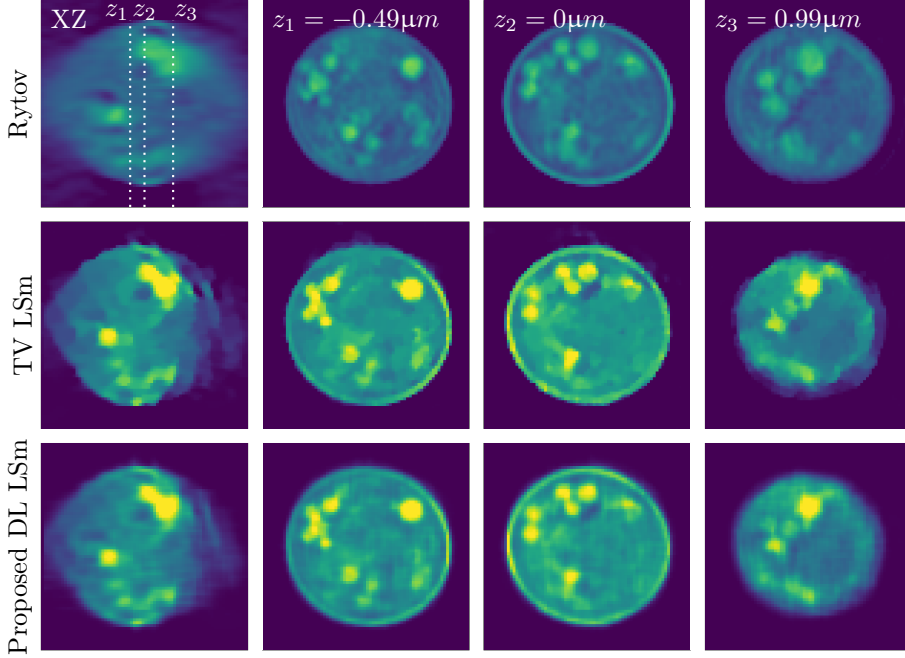


Figure 4.12: Yeast reconstructions. Views of the reconstructed sample at the XZ plane and three different XY positions. The Rytov-based solution (Rytov), the TV-regularized solution (TV LSm), and the proposed regularized solution (Proposed DL LSm) are displayed in the top, middle, and bottom rows, respectively. The TV-regularized solution was obtained with $\tau_{TV} = 0.3/96^3$.

its effect. In addition, some features are enhanced with the proposed solution in comparison to the TV solution (Fig. 4.12). Finally, the proposed method is able to recover features in deeper axial position whereas the TV-regularized solution is over-regularized (Fig. 4.12, right column).

Discussion

We designed an adaptive regularization that allowed us to improve the quality of ODT reconstructions in the axial direction using features learned in lateral planes. The proposed regularization relies on a dictionary that is learnt from the lateral planes of an initial TV reconstruction. This dictionary is then used in a final step to enhance the quality of the reconstruction in all XY, XZ, and YZ sections. We applied this strategy to the reconstruction of real ODT measurements. Our results show the superior performance of the proposed pipeline over conventional regularization.

4.8 Summary

3D ODT reconstruction is a challenging inverse problem. Its success depends on the accuracy of the implementation of the physical model. In this chapter, we used our model LS_m (Chapter 3) to reconstruct 3D RI maps. To that end, we tackled important difficulties that are related to the computational and memory burden, as well as the calibration of the incident field. Finally, we showed on both simulated and real data that the use of the proposed model improves the quality/faithfulness of the reconstructions. In addition, we designed a new regularization scheme based on dictionary learning that improves the axial resolution by exploiting the superior lateral resolution in ODT. In a similar context, we also developed a deep-learning projector for ODT [100].

Until now, we have worked with complex-valued measurements; a setting that requires an interferometric apparatus. ODT from intensity-only measurements is a popular alternative to simplify the acquisition setup and reduce its cost. However, this comes at the price of a harder inverse-scattering problem. In the next chapter, using our LS_m model, we will present a reconstruction framework adapted to the challenging setting of intensity-only measurements.

Chapter 5

ODT from Intensity-only Measurements

5.1 Introduction

In this chapter, we use our LiSc-based model (LSm, see Chapter 3) for ODT from intensity-only measurements.¹ This setting allows us to get rid of the interferometric system required to record holographic data (Chapter 4). The price to pay, however, is that the reconstruction problem becomes more challenging. In practice, this task usually addressed by alternating between phase retrieval and RI estimation [7, 45, 63, 77].

5.2 Contributions

Our contribution is the design of a versatile reconstruction framework which permits the use of any physical model (Chapter 1) and leverages recent advances in proximal algorithms. In Section 5.3, we present the versatile framework and comparisons between 2D reconstructions from intensity and complex measurements. In Section 5.5, we extend our comparisons to the 3D setting.

¹ The content of this chapter is based on [22, 23].

5.3 Unified Regularized Reconstruction Framework

5.3.1 Problem Formulation

Let us define the operator $\mathbf{H}^{\text{tot}} : \mathbb{R}^N \rightarrow \mathbb{C}^N$ that, given the scattering potential $\mathbf{f} \in \mathbb{R}^N$, gives the total field on the detector region Γ (Fig. 5.1). Note that in Chapter 4 \mathbf{H} referred to our LiSc based model (LSm) which computes the *scattered* field on the detector region.² In addition, \mathbf{H}^{tot} can be any model of wave scattering. Two specific models will be used in the experiments of Section 5.4: BPM (Chapter 1) and LSm (Chapter 3). The intensity-only measurements $\{\mathbf{y}_q \in \mathbb{R}^M\}_{q \in [1 \dots Q]}$ are related to the model by

$$\mathbf{y}_q = |\mathbf{H}_q^{\text{tot}}(\mathbf{f})|^2 + \boldsymbol{\xi}_q, \quad \forall q \in [1 \dots Q], \quad (5.1)$$

where the notation $\mathbf{H}_q^{\text{tot}}(\cdot)$ refers to total field obtained with the incident field \mathbf{u}_q^{in} , $\boldsymbol{\xi}_q \in \mathbb{R}^M$, $\forall q \in [1 \dots Q]$, represent noise and $|\cdot|^2$ is a component-wise squared magnitude. Similar to Chapter 4, we adopt a variational approach to estimate the scattering potential $\mathbf{f} \in \mathbb{R}^N$ from the measurements $\{\mathbf{y}_q \in \mathbb{R}^M\}_{q \in [1 \dots Q]}$ by solving the optimization problem

$$\hat{\mathbf{f}} \in \left\{ \arg \min_{\mathbf{f} \in B} \sum_{q=1}^Q \mathcal{D}(|\mathbf{H}_q^{\text{tot}}(\mathbf{f})|^2, \mathbf{y}_q) + \tau \mathcal{R}(\mathbf{L}\mathbf{f}) \right\}. \quad (5.2)$$

Let us recall that the functional $\mathcal{D} : \mathbb{R}^M \times \mathbb{R}^M \rightarrow \mathbb{R}_{\geq 0}$ measures the fidelity of the model to the data and that, from a Bayesian point of view, we can relate \mathcal{D} to the log-likelihood of the noise distribution.

5.3.2 Optimization with the Alternating Direction Method of Multipliers (ADMM)

In this section, we leverage recent advances in phase retrieval, nonlinear physical models, and modern regularization. We propose a unified framework that can cope with forward models at various levels of sophistication (*e.g.*, Born [12], BPM [146], LiSc-based models [18, 107]) and with various sparse regularizers (*e.g.*, TV [125],

² The computation of the total field is then trivial, since we just have to add the incident field on the detector region to the scattered field.

HS [126]). This is possible because of the modularity of the proposed approach, which comes from an adequate splitting of the initial problem into simpler subproblems. Moreover, our method can be easily adapted to different types of noise by the way of specific data-fidelity terms for which an explicit expression of the proximity operator is available. Finally, we validate the proposed method on several simulated and real datasets using both BPM and LSm together with a TV regularizer.

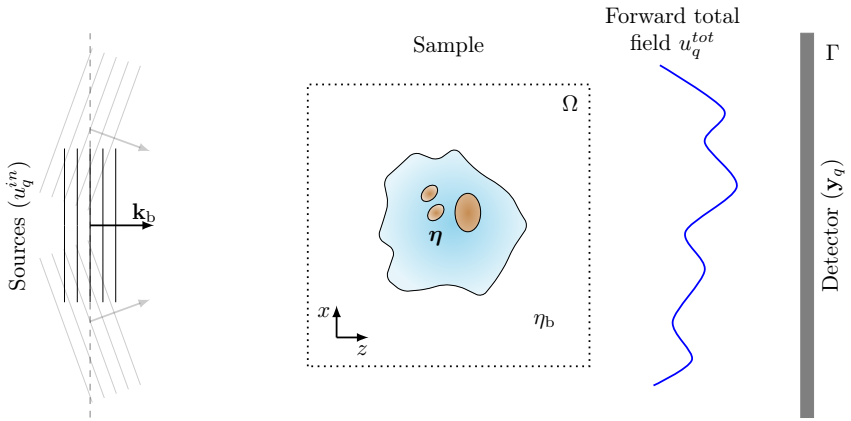


Figure 5.1: ODT setup (intensity-only). A sample with the RI $\eta \in \mathbb{R}^N$ is immersed in a background medium of index η_b and impinged by an incident plane wave with a given orientation (wave vector \mathbf{k}_b). The interaction of the incident field with the object produces a scattered field. The squared magnitude of the total field, which corresponds to the sum of the incident and scattered fields, is recorded by the detector.

Splitting Strategy

Inspired by the success of ADMM [147], we propose to split the optimization task in a way that decouples the complex-field-based reconstruction from the phase retrieval. To that end, we introduce the auxiliary variables $\mathbf{v}_q \in \mathbb{C}^M$, $q \in [1 \dots Q]$,

and reformulate the problem in (5.2) as

$$(\widehat{\mathbf{f}}, \widehat{\mathbf{v}}_1, \dots, \widehat{\mathbf{v}}_Q) \in \left\{ \arg \min_{(\mathbf{f}, \mathbf{v}_1, \dots, \mathbf{v}_Q) \in \mathcal{X}} \sum_{q=1}^Q \mathcal{D}(|\mathbf{v}_q|^2, \mathbf{y}_q) + \tau \mathcal{R}(\mathbf{L}\mathbf{f}) \right\}, \quad (5.3)$$

where

$$\mathcal{X} = \{(\mathbf{f}, \mathbf{v}_1, \dots, \mathbf{v}_Q) \in B \times \mathbb{C}^{M \times Q} \text{ s.t. } \mathbf{v}_q = \mathbf{H}_q^{\text{tot}}(\mathbf{f}) \quad \forall q \in [1 \dots Q]\}. \quad (5.4)$$

The augmented-Lagrangian form of this problem is

$$\mathcal{L}(\mathbf{f}, \mathbf{v}_1, \dots, \mathbf{v}_Q, \mathbf{w}_1, \dots, \mathbf{w}_Q) = \sum_{q=1}^Q \mathcal{D}(|\mathbf{v}_q|^2, \mathbf{y}_q) + \frac{\rho}{2} \|\mathbf{H}_q^{\text{tot}}(\mathbf{f}) - \mathbf{v}_q + \mathbf{w}_q / \rho\|_2^2 + \tau \mathcal{R}(\mathbf{L}\mathbf{f}), \quad (5.5)$$

where \mathbf{w}_q are the Lagrangian multipliers and ρ is a positive scalar. Then, (5.5) is minimized using ADMM, which results in the procedure given in Algorithm 3. The problem is now reduced to three simpler subproblems: a phase retrieval that requires the computation of the proximity operator of $\mathcal{D}(|\cdot|^2, \mathbf{y}_q)$, an RI reconstruction problem from complex measurements (Chapter 4), and the Lagrangian update of \mathbf{w}_q .

Proximity Operator for Phase-Retrieval

At Step 5 of Algorithm 3, we must compute the proximity operator of $\frac{1}{\rho} \mathcal{D}(|\cdot|^2, \mathbf{y}_q)$, like in

$$\text{prox}_{\frac{1}{\rho} \mathcal{D}(|\cdot|^2, \mathbf{y}_q)}(\mathbf{x}) = \arg \min_{\mathbf{v} \in \mathbb{C}^M} \frac{1}{2} \|\mathbf{v} - \mathbf{x}\|_2^2 + \frac{1}{\rho} \mathcal{D}(|\mathbf{v}|^2, \mathbf{y}_q). \quad (5.6)$$

Here, we benefit from the closed-form expressions that have been recently derived for Gaussian likelihood in [21]. In the present work, we consider the weighted quadratic data-fidelity term

$$\mathcal{D}(|\mathbf{v}|^2, \mathbf{y}_q) = \frac{1}{2} \|\mathbf{v}^2 - \mathbf{y}_q\|_{\mathbf{W}_q}^2, \quad (5.7)$$

where $\mathbf{W}_q = \text{diag}(w_1^q, \dots, w_M^q)$ is a diagonal matrix and $\|\cdot\|_{\mathbf{W}_q}$ a weighted ℓ_2 -norm such that $\|\mathbf{v}\|_{\mathbf{W}_q}^2 = \mathbf{v}^T \mathbf{W}_q \mathbf{v}$. This scheme can be tuned to two scenarios.

Algorithm 3 ADMM for solving (5.5)

Require: $\{\mathbf{y}_q\}_{q \in [1 \dots Q]}$, $\mathbf{f} \in \mathbb{R}_{\geq 0}^N$, $\rho > 0$, $\tau > 0$

- 1: $\mathbf{f}^{(0)} = \mathbf{f}$
 - 2: $\mathbf{w}_q^{(0)} = \mathbf{0}_{\mathbb{C}^M}$, $\forall q \in [1 \dots Q]$
 - 3: $t = 0$
 - 4: **while** (not converged) **do**
 - 5: $\mathbf{v}_q^{t+1} = \text{prox}_{\frac{1}{\rho} \mathcal{D}(|\cdot|^2, \mathbf{y}_q)}(\mathbf{H}_q^{\text{tot}}(\mathbf{f}^t) + \frac{\mathbf{w}_q^t}{\rho})$, $\forall q \in [1 \dots Q]$ \triangleright Phase retrieval
 - 6: $\mathbf{f}^{t+1} = \arg \min_{\mathbf{f} \in B} \frac{\rho}{2} \sum_{q=1}^Q \|\mathbf{H}_q^{\text{tot}}(\mathbf{f}) - \mathbf{v}_q^{t+1} + \mathbf{w}_q^t / \rho\|_2^2 + \tau \mathcal{R}(\mathbf{L}\mathbf{f})$ \triangleright RI reconstruction
 - 7: $\mathbf{w}_q^{t+1} = \mathbf{w}_q^t + \rho(\mathbf{H}_q^{\text{tot}}(\mathbf{f}^{t+1}) - \mathbf{v}_q^{t+1})$ $\forall q \in [1 \dots Q]$ \triangleright Update Lagrangian
 - 8: $t \leftarrow t + 1$
 - 9: **end while**
 - 10: **return** \mathbf{f}^t
-

1. Log-likelihood for Gaussian measurement noise: We set $w_m^q = 1/\sigma^2$, where σ^2 is the variance of the noise.
2. Log-likelihood for Poisson measurement noise: We set $w_m^q = \max(y_{q,m}, b)^{-1}$, where the minimal value $b > 0$ accounts for background emission and the dark current of the detector.

Following [21], the proximity operator of $\mathcal{D}(|\cdot|^2, \mathbf{y}_q)$ given by (5.7) is computed component-wise according to

$$\forall \mathbf{x} \in \mathbb{C}^M, \left[\text{prox}_{\frac{1}{\rho} \mathcal{D}(|\cdot|^2, \mathbf{y}_q)}(\mathbf{x}) \right]_m = \varrho_m e^{j \arg(x_m)}, \quad (5.8)$$

where ϱ_m is the positive root of the cubic polynomial in ϱ

$$q_G(\varrho) = \frac{4w_m^q}{\rho} \varrho^3 + \varrho \left(1 - \frac{4w_m^q}{\rho} y_{q,m} \right) - |x_m| \quad (5.9)$$

which can be efficiently found with Cardano's method. Note that a closed-form expression has also been derived for an exact model of Poisson noise [21].

Reconstruction from Complex Fields

The minimization over \mathbf{f} (Step 6 of Algorithm 3) can be achieved by deploying an accelerated FBS algorithm [127, 128, 148] (see Chapter 4 for details).

5.4 Results for 2D Data

We first assess the suitability of our framework to reconstruct simulated samples using two physical models: BPM (Chapter 1) and LSm (Chapter 3). Then, we validate our approach on experimental data. Finally, we evaluate the performance of the method for limited measurements.

We compare the solutions of our framework to those obtained with the light field refocusing (LFR) method [149] which were also used as initial guesses for Algorithm 3. For the regularizer $\mathcal{R}(\mathbf{L}\cdot)$, we use the TV seminorm, known to attenuate the missing-cone problem. Moreover, we enforce a nonnegativity constraint on the scattering potential by setting $B = \mathbb{R}_{\geq 0}^N$. Because the RI reconstruction step can be computationally intensive, we adopted acceleration strategies. Similar to Chapter 4, the gradient required in FBS was computed for a subset of the angles $[1 \dots Q]$. This subset was changed at each iteration while keeping a constant angle difference between them. We implemented the algorithms using an inverse-problem library developed in our group [131] (Appendix A.1).

5.4.1 Simulated Data

Simulation setup

We consider the three samples presented in Fig. 5.2 (top row). They are immersed in water ($\eta_b = 1.33$) as well as the source and the sensors. They were impinged by thirty-one incident waves with angles ranging from -45° to 45° . These waves were propagated from the bottom to the top of the $(33\lambda \times 33\lambda)$ domain with $\lambda = 406$ nm. Simulations were performed on a fine grid (1024×1024) with a pixel area of $(0.03\lambda)^2$ using the LSm forward model. The 1024 sensors are evenly placed on a straight line of length 33λ above the sample at 16.5λ from the center. Finally, these measurements were reduced to $M = 512$ using averaging.

Reconstruction parameters

The regularization parameter τ was selected in order to minimize the relative error $\|\hat{\xi} - \xi_{\text{true}}\|_2 / \|\xi_{\text{true}}\|_2$.

The outer loop in Algorithm 3 (inner FBS at step 6 in Algorithm 3, respectively) was stopped when the relative change between two iterates is below 10^{-8} or after 20 (50, respectively) iterations. The step size in the FBS algorithm was set to $5 \cdot 10^{-4}$ and $5 \cdot 10^{-3}$ for BPM and LSm, respectively. The penalty parameter was set to $\rho = 10^{-3}$. Finally, the reconstructions were performed on a (512×512) grid. The regularization parameter τ was tuned by hand for each sample.

Observations

As shown in Fig. 5.2, the proposed framework is able to reconstruct the samples despite the lack of phase information. Both forward models obviously perform better than LFR which only relies on geometrical optics. We observe that the LSm forward model yields better reconstructions than the BPM forward model. Our framework with LSm is able to retrieve most details of the object. The shape as well as the RI of the samples are well estimated. These observations are quantified by the relative error presented in Table 5.1.

Table 5.1: Reconstruction performance. The relative error $\epsilon = \frac{\|\hat{\xi} - \xi_{\text{true}}\|_2}{\|\xi_{\text{true}}\|_2}$ is shown. The proposed method with BPM was 3 to 6 times faster than with LSm.

ϵ	Three fibers	Cell	Shepp-Logan
LFR	$1.4 \cdot 10^{-2}$	$1.36 \cdot 10^{-2}$	$2.06 \cdot 10^{-2}$
BPM	$4.74 \cdot 10^{-3}$	$6.05 \cdot 10^{-3}$	$1.28 \cdot 10^{-2}$
LSm	$1.33 \cdot 10^{-3}$	$4.04 \cdot 10^{-3}$	$1.02 \cdot 10^{-2}$

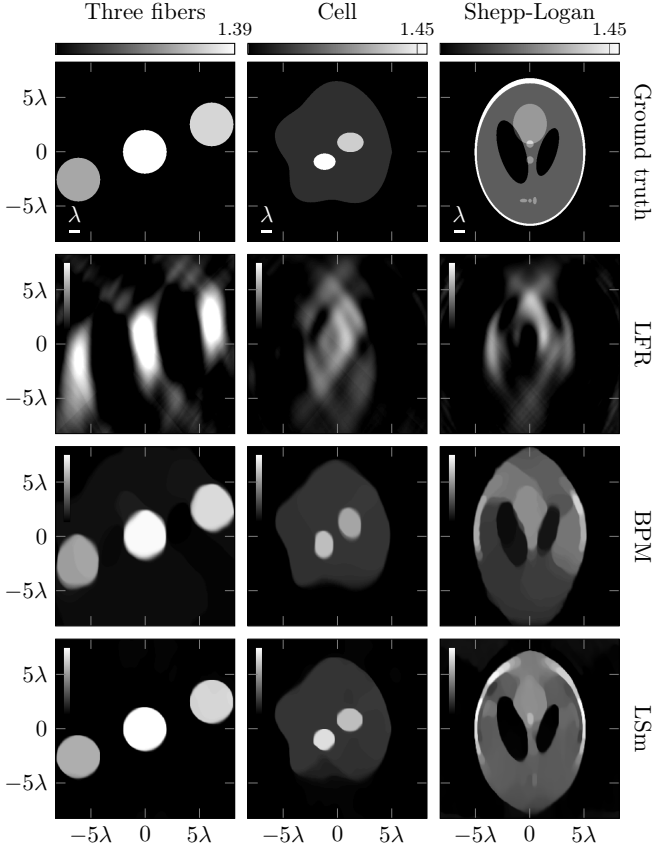


Figure 5.2: RI map for three fibers, a simulated cell, and the Shepp-Logan in the first, second, and third column, respectively. The ground truth and the reconstructions from the LFR, BPM, and LSm proposed methods are shown in Row 1 to 4, respectively. The samples are immersed in water ($\eta_b = 1.33$). Thirty-one views were acquired with a tilted plane-wave illumination. The angles ranged from -45° to 45° . The sample is illuminated from below. The 1024 sensors are evenly placed on a straight line of length 33λ above the sample at 16.5λ from the center. The measurements were reduced to 512 using averaging.

5.4.2 Experimental Data

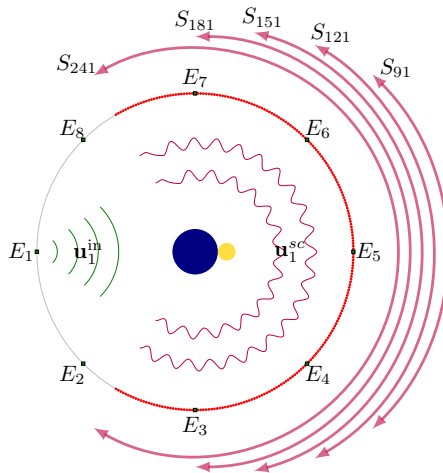


Figure 5.3: Acquisition setup for the Institut Fresnel’s dataset. The sensors (dots in the inner circle) correspond to the illumination angle of 0° (i.e., E_1). The measurements are restricted either by reducing the number of sensors (sensors sets S_{241}, \dots, S_{91}) or the number of acquired views (emitters E_1, \dots, E_8).

We validate our framework using the publicly available experimental datasets of the Institut Fresnel [132]. We used the same setting than in Chapter 4 (i.e., TM polarization at 3 GHz ($\lambda = 10$ cm), eight sources (E_{1-8} , 241 sensors (S_{241}) per source) We reconstructed the three targets *FoamDielExt*, *FoamDielInt*, and *FoamTwinDiel* using the TM polarization at 3 GHz (i.e., $\lambda = 10$ cm). Each 2D inhomogeneous sample is depicted in Fig. 5.4 (top row). The indicated permittivities were experimentally measured and are subject to uncertainties [132].

For the reconstruction, we consider a $(15 \times 15 \text{ cm}^2)$ area discretized over (256×256) pixels. This yields a pixel area of about (0.0586 cm^2) . We reconstruct these samples with the LSm forward model and compare the results with the RI reconstruction from holographic measurements [18].

The chosen regularization parameters τ were tuned by hand for both algorithms. The penalty parameter ρ was set to 5. We initialized both algorithms with the background value.

The results presented in Fig. 5.4 suggest that the two methods perform similarly in terms of quality. The shape and the permittivity of the samples are both remarkably well recovered despite the high contrasts. Furthermore, the bottom graphs in Fig. 5.4 show that the retrieved phase corroborates the measurement data for each sample. The similar performances observed for these samples suggest the intensity-only measurements still contain some phase information due to the diffraction.

Reducing the number of measurements

In this section, we assess the effect of a reduction in the number of measurements (Fig. 5.3). To that end, we combined two methods. On one hand, we incrementally ignored illumination angles. On the other hand, we reduced the number of sensors, starting from no restriction (*i.e.*, S_{241}) to the smallest set of sensors S_{91} (Fig. 5.3). This strategy allowed us to explore the missing-cone problem. By progressively limiting the available measurements, we converged to a setup similar to that of tomographic phase microscopy [68]. The reconstruction obtained for the easiest scenario (*i.e.*, 8 views and S_{241}) was considered as a reference. Then, the regularization parameter τ was tuned in order to minimize the relative error with respect to this reference.

As shown in Fig. 5.5, the quality of the reconstructions is remarkable, even in extreme cases. This is due to the use of modern regularization.

5.4.3 Discussion

We have proposed a variational formulation of the reconstruction of RI from intensity-only measurements. It allows us to take advantage of efficient algorithms to solve subproblems. Our framework is able to handle several forward models and any regularization. Notably, we showed that LS_m combined with TV regularization reconstructs highly scattering samples from intensity-only measurements, even in ill-posed configurations. Furthermore, our results suggest our method can reconstruct RI samples in even more difficult cases where few measurements are available.

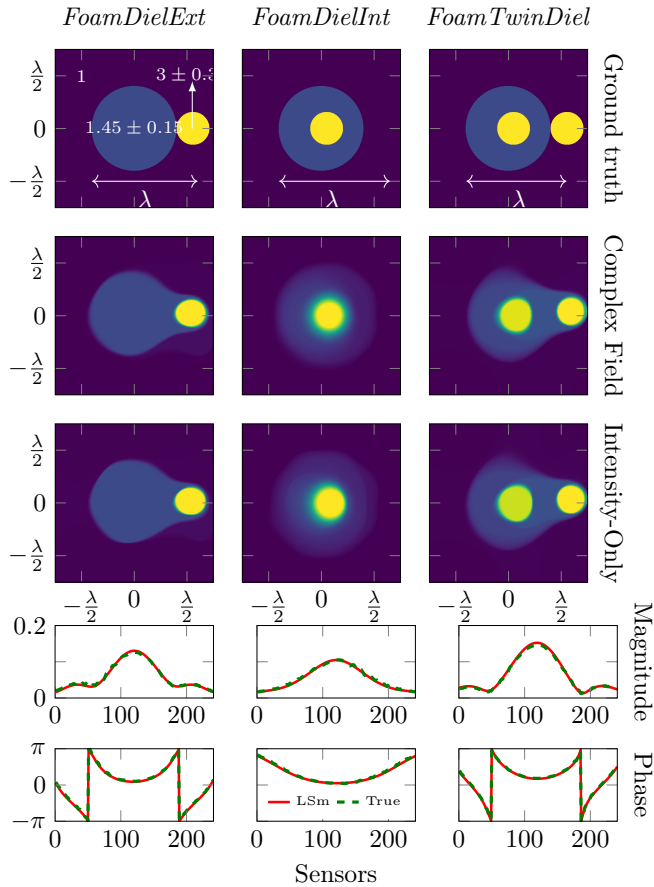


Figure 5.4: Permittivity reconstruction of the Institut Fresnel's datasets by LSm. From left to right: *FoamDielExt*, *FoamDielInt*, and *FoamTwinDiel*. From top to bottom: ground truth, reconstructions from complex (using [18]) and intensity-only (proposed method) measurements, respectively, and magnitude and phase of the predicted (solid curve) *vs* true (dashed curve) measurements (0° illumination angle). The two curves often overlap. For the solutions from complex measurements, the regularization parameters were set at $1.6 \cdot 10^{-2}$, $3 \cdot 10^{-3}$, and $9 \cdot 10^{-3}$ for *FoamDielExt*, *FoamDielInt*, and *FoamTwinDiel*, respectively. For the solutions from intensity-only measurements, the regularization parameters were set at $7 \cdot 10^{-2}$, $9 \cdot 10^{-3}$, and $4 \cdot 10^{-2}$ for *FoamDielExt*, *FoamDielInt*, and *FoamTwinDiel*, respectively.

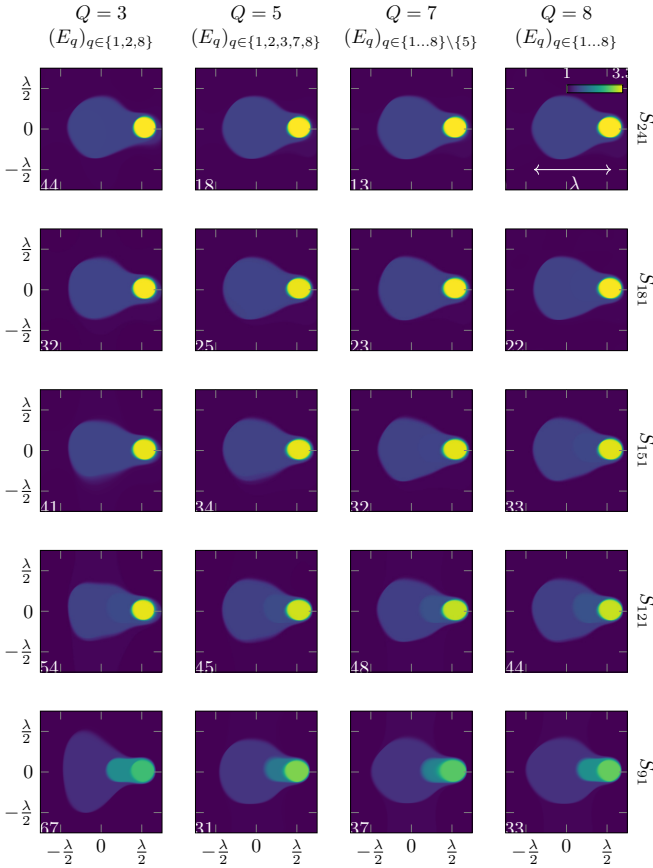


Figure 5.5: Permittivity reconstructions of the Institut Fresnel's dataset with a limited number of measurements. From left to right: $Q = 3, 5, 7,$ and 8 views were used to reconstruct the sample *FoamDielExt*. From top to bottom: The sensors were included in the sets $S_{241}, S_{181}, S_{151}, S_{121},$ and S_{91} , respectively. The reconstruction error with respect to the best solution (*i.e.*, E_8, S_{241}) is shown at the top left of each image.

5.5 Reconstruction Framework Revisited

5.5.1 Optimization for 3D Data

Despite its appealing features, our unifying framework does not scale well with 3D optical setting. In particular, the update of the Lagrangian in Algorithm 3 involves the computation of all the forward models, a time-consuming step when many views are used. We could not adopt strategies similar to the previous chapter which have alleviated the computational burden. For instance, the counterpart of a stochastic FBS algorithm for ADMM did not show satisfying results in our preliminary experiments.

Similar to the previous chapter, we then deploy a stochastic FBS algorithm to minimize (5.2); here, it is closely related to the Wirtinger flow techniques used in FP [65, 67, 150, 151].

Computation of the Gradient for Intensity-only ODT

Similar to Section 4.5.3, let us first denote $\mathcal{E}_q^{\text{int}}(\mathbf{f}) = \mathcal{D}(|\mathbf{H}_q^{\text{tot}}(\mathbf{f})|^2, \mathbf{y}_q)$ and the data-fidelity term in (5.2) as

$$\mathcal{E}_{\text{tot}}^{\text{int}}(\mathbf{f}) = \sum_{q \in \mathcal{Q}} \mathcal{E}_q^{\text{int}}(\mathbf{f}) \quad (5.10)$$

For $\mathcal{D}(|\mathbf{H}_q^{\text{tot}}(\mathbf{f})|^2, \mathbf{y}_q) = \frac{1}{2\|\mathbf{y}_q\|^2} \sum_{q \in \mathcal{Q}} \|\mathbf{H}_q^{\text{tot}}(\mathbf{f})\|^2 - \mathbf{y}_q\|^2$, the gradient of (5.10) is given by

$$\nabla \mathcal{E}_{\text{tot}}^{\text{int}}(\mathbf{f}) = \sum_{q \in \mathcal{Q}} \nabla \mathcal{E}_q(\mathbf{f}), \quad (5.11)$$

with

$$\nabla \mathcal{E}_q^{\text{int}}(\mathbf{f}) = \frac{2}{\|\mathbf{y}_q\|^2} \text{Re} \left(\mathbf{J}_{\mathbf{H}_q^{\text{tot}}}^H(\mathbf{f}) \text{diag}(\mathbf{H}_q^{\text{tot}}(\mathbf{f})) (|\mathbf{H}_q^{\text{tot}}(\mathbf{f})|^2 - \mathbf{y}_q) \right), \quad (5.12)$$

where $\mathbf{J}_{\mathbf{H}_q^{\text{tot}}}(\mathbf{f})$ denotes the Jacobian matrix of the physical model. For instance, the Jacobian matrix of BPM is provided in [14]. The forward model for LSm for the total field is simply

$$\mathbf{y}_q = \mathbf{H}_q(\mathbf{f}) + \mathbf{u}_{\Gamma, q}^{\text{in}}, \quad (5.13)$$

where $\mathbf{H}_q(\mathbf{f})$ is defined in (4.3)-(4.4) and $\mathbf{u}_{\Gamma,q}^{\text{in}} \in \mathbb{C}^M$ is the incident field on the measurements plane. Then, the Jacobian matrix is given by

$$\mathbf{J}_{\mathbf{H}_{\text{tot}}}^H(\mathbf{f}) = \mathbf{J}_{h_q}^H(\mathbf{f})\tilde{\mathbf{G}}^H, \quad (5.14)$$

with $\mathbf{J}_{h_q}^H(\mathbf{f})$ defined in Proposition 4.5.1.

Computation of the 3D Incident Field

Let us recall that our forward model LSm requires the knowledge of the 3D incident field $\mathbf{u}^{\text{in}} \in \mathbb{C}^N$, but we only acquire 2D intensity measurements for each view in real data. We then assume that the phase of the incident fields is an ideal tilted plane wave and proceed as described in Section 4.4.3 to obtain the 3D incident field. In case where the angles are approximately known, a simple yet efficient tool can estimate them from the intensity-only measurements [70].

5.6 Results for 3D Data

To recover a good 3D RI map with nonlinear models, we have observed that the initial guess plays a key role in the quality of the RI map obtained by our method. From complex measurements, Rytov model often provides a good initial solution. From intensity-only measurements, the LFR method [149] fulfilled this role for our 2D experiments but failed to provide a satisfying initial guess in our 3D experiments. As an alternative, Ayoub *et al* recover more accurately sample features via the Wolf transform from intensity-only measurements [152]. To obtain an initial guess of RI map, we post-process the non-quantitative solution obtained by their method (Wolf transform). In all our experiments, we compare with the solutions obtained from complex measurements (Chapter 4).

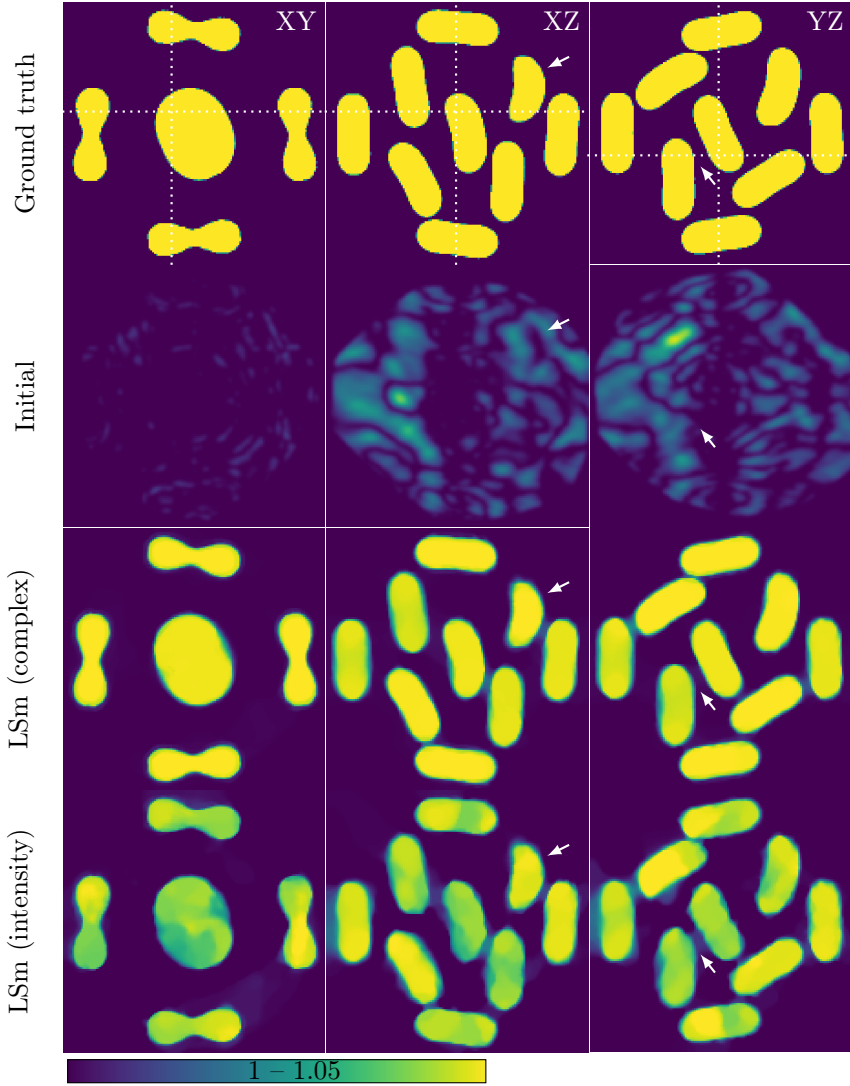


Figure 5.6: RI reconstructions of the simulated RBCs by the Wolf transform (Initial), LSm (complex), and LSm (intensity).

Table 5.2: Relative error of the RI RBCs reconstructions.

Method	Wolf transform	LSm (complex)	LSm (intensity)
$\frac{\ \hat{\boldsymbol{\eta}} - \boldsymbol{\eta}_{\text{gt}}\ ^2}{\ \boldsymbol{\eta}_{\text{gt}}\ ^2}$	3.004×10^{-4}	9.0120×10^{-6}	1.954×10^{-5}

5.6.1 Simulated Data

We used the same simulation setting than in Section 4.6.1. We regularize our solution with TV.

We display in Fig. 5.6 the reconstructed 3D RI maps and their obtained SNRs are reported in Table 5.2. As expected, the reconstruction method from complex measurements obtains the best quality (Table 5.2). However, the 3D RI map recovered from intensity-only measurements remains fairly impressive (Fig. 5.6, fourth row), given the quality of the initial guess (Fig. 5.6, second row).

5.6.2 Experimental Data

We used the same real data than in Section 4.6.2, which allows us to compare between reconstructions from complex and intensity-only measurements. We took the intensity of the holographic measurements to simulate intensity-only measurements. Here, we used HS as regularizer.

We display in Fig. 5.7 the RI maps obtained with LSm from complex and intensity-only measurements (second and third row, respectively).

5.6.3 Discussion

As expected, the loss of phase information can impact the quality of reconstruction. Despite the decrease in quality, the RI maps reconstructed from intensity-only measurements still recover features similar to the ones of the RI maps obtained from complex measurements. Here, our illumination angles are restricted to a cone, which leads to a strong missing-cone problem. Such challenging settings seem to strongly benefit from the phase information in the measurements. For instance, we ignored other optical aberrations in the phase of the incident field for the 3D real data, since we assumed an ideal plane wave. This probably explains the observed

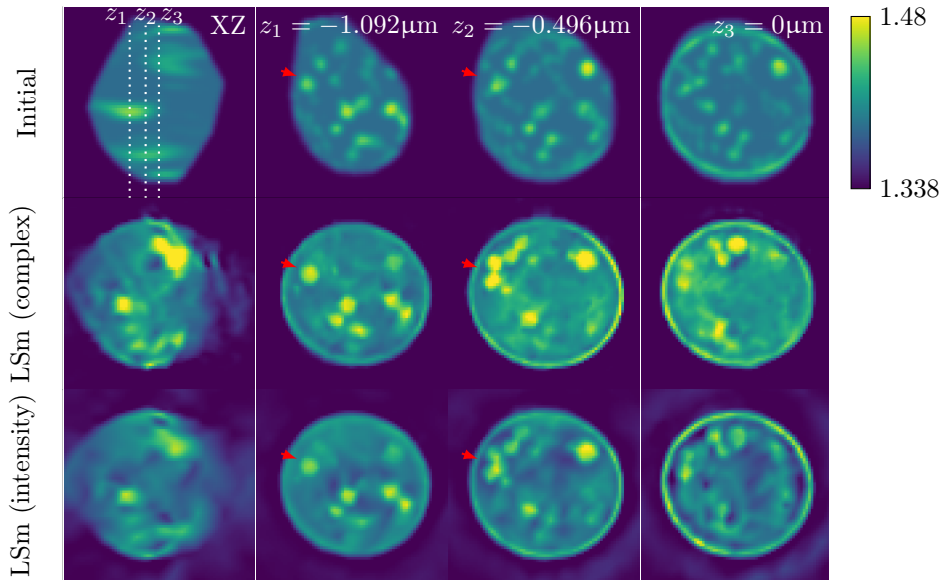


Figure 5.7: RI reconstructions of the yeast cell with the Wolf transform (Initial), LSm (complex), and LSm (intensity) from top to bottom, respectively. The first column corresponds to the central XZ slice of the sample. Then, from left to right: XY slices at depths $z_1 = -1.092\mu\text{m}$, $z_2 = -0.496\mu\text{m}$, and $z_3 = 0\mu\text{m}$.

difference in quality between the RI maps reconstructed from complex-valued and intensity-only measurements.

Furthermore, we have observed that the initial guess plays an essential role in the quality of reconstruction for the real data, which emphasizes the importance of the Wolf transform and Rytov method for the success of nonlinear models.

5.7 Summary

In this chapter, we applied our novel LSm model to the challenging inverse-scattering problems involving intensity-only measurements. To solve the inverse problem in 2D, we proposed a variational framework which splits the original optimization problem into simpler subproblems. Thanks to this modular approach, our framework can handle any forward model and any regularization. We have illustrated the advantages of the proposed framework by reconstructing highly-scattering samples from intensity-only measurements. Here, the quality of the reconstructed 2D RI maps is similar to that of the RI maps obtained from complex measurements.

To solve the 3D inverse-scattering problem, we adopted a computationally-efficient proximal gradient-based optimization technique. Given the lack of phase information, the 3D RI maps obtained from intensity-only measurements are of quite remarkable quality. However, the quality of reconstruction decreases in comparison to the 3D RI maps obtained from complex measurements. This slightly contrasts with our observations for the 2D experiments. Although the experimental conditions remain different (beyond the obvious additional dimension), this calls for further investigation in future works. In particular, we shall study the effects of the initial guess, the missing-cone problem, and the optical aberrations.

In the next chapter, we will apply our reconstruction framework for intensity-only measurements to fluorescence-based SMLM.

Chapter 6

Single-Molecule Localization Microscopy (SMLM) Meets ODT

6.1 Introduction

In this chapter, we capitalize on our previous contributions to propose a novel extension of SMLM.¹ SMLM delivers nanoscale resolution by sequentially activating a subset of fluorescent molecules and by extracting their super-resolved positions from the microscope images. The emission patterns of individual molecules can be distorted by the RI map of the sample, which reduces the accuracy of the molecule localization if not accounted for. By building upon the previous Chapters 3-5, we show that one can exploit these sample-induced aberrations to recover the RI map. To that end, we propose an optimization framework in which we reconstruct the RI map and optimize the positions of the molecules in a joint fashion. The benefits of our method are twofold. On one side, we effectively recover the RI map of the sample. On the other side, we further improve the molecule localization—the primary purpose of SMLM.

¹ The content of this chapter is based on [24, 25].

6.2 Context

SMLM is a method of choice for the observation of biological phenomena at nanoscale resolution [153–155]. SMLM is a prime example of computational microscopy where suitable acquisitions and algorithmic reconstruction are combined in order to enhance the capabilities of traditional systems. Although SMLM acquisitions are 2D, innovative point-spread functions (PSF), whose shapes vary with depth, have been designed to encode the axial position of molecules. These include the popular astigmatism [156] or double-helix [157] PSFs. Therefore, in addition to efficient localization algorithms, well-calibrated models of these PSFs are essential to reach the promised nanoscale resolution [27].

The standard practice is to estimate these PSFs from acquisitions of sub-resolved objects (*e.g.*, fluorescent microspheres) [158, 159]. However, this strategy ignores sample-induced distortions. Indeed, the heterogeneity of biological specimens—through variations in their RI—induces scattering of the emitted light. This distorts the recorded emission patterns and compromises the accurate localization of molecules. To mitigate this effect, Xu *et al.* [160] proposed an algorithm to jointly localize fluorescent molecules and estimate an *in situ* PSF model that has the ability to capture sample-induced aberrations and, hence, improve localization accuracy.

If we could estimate both the RI and the position of molecules from the SMLM acquisition stack alone, then we would have a unique combination of structural (RI) and functional (fluorescence) information about the sample [4]. To our knowledge, such a reconstruction of both RI and fluorescence density from the same fluorescent dataset (*i.e.*, without phase measurements) has been investigated only recently by Xue and Waller [161]. They consider two-layers samples where the bottom layer contains fluorescence-labeled objects and the top layer contains non-labelled objects. In this context, they demonstrated that the 3D RI map of the non-labelled objects can be reconstructed from defocused fluorescence images that are collected by sequentially stimulating small regions of the fluorescence-labeled layer of the sample. Moreover, they showed that the reconstructed RI map can be exploited to obtain the scattered PSF and improve the fluorescence signal through deconvolution. This setting differs in two ways from the exploitation of the individual emission of fluorophores in SMLM that we propose here. First, RI and fluorescence objects are mixed (*i.e.*, no two-layers samples). Second, fluorescence measurements are recorded at two distinct focal planes (*i.e.*, biplane SMLM modality).

In SMLM, the recovery of the RI has been addressed in [162]. This work exploits

the fact that SMLM data can be seen as measurements of an ODT system with point-source illuminations inside the sample. In [162], the authors assumed that the phase of the measurements was accessible, an assumption which is not met in practice. Moreover, their proposed approach relies on a linear model whose validity is limited to weakly scattering samples [12].

6.3 Contributions

In this chapter, we introduce a RI-reconstruction approach from (intensity) SMLM measurements. We consider a realistic image-formation model (described in Section 6.4) that integrates background fluorescence as well as the shot noise inherent to fluorescence microscopy. Importantly, we consider that the positions of the molecules are known only approximately, and then take advantage of our model-based scheme to refine them.

To cope with this challenging scenario, we propose a joint-optimization framework (Section 6.5). Our method simultaneously reconstructs the RI and refines the positions and amplitudes of the molecules. The benefits of our framework are twofold. On one side, we accurately estimate structural information (RI) from SMLM acquisitions. On the other side, we significantly improve the localization of the molecules—the primary objective of SMLM. We validate our framework on simulated data in Section 6.6.

6.4 Image-Formation Model

6.4.1 SMLM: Perspective from ODT

The space-varying RI of the sample under consideration is represented by the function $\eta : \Omega \rightarrow \mathbb{R}$ with $\Omega \subseteq \mathbb{R}^3$. The sample is populated with L fluorophores located at spatial position $\{\mathbf{x}_l \in \Omega\}_{l=1}^L$. Without loss of generality, we consider an SMLM acquisition stack where a single fluorophore is activated on each frame. Indeed, because fluorophores are incoherent sources, the image produced upon activation of multiple emitters is simply the sum of the individual contribution of each emitter [31].

When activated, the l th fluorophore at position $\mathbf{x}_l \in \Omega$ emits a spherical wave

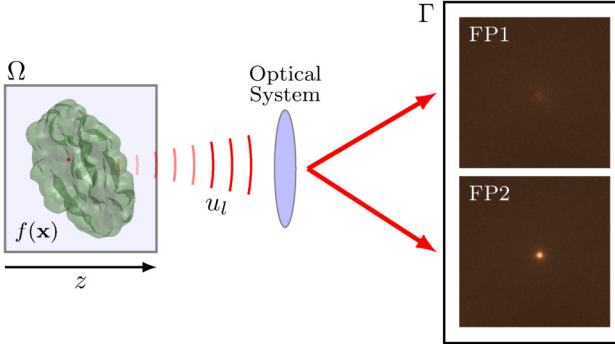


Figure 6.1: Biplane SMLM. A fluorophore emits fluorescent light which scatters through the sample. Then, an optical system records the intensity of the total field at two different focal planes.

with intensity $a_l > 0$, which leads to

$$u^{\text{in}}(\mathbf{x}; \mathbf{x}_l, a_l) = a_l \frac{\exp(jk_b \|\mathbf{x} - \mathbf{x}_l\|_2)}{4\pi \|\mathbf{x} - \mathbf{x}_l\|_2}, \quad (6.1)$$

where j is the imaginary unit and $k_b = \frac{2\pi\eta_b}{\lambda}$ is the wavenumber determined by the emission wavelength λ and the RI $\eta_b > 1$ of the surrounding medium. The spherical wave acts as an “incident” field that illuminates from within the sample. As such, it scatters through the sample and produces a field $u_l : \mathbb{R}^3 \rightarrow \mathbb{C}$ that satisfies the LiSc equation—which we recall here with the explicit dependence on \mathbf{x}_l, a_l —

$$u_l(\mathbf{x}) = u^{\text{in}}(\mathbf{x}; \mathbf{x}_l, a_l) + \int_{\Omega} g(\mathbf{x} - \mathbf{z}) f(\mathbf{z}) u_l(\mathbf{z}) d\mathbf{z}, \quad (6.2)$$

where $f(\mathbf{x}) = k_b^2 \left(\frac{\eta(\mathbf{x})^2}{\eta_b^2} - 1 \right)$ is the scattering potential and $g : \mathbb{R}^3 \rightarrow \mathbb{C}$ is the Green’s function that corresponds to the centered spherical wave $u^{\text{in}}(\mathbf{x}; \mathbf{0}, 1)$ [163]. The intensity of the field u_l at the camera plane Γ is then recorded by an optical system to form the l th SMLM frame $\mathbf{y}_l \in \mathbb{R}^M$. Formally, we have, $\forall l \in \{1, \dots, L\}$, that

$$\mathbf{y}_l = \text{Pois}(|Pu_l|_{\Gamma}|^2 + \mathbf{b}_l), \quad (6.3)$$

Algorithm 4 Joint-Optimization Framework

Require: $\mathbf{f}^0 \in \mathbb{R}_{\geq 0}^N$, $[\mathbf{x}_1^0 \cdots \mathbf{x}_L^0] \in \Omega^L$, $\mathbf{a}^0 \in \mathbb{R}_{> 0}^L$

```

1:  $t = 0$ 
2: while (Not converged) do
3:   Select a subset  $\mathcal{L} \subset \{1, \dots, L\}$ 
    $\triangleright$  Update amplitudes and positions
4:   for  $l \in \mathcal{L}$  do
5:      $(a_l^{t+1}, \mathbf{x}_l^{t+1}) = \text{Refine}(\mathcal{J}_l(\mathbf{f}^t, \cdot, \cdot); a_l^t, \mathbf{x}_l^t)$ 
6:   end for
    $\triangleright$  Update the scattering potential:
7:    $\mathbf{f}^{t+1} = \text{accel.FBS}(\sum_{l \in \mathcal{L}} \mathcal{J}_l(\cdot, \mathbf{x}_l^{t+1}, a_l^{t+1}); \mathbf{f}^t)$ 
8:    $t \leftarrow t + 1$ 
9: end while
10: return  $\mathbf{f}^t, \mathbf{X}^t, \mathbf{a}^t$ 

```

where Pois denotes Poisson's distribution (shot noise), $u_l|_{\Gamma}$ denotes the restriction of u_l to Γ , and $\mathbf{b}_l \in \mathbb{R}^M$ is a background signal that can originate from autofluorescence or spurious out-of-focus fluorophore emissions. Finally, $P : \mathbb{C}^2 \rightarrow \mathbb{R}^M$ is a linear operator that models both the effect of the optical system (*i.e.*, pointwise multiplication with the pupil function in the Fourier domain) and the sampling on the M camera pixels.

6.4.2 Discrete Forward Model

Let us rasterize Ω into N voxels of length h . Similar to our previous chapters, we define the discrete forward model by

$$\mathbf{H}^{\text{SMLM}} : \mathbb{R}_{\geq 0}^N \times \Omega \times \mathbb{R}_{> 0} \rightarrow \mathbb{R}^M$$

$$(\mathbf{f}, \mathbf{x}_l, a_l) \mapsto \mathbf{B}|\mathbf{P}[\mathbf{A}(\mathbf{f}), \mathbf{I}_M] \mathbf{s}_{\text{in}}(\mathbf{x}_l, a_l)|^2 \quad (6.4)$$

with

$$\mathbf{A}(\mathbf{f}) = \tilde{\mathbf{G}} \text{diag}(\mathbf{f}) (\mathbf{I}_N - \mathbf{G} \text{diag}(\mathbf{f}))^{-1}, \quad (6.5)$$

$$\mathbf{s}_{\text{in}}(\mathbf{x}_l, a_l) = [(\mathbf{u}_l^{\text{in}, \Omega})^T, (\mathbf{u}_l^{\text{in}, \Gamma})^T]^T. \quad (6.6)$$

Here, $\mathbf{f} \in \mathbb{R}^N$ is a sampled version of f within Ω . The vectors $\mathbf{u}_l^{\text{in},\Omega} \in \mathbb{C}^N$ and $\mathbf{u}_l^{\text{in},\Gamma} \in \mathbb{C}^M$ are the sampled versions of $u^{\text{in}}(\cdot; \mathbf{x}_l, a_l)$ within Ω and Γ , respectively. We denote by $\{\mathbf{x}_n^\Omega\}_{n=1}^N$ and $\{\mathbf{x}_m^\Gamma\}_{m=1}^M$ the sampling points within Ω and Γ . Similar to previous chapters, the matrix $\mathbf{G} \in \mathbb{C}^{N \times N}$ encodes the convolution with the Green’s function in (6.2). Similarly, $\tilde{\mathbf{G}} \in \mathbb{C}^{M \times N}$ is a matrix that, given the total field within Ω , gives the scattered field at the measurement plane Γ . Next, $\mathbf{P} \in \mathbb{C}^{M \times M}$ is the discrete version of P and $|\cdot|^2$ denotes the pointwise-squared magnitude. A full description of \mathbf{G} , $\tilde{\mathbf{G}}$, and \mathbf{P} is provided in Chapter 4. Finally, the matrix $\mathbf{B} \in \mathbb{R}^{M \times M}$ encodes a convolution with a Gaussian filter of length $\sigma_b = 0.7h$. It accounts for the mismatch between our physical model derived from the scalar diffraction theory and the vectorial nature of light [164, 165].

In this work, we adopt a biplane configuration [166] that involves two pupil functions with separate focal planes. To keep the notation simple, we shall use a single matrix \mathbf{P} to represent the effect of the two pupil functions (*i.e.*, two focal planes). Given the discrete forward model (6.4), the image formation model (6.3) writes as, $\forall l \in \{1, \dots, L\}$,

$$\mathbf{y}_l = \text{Pois}(\mathbf{H}^{\text{SMLM}}(\mathbf{f}, \mathbf{x}_l, a_l) + \mathbf{b}_l). \quad (6.7)$$

Remark 6.4.1. *Although we consider a biplane modality in our experiments, the proposed joint optimization framework (Section 6.5) can be deployed with any number of focal planes. In this proof-of-concept work, we considered two focal planes because i) it corresponds to a standard SMLM modality ii) it helps to compensate for the lack of phase measurements.*

6.5 Joint Recovery of the Molecule Localization and Refractive Indices (RI)

6.5.1 Joint-Optimization Framework

Our goal is to jointly recover the distribution of the RI and the localization of fluorescent molecules. To that end, we propose to solve the minimization problem

$$(\mathbf{f}_*, \mathbf{X}_*, \mathbf{a}_*) \in \arg \min_{\substack{\mathbf{f} \in \mathbb{R}_{\geq 0}^N, \\ \mathbf{X} \in \Omega^L, \mathbf{a} \in \mathbb{R}_{> 0}^L}} \sum_{l=1}^L \mathcal{J}_l(\mathbf{f}, \mathbf{x}_l, a_l) + \tau \mathcal{R}(\mathbf{L}\mathbf{f}), \quad (6.8)$$

where, for all $\mathbf{f} \in \mathbb{R}_{\geq 0}^N$, $\mathbf{x} \in \Omega$, and $a > 0$,

$$\mathcal{J}_l(\mathbf{f}, \mathbf{x}, a) = \mathcal{D}_{\text{KL}}(\mathbf{H}^{\text{SMLM}}(\mathbf{f}, \mathbf{x}, a) + \mathbf{b}_l; \mathbf{y}_l). \quad (6.9)$$

The matrix $\mathbf{X} = [\mathbf{x}_1 \cdots \mathbf{x}_L] \in \Omega^L$ and the vector $\mathbf{a} = (a_1, \dots, a_L) \in \mathbb{R}_{> 0}^L$ are the concatenation of positions and amplitudes of the fluorophores, respectively. In this work, we use a TV regularization [125], although alternatives such as HS [126] or learnt regularizers [100, 167–169] can be easily plugged into our framework. The data-fidelity term \mathcal{D}_{KL} is the Kullback-Leibler divergence [170] defined as, $\forall(\mathbf{z}, \mathbf{y}) \in \mathbb{R}_{\geq 0}^M \times \mathbb{R}_{\geq 0}^M$,

$$\mathcal{D}_{\text{KL}}(\mathbf{z}; \mathbf{y}) = \mathbf{z}^T \mathbf{1}_M - \mathbf{y} \odot \log(\mathbf{z} + \beta), \quad (6.10)$$

where $\beta > 0$ is a stabilizing parameter. Note that the Kullback-Leibler divergence corresponds to the Poisson negative log-likelihood up to some constant term.

To optimize (6.8), we alternate between an update of the RI and an update of the amplitudes and positions of the fluorophores (Algorithm 4), inspired by the self-calibrating reconstruction techniques developed for other modalities [1, 171]. Updates are performed on a subset of molecules (Line 3) in a stochastic fashion. In Algorithm 4, `accel.FBS` ($\sum_{l \in \mathcal{L}} \mathcal{J}_l(\cdot, \mathbf{x}_l^{t+1}, a_l^{t+1}); \mathbf{f}^t$) refers to the minimization of $\sum_{l \in \mathcal{L}} \mathcal{J}_l(\cdot, \mathbf{x}_l^{t+1}, a_l^{t+1})$ with the accelerated FBS initialized with \mathbf{f}^t . We use the same notation for the refinement step at Line 5. Details on the algorithms deployed for each sub-problem are provided in Sections 6.5.2 and 6.5.3. We implemented the method within the `GlobalBioIm` library [131].

6.5.2 Update of Molecule Amplitudes and Positions

For the refinement procedure in Line 5 of Algorithm 4, we again adopt an alternating scheme between an update of the amplitude and the position, as summarized in Algorithm 5. In the Sections 6.5.2 and 6.5.2, we describe the Newton and gradient update steps used to refine the amplitude and position, respectively.

Amplitudes

Let $\mathbf{f} \in \mathbb{R}_{\geq 0}^N$ and $\mathbf{X} \in \Omega^L$ be fixed. First of all, one can see from (6.4) that, for $a_l > 0$,

$$\mathbf{H}^{\text{SMLM}}(\mathbf{f}, \mathbf{x}_l, a_l) = a_l^2 \mathbf{H}^{\text{SMLM}}(\mathbf{f}, \mathbf{x}_l, 1), \quad (6.11)$$

Algorithm 5 Refinement procedure for the l th molecule

Require: $\mathbf{x}_l^0 \in \Omega$, $a_l^0 > 0$, $T_{\text{mol}} \in \mathbb{N}$

- 1: $t = 0$
 - 2: **while** (Not converged or $t < T_{\text{mol}}$) **do**
 - 3: $a_l^{t+1} = \text{NewtonUpdate}(\mathcal{J}_l(\mathbf{f}, \mathbf{x}_l^t, \cdot); a_l^t)$
 - 4: $\mathbf{x}_l^{t+1} = \text{GradientUpdate}(\mathcal{J}_l(\mathbf{f}, \cdot, a_l^{t+1}); \mathbf{x}_l^t)$
 - 5: $t \leftarrow t + 1$
 - 6: **end while**
 - 7: **return** \mathbf{x}_l^t, a_l^t
-

which is very helpful to reduce the computational cost of our joint-optimization procedure. Indeed, denoting $\mathbf{d}_l = \mathbf{H}^{\text{SMLM}}(\mathbf{f}, \mathbf{x}_l, 1)$, we have that

$$\mathcal{J}_l(\mathbf{f}, \mathbf{x}_l, a_l) = \mathcal{D}_{\text{KL}}(a_l^2 \mathbf{d}_l + \mathbf{b}_l; \mathbf{y}_l) \quad (6.12)$$

$$= (a_l^2 \mathbf{d}_l + \mathbf{b}_l)^T \mathbf{1}_M - \mathbf{y}_l \odot \log(a_l^2 \mathbf{d}_l + \mathbf{b}_l + \beta). \quad (6.13)$$

The function \mathcal{J}_l is twice differentiable with respect to a . Its first derivative is given by

$$\partial_a \mathcal{J}_l(\mathbf{f}, \mathbf{x}_l, a_l) = 2a_l \sum_{m=1}^M v_{lm} \left(1 - \frac{y_{lm}}{a_l^2 v_{lm} + b_{lm} + \beta} \right). \quad (6.14)$$

Its second derivative reads as

$$\begin{aligned} \partial_a^2 \mathcal{J}_l(\mathbf{f}, \mathbf{x}_l, a_l) &= 2 \sum_{m=1}^M v_{lm} \left(1 - \frac{y_{lm}}{a_l^2 v_{lm} + b_{lm} + \beta} \right) \\ &\quad + \sum_{m=1}^M \frac{(2a_l v_{lm})^2 y_{lm}}{(a_l^2 v_{lm} + b_{lm} + \beta)^2}. \end{aligned} \quad (6.15)$$

As such, we can perform a Newton update on a_l as

$$a_l^{t+1} = a_l^t - s \frac{\partial_a \mathcal{J}_l(\mathbf{f}, \mathbf{x}_l, a_l^t)}{\partial_a^2 \mathcal{J}_l(\mathbf{f}, \mathbf{x}_l, a_l^t)}, \quad (6.16)$$

where s is the length of a step computed via line-search so as to satisfy Wolfe's conditions [172].

Positions

Let $\mathbf{f} \in \mathbb{R}_{\geq 0}^N$ and $\mathbf{a} \in \mathbb{R}_{> 0}^L$ be fixed. We want to perform a gradient update on the position \mathbf{x}_l of the l th molecule. However, one can see that the spherical wave in (6.1) is not differentiable whenever $\mathbf{x} = \mathbf{x}_l$. Consequently, we prefer to consider the smoothed version of the spherical wave

$$u_{\text{smth}}^{\text{in}}(\mathbf{x}; \mathbf{x}_l, a_l) = a_l \frac{\exp(jk_b \|\mathbf{x} - \mathbf{x}_l\|_{2,\epsilon})}{4\pi \|\mathbf{x} - \mathbf{x}_l\|_{2,\epsilon}}, \quad (6.17)$$

where $\|\cdot\|_{2,\epsilon} = \sqrt{\|\cdot\|_2^2 + \epsilon}$ with $0 < \epsilon \ll 1$. Then, the gradient of \mathcal{J}_l with respect to \mathbf{x} , evaluated at \mathbf{x}_l , is given by

$$\begin{aligned} \nabla_{\mathbf{x}} \mathcal{J}_l(\mathbf{f}, \mathbf{x}_l, a_l) &= 2\mathbf{J}_{\mathbf{s}_{\text{in},l}}^H [\mathbf{A}(\mathbf{f}), \mathbf{I}_M]^H \mathbf{P}^H \mathbf{P} [\mathbf{A}(\mathbf{f}), \mathbf{I}_M] \mathbf{s}_{\text{in},l} \\ &\quad \odot \mathbf{B}^T \nabla_{\mathbf{z}} \mathcal{D}_{\text{KL}}(\mathbf{H}^{\text{SMLM}}(\mathbf{f}, \mathbf{x}_l, a_l) + \mathbf{b}_l), \end{aligned} \quad (6.18)$$

where $\mathbf{s}_{\text{in},l} = \mathbf{s}_{\text{in}}(\mathbf{x}_l, a_l) \in \mathbb{C}^{N+M}$. The gradient of \mathcal{D}_{KL} in (6.10) with respect to the first variable \mathbf{z} is given by

$$\nabla_{\mathbf{z}} \mathcal{D}_{\text{KL}}(\mathbf{z}; \mathbf{y}) = \mathbf{1}_M - \mathbf{y}_l \oslash (\mathbf{z} + \beta). \quad (6.19)$$

Finally, it remains to provide the expression of the Hermitian transpose of the Jacobian matrix of $\mathbf{s}_{\text{in}}(\cdot, a_l)$, evaluated at \mathbf{x}_l , which we denote $\mathbf{J}_{\mathbf{s}_{\text{in},l}}^H \in \mathbb{C}^{3 \times (N+M)}$. Its q th column is given by

$$[\mathbf{J}_{\mathbf{s}_{\text{in},l}}^H]_q = [\mathbf{s}_{\text{in},l}]_q^* \left(jk_b + \frac{1}{\|\mathbf{r}_q - \mathbf{x}_l\|_{2,\epsilon}} \right) \frac{(\mathbf{r}_q - \mathbf{x}_l)}{\|\mathbf{r}_q - \mathbf{x}_l\|_{2,\epsilon}}. \quad (6.20)$$

Let us emphasize that $\mathbf{r}_q = \mathbf{x}_q^\Omega$ (Ω sampling points) for $q \leq N$ and $\mathbf{r}_q = \mathbf{x}_{q-N}^\Gamma$ (Γ sampling points) for $N < q \leq N + M$. Equipped with this closed-form gradient, we can deploy a projected-gradient update on \mathbf{x}_l as

$$\mathbf{x}_l^{t+1} = \mathcal{P}_\Omega \left(\mathbf{x}_l^t - s \nabla_{\mathbf{x}} \mathcal{J}_l(\mathbf{f}, \mathbf{x}_l^t, a_l) \right), \quad (6.21)$$

where s is a step-size computed via a backtracking line-search [173]. The projector $\mathcal{P}_\Omega : \mathbb{R}^3 \rightarrow \Omega$ constrains the fluorophore positions to remain in Ω .

Algorithm 6 accel. FBS

Require: $\mathbf{f}^0 \in \mathbb{R}_{\geq 0}^N$, $T_{\text{RI}} \in \mathbb{N}$, $\gamma > 0$, $\alpha \in [0, 1]$

- 1: $t = 0$, $\mathbf{w}^0 = \mathbf{f}^0$, $v^0 = 1$
 - 2: **while** (Not converged or $t < T_{\text{RI}}$) **do**
 - 3: $\mathbf{g} = \sum_{l \in \mathcal{L}} \nabla \mathcal{J}_l(\cdot, \mathbf{x}_l, a_l)(\mathbf{w}^t)$
 - 4: $\mathbf{f}^{t+1} = \text{prox}_{\gamma\tau\mathcal{R}(\mathbf{L}\cdot)}(\mathbf{w}^t - \gamma\mathbf{g})$
 - 5: $v^{t+1} = \frac{1 + \sqrt{1 + 4(v^t)^2}}{2}$
 - 6: $\mathbf{w}^{t+1} = \mathbf{f}^t + \alpha \frac{v^t - 1}{v^{t+1}}(\mathbf{f}^t - \mathbf{f}^{t+1})$
 - 7: $t \leftarrow t + 1$
 - 8: **end while**
 - 9: **return** \mathbf{f}^t
-

6.5.3 Update of the RI

When the positions $\mathbf{X} \in \Omega^L$ and amplitudes $\mathbf{a} \in \mathbb{R}_{>0}^L$ are fixed, the RI update consists in solving

$$\mathbf{f}^* \in \arg \min_{\mathbf{f} \in \mathbb{R}_{\geq 0}^N} \sum_{l=1}^L \mathcal{J}_l(\mathbf{f}, \mathbf{x}_l, a_l) + \tau\mathcal{R}(\mathbf{L}\mathbf{f}). \quad (6.22)$$

It corresponds to an inverse-scattering problem from intensity measurements [7, 22]. To solve (6.22), we deploy a relaxed variant [117] of the accelerated FBS algorithm [127, 128] (Algorithm 6). It requires the computation of two quantities.

1. The gradient of $\mathcal{J}_l(\cdot, \mathbf{x}_l, a_l)$ which involves the Jacobian of $\mathbf{A}(\mathbf{f})$ in (6.4) whose expression is provided in [18].
2. The proximal operator of $\mathcal{R}(\mathbf{L}\cdot)$ which, for TV, can be efficiently evaluated by using the fast gradient-projection algorithm [129].

6.5.4 Initialization Strategies

Initialization of the RI

In ODT from intensity-only measurements, the LFR method is a standard tool to obtain an initial guess of the RI distribution [7, 64]. However, this initialization

requires coherent light sources with known geometry, which prevents its use on SMLM data. We therefore adopt an alternative approach that comprises two steps. We first replicate the widefield image (sum of the SMLM stack) along the axial direction and then blur the obtained volume with a Gaussian filter. The rationale behind this choice is that we can only expect to recover the RI where fluorophore emissions have propagated, that is, at the vicinity of fluorescent molecules. We then define \mathbf{f}^0 as a scaled version of this filtered volume so that its values belong to an admissible range of RI (Fig. 6.3).

Single-Molecule Localization

Any SMLM localization software can be used to compute the initial positions $\{\mathbf{x}_l^0\}_{l=1}^L$. However, we found that existing software packages for a biplane modality were not performing well on our simulated dataset. We believe that this is due to the high thickness of the sample together with the small number of acquisitions.

Therefore, we adopted a simple yet efficient method. We localize the position of the l th fluorophore based on cross-correlations between the measurements \mathbf{y}_l and a set $\{\mathbf{k}_p\}_{p=1}^P$ of PSF models in \mathbb{R}^M . We define them as the the output of the forward model with no scatterer, like in

$$\mathbf{k}_p = \mathbf{H}^{\text{SMLM}}(\mathbf{0}_N, \mathbf{x}_p^{\text{psf}}, 1), \quad (6.23)$$

where the positions $\mathbf{x}_p^{\text{psf}} = (0, 0, p\Delta z)$ for $p = \{-P, \dots, P\}$ vary along the axial direction. We then initialize

$$\mathbf{x}_l^0 = (\hat{m}h, \hat{n}h, \hat{p}\Delta z) \quad (6.24)$$

where

$$(\hat{m}, \hat{n}, \hat{p}) = \arg \max_{m,n,p} [\mathbf{y}_l * \mathbf{k}_p^\vee]_{m,n}, \quad (6.25)$$

Once localized, we initialize the amplitude as

$$a_l^0 = \left(\|\mathbf{M}_{\mathbf{x}_l^0}(\mathbf{y}_l - \hat{\mathbf{b}}_l)\|_1 / \|\mathbf{k}_{\hat{p}}\|_1 \right)^{\frac{1}{2}}, \quad (6.26)$$

where $\mathbf{M}_{\mathbf{x}_l^0} \in \mathbb{R}^{R \times M}$ crops a region-of-interest centered at \mathbf{x}_l^0 and $\hat{\mathbf{b}}_l$ denotes the estimated background (Section 6.5.4).

Background Estimation

To estimate $\{\mathbf{b}_l\}_{l=1}^L$, we apply a simple algorithm suitable for a background that slowly varies in space and time. In SMLM, this is a common assumption [174]. Our procedure proceeds in two steps.

1. For each measurement \mathbf{y}_l , we mask an area around the estimated position \mathbf{x}_l and inpaint it using the function `regionfill` of Matlab² to obtain $\bar{\mathbf{y}}_l$.
2. We apply a spatio-temporal (3D) median filter along the stack of masked and inpainted measurements $\bar{\mathbf{Y}} = [\bar{\mathbf{y}}_1 \cdots \bar{\mathbf{y}}_L]$ to take advantage of the spatio-temporal smoothness of the background.

6.6 Results on Simulated Data

6.6.1 Simulation Setting

We created an RI map immersed in water ($\eta_b = 1.339$), fully included in the region Ω of size $(7.2 \times 7.2 \times 3.2)\mu\text{m}^3$ (Fig. 6.2). This sample presents small features with RI values that are lower or higher than their surroundings. Then, we populated this sample with fluorophores randomly placed on a structure that is composed of an outer membrane as well as inner compartments. The smallest distance between two fluorophores is 20nm. We simulated $L = 1000$ SMLM acquisitions with a biplane modality, each corresponding to the activation of a single fluorophore. The two focal planes were set at $\pm 300\text{nm}$. The amplitude a_l of each fluorophore emission was drawn from a Poisson distribution with mean $A = 1000$ and the wavelength of the emitted light is set at $\lambda = 647\text{nm}$. In addition, we simulated a pupil function for each focal plane with $\text{NA} = 1.45$ and 25 Zernike coefficients. Their values were drawn from the uniform distribution $U(-0.5, 0.5)$, except that the three first coefficients were set to 0 and that the fourth coefficient was drawn from $U(-0.1, 0.1)$ to better match the PSFs observed in real SMLM acquisitions. The background signals \mathbf{b}_l for $l \in \{1, 100, 200, \dots, 1000\}$ were simulated by convolving a Gaussian kernel with a random image generated from a uniform distribution. We then scaled

² Matlab’s command `regionfill` performs a smooth interpolation inward from the pixel values that are on the outer boundary of the mask.

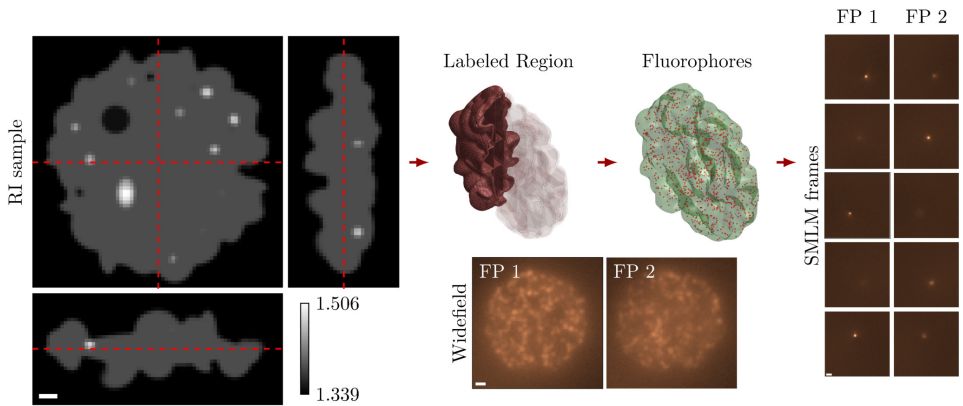


Figure 6.2: Simulation setup. The RI map, immersed in water ($n_b = 1.339$), is depicted on the left orthoviews. The sample is populated with fluorescent molecules that belong to the labeled region. They sequentially emit a spherical wave which is then propagated through the sample using LSm (Chapter 3). Two focal planes (with pupil functions) are acquired. The widefield images are generated by summing all SMLM frames. The fluorescence images were saturated for visualization purpose. We display the labeled region with partial transparency so as to make the inner compartments visible. Scale bars: 500nm.

the obtained images so that their pixel values belong to the range $[350, 450]$. Backgrounds for intermediate frames were then obtained through interpolation. We set a large width for the Gaussian kernel so as to obtain a slowly varying background in both space and time. Finally, to control the noise, we scaled the noiseless measurements with a factor $r \in (0, 1]$ before applying the Poisson noise so that (6.4) writes as, $\forall l \in \{1, \dots, L\}$,

$$\mathbf{y}_l = \text{Pois}(r(\mathbf{H}^{\text{SMLM}}(\mathbf{f}, \mathbf{x}_l, a_l) + \mathbf{b}_l)). \quad (6.27)$$

By doing so, r can be interpreted as the product between the excitation photon flux and the integration time. A small r yields a higher level of noise, which increases the difficulty of the localization of molecules and the RI reconstruction.

We compare our joint-optimization framework with two baselines. They consist on the sole RI reconstruction with i) perfectly characterized molecules (*i.e.*, true amplitudes and positions) or ii) the initial estimation of the amplitudes and positions obtained as described in Section 6.5.4. By doing so, we somehow obtain the worst-case and best-case scenarios. For each case, we obtained the best reconstruction by performing a grid search on the regularization parameter τ .

For our joint-optimization framework, we set the parameters $T_{\text{mol}} = 4$, $T_{\text{RI}} = 1$, and $\alpha = 0.85$. In our implementation, \mathbf{w}^0 and v^0 in Line 1 of Algorithm 6 are initialized from the previous call. We ran our optimization on a PowerEdge c4140 equipped with Intel Xeon Gold 6240 CPUs (2.60GHz) and a GPU NVIDIA Tesla V100 SXM3 (32 GB). An iteration of Algorithm 4 took 20 seconds on average. We used up to 2000 iterations, which corresponds to about 10 hours of computation.

6.6.2 Metrics and Visualization

To assess the quality of the reconstructed RI map, we compute the relative error as well as the structural similarity index measure (SSIM) [175] with respect to the ground truth. To assess the accuracy of the localization of the molecules, we compute the root-mean-square error (RMSE) with respect to the true positions. Note that we do not report detection metrics such as true/false detections as they are not really relevant in our setting where we consider only frames containing one molecule. Finally, given a list of molecule positions, we generate a 3D image through the Gaussian rendering technique [27]. To that end, we represent the fluorophore

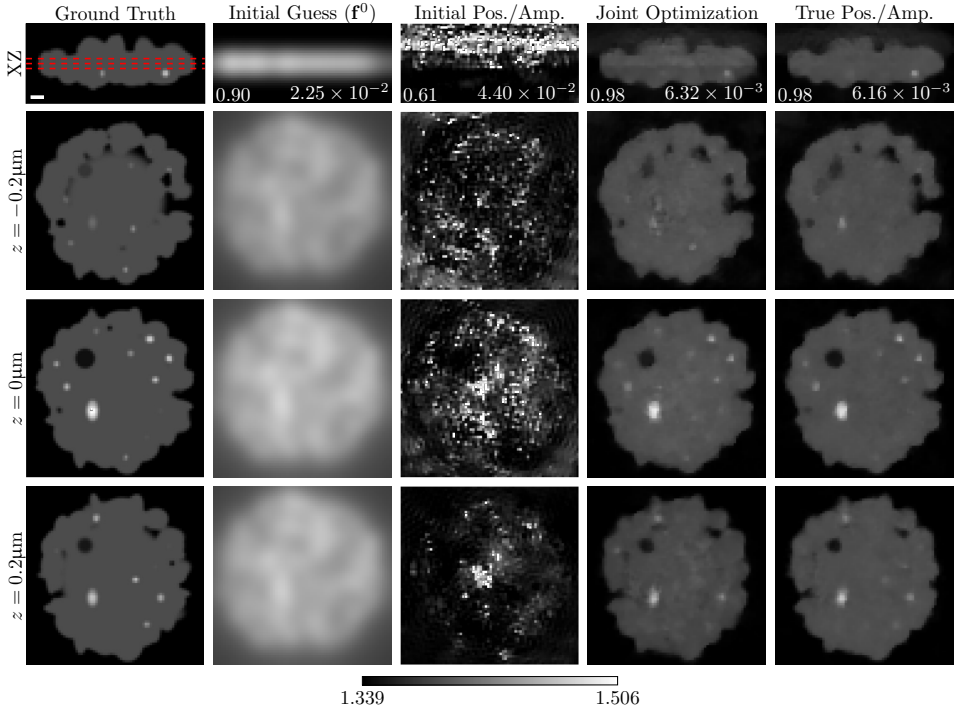


Figure 6.3: Reconstructions of the RI Map. From left to right: Ground truth, initial guess, reconstruction with positions and amplitudes fixed to their initial values (Section 6.5.4), reconstruction with the proposed joint-optimization framework, and reconstruction with positions and amplitudes fixed to their true values (gold-standard). The SSIM and relative errors are displayed in the first row at the left and right corners, respectively, of each corresponding reconstruction. Scale bar: 500nm.

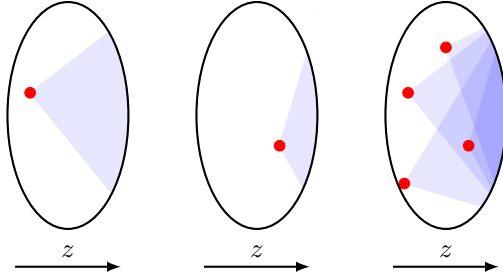


Figure 6.4: Observable region of the sample. Illustration of the region of the sample that is “illuminated” by a fluorophore far from (left) and close to (middle) the detection system. The right scheme illustrates the fact that SMLM data carry more information about RI regions that are close to the detection system (positive z).

positions as a sum of shifted Dirac

$$s(\mathbf{x}) = \sum_{l=1}^L \delta(\mathbf{x} - \mathbf{x}_l). \quad (6.28)$$

Gaussian rendering then consists in convolving s with an isotropic Gaussian kernel and sample the result on a grid. Here, we set the standard deviation of the Gaussian kernel to 10nm and the grid step to $h/10 = 10\text{nm}$.

6.6.3 Results

We first fix the noise level to $r = 1$ in (6.27).

Reconstructed RI

We display the RI maps in Fig. 6.3 and report there the relative errors and SSIM. When the positions and amplitudes of the molecules are perfectly known, we recover most of the details of the ground truth. On the contrary, the reconstruction

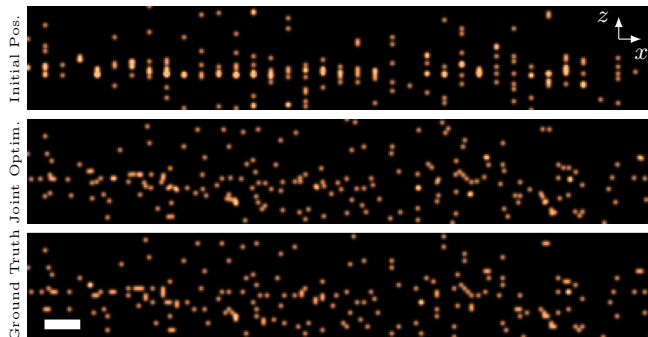


Figure 6.5: Rendering of localized molecules (Y-projection). Region-of-interest of the projection along Y of the rendered fluorescent volume. From top to bottom: Initial positions, positions refined with the joint-optimization framework, ground truth. Field-of-view (XZ): $(3600 \times 600)\text{nm}^2$. The images were saturated for visualization purpose. Scale bar: 200nm.

obtained with the initial positions and amplitudes is unsuccessful. This highlights the importance of refining molecule positions and amplitudes jointly with RI reconstruction. We effectively see that our joint-optimization framework is able to recover an RI map that is visually similar to the best-case scenario. The metrics confirm the visual assessment. Yet, one can observe some high frequency artifacts (ringing) on the reconstruction obtained with the joint optimization framework (plane $z = -0.2\mu\text{m}$). They are due to few badly refined molecule positions (outliers in Figure 6.8) that lead to a mismatch in the model. Finally, it should be noted that we could expect that the quality of the reconstruction varies with the axial position z . The reason is that an SMLM frame (from the activation of one molecule) carries information about the part of sample that lies between the activated molecule and the optical system (Figure 6.4). As such, there are more SMLM frames that carry information about z -planes with positive z than frames that carry information about z -planes with negative z . Moreover, waves produced by fluorophores with negative z -positions propagate through a larger layer of the

Table 6.1: RMSE for the estimated positions and amplitudes. First row: Initial positions and amplitudes from our standard single-molecule localization. Second row: Positions and amplitudes from our joint-optimization framework. Third and fourth rows: Positions and amplitudes refined with the RI map fixed to the initial guess \mathbf{f}^0 and the ground truth (GT), respectively. Amp.: Amplitude. Lat.: Lateral. Ax.: Axial.

	3D [nm]	Lat. [nm]	Ax. [nm]	Amp.
Initial	163	69	148	109
Joint	74	15	72	76
with \mathbf{f}^0	142	38	136	194
with \mathbf{f}_{GT}	72	18	70	76

sample, inducing more scattering. These facts make that i) fluorophores with negative z -positions are harder to localize, and ii) z -planes of RI with negative z are harder to reconstruct.

Molecule Localization

It is noteworthy to recall that the primary objective of SMLM is to localize the fluorescent molecules with nanometric precision. It follows that another benefit of our joint-optimization framework is an improvement of this localization. Indeed, our model accounts for sample-induced distortions that usually compromises the accurate localization of molecules [160].

We report in Table 6.1 the RMSE of the initial and refined positions, as well as the RMSE of the initial and refined amplitudes. In addition, we provide the RMSE of the refined positions and amplitudes when the RI map is fixed to the initial guess \mathbf{f}^0 or the ground truth (best-case scenario).

There is a gain of 89nm in the 3D RMSE for our joint-optimization framework. One sees that the lateral and axial RMSE are improved by 54nm and 76nm, respectively. Not only does our joint-optimization framework successfully recover the RI map, but it also improves significantly the localization of the molecules. The proposed joint-optimization framework performs better than the refinement of

the positions and amplitudes with the RI map fixed to \mathbf{f}^0 . Moreover, it performs similarly to the refinement with the RI map fixed to the ground truth. Those observations confirm that the joint-optimization framework is necessary to improve the localization and can even reach similar performance to the best-case scenario.

In Figure 6.5, we display a Y-projection of the fluorescent volume rendered from the molecule positions, where one can visually appreciate the gain in accuracy. The estimation of the amplitudes is improved as well. This can help to better estimate the uncertainty of localization [176, 177].

Influence of the Distribution of Fluorophores

From the phenomenon illustrated in Figure 6.4, one can expect that the quality of the reconstructed RI map is closely related to the spatial distribution of the fluorescent probes. In this section, we investigate this question by comparing the reconstructions obtained with the four fluorophore distributions illustrated in Figure 6.6 (Panel A). These include the rather homogeneous distribution depicted in Figure 6.2 and a more concentrated distribution, both with two different numbers of molecules (*i.e.*, numbers of frames).

Table 6.2: RMSE of the estimated positions and amplitudes for the four distributions of fluorophores depicted in Figure 6.6 (Panel A). Amp.: Amplitude. Lat.: Lateral. Ax.: Axial. Dist.: Distribution.

	#Fluo	3D [nm]	Lat. [nm]	Ax. [nm]	Amp.
Dist. 1	1000	74	15	72	76
	100	80	13	79	76
Dist. 2	1000	85	3	85	77
	100	82	3	82	55

As expected, the reconstructed RI map is significantly degraded when the distribution of fluorophores is more concentrated (Figure 6.6B, right column). Indeed, the emitted light has mainly propagated through a restricted area of the sample, limiting the information on the RI map carried by the measurements. On the contrary, the quality of the reconstructed RI map seems less sensitive to the number of

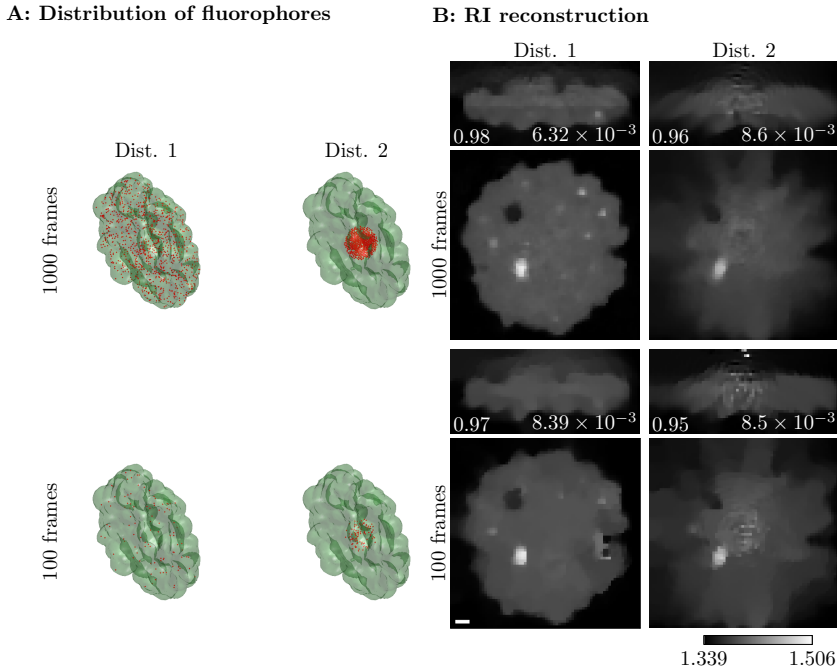


Figure 6.6: Reconstructions of the RI map with different fluorophore distributions. A: The four considered fluorophore distributions. B; Reconstructed RI maps. The SSIM and relative errors are displayed in the XZ view at the left and right corners of each reconstruction, respectively. The SNR is displayed at the bottom-left corner for each noise level. Scale bar: 500nm.

fluorophores. Although some details are lost, the RI maps reconstructed with 100 frames remain qualitatively similar to their counterparts reconstructed from 1000 frames (Figure 6.6B).

Finally, we display in Table 6.2 the RMSE obtained after the joint optimiza-

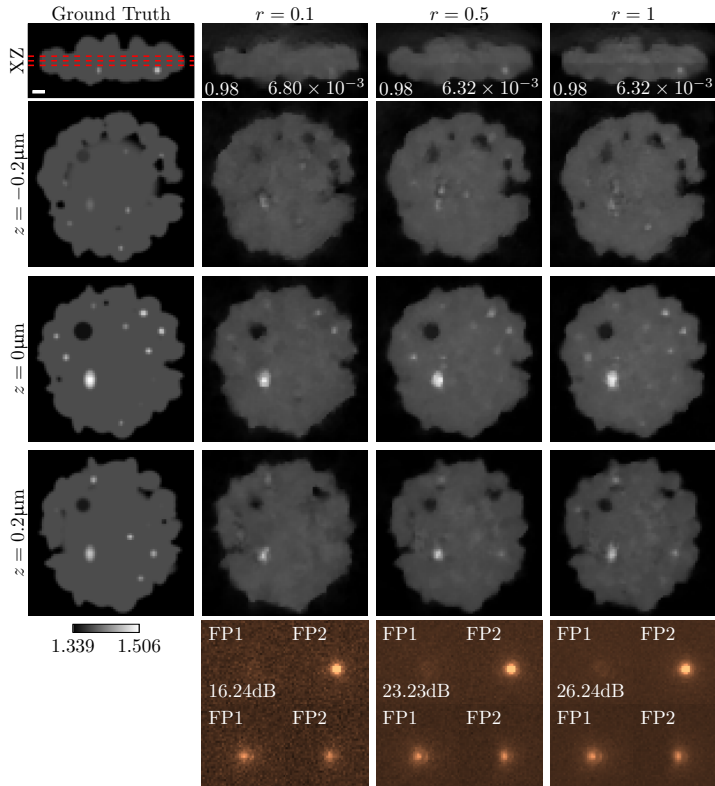


Figure 6.7: Reconstructions of the RI map with different noise levels. From left to right: Ground truth, reconstruction with the proposed joint optimization framework for $r = 0.1, 0.5$, and 1 . The SSIM and relative errors are displayed in the first row at the left and right corners of each reconstruction, respectively. The last row contains two examples of SMLM acquisition (ROI) for two different molecules at axial positions $z = 440\text{nm}$ (top) and $z = 0\text{nm}$ (bottom). The SNR is displayed at the bottom-left corner for each noise level. Scale bar: 500nm .

tion. Interestingly, the refinement of the positions and amplitudes of the molecules remains stable when reducing the number of frames. For the concentrated distribution, the axial RMSE is slightly degraded and, on the contrary, the lateral RMSE is drastically reduced, which might be due to the concentration of the distribution.

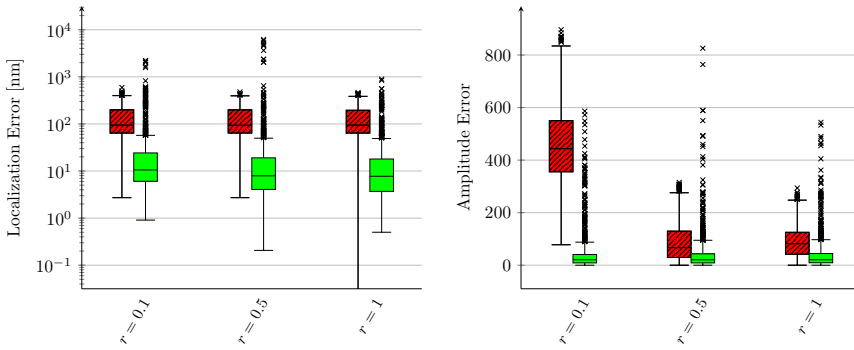


Figure 6.8: Box plots of the localization (left) and amplitude (right) error for different noise levels. Three noise levels are displayed with $r = 0.1, 0.5$, and 1 . For each case, the left box plot (hatched) corresponds to the initial positions/amplitudes and the right box plot (solid) corresponds to the refined positions/amplitudes. Note that the estimated amplitudes were scaled by r^{-1} to compare with the same ground truth. For the box plots of the localization error after refinement (solid), we set the upper whiskers to 50nm so as to consider any larger error as outliers. This is in line with the expected 3D localization error in SMLM [27]. This bound is not relevant for the initial errors (hatched) as they are too large. For the hatched box plots, we thus set the default upper whiskers to $Q3 + 1.5\text{IQR}$, where $\text{IQR} = (Q3 - Q1)$ is the interquartile range and $Q1$, $Q3$ are the 25th and 75th percentile, respectively. Finally, the lower whiskers are always set to the smallest error among all molecules. Outliers are indicated by \times .

Robustness to Noise

Next, we are interested in the robustness of our framework to the measurement noise. To that end we vary the parameter r in (6.27) from 0.1 to 1. Some examples of obtained measurements are shown in Figure 6.7 (last row), where one can observe that the noise is stronger when r is smaller.

The RI reconstructions for each noise level are displayed in Figure 6.7. Although the quality of reconstruction degrades when the noise increases, the shape and the most prominent features are recognizable even for $r = 0.1$. This suggests that our method is quite robust to noise.

The box plots of the localization errors are displayed in Figure 6.8. For each noise level, we show the box plot for the initial and refined positions to illustrate the improvement. We again observe a certain robustness to noise, even for the case $r = 0.1$ where the amplitudes were badly initialized.

It is noteworthy to mention the presence of outliers in the displayed box plots even for $r = 1$. For some molecules, we observed that the joint-optimization could not refine the positions and amplitudes well. In few cases, the estimates did even worsen. Fortunately, the number of such failures is limited (*e.g.*, 60 over 1000 molecules for $r = 0.1$).

6.7 Summary

In this chapter, we presented a joint-optimization framework to estimate both the RI map and the position of fluorescent molecules from an SMLM acquisition stack. Our method takes advantage of the sample-induced aberrations to unveil the map of the RI of the sample. Such structural information ideally complements fluorescence imaging [4]. In addition to this unique feature, our framework is able to improve the accuracy of molecule localization. Our work shows that additional information about the sample can be recovered from SMLM data. This is a first step towards an exciting and novel extension of SMLM.

In the next chapter, we come back to ODT from complex measurements described in Chapter 4), and are interested in a processing step of the measurements—phase unwrapping. We will present a deep-learning based method to unwrap challenging phase images, with many prospects for 2D and 3D QPI.

Chapter 7

Phase Unwrapping with Deep Image Prior (PUDIP)

7.1 Introduction

In Chapter 4, we presented a reconstruction framework for ODT with complex measurements. The phase of these complex images was acquired by DHM. In practice, the measured phase suffers from wrapping (*i.e.*, modulo 2π of the original phase), which introduces non-representative discontinuities in its distribution. Once recovered from the measurements, the unwrapped version provides quantitative information on the sample [178] or is used for tomographic reconstruction (Rytov model) [13]. This process, known as phase unwrapping, is an important step for phase imaging. However, its application to biological specimens such as organoids is challenging; in particular, the advent of thick and complex samples calls for advanced methods. Classical methods, largely optimized for the analysis of 2D samples, exhibit important unwrapping artifacts and thus remain unreliable for these complex samples (Fig. 7.1). In this chapter, we propose a phase unwrapping method based on untrained convolutional neural networks (CNN) to solve this challenging task.¹

¹ The content of this chapter is based on [26].

7.2 Context

7.2.1 Classical Methods

In the past decades, numerous 2D phase-unwrapping algorithms have been proposed. These approaches generally fall into four categories: path following [179, 180], minimum L_p -norm [181–183], Bayesian/regularization [184, 185], and parametric modeling [186].

Most of the path-following algorithms perform a line integration along some path established by techniques such as the branch-cut algorithm [179]. Generally, the path-following methods encounter issues of consistency as the resulting unwrapped phase depends on the path.

By contrast, the minimum-norm methods are global. They estimate the unwrapped phase by minimizing an L_p -norm. When $p = 2$ (least-squares methods) [187], there exist approximate solutions which can be obtained by fast Fourier transforms or discrete cosine transforms [182]. However, the L_2 -norm tends to smooth image edges, especially at the discontinuities [181]. The drawback associated to $p = 2$ can be overcome by setting $0 \leq p \leq 1$, which usually increases the computational cost. Bioucas-Dias and Valadao [188] introduced a specific energy-minimization framework for phase unwrapping that is solved via graph-cut optimization (PUMA). Recent works have extended this method for other imaging modalities [189, 190]. In the same spirit, Condat et al. recover the wrap-count with a convex relaxation of the original integer-optimization problem [191]. In [192], the authors describe a weighted energy function combined with an HS regularization [126]. They optimize the minimization problem with an iterative algorithm (IRTV) based on ADMM [147].

Bayesian approaches take into account a data-acquisition model and statistical prior knowledge on the phase. Such approaches are usually computationally prohibitive, but an efficient algorithm was proposed in [185] using a series of dynamic-programming procedures connected by the iterated conditional-modes algorithm [193].

The parametric-modeling algorithms constrain the unwrapped phase to a parametric surface, usually a low-order polynomial [186], which makes the unwrapping method computationally efficient. These approaches yield excellent performance only if the parametric model accurately represents the true phase.

Importantly, an assumption considered by most phase-unwrapping approaches

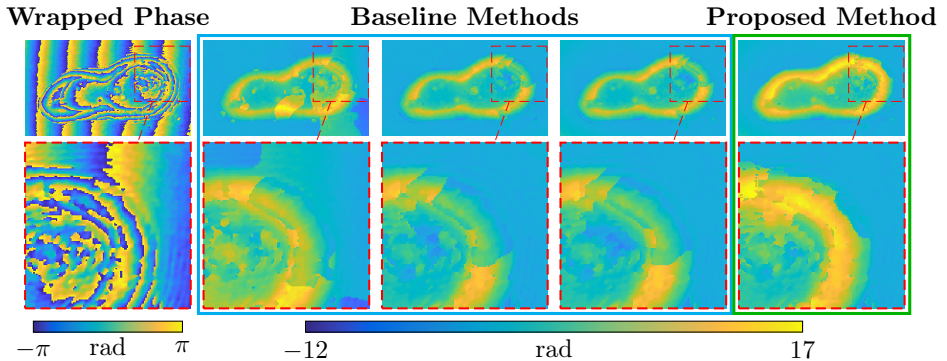


Figure 7.1: Example of phase image of organoids. First column: measured (wrapped) phase image. Second to fifth columns: baseline methods (LS, IRTV, and PUMA) and the proposed method (PUDIP). First row: reconstructed phase. Second row: zoomed inset. The size of the unwrapped phase image is (200×350) . For the sake of clarity, we removed the non-flat (smooth) background of each unwrapped phase.

is that the absolute value of the unwrapped phase difference between neighboring pixels is less than π , the so-called Itoh condition [194].

It is worthy to note that there exist alternative methods for quantitative phase-imaging methods that rely on multiple wavelengths or broadband sources [195–198]. An imaging system with multiple wavelength sources typically acquires several images so that the wrapping events occur at different locations, thus facilitating the unwrapping task. While our work mainly focuses on a single-wavelength source, our proposed framework can be adapted to the multi-wavelength setting. For more information, we refer the reader to recent reviews on QPI [2, 4].

7.2.2 Deep-Learning-Based Approaches

Recently, deep-learning methods, in particular, CNN, have achieved unprecedented performance in a variety of applications. They have surpassed conventional methods in diverse fields such as image reconstruction [199, 200], superresolution [201], x-

ray computed tomography [202], and others [203–205]. Overall, deep learning in computational imaging is an emerging and promising field of research [206, 207].

To address the 2D phase-unwrapping problem, several works based on deep learning have been proposed. In [208], the authors used a supervised feedforward multilayer perceptron to detect the phase discontinuities in optical Doppler tomography images. More recently, a residual neural network using supervised learning [209] was adopted in [210] to approximate the mapping between the wrapped and the unwrapped phase in the presence of steep gradients. In [211], a CNN-based framework, termed PhaseNet, has been designed. It predicts the wrap-count (integer multiple of 2π) at each pixel, similar to the task of semantic segmentation. Furthermore, a clustering-based postprocessing enforces smoothness by incorporating complementary information. Similar ideas were also proposed in [212, 213]. In [214], the authors improved upon [211] by integrating a network to denoise the noisy wrapped phase. In [215], a generative adversarial network was introduced to effectively suppress the influence of noise. In addition, a framework [216] composed of a residual neural network and of the objective function in [192] was proposed to unwrap quantitative phase images of biological cells.

The aforementioned works rely on supervised learning to learn the mapping between the input-output data pairs. This paradigm needs a large representative training dataset composed of the measured phase and the corresponding ground truth, which may not be available in many practical applications. In addition, the solutions obtained by direct feedforward networks might be inconsistent with the measurements due to the lack of a feedback mechanism [100, 168, 217]. Nevertheless, these works suggest that CNNs are an appealing solution to the peculiar challenges of phase unwrapping.

7.3 Contributions

In this work, we introduce a framework based on untrained CNNs for 2D phase unwrapping. Our approach uses the concept of deep image prior recently introduced by Ulyanov *et al.* [218]. We incorporate an explicit feedback mechanism and do not require prior training of the neural network. Taking advantage of these features, we propose a robust and versatile method for phase unwrapping with deep image prior (PUDIP).

The original formulation of phase unwrapping is a non-convex integer-optimization

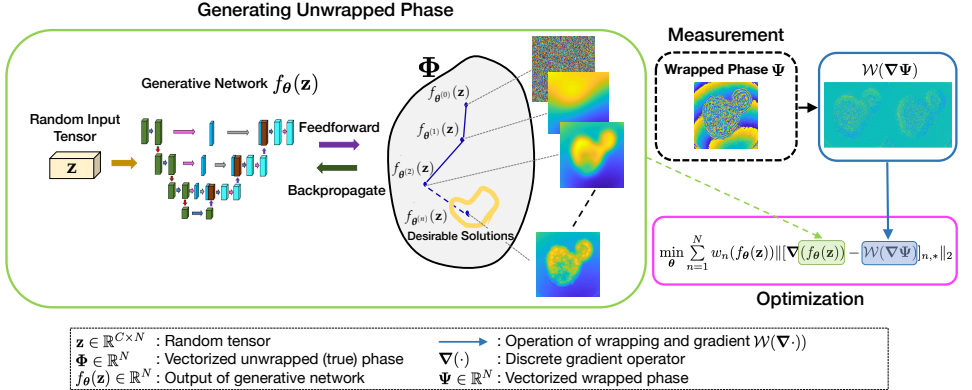


Figure 7.2: Schematic diagram of the proposed PUDIP, for 2D phase unwrapping. The architecture of the generative network is fully described in A.5.1.

problem, which is different from the usual restoration problems to which deep image priors (DIP) have been applied [218, 219]. In this work, we show that DIP is also suitable for phase unwrapping, a difficult ill-posed inverse problem. To the best of our knowledge, this is the first time that DIP is combined with an adaptive loss, which makes our method a sequence of DIPs instead. Not only does this approach improve the reconstructions, but also avoids the destabilization (*i.e.*, significant loss increase and blurred image) that was reported in [218].

In Section 7.4, we introduce the physical model and formulate the computational problem in a variational framework. In Section 7.5, we describe the proposed scheme based on untrained deep neural networks. In Section 7.7, we compare the proposed method against other state-of-the-art (*e.g.*, IRTV, PUMA) approaches on experimental data of organoids. In Section 7.6, we quantitatively assess PUDIP on several simulated datasets with diverse configurations. We extensively compare our framework with other methods such as the recent deep-learning-based PhaseNet method. Our results show that PUDIP improves upon other approaches by taking advantage of the model-based and deep-learning worlds. Our work shows that QPI can be applied to large and complex 3D samples with higher reliability.

7.4 Problem Formulation

In this section, we formulate the problem of phase unwrapping in a variational framework. Let the region of interest $\Omega \subset \mathbb{R}^2$ be discretized into N pixels. To represent the phase of our specimen, we consider the observation model

$$\Phi = \Psi + 2\pi\mathbf{k}, \quad (7.1)$$

where $\Phi = (\phi_n) \in \mathbb{R}^N$ and $\Psi = (\psi_n) \in [-\pi, \pi)^N$ denote the vectorized unwrapped and wrapped phase images, respectively; $\mathbf{k} \in \mathbb{Z}^N$ represents the integer multiple of 2π referred to as “wrap-count” to be added to the wrapped phase to recover the unwrapped phase. The wrapping process is represented by a function \mathcal{W} applied on the n th component of (7.1) as

$$\psi_n = \mathcal{W}(\phi_n) = ((\phi_n + \pi) \bmod(2\pi)) - \pi \in [-\pi, \pi). \quad (7.2)$$

The discrete gradient operator $\nabla : \mathbb{R}^N \mapsto \mathbb{R}^{N \times 2}$ is given by

$$\nabla\Phi = [\nabla_x\Phi \quad \nabla_y\Phi], \quad (7.3)$$

where $\nabla_x : \mathbb{R}^N \mapsto \mathbb{R}^N$ and $\nabla_y : \mathbb{R}^N \mapsto \mathbb{R}^N$ denote the horizontal and vertical finite-difference operations, respectively. The phases Φ and Ψ are related by the equality

$$\mathcal{W}([\nabla\Phi]) = \mathcal{W}([\nabla\Psi]), \quad (7.4)$$

where \mathcal{W} is applied component-wise. For 2D phase-unwrapping problems, the phase Φ satisfies the Itoh continuity condition [194] if

$$\|[\nabla\Phi]_{n,*}\|_2^2 \leq \pi^2, \quad n \in [1 \dots N], \quad (7.5)$$

where $[\nabla\Phi]_{n,*} \triangleq ([\nabla_x\Phi]_n, [\nabla_y\Phi]_n)$ represents the n th component 2D vector of the discrete gradient (*i.e.*, the n th row of the matrix $\nabla\Phi$). If (7.5) is satisfied, then (7.4) simplifies as

$$[\nabla\Phi]_{n,*} = \mathcal{W}([\nabla\Psi]_{n,*}), \quad n \in [1 \dots N]. \quad (7.6)$$

Under the hypothesis that a great majority of pixels in Φ satisfy the constraint condition in (7.5), we can reconstruct the unwrapped phase by minimizing the

Algorithm 7 PUDIP

-
- 1: $w_n^0 = 1$ for $n = 1, \dots, N$
 - 2: $k = 0$
 - 3: **while** (not converged) **do**
 - 4: $\theta^{k+1} = \arg \min_{\theta} \sum_{n=1}^N w_n^k \|[\nabla(f_{\theta^k}(\mathbf{z})) - \mathcal{W}(\nabla\Psi)]_{n,*}\|_2$
 - 5: Update w_n^{k+1} using (7.8)
 - 6: $k \leftarrow k + 1$
 - 7: **end while**
 - 8: **return** $f_{\theta^k}(\mathbf{z}) + \mathcal{W}(\Psi - f_{\theta^k}(\mathbf{z}))$
-

weighted energy function [192]

$$\hat{\Phi} = \arg \min_{\Phi \in \mathbb{R}^N} \sum_{n=1}^N w_n(\Phi) \|[\nabla\Phi - \mathcal{W}(\nabla\Psi)]_{n,*}\|_2, \quad (7.7)$$

where $w_n(\Phi) \in \mathbb{R}_{\geq 0}$ is the adaptive nonnegative weight for the n th component of the cost to relax the restriction. It is defined as

$$w_n(\Phi) = \begin{cases} \frac{1}{\|[\epsilon]_{n,*}\|_2}, & \epsilon_{\min} \leq \|[\epsilon]_{n,*}\|_2 \leq \epsilon_{\max} \\ \frac{1}{\epsilon_{\max}}, & \|[\epsilon]_{n,*}\|_2 \geq \epsilon_{\max} \\ \frac{1}{\epsilon_{\min}}, & \|[\epsilon]_{n,*}\|_2 \leq \epsilon_{\min}, \end{cases} \quad (7.8)$$

where $\epsilon = (\nabla\Phi - \mathcal{W}(\nabla\Psi))$, and where ϵ_{\min} and ϵ_{\max} are the user-defined minimum and maximum boundary weights, respectively. Note that (7.7) can be seen as a shifted isotropic TV and other variants could be of interest for future works [220]. In addition, the solutions can be improved by imposing prior knowledge (*i.e.*, a regularization term) such as HS [126] in an attempt to compensate for the ill-posed nature of the problem.

It is worthy to note that the solution obtained by iteratively minimizing the objective function (7.7) offers no guarantee regarding the consistency between the rewrapped phase $\mathcal{W}(\hat{\Phi})$ and the wrapped phase Ψ [192]. This is because (7.7) relies on continuous optimization to solve the discrete-optimization problem (7.1). Therefore, we adopt the single postprocessing step [221]

$$\tilde{\Phi} = \hat{\Phi} + \mathcal{W}(\Psi - \hat{\Phi}), \quad (7.9)$$

where $\tilde{\Phi}$ is the final solution, congruent with the measurement Ψ .

7.5 Phase Unwrapping with Deep Image Prior

Deep image prior (DIP) is a scheme recently introduced in [218]. Rather than learning the mapping between input and output with a large training dataset, DIP handles the inverse problem by assuming that the unknown image can be represented well by the output of an untrained generative network. Recent works have shown the effectiveness of DIP for computational imaging [17, 219, 222, 223]. In the spirit of this approach, we propose a framework where we restore the unwrapped phase based on this implicit prior.

The unwrapped phase is generated by the CNN given by

$$\Phi = f_{\theta}(\mathbf{z}), \quad (7.10)$$

where f denotes the neural network and θ stands for the network parameters to be learned. The fixed randomly-initialized vector $\mathbf{z} \in \mathbb{R}^{C \times N}$ acts as input to the generative network, while C is the number of input channels.

Plugging (7.10) in (7.7) leads to the optimization problem

$$\hat{\theta} = \arg \min_{\theta} \sum_{n=1}^N w_n (f_{\theta}(\mathbf{z})) \|[\nabla(f_{\theta}(\mathbf{z})) - \mathcal{W}(\nabla\Psi)]_{n,*}\|_2. \quad (7.11)$$

In our optimization approach, we aim at minimizing this loss function by taking advantage of the family of stochastic gradient-descent methods. The schematic diagram of PUDIP is shown in Fig. 7.2.

Finally, we achieve congruence with the single step

$$\tilde{\Phi} = f_{\hat{\theta}}(\mathbf{z}) + \mathcal{W}(\Psi - f_{\hat{\theta}}(\mathbf{z})). \quad (7.12)$$

The process is described in Algorithm 7, where one can see that PUDIP consists in a sequence of minimization problems.

7.5.1 Architecture

We design a CNN based on the U-Net-like encoder-decoder architecture [218, 224]. The setup includes skip connections with convolution and concatenation. This enables the network to reconstruct the feature maps with both local details and global

texture. We set a constant number of channels (*i.e.*, 128) in all the convolutional layers, except for those included in the skip connection whose channel number is 4. We chose the parametric rectified linear unit [225] as the nonlinear activation function. Furthermore, the downsampling operation is implemented by convolutional modules with strides of 2, so that the size of the feature map is halved in the contracting path. The upsampling operation doubles the size through bilinear interpolation. The scaling-expanding structure makes the effective receptive field increase at deeper layers [224]. As last stage, we have set one layer that subtracts a scalar value from the image. This scalar takes care of the bias intrinsic to phase unwrapping, which can recover phase only up to a constant. For simulated data, we subtracted the minimum value of the entire image to enforce nonnegativity. For real data, we subtracted the mean value of a top-left area whose dimension is (30×30) and corresponds to a background region (see A.5.1 for detailed architecture).

7.5.2 Optimization Strategy

In our experiments, we adopt the following strategy: The input variable \mathbf{z} is a random vector filled with the uniform noise $\mathcal{U}(0, 0.1)$. To avoid undetermined gradients with respect to θ in (7.11), we offset the norm there by the small constant $\delta = 10^{-18}$. In practice, the adaptive weights w_n are updated every N_w iterations to enforce sparsity in the loss function (7.11) [192]. We optimize (7.11) by using the adaptive moment-estimation algorithm (Adam, $\beta_1 = 0.9$ and $\beta_2 = 0.999$) [226]. The optimization is performed on a desktop workstation (Nvidia Titan X GPU, Ubuntu operating system) and implemented on PyTorch [227]. In our experiments, the random initialization of the input variable did significantly impact neither the performance, nor the time of computation.

7.5.3 Parameter Setting

We set the maximum number of iterations as 2000 (A.5.2). The hyperparameters of the network were initialized to default values by PyTorch. We used a learning rate of 0.01. The weights w_n were updated every $N_w = 100$ iterations with $[\epsilon_{\min}, \epsilon_{\max}] = [0.1, 8]$. During a typical optimization, the weights w_n will be large in the area around sharp edges [192]. The parameter ϵ_{\min} prevents that the weights from becoming too large in the early iterations of the global optimization, which would

force the corresponding pixels to be irreversibly set to zero. Similarly, ϵ_{\max} ensures that the weights do not become too small.

To optimize over the synthetic samples, we updated the weights w_n with $[\epsilon_{\min}, \epsilon_{\max}]$. We tried $[\epsilon_{\min}, \epsilon_{\max}] = [0.1, 10]$, $[0.05, 20]$, $[0.02, 50]$, and $[0.01, 100]$, choosing the best performance. The weights were updated every $N_w = 200$ for the first sample, 100 otherwise. As we randomly initialized the parameters of the network θ , we repeated each experiment five times and report the average performance.

7.6 Results On Simulated Data

In this section, we quantitatively assess the quality of our proposed method. To that end, we simulated the acquisition of phase images of organoid-like samples. In addition, we generated diverse artificial data which are similar to those found in [188] and [213] (see the details in A.5.4).

7.6.1 Baseline Methods

We compare the proposed method with other state-of-the-art conventional or CNN-based methods such as Goldstein’s algorithm (GA) [179], unweighted least-squares algorithm (LS) [182], IRTV [192],² PUMA [188],³ and PhaseNet [211] (Table 7.1). Goldstein’s algorithm is a path-following method that adopts the branch-cut strategy based on the phase residues and needs the knowledge of a phase-reference point. By contrast, the LS, IRTV, and PUMA approaches aim at minimizing an objective function and belong to the minimum-norm category. Note that the original LS method, which relies on a continuous optimization, may result in an inconsistent solution, while GA, IRTV, and PUMA always return consistent solutions. To enforce measurement consistency for LS, we adopted the strategy defined by (7.9). We also compare PUDIP to the recently proposed PhaseNet [211]. We adopted the strategy of [213] to generate a training dataset in two steps. First, the elements of a square matrix whose size varies between (3×3) and (11×11) were randomly generated following a uniform distribution $U(0, 1)$ for half of the samples and a Gaussian distribution $\mathcal{N}(0, 1)$ followed by the subtraction of the minimum of the

² The source code for IRTV is available from <https://cigroup.wustl.edu/publications/open-source/>

³ The source code for PUMA is available from <http://www.lx.it.pt/~bioucas/code.htm>

Table 7.1: Baseline methods. CNN¹ denotes the supervised-learning method, while CNN² denotes our method with untrained network.

Method	Reference	Regularization	Optimization	
GA	[179]	–	branch-cut	model-based
LS	[182]	–	least-squares	
IRTV	[192]	HS [126]	ADMM [147]	
PUMA	[188]	–	graph cut	
PhaseNet	[211]	–	CNN ¹	CNN-based
PUDIP		–	CNN ²	

matrix for the other half. Then, we multiplied the matrix by a scalar randomly generated following a uniform distribution $U(3\pi, 12\pi)$ and upsampled the matrix to a (256×256) image using bicubic interpolation [228]. The obtained data had a maximum value ranging from 2π to 40π . In addition, we only kept the central disk of the generated phase images and filled the background with 0. The training dataset is composed of 9,600 samples; the size of each image is (256×256) . The wrap-count in the training data varies between 0 and 20, which makes it a 21-class problem (see the details in A.5.3). We set the other hyperparameters as in [211] and trained PhaseNet with this generated dataset for all the experiments.

All model-based methods were run on a desktop computer (Intel XeonE5-1650 CPU, 3.5 GHz, 32 GB of RAM) and implemented in MATLAB R2019a. For their implementation, we initialized the unwrapped phase with $\mathbf{0} \in \mathbb{R}^N$. All parameters were set and optimized according to the guidelines provided by the authors. Specifically, the regularization parameter for the HS regularization in IRTV was set between 10^{-3} and 10^{-1} . In PUMA, we set the non-convex quantized potential of exponent $p = 0.5$, the quadratic region threshold as 0.5, and the high-order cliques

$[1, 0]$, $[0, 1]$, $[1, 1]$, and $[-1, 1]$.

PUDIP takes about 100 seconds on GPU to unwrap a (256×256) image with 1000 iterations. In comparison, PUMA and IRTV take about 2 and 380 seconds on CPU, respectively.

7.6.2 Quantitative Evaluation

We quantitatively evaluate the quality of the reconstructed phase $\tilde{\Phi}$ with respect to the ground truth Φ . Our first metric is the regressed signal-to-noise ratio (RSNR) defined as

$$\text{RSNR}(\tilde{\Phi}, \Phi) = \max_{b \in \mathbb{R}^+} \left(20 \log_{10} \left(\frac{\|\Phi\|_2}{\|(\tilde{\Phi} + b) - \Phi\|_2} \right) \right), \quad (7.13)$$

where $\|\cdot\|_2$ denotes the L_2 norm and where b adjusts for a potential global offset. This adjustment is used in the interest of fairness, because phase unwrapping can only recover the phase up to a constant. When the RSNR is more than 100 dB, the recovered phase image differs from the ground truth because of numerical imprecision and not because of wrong unwrapping. We therefore set the corresponding value to infinity. In addition, we compute the SSIM [175].

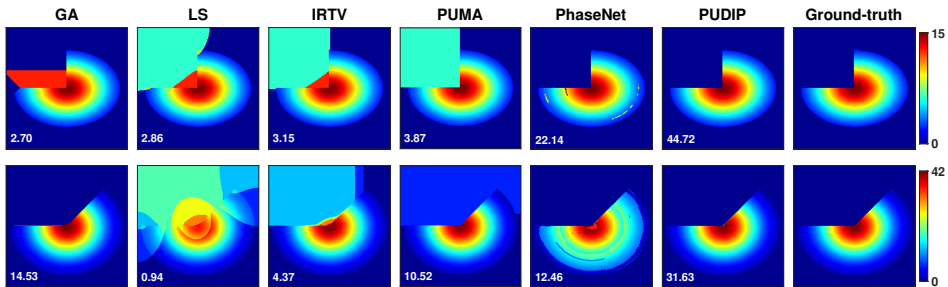


Figure 7.3: Unwrapped phases of two simulated samples. From left to right, the results are obtained by GA, LS, IRTV, PUMA, PhaseNet, and our approach (PUDIP). The ground truth images are presented in the last column. The corresponding RSNR [dB] is shown at the left bottom of each subfigure.

Table 7.2: RSNR [dB] and SSIM of the reconstructed-phase images versus the angle of cropping. The RSNR and SSIM of our method (PUDIP) are the average of five experiments.

	Angle	GA	LS	IRTV	PUMA	PhaseNet	PUDIP
RSNR	0°	∞	∞	∞	∞	24.79	∞
	45°	6.80	5.15	8.61	10.20	14.10	15.99
	90°	2.70	2.86	3.15	3.87	22.14	37.75
	135°	-0.56	1.32	2.46	2.06	22.01	43.52
	180°	-5.15	-0.13	0.84	∞	19.33	∞
	225°	-6.70	-0.43	-0.24	2.21	19.96	41.44
	270°	-8.00	-1.85	-1.66	2.01	21.23	∞
SSIM	0°	1.0000	1.0000	1.0000	1.0000	0.9799	1.0000
	45°	0.8975	0.8346	0.9429	0.9595	0.9680	0.9866
	90°	0.9074	0.7180	0.7337	0.7418	0.9772	0.9995
	135°	0.8360	0.5716	0.6510	0.5576	0.9769	1.0000
	180°	0.4863	0.4772	0.4893	1.0000	0.9771	1.0000
	225°	0.4269	0.3411	0.3225	0.1183	0.9858	1.0000
	270°	0.3655	0.2395	0.2246	0.0838	0.9907	1.0000

7.6.3 Simulated Phase Images of Organoid-Like Sample

In order to obtain a physically-realistic ground truth, we simulated the wave propagation through the sample with BPM [43] (Chapter 1). From the 3D simulation, we directly obtain the wrapped phase (A.5.4). Under the straight-ray approximation [35], we expect that the unwrapped phase is proportional to the integral of the RI differences. We therefore refer to the straight-ray approximation Φ_{sr} as the ground truth. As shown in Fig. 7.4, the phase unwrapped by PUDIP is consistent with Φ_{sr} . The solutions of the other methods have wrongly unwrapped areas. The entanglement of several elements complicates the wrapping events in those areas (Fig. 7.4 top right panel). The fact that some parts are defocused adds to the challenge since ripples are present around the border. The slightly defocused parts are wrongly estimated by baseline methods, which impacts the whole

Table 7.3: RSNR [dB] and SSIM of the reconstructed-phase images versus the maximal value. The RSNR and SSIM of our method (PUDIP) are the average of five experiments.

	Max value	GA	LS	IRTV	PUMA	PhaseNet	PUDIP
RSNR	6	5.69	13.12	∞	∞	-5.71	∞
	12	1.02	-0.39	11.31	∞	1.25	∞
	18	1.45	1.20	3.22	∞	5.62	∞
	24	3.85	0.21	4.99	5.69	8.95	78.54
	30	5.20	1.04	7.38	7.62	8.35	28.53
	36	4.62	0.48	8.71	9.18	10.13	25.70
	42	14.53	0.94	4.37	10.52	12.46	27.74
SSIM	6	0.9299	0.9834	1.0000	1.0000	0.7105	1.0000
	12	0.9258	0.5989	0.3616	1.0000	0.7788	1.0000
	18	0.9311	0.5539	0.6481	1.0000	0.8067	1.0000
	24	0.9453	0.5312	0.6411	0.5873	0.8298	0.9990
	30	0.9551	0.5160	0.6435	0.5866	0.8168	0.9977
	36	0.9532	0.5044	0.6416	0.5796	0.8224	0.9957
	42	0.9782	0.4951	0.6364	0.5784	0.8597	0.9959

unwrapping result. It is worthy to note that real data also have ripples around the border, which might partially explain the difficulty to unwrap phase images of organoids (Section 7.7). We provide more examples in A.5.5.

7.6.4 Phase Unwrapping of Artificial Images

We generated three kinds of samples similar to previous works [188, 213]. The first and second categories consist of ellipses. In the first type of sample, we cropped the ellipses with angles ranging from 0° to 270° with an increment of 45° . In the second type of sample, we scaled the phase image (*i.e.*, an ellipse cropped with a fixed angle) so that its maximum was in the range of 6 to 42 with an increment of 6. The last kind of sample is the same as the one we used to train PhaseNet (Section 7.6.1). We use these images to test our method on samples

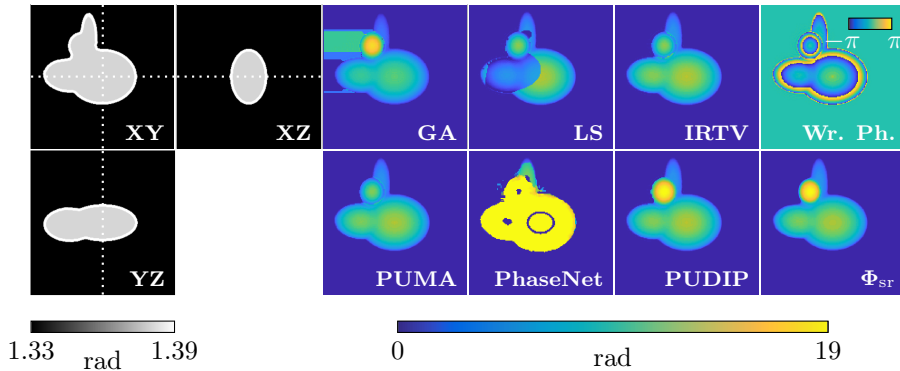


Figure 7.4: Organoid-like reconstructions. The images were saturated for visualization purpose. The size of the unwrapped phase image is (159×159) . The first two columns are orthographic slices of the 3D distribution of RI. All slices include the center of the volume. From the third to fifth column, the text gives the method used to unwrap. The wrapped phase resulting from 3D simulation and the ground truth Φ_{sr} are displayed in the last column (from top to bottom). Wr. Ph.: Wrapped Phase.

usually seen in other modalities [188].

When the unwrapping task is relatively simple, all the baseline methods, as well as our method, perform well (see the first row in Tables 7.2 and 7.3). When the phase images are more complex (*e.g.*, when a few pixels violate the Itoh condition), all the conventional methods lead to blocky errors. As expected, PhaseNet wrongly estimates the unwrapped phases when they differ from the training set. On the contrary, our framework based on untrained CNNs faithfully unwraps the phase for nearly all configurations (Tables 7.2 and 7.3). In Fig. 7.3, one can observe some typical unwrapping behavior of the different methods, as well as the obtained RSNR.

For the last type of samples, deep learning techniques perform better than the conventional techniques (Table 7.4). Since the training and testing sets match, PhaseNet is quantitatively more accurate than PUDIP. As reported in [218], supervised schemes tend to outperform unsupervised approaches when the training and

testing sets are consistent. It is noteworthy that PUDIP commits errors only at the border of the disk and that the large discrepancy in the RSNR between PhaseNet and PUDIP mainly comes from the fact that any error is likely to be a multiple of 2π . The SSIM metric is less sensitive to isolated erroneous cases and the discrepancy is much smaller. However, for some samples, PhaseNet wrongly estimates the phase over large areas inside the object (third column of Fig. 7.5). Our method is more stable in its ability to unwrap the phase due to its feedback mechanism.

Let us observe that the results of PUDIP are still imperfect, in the sense that a few pixels of the output deviate from the ground truth. However, these are inconspicuous. Based on our experiments, it appears that the results of PUDIP are generally superior to those of the other methods when the conditions are difficult, and otherwise equivalent, which should make PUDIP of interest for practitioners. Note that when the task of phase unwrapping is extremely difficult, there are few failure cases. However, the failed results obtained by our approach are not worse than other methods. We provide all the results in A.5.5.

7.6.5 Phase Unwrapping in Presence of Structured Noise

In DHM, the noise is mainly characterized by speckle noise [229] that corrupts the image before the wrapping operation. To assess the robustness of our method, we perturbed the (unwrapped) first kind of sample (cropping angle 135°) with speckle noise [230]. We added three levels of noise $\{11.8, 15.7, 22.8\}$ dB (Fig. 7.6) and computed the metrics with respect to the perturbed images.

The performances of the baseline methods are affected by the structured noise and fail to correctly unwrap the images (Table 7.5). Note that their poor performance mainly comes from the blocky errors mentioned in the previous experiments of Section 7.6.4. The noise exacerbates the difficulty to recover the edges of the cropped ellipses. In the presence of noise, the performance of PhaseNet collapses, which is expected as this supervised method was trained on a noiseless dataset. PUDIP is stable, in that it correctly unwraps the phase, at the possible exception of few pixels at the border. It is worthy to mention that the robustness to noise is different from denoising, since we do not target at reducing the noise during the unwrapping process. This happens to other methods as well. When unwrapping is successful, one can then denoise the recovered phase image with any state-of-the-art denoising algorithms.

Table 7.4: RSNR [dB] and SSIM of the reconstructed-phase images versus the size of the random matrix. The metrics are averaged over four samples for each size. For each sample, we repeated five times the reconstructions of our method. The reported RSNR and SSIM of PUDIP are then the average of twenty experiments for each size.

		Matrix size	GA	LS	IRTV	PUMA	PhaseNet	PUDIP
RSNR	(3 × 3)	4.18	3.84	3.60	3.72	36.30	21.94	
	(5 × 5)	5.57	5.55	4.87	5.39	31.89	21.51	
	(7 × 7)	5.32	6.28	5.72	5.41	21.97	19.98	
	(9 × 9)	5.53	6.19	5.47	5.99	39.71	20.80	
	(11 × 11)	5.71	6.88	6.82	6.88	23.63	18.65	
SSIM	(3 × 3)	0.7361	0.7222	0.7253	0.7065	0.9920	0.9699	
	(5 × 5)	0.6828	0.6506	0.6592	0.6478	0.9567	0.9588	
	(7 × 7)	0.6636	0.6495	0.6348	0.6403	0.9576	0.9530	
	(9 × 9)	0.6511	0.7020	0.6579	0.6872	0.9637	0.9294	
	(11 × 11)	0.6532	0.6481	0.6574	0.6557	0.9234	0.9344	

Table 7.5: RSNR [dB] and SSIM of the reconstructed-phase images versus the noise level. The RSNR and SSIM of our method (PUDIP) are the average of five experiments.

		Noise level (dB)	GA	LS	IRTV	PUMA	PhaseNet	PUDIP
RSNR	22.80	-3.58	1.67	2.32	2.34	3.24	20.51	
	15.70	-3.21	2.01	2.84	2.72	0.95	20.94	
	11.82	2.81	2.36	3.13	3.13	2.45	20.80	
SSIM	22.80	0.0072	0.1488	0.1619	0.1638	-0.2946	0.9895	
	15.70	0.0081	0.1260	0.1493	0.1502	-0.1402	0.9913	
	11.82	0.0023	0.1022	0.1195	0.1318	0.2046	0.9905	

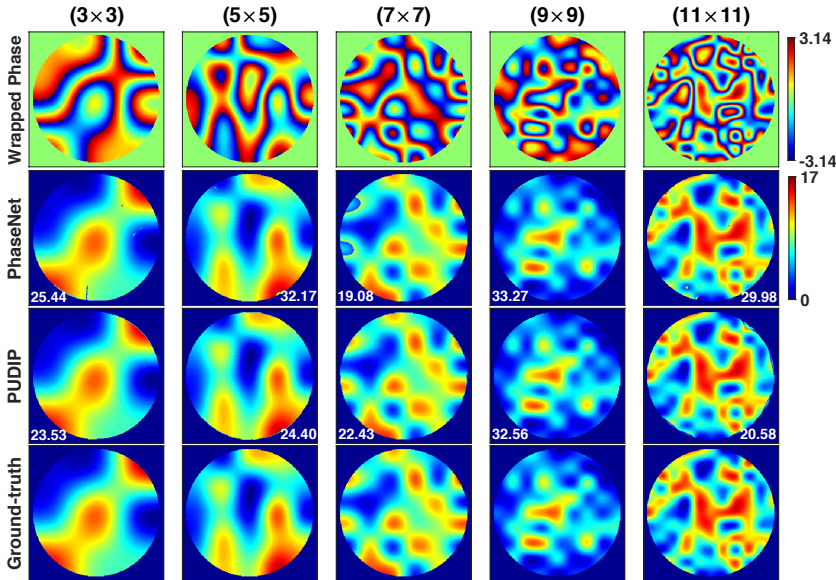


Figure 7.5: Unwrapped-phase images of simulated samples with diverse random distributions. From top to bottom: wrapped phase, results obtained by PhaseNet and our approach (PUDIP). The ground truth images are presented in the last row. The numbers give the corresponding RSNR [dB].

7.7 Results on Experimental Data

Thick and complex samples present complicated wrapping events and potentially contain a few sharp edges at which the Itoh condition may not hold in the true phase. These combined factors increase the difficulty to unwrap their phase. To illustrate these challenges, we acquired images of organoids with DHM and unwrapped their phase using the proposed method as well as other baseline methods.

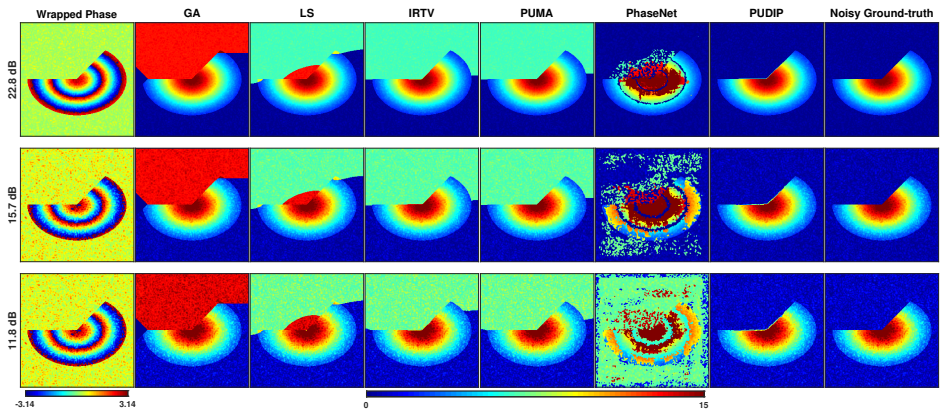


Figure 7.6: Reconstructed unwrapped-phase images of simulated samples with diverse speckle noise. From left to right: wrapped phase, results obtained by GA, LS, IRTV, PUMA, PhaseNet, and our approach (PUDIP). The noisy ground truth images are presented in the last column.

The quality of unwrapped images will impact the subsequent steps of image analysis. Hence, we additionally illustrate how segmentation—a typical image processing for QPI [231]—can be altered by the outcome of phase unwrapping.

7.7.1 Experimental Setup

Mouse organoids of the small intestine were released from Matrigel® (Corning) and dissociated into single cells. After centrifugation, the cells were re-suspended at the appropriate density in ENR-CV medium supplemented with Thiazovivin (ReproCell) and seeded to deposit about 100 cells per microwell onto imaging bottom Gri3D hydrogel microwell array plates (SUN bioscience) of 300 micrometer in diameter. The cells were then let to sediment for 30 minutes as such and 150 μ L of self-renewal medium supplemented with 2% Matrigel. The stem cells were expanded in self-renewal for 3 days, and the organoids were differentiated for another 3 days in differentiation medium (ENR) [232]. Once the stem cells underwent morphogenesis and formed fully matured organoids, the organoids were imaged using a DHM (T1000-Fluo, LynceeTec). The holograms, phases, and amplitudes were acquired for downstream reconstruction with a pixel of physical length of 6.45 μ m (NA = 0.3, magnification 10 \times , and wavelength 684.6nm). The time interval between each frame was 1 minute for the time-lapse measurements.

7.7.2 Post-Processing of the Unwrapped Phase

The microwells in which the organoids are loaded induce a non-flat (smooth) background. For the sake of clarity, we removed the background of each unwrapped phase. We estimated the background by fitting a polynomial of degree 3 in background areas. To detect the background, we applied a (3 \times 3) standard-deviation filter on the unwrapped image. We defined the background as any pixel below a certain threshold $T_\sigma \in [0.5, 1]$.

7.7.3 Phase Unwrapping of Organoids

The results of various methods are shown in Fig. 7.7. The LS method yields inaccurate results over large areas, such as non-flat background or disrupted structures. In comparison, the three other approaches perform better. However, some areas pointed out by the rectangle exhibit sudden breaks in the phase unwrapped by

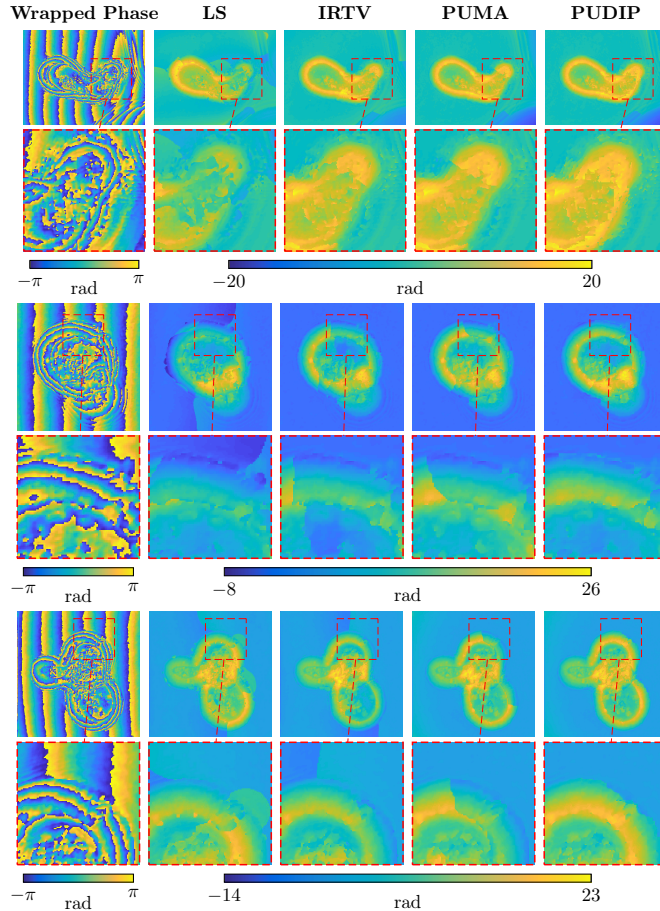


Figure 7.7: Reconstructed phase images of organoids. First column: measured (wrapped) phase image. Second to fifth columns: algorithms using LS, IRTV, PUMA, and the proposed method (PUDIP). First row: reconstructed phase. Second row: zoomed inset. The size of the unwrapped phase image is (350×450) , (260×250) , and (360×350) , respectively. For the sake of clarity, we removed the non-flat (smooth) background of each unwrapped phase.

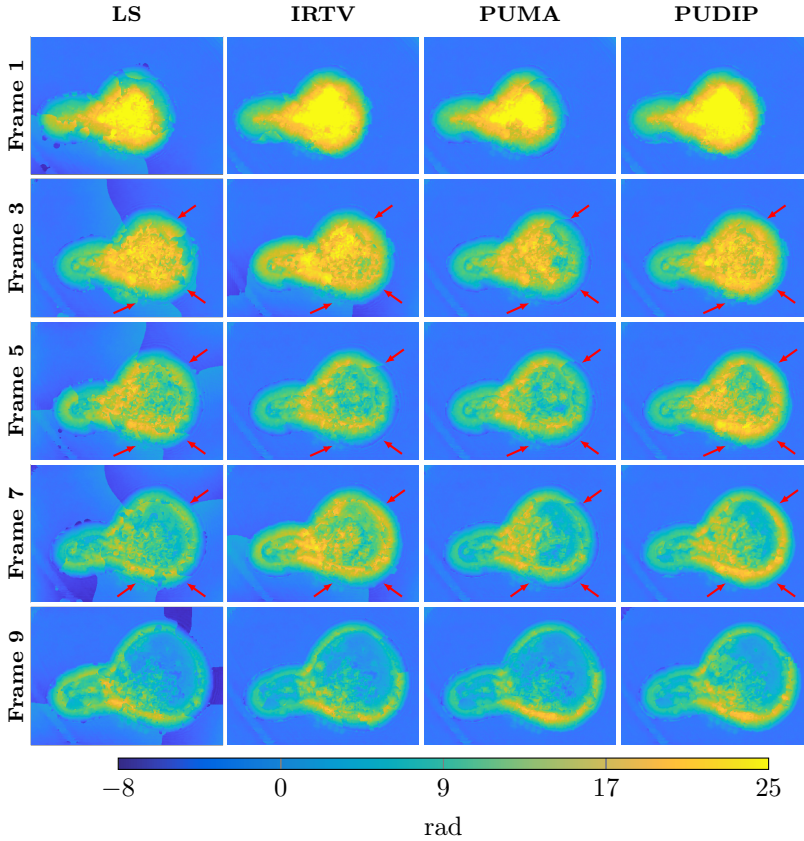


Figure 7.8: Time-lapse reconstructions. The images were saturated for visualization purpose. The size of the unwrapped phase image is (280×390) . For the sake of clarity, we removed the non-flat (smooth) background of each unwrapped phase.

IRTV and PUMA. The phase is expected to be relatively smooth since the epithelium of the organoids consists in a continuous layer of cells, forming then the border

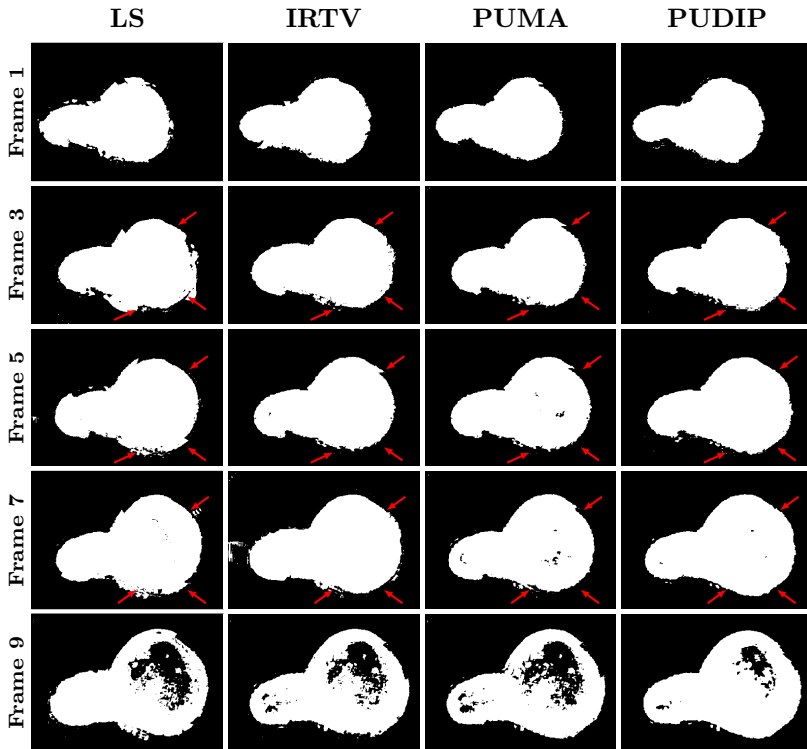


Figure 7.9: Segmentation of time-lapse reconstructions. We thresholded at 20% of the maximum value of the image.

of the sample [233]. By contrast, PUDIP better recovers it for all samples.

PhaseNet failed to reconstruct the unwrapped phase in all cases (A.5.6), most probably because the training set is not adequate for our experimental data. Likewise, GA was unable to recover the samples. The solutions found by PhaseNet and GA exhibit several areas with values higher than their surrounding, which does not accurately represent the characteristic features found in intestinal organoids, such

as the epithelium and the lumen.

In the first row of Fig. 7.7, the unwrapped phase might deviate from the phase image predicted by the straight-ray approximation [35] in the center part where it is non-smooth. The approximation is accurate if the wavelength is much smaller than the features of the sample (*e.g.*, local inhomogeneity of the RI). The mismatches are then likely to occur in the areas where the features are, which suggests that local inhomogeneities are present in the inner part.

In addition, we computed the relative error between the rewrapped phase $\mathcal{W}(\tilde{\Phi})$ and the wrapped phase Ψ defined as

$$\Delta\epsilon(\mathcal{W}(\tilde{\Phi}), \Psi) = \frac{\|\Psi - \mathcal{W}(\tilde{\Phi})\|_2}{\|\Psi\|_2}. \quad (7.14)$$

The relative errors of all methods are lower than 10^{-13} , which indicates that the results are congruent with the measurements up to rounding errors.

7.7.4 Phase Unwrapping of Time-Lapse Measurements

Further, we acquired time-lapse measurements of organoids to validate the benefits of our approach in sequential imaging. In the last frames, the size of the organoids increases and the intra-organoid composition becomes visibly more heterogeneous. It is noteworthy that the intestinal organoids are absorbing water as they grow over time [234], which explains that the phase value gets closer to the background value. Because of more complex wrapping events, the unwrapping task becomes even more challenging. By using PUDIP, we show here that the borders as well as the flatness of the background are well preserved (Fig. 7.8). On the contrary, the unwrapped phase of the other methods either result in a background with unlikely 2π jumps or borders with sudden breaks.

7.7.5 Segmentation of Time-Lapse Measurements

Image segmentation is a step that one would usually perform on the unwrapped phase [231]. Our aim now is to illustrate how unwrapping can affect the segmentation results. To that end, we simply thresholded the images obtained from the different methods with a threshold set at 20% of the maximal value.

In Fig. 7.9, we observe that the segmentation is especially impacted at the borders where sudden breaks occur in the unwrapped phase. In all frames, the

segmentation of PUDIP solutions preserves the integrity of the boundaries better than the other methods.

7.8 Summary

In this chapter, we proposed a general iterative framework PUDIP that takes advantage of model-based approaches and deep priors for 2D phase unwrapping. The iterative inversion algorithm is based on a forward model that ensures consistency with the measurements and a prior knowledge implicitly induced by an untrained CNN, which overcomes the limitation of conventional supervised-learning strategies which need large-scale or tailored training datasets. We have validated our approach on simulated data with diverse challenging settings in which the unwrapped phase has many discontinuities. Our numerical experiments have shown that the proposed method outperforms state-of-the-art conventional or network-based methods in many configurations. In addition, we have also applied our framework to single and time-lapse measurements of organoids, which are particularly large and complex samples. PUDIP can help in all instances of optical imaging that acquire wrapped phase data, 2D QPI as well as ODT. We believe that PUDIP should be of interest to practitioners. The substantial improvement in the quality of reconstruction by PUDIP effectively allows the application of QPI to thick and complex 3D samples, and also allows subsequent image processing tasks to be carried out with higher reliability.

Chapter 8

Metrics for ODT and SMLM

8.1 Introduction

In this chapter, we study metrics that assess the quality of reconstructions in computational microscopy.¹ As such, our contributions in this chapter complement well the previous chapters. Beyond the classical SNR, there are a plethora of metrics that each account for different characteristics of an algorithm’s performance. We consider two cases: metrics with or without requirement of ground truth. The latter category is applicable to any sample, which is an appealing feature since the ground truth is usually not available for biological samples.

8.2 Contributions

In Section 8.3, our contribution is a metric with no ground-truth requirement for ODT reconstructions using structured illumination.

Next, we are interested in SMLM; in particular, we leverage the unique features of SMLM (*i.e.*, list of estimated positions, image rendering) to investigate metrics from new perspectives. In [27], we quantitatively assess 2D and 3D SMLM software packages with a large panel of quality metrics on realistic simulated datasets. Building upon this broad benchmarking, we propose a novel optimal-transport-based

¹ The content of this chapter is based on [28–30].

metric for SMLM which captures both detection and localization performance and relies on solid mathematical foundations (Section 8.4). Finally, in Section 8.5, we derive a closed-form expression of the FRC for the particular case of SMLM, which allows us to investigate the classical way of computing FRC (*i.e.*, SMLM image rendering and DFT).

8.3 Assessment Tool for ODT using Structured Illumination

A fundamental challenge in ODT is the difficulty of comparing different reconstruction methods on real data. Excluding samples for which we have *a priori* knowledge (*i.e.*, 3D printed samples), we generally lack information about the ground truth of 3D samples in ODT. This can have particularly serious issues in biomedical applications since accurate characterization is necessary for diagnosis and cure. For example, in cellular imaging, this uncertainty leads to miscalculated intracellular protein concentrations [69], which are derived from RI values. One way to quantify this uncertainty is through the use of phantom objects such as beads or microspheres. However, this way cannot be generalized to biological samples since their ground truth is not available. In this section, we describe a metric that allows us to quantitatively compare between reconstruction algorithms with no ground-truth requirement.

8.3.1 Context

As shown in the previous chapters, an optical field that propagates through an inhomogeneous medium will be distorted. If there is negligible absorption, such distortions can be undone if the transmitted field is holographically recorded and the phase-conjugate reconstruction of the hologram is made to propagate backwards through the sample [235–238]. This is conveniently done in the optical domain by illuminating the recorded hologram with a plane wave counter-propagating to the plane wave used to record the hologram. When the incident beam that illuminates the object is spatially modulated by a 2D pattern (an image), the field arriving at the hologram plane is a distorted version of the 2D illumination pattern. Through phase conjugation, this distortion is removed and the field arriving back at the input plane is ideally an exact replica of the original image. Deviations from this ideal

condition can occur due to limited spatial bandwidth, absorption or other losses in the optical path. Any imperfection in the holographic recording and play-back of the hologram (including speckle) also contributes to deviations of the phase-conjugate reconstruction from the original image projected through the sample. In a carefully designed optical system in which the coherent noise is minimal,² we can generally obtain excellent phase-conjugate reconstructions since the medium where the beam propagates through is well defined. The phase-conjugate image is also strongly affected by any changes in the 3D object over time between the recording of the hologram and the play-back. If the noise effect is negligible, any distortions in the phase-conjugate image can be attributed to changes in the object itself. This effect has been used for many applications including imaging through diffusing media [235], turbidity suppression in biological samples [236, 237] and imaging through turbid media [238].

8.3.2 Proposed Metric

We exploit this effect to assess the accuracy of the reconstructed 3D RI map. Fig. 8.1 shows the overall idea behind the proposed assessment technique. First, a classical ODT acquisition procedure is performed (Chapter 4 and Appendix A.4). From this collection of measurements, we can reconstruct 3D RI maps using well-known algorithms (*e.g.*, Radon [88, 239], Born [12], and Rytov [13, 111, 240, 241]). To comparatively assess the accuracy of the reconstructed 3D RI map, we perform a numerical phase conjugation using a four-step procedure:

1. Using the same setup and sample, we experimentally illuminate a known pattern onto the sample with structured illumination, which is performed by recording a pattern on the spatial light modulator (SLM). The pattern gets distorted as it propagates through the 3D sample along the optical path. We holographically record the resulting field.
2. We take the complex-conjugate of the experimentally-measured field.
3. We numerically back-propagate this field through the reconstructed 3D RI map. We use our accurate forward model LSm described in Chapter 3. After this step, we obtain a digital reconstruction of the pattern.

² Coherent noise are usually due to dust particles or multiple reflections from optical elements

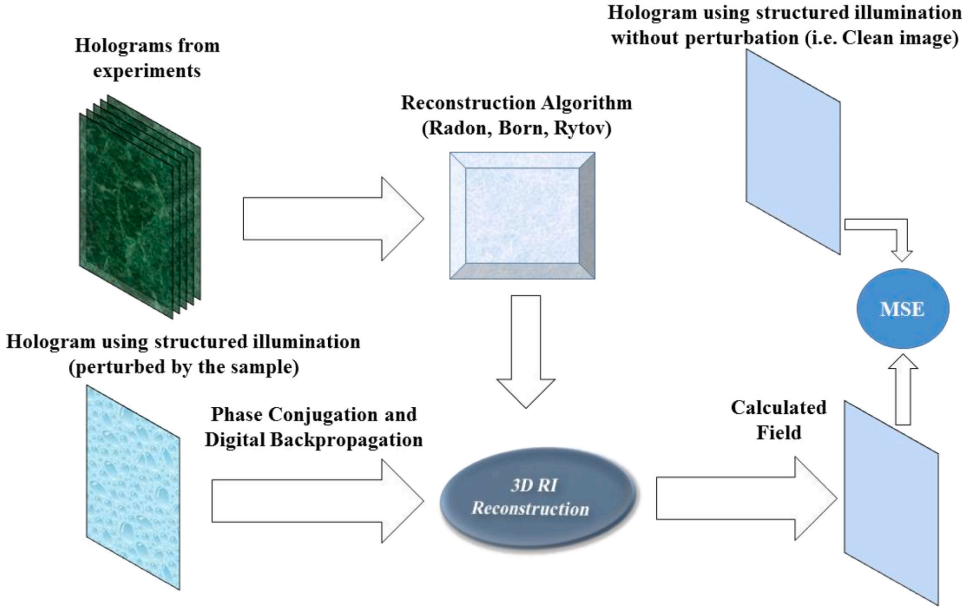


Figure 8.1: Overall scheme of the proposed metric for ODT.

4. We compute an image-based metric (*e.g.*, mean-square error (MSE)) between the original and reconstructed patterns. The differences are imputed to inaccuracies of the 3D reconstruction.

This procedure provides a quantitative metric that permits comparisons between reconstruction methods. Next, we provide a case study by applying our metric to three commonly used reconstruction algorithms: Radon [88, 239], Born [12], and Rytov [13, 111, 240, 241]. Comparisons between Born and Rytov have been performed in literature in different optical regimes [242, 243]; however, such studies cannot be directly translated to arbitrary samples such as biological ones. Note that the proposed method can act as a reconstruction assessment tool for other reconstruction method as well [73, 235–238, 242–248].

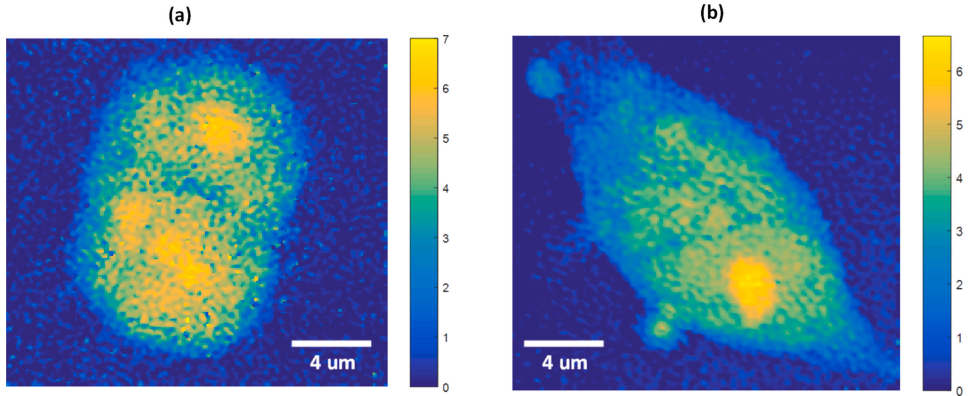


Figure 8.2: Unwrapped phase images of (a) HCT-116 cell and (b) Panc-1 cell for normal incidence. Phase unwrapping was done using PUMA algorithm [188]. Color bars are in Radians.

8.3.3 Materials and Reconstruction Methods

The experimental setup is described in the Appendix A.4.

Samples

We used two samples of HCT-116 human colon cancer cells and Panc-1 human pancreas cancer cells which were cultured in McCoy 5A growth medium (Gibco) supplemented with 10% fetal bovine serum (Gibco). #1 coverslips were treated with a 5 $\mu\text{g}/\text{mL}$ solution of fibronectin (Sigma) in phosphate-buffered saline (PBS) and let to dry at room temperature. Cells at passage 18 were removed from culture flasks using trypsin, seeded directly onto the fibronectin-treated coverslips, and incubated 24 h in a 37°C/5% CO₂ atmosphere until cells adhered and spread on the coverslips. Each sample was fixed for 10 min at room temperature in 4% paraformaldehyde in PBS, rinsed twice with PBS, and sealed with a second coverslip.

Tomographic Reconstruction Methods

We display in Fig. 8.2 two examples of unwrapped phase images. We unwrap the phase images of the recorded holograms using a classical algorithm [188] (*i.e.*, for the Radon and Rytov methods). The accumulated phase of the studied samples (*i.e.*, HCT-116 cells and Panc-1 cells), whose thickness is around 8 μm , exceeds 2π at some regions, depending on the proteins distributions as shown in Fig. 8.2. As previously said, we compare three reconstruction methods: Radon [88], Born [12], and Rytov [13] methods. Both Radon and Born methods fail to reconstruct the 3D RI map due to considerable diffraction, and high phase accumulation, respectively. We display in Fig. 4 the XY and XZ slices of the 3D reconstructions of the two samples. Notice that the Born and Rytov approximations produce significantly different 3D RI maps.

Cancer cells usually have a RI of cytoplasm that range between 1.36-1.39 due to excess of RNA and protein [10, 249–252]. As observed in Fig. 8.3a, this index range is probably under-estimated by the Born method (*i.e.*, around 1.32), because the high phase delay violates the model assumptions. On the contrary, the Rytov approximation shows better agreement with the expected biological values (around 1.365). Similarly, high-RI valued islets which are composed of fats, sugars and highly-concentrated proteins are visible in the Rytov reconstructions but not in the Born reconstructions. In Fig. 8.3b, we clearly see that Born underestimates the RI value of the nucleus since the surrounding media (*i.e.*, water) should have a much lower RI [10, 249–252].

8.3.4 Assessment Results

To compute the proposed metric, we modulated the phase of the incident beam with an image of Einstein or the 1951 USAF resolution test chart via the SLM (Fig. 8.4). We adopted structured illuminations instead of plane waves since structured illuminations can be thought of as many plane waves propagating at the same time; hence, such illuminations probe a larger portion of the 3D spectrum of the object. In addition, assessment using structured illumination ensures fairness as these patterns were not used in the tomographic reconstruction. To obtain an unaltered pattern (*i.e.*, original), we measured the incident field by repeating the holographic measurement without the sample (*i.e.*, clear PBS liquid between two coverslips). Following the procedure described in Section 8.3.2, we computed our metric for the

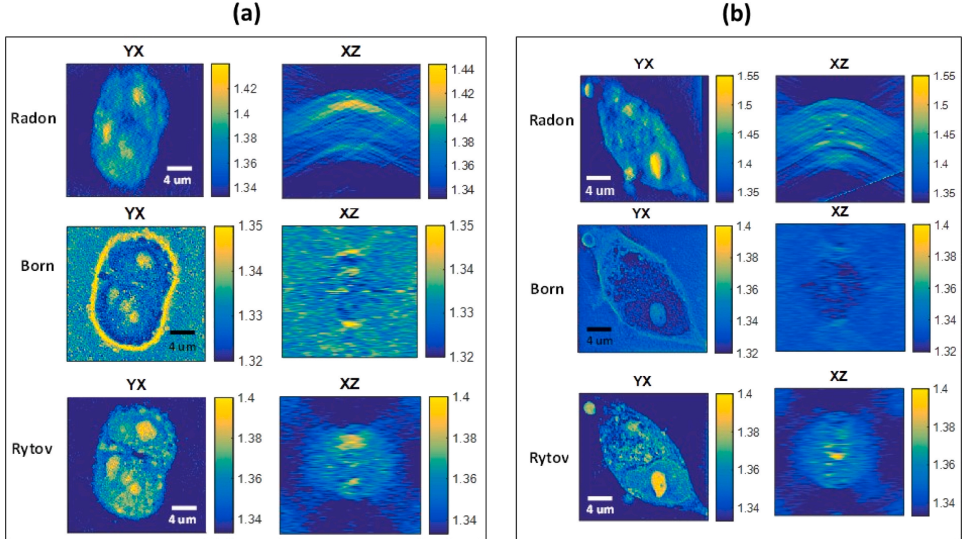


Figure 8.3: 3D reconstruction based on Radon, Born, and Rytov techniques for (a) HCT-116 cell and (b) Panc-1 cell.

3 recovered 3D RI maps by using the MSE for the step 4 (Table 8.1).

We display in Fig. 8.5 the retrieved Einstein and 1951 USAF resolution test chart for the case of Radon, Born, and Rytov approximations and the original pattern. For both samples, the MSEs for the Born method are the largest (3 times larger than the MSEs for the Rytov method). This significant difference comes from the fact that both Radon and Rytov rely on the unwrapped phase, while the Born method is not. However, the Radon method ignores diffraction, which limits its performance. The Rytov method has the best performance as it takes advantages of phase unwrapping and accounts for diffraction (but not multiple scattering).

8.3.5 Discussion

In this section, we have proposed a new metric without ground truth for ODT. Here, SLM was used for both angular scanning (classical ODT) and structured

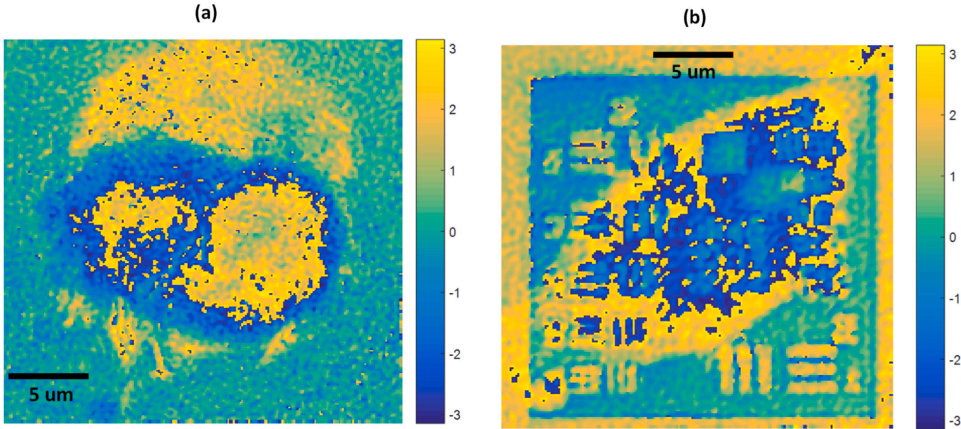


Figure 8.4: Wrapped phase images of Einstein/USAF chart after propagating through the HCT-116/Panc-1 cell.

illumination (proposed metric). The latter has allowed us to assess the performance of different reconstruction schemes. Sharing the experimental setup for angular and structured illumination has alleviated the burden of alignment and/or mechanical instabilities. Our metric relies on a four-steps procedure. Using the phase-conjugated measured field as a numerical incident field, we numerically back-propagate it through a reconstructed 3D RI map. If perfectly reconstructed, the distortions that the real incident field has undergone would be undone. Otherwise, we ascribe any deviation to inaccuracies in the reconstructions. We have illustrated the advantages of our metric on two real biological samples and three different reconstruction algorithms. Our results have shown that the Rytov method is more accurate than the Born and Radon methods, which is consistent with previous observations [242, 243].

Table 8.1: MSE percentage for Radon, Born and Rytov based reconstruction techniques for Einstein and 1951 USAF resolution test chart.

	Radon	Born	Rytov
Einstein	8.83%	34.73%	6.39%
1951 USAF	16.19%	24.58%	7.97%

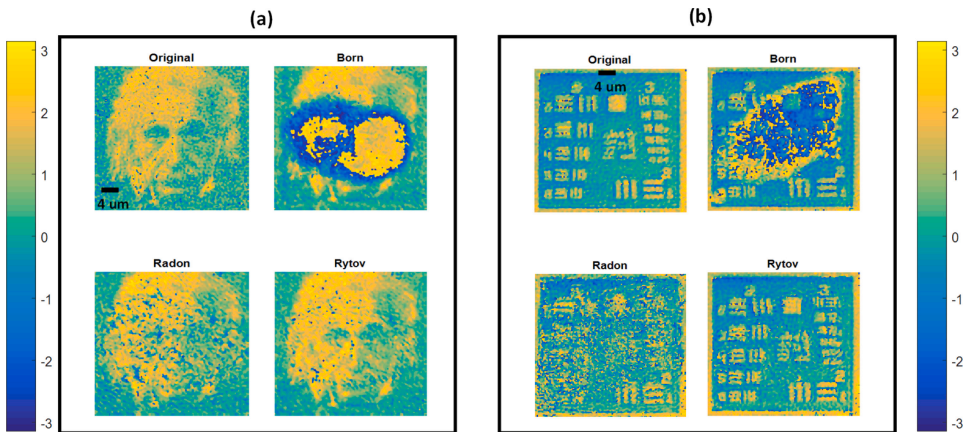


Figure 8.5: Retrieved projected fields using Radon, Born, and Rytov for (a) Einstein through HCT-116 cell, and (b) USAF chart through Panc-1 cell.

8.4 Optimal-Transport-Based Metric For SMLM

8.4.1 Context

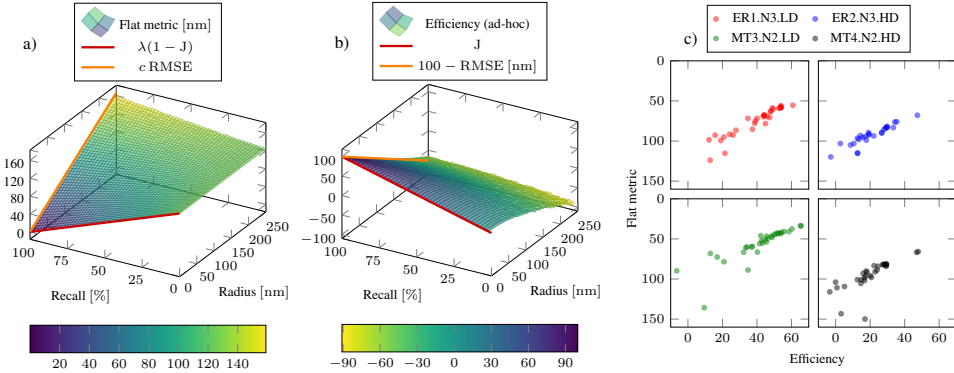


Figure 8.6: a) Flat Metric (low: good). b) Efficiency (low: bad). These metrics take into account a continuum in both localization and detection errors in SMLM. Locations (100) were uniformly drawn to create ground-truth points and modified to create artificial sets of detections with 100% precision, recall ranging from 0% to 100%, and localization errors uniformly sampled in a circle of a given radius. c) High degree of correlation between efficiency and Flat Metric on four datasets from the SMLM 2016 Challenge.

In SMLM, it is crucial to have at one’s disposal an objective evaluation of the recovery performance of available reconstruction algorithms. Similar to the assessment performed in the previous section, the present section studies this topic, under the hypothesis that a ground-truth reference for every captured frame is available. Metrics that do not require ground-truth information also exist [253–256], even some using optimal transport concepts [257]. However, these are outside of the scope of this section, and our proposal is completely new. Similarly, simpler optimal-transport-based metrics were used before in other point-source localization problems [258, 259].

The localization of point sources is traditionally assessed using either detection

metrics, such as precision, recall, and the Jaccard index; or localization metrics, such as the RMSE or the root-mean-square minimum distance (RMSMD) [260]. In the SMLM 2016 Challenge [27], a large panel of metrics was computed for performance assessment. The participating localization algorithms typically focused on one of two main key metrics: the Jaccard index (J) or the RMSE. To encompass both, Sage *et al.* proposed the efficiency, a metric born from the analysis of the empirical results in [27] and designed to evaluate the SMLM 2016 Challenge. It is computed as

$$\text{efficiency} = 100 - \sqrt{(100 - J)^2 + \alpha_{\text{eff}}^2 \text{RMSE}^2}. \quad (8.1)$$

The parameter α_{eff} was introduced to regulate the tradeoff between localization and detection. It was set to $\alpha_{\text{eff}} = 1 \text{ nm}^{-1}$ for the 2D (lateral) efficiency after analysis of the results for the best algorithms. With this empirical choice, an improvement of 1nm in RMSE is equivalent to a 1% improvement in J.

In this section, we propose to use *Flat Metric*, also known in the literature as the flat norm or the Kantor-Rubinstein norm [261–264], to assess the recovery performance of algorithms for SMLM. This metric has already been used to assess the recovery performance of point source signals [265]. It can be related to optimal transport which is a well-studied field both on a theoretical [266, 267] and numerical [262] standpoint. By using a valid metric on the space of Radon measures, in which detections and ground-truth data lie, we expose the natural connection between the localization-detection performance tradeoff and the radius of tolerance used to judge a detected location as correct or incorrect. Furthermore, like other metrics introduced recently for SMLM [260], Flat Metric does not require arbitrary pairing decisions between detected and ground-truth locations. Nonetheless, in opposition to RMSMD, Flat Metric still resolves pairings implicitly, thus yielding interpretable and explainable assessments.

The part is structured as follows: First, we introduce Flat Metric mathematically, expose its link with unbalanced optimal transport and explain how to compute it numerically. Then, we illustrate its behavior on a simple example. Finally, we compare it to the efficiency (8.1) on both synthetic data and the SMLM 2016 challenge data.

8.4.2 Flat Metric for SMLM

Mathematical Definition

Without loss of generality, we assume that the ground-truth and detected locations are in $\mathcal{X} = [0, 1]^D$, for $D \in \{2, 3\}$. We use the Euclidean distance $d(\mathbf{x}, \mathbf{y}) = \|\mathbf{x} - \mathbf{y}\|_2$ to measure the distances between two points. We denote by $\mathcal{M}(\mathcal{X})$ the space of Radon measures defined on \mathcal{X} . Mathematically, $\mathcal{M}(\mathcal{X})$ is the continuous dual of the space $\mathcal{C}(\mathcal{X})$ of continuous functions on \mathcal{X} endowed with the uniform norm $\|\cdot\|_\infty$. The canonical norm on $\mathcal{M}(\mathcal{X})$ is thus

$$\forall \mu \in \mathcal{M}(\mathcal{X}), \quad \|\mu\|_{\mathcal{M}} \triangleq \sup_{f \in \mathcal{C}(\mathcal{X}), \|f\|_\infty \leq 1} \int_{\mathcal{X}} f d\mu, \quad (8.2)$$

and is known as the total-variation norm or \mathcal{M} norm. The Banach space $\mathcal{M}(\mathcal{X})$ contains point-source signals, referred to as the Dirac masses $\delta_{\mathbf{x}} \triangleq \delta(\cdot - \mathbf{x})$ for $\mathbf{x} \in \mathcal{X}$. This makes it particularly well-suited for SMLM because individual fluorescent emitters can be seen as Dirac masses, which suggests the representation of SMLM data as sums of Dirac masses.

The total-variation norm is not a good candidate metric for SMLM because, for all $\mathbf{x} \neq \mathbf{y}$, $\|\delta_{\mathbf{x}} - \delta_{\mathbf{y}}\|_{\mathcal{M}} = 2$. Instead, we build our metric from the flat norm on $\mathcal{M}(\mathcal{X})$ given in Definition 8.4.1.

Definition 8.4.1 (Flat norm [263]). *The flat norm of a given $\mu \in \mathcal{M}(\mathcal{X})$ is defined as*

$$\|\mu\| \triangleq \sup \left(\left\{ \int_{\mathcal{X}} f d\mu : f \in \mathcal{C}(\mathcal{X}), \|f\|_\infty \leq \lambda, \text{Lip}(f) \leq 1 \right\} \right), \quad (8.3)$$

where $\text{Lip}(f)$ is the Lipschitz constant of f . This definition induces a norm on $\mathcal{M}(\mathcal{X})$.

Using the flat norm to measure the difference between two Radon measures leads to Flat Metric.

Definition 8.4.2 (Flat Metric). *Flat Metric is defined for any two $\mu, \nu \in \mathcal{M}(\mathcal{X})$ as*

$$F_\lambda(\mu, \nu) \triangleq \|\mu - \nu\|. \quad (8.4)$$

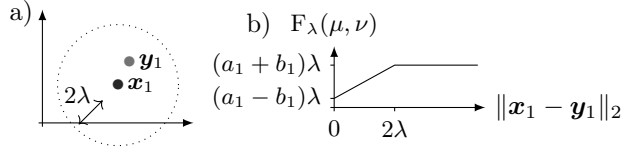


Figure 8.7: a) Example of two discrete measures in $\mathcal{X} = [0, 1]^2$, $\mu = a_1\delta_{\mathbf{x}_1}$ and $\nu = b_1\delta_{\mathbf{y}_1}$, where a_1 and b_1 are represented by the opacity of the \bullet marks. b) Dependence of the metric $F_\lambda(\mu, \nu)$ on $\|\mathbf{x}_1 - \mathbf{y}_1\|_2$ from a) for fixed values $a_1 > b_1$, growing linearly with $\|\mathbf{x}_1 - \mathbf{y}_1\|_2$ and saturating at $\|\mathbf{x}_1 - \mathbf{y}_1\|_2 = 2\lambda$.

Flat Metric is linked to unbalanced optimal transport [262, 268]. This makes Flat Metric interpretable, which is key for its application to SMLM.

Proposition 8.4.1 (Interpretation of Flat Metric - [268], Prop. 2.26). *For all $\mu, \nu \in \mathcal{M}(\mathcal{X})$,*

$$F_\lambda(\mu, \nu) = \min_{\pi \in \mathcal{M}_+(\mathcal{X} \times \mathcal{X})} \left\{ \int_{\mathcal{X} \times \mathcal{X}} d(\mathbf{x}, \mathbf{y}) d\pi(\mathbf{x}, \mathbf{y}) + \lambda \left\| \mu - \text{pr}_{\mathbf{x}\#} \pi \right\|_{\mathcal{M}} + \lambda \left\| \nu - \text{pr}_{\mathbf{y}\#} \pi \right\|_{\mathcal{M}} \right\}, \quad (8.5)$$

where $\pi \in \mathcal{M}_+(\mathcal{X} \times \mathcal{X})$ is a nonnegative Radon measure over $[0, 1]^D \times [0, 1]^D$ that specifies the transport plan between the marginals $\text{pr}_{\mathbf{x}\#} \pi = \int_{\mathcal{X}} d\pi(\cdot, \mathbf{y})$ and $\text{pr}_{\mathbf{y}\#} \pi = \int_{\mathcal{X}} d\pi(\mathbf{x}, \cdot)$ of π (which can be made arbitrary close to μ and ν , respectively, by setting $\lambda \rightarrow +\infty$).

The first term in the minimization problem (8.5) penalizes the cost of transporting $\text{pr}_{\mathbf{x}\#} \pi$ to $\text{pr}_{\mathbf{y}\#} \pi$ (or vice versa). This is, in fact, the same cost function as in the 1-Wasserstein distance, one of the classical optimal-transport problems. Optimal-transport metrics quantify how different two measures are by assessing the cost of transforming (in other words, transporting) one measure onto the other. Unlike in standard optimal transport, the marginals $\text{pr}_{\mathbf{x}\#} \pi$ to $\text{pr}_{\mathbf{y}\#} \pi$ need not be

equal to the measures of interest μ and ν . Instead, the constraints are relaxed using the second and third discrepancy terms in (8.5) which involve the total-variation norm. This relaxation allows for the creation and destruction of mass before transport and, therefore, for an optimal transport between measures with different total mass. This key feature is essential for SMLM, as it accounts for the errors both of localization (by the cost of transport) and of detection (by the cost of creation or destruction of mass). Their balance is controlled by the physically interpretable parameter $\lambda > 0$ [nm], as illustrated in Fig. 8.7. When the two Dirac masses are at the same position, the cost is proportional to the difference of weights. Then, it grows linearly with $\|\mathbf{x}_1 - \mathbf{y}_1\|_2$ as the Dirac mass $b_1\delta_{\mathbf{y}_1}$ is transported to the position \mathbf{x}_1 . This keeps happening until $\|\mathbf{x}_1 - \mathbf{y}_1\|_2 \geq 2\lambda$, where the masses are no longer moved and the cost results from the pure creation and destruction of mass.

It is also important to note that Flat Metric is homogeneous to nanometers so that it can be physically associated to a specific scale (in nanometers for the SMLM problem). Hence, when the number of locations is estimated correctly, Flat Metric represents the mean error in terms of localization, similar to the RMSE (see Fig. 8.6). When $\lambda \rightarrow +\infty$ and μ and ν have the same mass, we recover the 1-Wasserstein distance ($\|\cdot\|_{W_1}$). Finally, when $\lambda \rightarrow 0$, we recover the total-variation norm. Consequently, Flat Metric is an interpolating distance between $\|\cdot\|_{W_1}$ and $\|\cdot\|_{\mathcal{M}}$.

How to Compute Flat Metric

The ground-truth data can be represented as the discrete Radon measure

$$\mu = \sum_{n=1}^N a_n \delta_{\mathbf{x}_n} \in \mathcal{M}(\mathcal{X}) \quad \text{with} \quad a_n > 0, \mathbf{x}_n \in \mathcal{X}, \quad (8.6)$$

which contains the locations of the fluorescent emitters in a frame. The reconstructed locations given by any software can also be represented as the discrete Radon measure

$$\nu = \sum_{m=1}^M b_m \delta_{\mathbf{y}_m} \in \mathcal{M}(\mathcal{X}) \quad \text{with} \quad b_m > 0, \mathbf{y}_m \in \mathcal{X}. \quad (8.7)$$

In this discrete setting, we simplify the computation of Flat Metric $F_\lambda(\mu, \nu)$ in (8.4) as detailed in Proposition 8.4.2.

Proposition 8.4.2. *When μ and ν are discrete Radon measures, one can compute (8.4) as*

$$F_\lambda(\mu, \nu) = - \min_{\mathbf{f} \in \mathbb{R}^{N+M} \text{ s.t. } \mathbf{L}\mathbf{f} \in \mathcal{B} \times \mathcal{C}} \langle \mathbf{f}, -\mathbf{c} \rangle, \quad (8.8)$$

where $\mathbf{L} : \mathbb{R}^{N+M} \rightarrow \mathbb{R}^{N \times M} \times \mathbb{R}^{N+M}$ is defined by

$$\mathbf{L}\mathbf{f} = \left((\mathbf{f}_n - \mathbf{f}_{N+m})_{1 \leq n \leq N, 1 \leq m \leq M}, \mathbf{f} \right), \quad (8.9)$$

where $\mathbf{c} = (\mathbf{a}, -\mathbf{b}) \in \mathbb{R}^{N+M}$, and \mathcal{B} and \mathcal{C} are hyper-rectangles such that $\mathcal{B} = \{\mathbf{G} \in \mathbb{R}^{N \times M}; |G_{n,m}| \leq d(\mathbf{x}_n, \mathbf{y}_m)\}$ and $\mathcal{C} = \{\mathbf{f} \in \mathbb{R}^{N+M} : \forall k \in \{1, 2, \dots, N+M\}, |f_k| \leq \lambda\}$.

In fact, (8.8) holds because the dual problem of that minimization is exactly the unbalanced optimal transport problem (8.5) for discrete measures, and strong duality holds.

Therefore, to compute $F_\lambda(\mu, \nu)$, one simply needs to solve the minimization problem given in (8.8), which is a finite-dimensional linear program. This problem is then solved using any standard linear programming toolbox.

Note that if one considers only the first part of the operator \mathbf{L} in (8.9) then (8.8) is exactly the dual problem of the 1-Wasserstein optimal transport problem, see [262, ch. 6]. The second part accounts for the relaxation allowing creation and destruction of mass, as explained above.

8.4.3 Results on Simulated Data

In this section, we first propose an example to illustrate the behavior of Flat Metric. Then, we detail how we generated Fig. 8.6, which confirms that Flat Metric has a behavior similar to that of the efficiency [27] and that it provides a continuum between detection and localization errors. Finally, we report Flat Metric as obtained by 31 participants of the SMLM 2016 Challenge on the 2D dataset and compare it with their efficiency and RMSMDs. Note that, in all our experiments, the weights of the ground truth are uniform and the obtained scale is applied for the reconstruction, with $a_n = b_m = 1/N$. We use the normalizing scaling of the ground truth for the reconstruction as it provides a coherent way to compare different software which do not detect the same number of point sources.

Interpretation of Flat Metric

We show in Fig. 8.8 an example of a ground-truth dataset (\bullet), and its reconstructed dataset (\bullet), and how Flat Metric accounts for the difference between these two measures. Ground-truth locations were chosen randomly in the rectangle $[0, 1] \times [0, 0.5]$ with weights $a_n = b_m = 1/N$ with $N = 15$. Here, $\lambda = 0.1$, which constrains the maximal transport distance between two isolated point sources to 0.2 (see Fig. 8.7). Our interpretation of Flat Metric comes from its link with unbalanced optimal transport (see Proposition 8.4.1). As a metric, it is symmetric. Therefore, we arbitrarily choose to interpret it as the cost of transporting the estimation towards the ground truth (GT). As a result, we have the following behaviors.

- *Transport*: A Dirac mass $\delta_{\mathbf{y}}/N$ of the reconstruction is moved towards one in the ground-truth data $\delta_{\mathbf{x}}/N$. The cost of this transport is $d(\mathbf{x}, \mathbf{y})/N$.
- *Destruction of mass*: A Dirac mass $\delta_{\mathbf{y}}/N$ of the reconstruction is destroyed because there is no corresponding ground-truth location nearby. The cost of this destruction of mass is $\lambda \|\delta_{\mathbf{y}}/N\|_{\mathcal{M}} = \lambda/N$.
- *Creation of mass*: A Dirac mass $\delta_{\mathbf{y}}/N$ is created at a position \mathbf{y} to match a ground-truth location when there is no corresponding Dirac mass in the reconstruction. This cost is λ/N .

Note that we have only these three alternatives because of our choice of weights. To have more complex phenomena such as simultaneous transport, creation, and destruction of mass, discrete measures with Dirac masses of different weights should be used. This could certainly be of interest to the evaluation of other point-source localization problems.

Synthetic Experiments on Flat Metric and Efficiency

We show in Fig. 8.6 how Flat Metric, just as efficiency, interpolates between detection and localization metrics. To its benefit, Flat Metric has strong foundations in the theory briefly presented in Section 8.4.2, by contrast with the efficiency measure which is based on empirical results. Consistently, Flat Metric is also well-defined for 0% recall, thus being a more robust tool for any use-case.

In order to exhibit this link in conditions relevant to SMLM, we chose to focus on recall as a detection metric. Indeed, recall is typically the most relevant

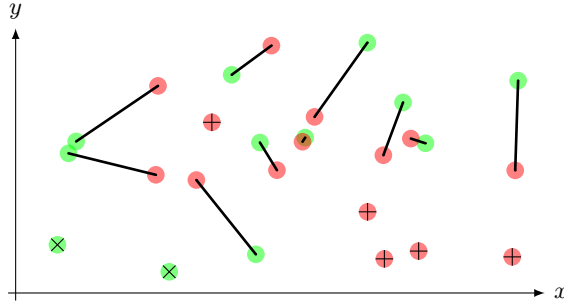


Figure 8.8: Illustration of how Flat Metric (here equal to 0.125) is computed. When an estimated location (●) is linked by a line to a ground-truth location (●), the cost ($d(\mathbf{x}, \mathbf{y})/N$) comes from moving the former to the latter. The presence of a cross (×) means that the point has been destroyed, at the cost of λ/N . A ground-truth location with a plus sign (+) means a mass has been created at this position to match it, also at the cost of λ/N .

factor to characterize detection in SMLM, as most leading algorithms achieve very high precision [27]. We modeled this situation by randomly sampling 100 ground-truth locations uniformly in a square of $(6.4 \times 6.4) \mu\text{m}$, and simply removing the corresponding percentage of locations to initialize the set of recovered locations.

For the joint evaluation of detection and localization effects, we modeled localization errors in detected locations as independent and identically distributed uniform vectors in disks of radius up to 250 nm.

The results in Fig. 8.6 were generated by averaging 50 randomized trials for each combination of radius and recall, using $\lambda = 125 \text{ nm}$. Finally, the expectations of Flat Metric and efficiency are shown on the planes with 100% recall and vanishing perturbation radius, respectively. They are related to the expectations of J and RMSE in those cases, where $c = 2/3\sqrt{2}$.

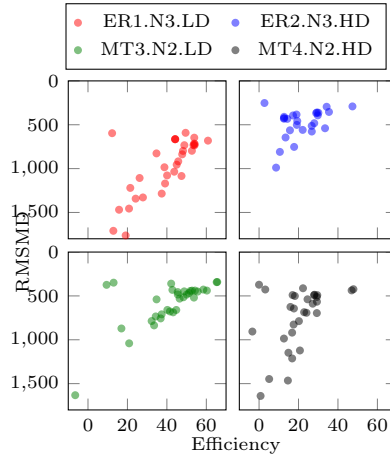


Figure 8.9: Low degree of correlation between efficiency and the RMSMD on four datasets from the SMLM 2016 Challenge.

Application to the 2016 Challenge

We compare efficiency, a thoroughly validated empirical metric for SMLM, to both Flat Metric and RMSMD, on four 2D datasets from the SMLM 2016 Challenge.³ As shown in Figs. 8.6 and 8.9, Flat Metric is strongly correlated with efficiency, while RMSMD is not. Indeed, one only observes few outliers on the efficiency vs. Flat Metric comparison, mainly for reconstruction methods that work rather poorly on the datasets MT3 and MT4.

8.4.4 Discussion

We proposed Flat Metric to quantitate SMLM reconstruction errors when ground-truth data are available. Here, we have presented and exemplified the strong links between Flat Metric and unbalanced optimal transport problems, which underpin this robust metric. We also provided exhaustive evidence that Flat Metric is con-

³ <http://bigwww.epfl.ch/smlm/challenge2016/index.html?p=results>

ceptually similar to efficiency, a very well established empirical metric designed in the organization of the SMLM 2016 Challenge. Consequently, we provided a robust and practical metric for SMLM evaluation. We have also exemplified and explained how Flat Metric works internally, providing intuition on how this optimal assessment is obtained. Further, we have emphasized the interpretability of Flat Metric, which can be read as an equivalent localization accuracy.

8.5 Closed-Form Expression of the Fourier-Ring Correlation (FRC) for SMLM

8.5.1 Context

In SMLM, once the localization task is performed, it is customary to render an image from this set of estimated positions. The rendering process usually involves a kernel that determines the contribution of each position to the reconstructed image [269, 270]. Since the emergence of SMLM, the determination of image resolution has become a primordial matter as the reconstructed image is a combination of optics and numerics.

The FRC [271] or, equivalently, the spectral SNR [272] is a standard tool for resolution assessment in electron microscopy. It has been recently extended to SMLM [253, 254] and quickly adopted by the community as a standard indicator of resolution. The FRC is computed from discretized rendered images. It therefore depends on experimental parameters such as the pixel size or the choice of density estimator.

Here, we take into consideration the specificity of SMLM to derive a closed-form expression of the FRC. It is noteworthy to mention that, in the current development of localization microscopy, doing post-analysis directly on the coordinates itself and bypassing the image binning step is popular [273, 274]. We first proceed by introducing the mathematical definition of the FRC (Section 8.5.2) and its conventional (discrete) computation, for which we derive an error bound (Section 8.5.3). We then derive the closed-form expression in the continuous domain and we address specific points of implementation (Section 8.5.4). Finally, we assess the difference between a FRC computed in a conventional way (discretized) and the proposed closed-form expression with a dataset from the SMLM challenge [275] (Section 8.5.5).

8.5.2 Notations and Definitions

Definition 8.5.1 (SMLM image rendering). *Given the set $\mathcal{P} = \{\mathbf{p}_n \in \mathbb{R}^2\}_{n=1}^N$ that contains the positions of $N \in \mathbb{N}$ molecules, we define the image $f_{\mathcal{P}} \in L_2(\mathbb{R}^2)$ by*

$$f_{\mathcal{P}}(\mathbf{x}) = \sum_{n=1}^N (\Phi_n * \delta(\cdot - \mathbf{p}_n))(\mathbf{x}), \quad \mathbf{x} \in \mathbb{R}^2, \quad (8.10)$$

where the elements of $\{\Phi_n \in L_2(\mathbb{R}^2)\}_{n=1}^N$ are called the rendering kernels.

Assumption 8.5.2. *The rendering kernels are compactly supported radial functions (i.e., there exist compactly supported 1D functions $\phi_n \in L_2(\mathbb{R}_{\geq 0})$ such that $\Phi_n(\mathbf{x}) = \phi_n(\|\mathbf{x}\|)$). Hence, their Fourier transform is also radial, so that we write $\hat{\Phi}_n(\boldsymbol{\omega}) = \hat{\phi}_n(\|\boldsymbol{\omega}\|)$.*

From Definition 8.5.1, each molecule can be rendered using a different kernel. For instance, one can use truncated Gaussian kernels whose variances are related to the number of detected photons [176, 276–280]. From Assumption 8.5.2 and Definition 8.5.1, we readily deduce that the rendered image $f_{\mathcal{P}}$ is compactly supported. Using the translation property of the Fourier transform, we also get that

$$\hat{f}_{\mathcal{P}}(\boldsymbol{\omega}) = \sum_{n=1}^N \hat{\Phi}_n(\boldsymbol{\omega}) e^{-i\mathbf{p}_n^T \boldsymbol{\omega}}. \quad (8.11)$$

Definition 8.5.3 (FRC [253, 254]). *Let $f \in L_2(\mathbb{R}^2)$ and $g \in L_2(\mathbb{R}^2)$. Then, the FRC between the images f and g is defined $\forall \rho > 0$ as*

$$\text{FRC}_{\{f,g\}}(\rho) = \frac{\langle \hat{f}, \hat{g} \rangle_{\mathcal{C}_\rho}}{\sqrt{\langle \hat{f}, \hat{f} \rangle_{\mathcal{C}_\rho} \langle \hat{g}, \hat{g} \rangle_{\mathcal{C}_\rho}}}, \quad (8.12)$$

where $\mathcal{C}_\rho := \{\boldsymbol{\omega} \in \mathbb{R}^2 : \|\boldsymbol{\omega}\|_2 = \rho\}$ is a circle of radius $\rho > 0$ and

$$\langle \hat{f}, \hat{g} \rangle_{\mathcal{C}_\rho} := \oint_{\mathcal{C}_\rho} \hat{f}^*(\boldsymbol{\omega}) \hat{g}(\boldsymbol{\omega}) d\boldsymbol{\omega}. \quad (8.13)$$

8.5.3 Conventional FRC Computation in SMLM

To compute the FRC, the standard practice is to sample the continuously rendered images $f_{\mathcal{P}} \in L_2(\mathbb{R}^2)$ and $f_{\mathcal{Q}} \in L_2(\mathbb{R}^2)$ as

$$\mathbf{f}_{\mathcal{P}} \in \mathbb{R}^K \quad \text{such that} \quad [\mathbf{f}_{\mathcal{P}}]_k = f_{\mathcal{P}}(\mathbf{x}_k) \quad (8.14)$$

$$\mathbf{f}_{\mathcal{Q}} \in \mathbb{R}^K \quad \text{such that} \quad [\mathbf{f}_{\mathcal{Q}}]_k = f_{\mathcal{Q}}(\mathbf{x}_k), \quad (8.15)$$

where $\{\mathbf{x}_k \in \mathbb{R}^2\}_{k=1}^K$ is a set of sampling points on a uniform Cartesian grid. We denote by $s > 0$ the spatial sampling step. The size of the grid is chosen such that the (compact) support of $f_{\mathcal{P}}$ ($f_{\mathcal{Q}}$, respectively) is fully contained within the discrete image $\mathbf{f}_{\mathcal{P}}$ ($\mathbf{f}_{\mathcal{Q}}$, respectively). Then, the FRC is computed from the DFT of $\mathbf{f}_{\mathcal{P}}$ and $\mathbf{f}_{\mathcal{Q}}$ (which are denoted $\hat{\mathbf{f}}_{\mathcal{P}}$ and $\hat{\mathbf{f}}_{\mathcal{Q}}$), using numerical integration and interpolation. Henceforth, we shall refer to this approach as discrete FRC. From the Poisson summation formula, we have that

$$[\hat{\mathbf{f}}_{\mathcal{P}}]_k = \sum_{\mathbf{m} \in \mathbb{Z}^2} \hat{f}_{\mathcal{P}}(\boldsymbol{\omega}_k + 2\pi s^{-1} \mathbf{m}), \quad (8.16)$$

where $\boldsymbol{\omega}_k$ is the pulsation that corresponds to $[\hat{\mathbf{f}}_{\mathcal{P}}]_k$. As a result, the sampling procedure yields the error

$$\begin{aligned} \left| [\hat{\mathbf{f}}_{\mathcal{P}}]_k - \hat{f}_{\mathcal{P}}(\boldsymbol{\omega}_k) \right| &\leq \sum_{\mathbf{m} \in \mathbb{Z}^2 \setminus \{\mathbf{0}\}} \left| \hat{f}_{\mathcal{P}}(\boldsymbol{\omega}_k + 2\pi s^{-1} \mathbf{m}) \right| \\ &\leq \sum_{\mathbf{m} \in \mathbb{Z}^2 \setminus \{\mathbf{0}\}} \sum_{n=1}^N \left| \hat{\Phi}_n(\boldsymbol{\omega}_k + 2\pi s^{-1} \mathbf{m}) \right|. \end{aligned} \quad (8.17)$$

Because the kernels Φ_n are compactly supported (Assumption 8.5.2), their Fourier transforms $\hat{\Phi}_n$ are not. Hence, the accuracy of the discrete FRC is related to the sampling step s as well as the decay of $|\hat{\Phi}_n|$. They have to be tuned so as to minimize the aliasing (*i.e.*, minimize the bound in (8.17)). In particular, the sampling step must be sufficiently small and $|\hat{\Phi}_n|$ must decrease fast enough. This will be further discussed along with the numerical experiments (Section 8.5.5).

8.5.4 Closed-Form Expression of The FRC in Continuous Domain

Main Result

We present our main result in Proposition 8.5.1 where we derive a closed-form expression of the FRC in the continuous domain. Henceforth, we shall refer to our approach as closed-form FRC.

Proposition 8.5.1. *Let $f_{\mathcal{P}} \in L_2(\mathbb{R}^2)$ and $f_{\mathcal{Q}} \in L_2(\mathbb{R}^2)$ be the rendered images of $\mathcal{P} = \{\mathbf{p}_n \in \mathbb{R}^2\}_{n=1}^N$ and $\mathcal{Q} = \{\mathbf{q}_m \in \mathbb{R}^2\}_{m=1}^M$, respectively. Then, the FRC is given by (8.12) with*

$$\langle \hat{f}_{\mathcal{P}}, \hat{f}_{\mathcal{Q}} \rangle_{\mathcal{C}_\rho} = \sum_{n=1}^N \sum_{m=1}^M (\hat{\phi}_n \hat{\phi}_m^*)(\rho) J_0(\|\mathbf{p}_n - \mathbf{q}_m\|_2 \rho), \quad (8.18)$$

where J_0 is the zero-order Bessel function of the first kind. The kernels $\hat{\phi}_n$ follow the conditions in Assumption 8.5.2.

Proof. Injecting (8.11) into $\langle \hat{f}_{\mathcal{P}}, \hat{f}_{\mathcal{Q}} \rangle_{\mathcal{C}_\rho}$, we obtain that

$$\langle \hat{f}_{\mathcal{P}}, \hat{f}_{\mathcal{Q}} \rangle_{\mathcal{C}_\rho} = \oint_{\mathcal{C}_\rho} \sum_{n,m=1}^{N,M} (\hat{\Phi}_n \hat{\Phi}_m^*)(\boldsymbol{\omega}) e^{-i(\mathbf{p}_n - \mathbf{q}_m)^T \boldsymbol{\omega}} d\boldsymbol{\omega}. \quad (8.19)$$

By definition, we have that $\forall \boldsymbol{\omega} \in \mathcal{C}_\rho$, $\|\boldsymbol{\omega}\|_2 = \rho$. Combining that fact with Assumption 8.5.2 and the linearity of the integral comes to

$$\langle \hat{f}_{\mathcal{P}}, \hat{f}_{\mathcal{Q}} \rangle_{\mathcal{C}_\rho} = \sum_{n,m=1}^{N,M} (\hat{\phi}_n \hat{\phi}_m^*)(\rho) \oint_{\mathcal{C}_\rho} e^{-i\mathbf{r}_{nm}^T \boldsymbol{\omega}} d\boldsymbol{\omega}, \quad (8.20)$$

where $\mathbf{r}_{nm} = (\mathbf{p}_n - \mathbf{q}_m)$. By converting to polar coordinates, *i.e.*, $\mathbf{r}_{nm} = r_{nm}(\cos(\theta_{nm}), \sin(\theta_{nm}))$ and $\boldsymbol{\omega} = \rho(\cos(\theta), \sin(\theta))$, we have that

$$\begin{aligned} \mathbf{r}_{nm}^T \boldsymbol{\omega} &= r_{nm} \rho (\cos(\theta_{nm}) \cos(\theta) + \sin(\theta_{nm}) \sin(\theta)) \\ &= r_{nm} \rho \cos(\theta - \theta_{nm}). \end{aligned} \quad (8.21)$$

The integral in (8.20) becomes

$$\begin{aligned} \oint_{\mathcal{C}_\rho} e^{-i\mathbf{r}_{nm}^T \boldsymbol{\omega}} d\boldsymbol{\omega} &= \int_{-\pi}^{\pi} e^{-ir_{nm}\rho \cos(\theta - \theta_{nm})} d\theta \\ &= \int_{-\pi}^{\pi} e^{-ir_{nm}\rho \sin(\theta)} d\theta \\ &= 2\pi J_0(r_{nm}\rho). \end{aligned} \quad (8.22)$$

The second equality comes from the fact that $\cos(\theta - \theta_{nm}) = \sin(\theta - \theta_{nm} + \pi/2)$ and that \sin is a 2π -periodic function. By inserting (8.22) into (8.20), we obtain (8.18). \square

This continuous-domain expression allows for computing the FRC over circles, while in the discrete case it must be computed over annuli (circles with a certain “width”). A direct consequence of Proposition 8.5.1 is that, when the same rendering kernel Φ is used for all the molecules, the FRC does not depend anymore on Φ .

Corollary 8.5.2. *Let $\Phi \in L_2(\mathbb{R}^2)$ be a rendering kernel that fulfills Assumption 8.5.2 and let $\Phi_n = \Phi_m = \Phi$ for all $n \in [1 \dots N]$, $m \in [1 \dots M]$. Then, the FRC does not depend on Φ .*

Proof. Because Φ fulfills Assumption 8.5.2, we have that $\hat{\Phi} = \hat{\phi}(\|\cdot\|)$ for a given $\hat{\phi} \in L_2(\mathbb{R}_{\geq 0})$. Hence, (8.18) becomes

$$\langle \hat{f}_{\mathcal{P}}, \hat{f}_{\mathcal{Q}} \rangle_{C_\rho} = |\hat{\phi}(\rho)|^2 \sum_{n,m=1}^{N,M} J_0(\|\mathbf{p}_n - \mathbf{q}_m\|_2 \rho). \quad (8.23)$$

The term $|\hat{\phi}(\rho)|^2$ is ultimately cancelled by the denominator in (8.12), which completes the proof. \square

Practical Implementation

To compute the closed-form FRC, we must compute three instances of an expression of the same type as (8.18). Each instance requires the calculation of the Euclidean distance between each point of one set of positions with each point of another set of positions (or itself). This yields a computational cost of $O(N^2 + MN + M^2)$ for one value of ρ . For illustration, we report running times with and without GPU in Table 8.2.

8.5.5 Results on Simulated Data

Continuous vs. Discrete FRC

Here, we compare the conventional FRC computation (Section 8.5.3) to the proposed closed-form expression (Section 8.5.4).

We consider the MT1.N1.LD dataset of the 3D SMLM challenge⁴ and we denote by \mathcal{P}^* the set containing the positions of the ground-truth molecules. The second

⁴ SMLM software benchmarking, <http://bigwww.epfl.ch/smlm/challenge2016/>, accessed October 16, 2018.

Table 8.2: Running time to compute the closed-form FRC. The two sets have $M = 3647$ and $N = 5514$ positions respectively. Three hundred samples of the closed-form FRC were computed. As a reference, the running times for the discrete FRC (three hundred points, image size 3200×3200) was 0.3 s on CPU.

CPU	283 s
GPU	6.6 s

set, \mathcal{P} , contains the positions of the molecules which were localized by one of the participants [159] for the MT1.N1.LD dataset. We use a unique rendering kernel for all the molecules and define it as the truncated Gaussian

$$\Phi_\sigma(\mathbf{x}) = \phi_\sigma(\|\mathbf{x}\|) \quad (8.24)$$

where, for $\sigma > 0$,

$$\phi_\sigma(x) = \begin{cases} \frac{1}{\sigma\sqrt{2\pi}} e^{-\frac{x^2}{2\sigma^2}} & |x| < 5\sigma \\ 0, & \text{otherwise.} \end{cases} \quad (8.25)$$

We computed some discrete FRC with different sampling steps ($s = 2, 4, 6, 8$ nm) and different widths of the kernel ($\sigma = \{0.42, 0.85, 1.27, 2.12, 4.25, 8.49\}$ nm). These values were computed from arbitrary chosen full width at half maximum (FWHM = $2\sqrt{2\log 2}\sigma = \{1, 2, 3, 5, 10, 20\}$). In Fig. 8.10, we show some of these curves for the sake of visibility. We observe that the conventional FRC curve reaches the closed-form FRC for some values of the sampling step of the discrete rendered image, as well as the parameters of the rendering kernels.

Quantitative Discrepancy of the Discrete FRC

In Fig. 8.11, we compute the relative discrepancy between the discrete FRC and the closed-form FRC defined as

$$\text{Relative discrepancy} = \frac{\|\text{FRC}_{\{f_{\mathcal{P}}, f_{\mathcal{P}^*}}\}}^{\text{disc.}} - \text{FRC}_{\{f_{\mathcal{P}}, f_{\mathcal{P}^*}}\}}^{\text{c.f.}}\|_2}{\|\text{FRC}_{\{f_{\mathcal{P}}, f_{\mathcal{P}^*}}\}}^{\text{c.f.}}\|_2}. \quad (8.26)$$

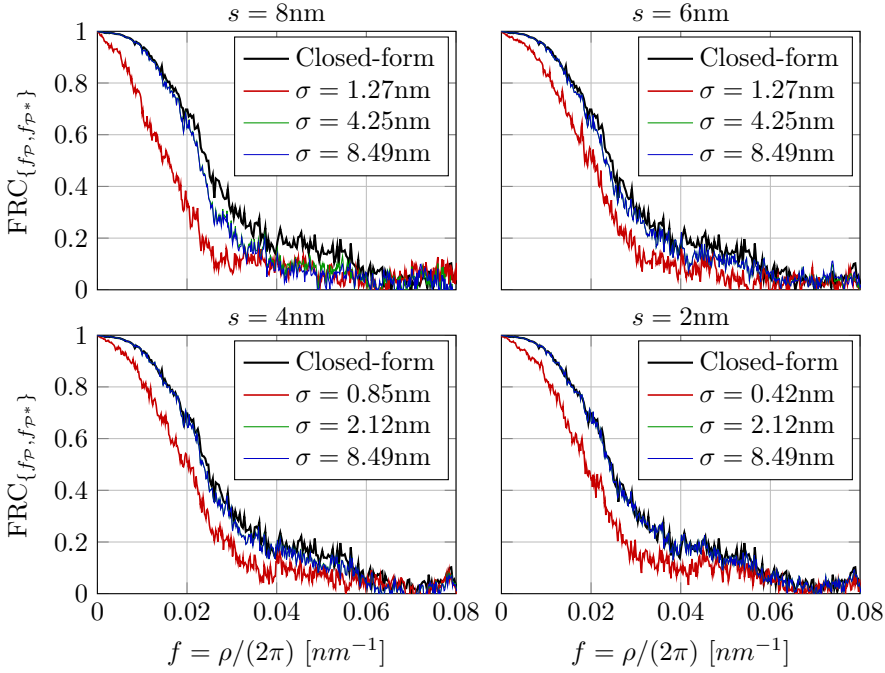


Figure 8.10: Comparison of the closed-form FRC curve with discrete FRC curves obtained using different sampling steps s and rendering kernels Φ_σ . The discrete FRC curves reach the closed-form FRC curve when the width of the kernel and the sampling step are appropriately set (e.g., $s = 2nm$ and $\sigma = 8.49nm$).

We observe that a smaller sampling step yields a better approximation, as expected. In addition, for each sampling step, there exists a range of widths of kernel for which the discrepancy is minimized. Finally, we can relate these observations to the error bound derived in Section 8.5.3. Indeed, when the step size is small enough, small values of σ are sufficient to minimize the error to the closed-form FRC. However, if one chooses a larger step size, the parameter σ has to be larger

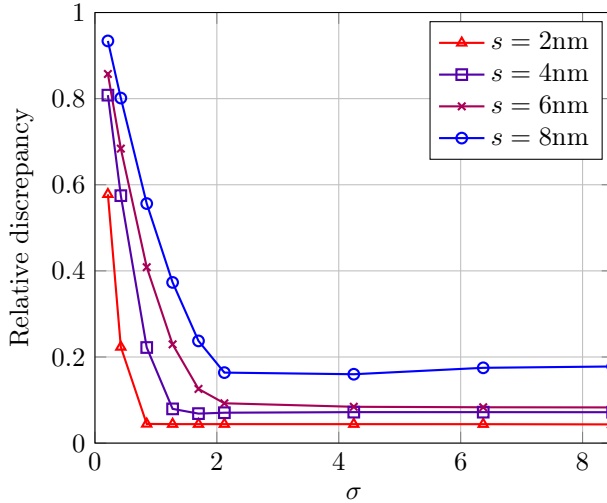


Figure 8.11: Relative discrepancy between the discrete and the closed-form FRC for different values of kernel width σ . For any sampling step, there exists a range of parameters for the discrete FRC which minimizes the discrepancy.

as well in order to reduce the aliasing effect and minimize the error.

8.5.6 Discussion

In this section, we obtained a closed-form expression to compute the FRC in the continuous domain for SMLM. Our method allows us to compute a parameter-free FRC. We showed that the conventional FRC computation reaches the closed-form FRC when the sampling parameters are set appropriately. Moreover, our approach could allow for an accurate computation of the local FRC [255].

8.6 Summary

In this chapter, we presented our contributions on metrics for computational microscopy. We proposed a metric with no ground-truth requirement for ODT. By illuminating the sample with a known pattern, we leveraged phase conjugation to assess the quality of 3D reconstructed RI maps. Actually, we performed digital phase conjugation by back-propagating the complex-conjugated measured field through the sample via our forward model LSm (Chapter 3). By doing so, the illumination pattern should be recovered unless the reconstructed RI maps are inaccurate. The proposed metric confirmed the superior performance of the Rytov model over the Born and Radon models for biological samples.

Further, we investigated metrics for SMLM by taking advantage of its particular outcome, *i.e.*, a list of estimated positions. Our first contribution was an optimal-transport-based metric (Flat Metric) which assesses the performance of both detection (Jaccard Index) and localization (RMSE). The main outcome is a robust and practical metric for SMLM evaluation with an intuition on how we can achieve an optimal assessment, which stems from solid mathematical grounds. Our second contribution was the derivation of a closed-form expression of the FRC for SMLM. Since this metric was originally built for pixel-based images, users have to render an SMLM image with arbitrary choices of hyper-parameters. By obtaining a tailored closed-form expression, our work provides instructions on optimal choices of such hyper-parameters.

Chapter 9

Conclusion

In this thesis, we have focused on developing novel computational methods for improving the quality of reconstructions in QPI. To achieve this objective, we have developed highly accurate models of the acquisition process and efficient algorithmic reconstruction methods. We have also proposed novel learning-based regularization schemes. In what follows, we summarize our contributions and discuss future prospects of QPI.

Summary of Results

Accurate Discretization of the LiSc Equation We derived an accurate and efficient model of light scattering that accounts for multiple-scattering events (both reflection and transmission). We properly discretized the LiSc equation and obtained a linear system, which we solved with the help of a Krylov-based method. In particular, we handled the singularity of the Green’s function using a truncation trick and a memory-saving strategy. In our experiments, our model LS_m achieved high accuracy and outperformed existing models.

ODT from Complex Measurements Using our novel forward model, we formulated an inverse-scattering problem within a modern variational framework and solved it to recover the 3D RI map of the sample when the measurements are

complex-valued. Our algorithmic reconstruction involves a nontrivial proximal gradient-based iterative scheme that requires the Jacobian matrix of the nonlinear operator. We were able to derive an explicit expression for the Jacobian matrix, which helped in alleviating the memory and computational burdens. To deploy our framework on real acquisitions, we built the volume of the incident field by numerical propagation of a real acquisition of it at the detector plane. In particular, we proposed a strategy that resulted in significantly reduced numerical errors. Further, we developed a novel adaptive regularization scheme to tackle the missing-cone problem. Our dictionary-learning-based approach learns 2D features of the lateral planes from the specimen and promotes such features on all the planes. By accounting for multiple scattering and adding suitable prior knowledge, we significantly improved the quality of reconstruction over the state of the art.

ODT from Intensity-only Measurements We proposed a versatile reconstruction framework to tackle the corresponding inverse-scattering problem with any physical model. We split the optimization task in a way that decouples the complex-field-based reconstruction from the phase retrieval. This allows us to take advantage of our previous contributions and of proximity operators for phase retrieval [21]. In our experiments, we reconstruct RI maps from intensity-only measurements with quality similar to the ones recovered from complex measurements. This shows that, in some settings, intensity information is sufficient for recovering RI maps.

SMLM Meets ODT In SMLM, the emission patterns of each fluorescent label can be distorted by the sample, which reduces the localization accuracy if not accounted for. We then exploited these sample-induced aberrations to recover the RI map. We proposed an optimization framework in which we reconstruct the RI map using LS_m and optimize the label positions in a joint fashion. In our numerical experiments, we effectively recovered the RI map of the sample and further improved the localization—the primary objective of SMLM.

PUDIP We addressed the unwrapping of 2D phase images from their wrapped counterparts. To tackle challenging cases such as phase images of organoids, we proposed an untrained deep-learning-based method, which incorporates an explicit

feedback mechanism. Our comparisons showed that our phase unwrapping with deep image prior significantly outperformed the state of the art.

Metrics for ODT and SMLM In this chapter, our first contribution was a metric with no ground-truth requirement for ODT reconstructions. We illustrated its adequacy for biological samples. Then, we leveraged the unique features of SMLM (*i.e.*, list of estimated positions, image rendering) to investigate metrics from new perspectives. Building upon a broad benchmarking of localization software packages [27], we proposed a novel optimal-transport-based metric for SMLM which captures both detection and localization performance and relies on solid mathematical foundations. Finally, we derived a closed-form expression of the FRC for the particular case of SMLM, which allowed us to investigate the classical way of computing FRC (*i.e.*, SMLM image rendering and DFT).

Future Prospects

QPI is a powerful tool for studying label-free biological samples. Precise knowledge of the acquisition parameters is decisive for the success of the reconstruction. For instance, miscalibration of the illumination angles generates structured artifacts in the reconstruction [70]. In Chapter 5, the 3D RI map of the Yeast cell reconstructed from intensity-only measurements is likely to suffer from optical aberrations which were not accounted for in this setting.

Self-calibration algorithms [70] constitute an interesting solution to such issues. Alternatively, deep learning methods can be trained to remove optical aberrations [281].

In this thesis, we developed our methods under the theory of scalar diffraction. Future directions of research could consider the polarization (*i.e.*, vectorial nature) of light and the dielectric tensor (the equivalent RI in Maxwell's equations), which would result in a four-dimension reconstruction problem [33, 282, 283]. We expect the research field to adopt highly-accurate models while mitigating the high computational burden.

Alternatively, the RI maps depend on the wavelength of the incident wave. Our techniques for ODT could be easily applied to hyperspectral ODT [284], which varies the wavelengths to acquire valuable information about the sample.

Further, supervised deep learning can be used to accelerate the computation of the physical model [53, 285] or the resolution of inverse-scattering problem [286].

In spite of being a fluorescence microscopy technique, our extension of SMLM described in Chapter 6 involves tools from QPI. Similar approaches open new avenues for developing novel multi-modal imaging [287]. The benefits are numerous and range from a precise calibration of the acquisition process to the recovery of new and complementary information about the sample.

Appendix A

Appendices

A.1 Short Remark on the GlobalBioIm Library

In this thesis, many of our contributions relied on efficient methods which were implemented in MATLAB[®] using the open-source library *GlobalBioIm* developed in our group [131]. This library exploits the strong commonalities between imaging modalities to enable the implementation of many forward models from elementary modules. Thanks to this modular philosophy, we could rapidly reuse operators between chapters. Simultaneously, this library has guided the implementation of new methods as to remain compatible with the modular approach of *GlobalBioIm*.

A.2 Proximity Operators

In this section, we describe how we can compute the proximity operator of the regularization term \mathcal{R} (see (4.8)). Proximity operators act as a generalization of the notion of a projection operator on a convex set [148]. The proximity operator [288] of a functional $\tau\mathcal{R}$, with $\tau > 0$, is defined as

$$\text{prox}_{\tau\mathcal{R}}(\mathbf{v}) = \arg \min_{\mathbf{f} \in \mathbb{R}^N} \|\mathbf{f} - \mathbf{v}\|_2^2 + \tau\mathcal{R}(\mathbf{f}). \quad (\text{A.1})$$

Here, we are interested in

$$\mathcal{R}(\mathbf{f}) = \|\mathbf{L}\mathbf{f}\| + i_B(\mathbf{f}), \quad (\text{A.2})$$

where $\|\cdot\| : \mathbb{R}^{S \times S'} \rightarrow \mathbb{R}_{\geq 0}$ is a (mixed) norm or seminorm, $\mathbf{L} : \mathbb{R}^N \rightarrow \mathbb{R}^{S \times S'}$ is a linear operator (*e.g.*, discrete gradient, Hessian), and the functional $i_B = \{0, f \in B; \infty, \text{otherwise}\}$ constrains the solution to lie in the convex set B such as $B = \mathbb{R}_{\geq 0}^N$. We then leverage this structure to solve (A.1) efficiently. In this thesis, we deploy two different strategies.

A.2.1 Proximity Operators via ADMM

In Chapter 4 (Section 4.5.3), we used the ADMM algorithm [289] to solve (A.1). More specifically, we tackled 2D ODT regularized with the anisotropic TV and the set constraint on the convex set B

$$\mathcal{R}(\mathbf{f}) = \|\nabla \mathbf{f}\|_{2,1} + i_B(\mathbf{f}) \quad (\text{A.3})$$

where $\nabla : \mathbb{R}^N \mapsto \mathbb{R}^{N \times D}$ encodes the discrete gradient operator for the dimension $D \in \{2, 3\}$. Below, we explicitly describe a solver for the proximity operator of (A.3) via ADMM, but the procedure is generic for (A.2). Let us start by reformulating (A.1) as

$$\begin{aligned} \text{prox}_{\tau \mathcal{R}}(\mathbf{v}) &= \arg \min_{\mathbf{f} \in \mathbb{R}^N} \left(\frac{1}{2} \|\mathbf{f} - \mathbf{v}\|_2^2 + \tau \|\mathbf{q}_1\|_{2,1} + i_B(\mathbf{q}_2) \right), \\ \text{s.t. } \quad \mathbf{q}_1 &= \nabla \mathbf{f}, \\ \mathbf{q}_2 &= \mathbf{f}, \end{aligned} \quad (\text{A.4})$$

which admits the augmented-Lagrangian form

$$\begin{aligned} \mathcal{L}(\mathbf{f}, \mathbf{q}_1, \mathbf{q}_2, \mathbf{w}_1, \mathbf{w}_2) &= \frac{1}{2} \|\mathbf{f} - \mathbf{v}\|_2^2 + \frac{\rho_1}{2} \left\| \nabla \mathbf{f} - \mathbf{q}_1 + \frac{\mathbf{w}_1}{\rho_1} \right\|_2^2 \\ &\quad + \frac{\rho_2}{2} \left\| \mathbf{f} - \mathbf{q}_2 + \frac{\mathbf{w}_2}{\rho_2} \right\|_2^2 + \tau \|\mathbf{q}_1\|_{2,1} + i_B(\mathbf{q}_2), \end{aligned} \quad (\text{A.5})$$

where ρ_1 and ρ_2 are positive scalars, and where $\mathbf{w}_1 \in \mathbb{R}^{N \times D}$ and $\mathbf{w}_2 \in \mathbb{R}^N$ are the Lagrangian multipliers. Then, one can minimize (A.5) using ADMM. The iterates are summarized in Algorithm 8.

Algorithm 8 ADMM for solving (A.1).

Require: $\mathbf{f}^0 \in \mathbb{R}^N$, $\tau > 0$, $\rho_1 > 0$, $\rho_2 > 0$

```

1:  $\mathbf{A} = ((1 + \rho_2)\mathbf{I} + \rho_1 \nabla^T \nabla)$ 
2:  $\mathbf{q}_1^0 = \nabla \mathbf{f}^0$ ,  $\mathbf{q}_2^0 = \mathbf{f}^0$ 
3:  $\mathbf{w}_1 = \mathbf{q}_1$ ,  $\mathbf{w}_2 = \mathbf{q}_2$ 
4:  $t = 1$ 
5: while (not converged) do
6:    $\mathbf{q}_1^{t+1} = \text{prox}_{\frac{\tau}{\rho_1} \|\cdot\|_{2,1}} \left( \nabla \mathbf{f}^t + \frac{\mathbf{w}_1^t}{\rho_1} \right)$ 
7:    $\mathbf{q}_2^{t+1} = \text{prox}_B \left( \mathbf{f}^t + \frac{\mathbf{w}_2^t}{\rho_2} \right)$ 
8:    $\mathbf{f}^{t+1} = \mathbf{A}^{-1} \left( \mathbf{v} + \rho_1 \nabla^T \left( \mathbf{q}_1^{t+1} - \frac{\mathbf{w}_1^t}{\rho_1} \right) + \rho_2 \mathbf{q}_2^{t+1} - \mathbf{w}_2^t \right)$    ▷ Fourier division
9:    $\mathbf{w}_1^{t+1} = \mathbf{w}_1^t + \rho_1 (\nabla \mathbf{f}^{t+1} - \mathbf{q}_1^{t+1})$ 
10:   $\mathbf{w}_2^{t+1} = \mathbf{w}_2^t + \rho_2 (\mathbf{f}^{t+1} - \mathbf{q}_2^{t+1})$ 
11:   $t = t + 1$ 
12: end while
13: return  $\mathbf{f}^t$ 

```

Steps 6 and 7 compute

$$\forall \mathbf{q} \in \mathbb{R}^N, [\text{prox}_B(\mathbf{q})] = \text{proj}(\mathbf{q}), \quad (\text{A.6})$$

$$\forall \mathbf{q} \in \mathbb{R}^{N \times D}, \left[\text{prox}_{\gamma \|\cdot\|_{2,1}}(\mathbf{q}) \right]_{n,d} = q_{n,d} \left(1 - \frac{\gamma}{\|\mathbf{q}_{n,\cdot}\|_2} \right)_+, \quad (\text{A.7})$$

of prox_B and $\text{prox}_{\gamma \|\cdot\|_{2,1}}$ where

$$\text{proj}(\mathbf{q}) := \arg \min_{\mathbf{x} \in B} \|\mathbf{x} - \mathbf{q}\|_2 \quad (\text{A.8})$$

is the orthogonal projection onto the convex set B . For instance, if $B = \mathbb{R}_{\geq 0}^N$, the projection becomes the elementwise operation

$$[\text{proj}(\mathbf{q})]_n = \max(q_n, 0). \quad (\text{A.9})$$

A.2.2 Proximity Operators via the Fast Gradient-Projection (FGP) Method

Although efficient in 2D settings, we observed that proximity operators via ADMM do not scale well to 3D settings. We then deployed the fast gradient-projection (FGP) method to solve the dual formulation of the proximity operator of (A.2) [126, 129]. This dual approach is possible if one can formulate the dual of $\|\mathbf{L}\mathbf{f}\|$. For instance, TV or HS fulfill this condition. The dual problem of (A.1) with (A.2) is defined as

$$\begin{aligned} \mathbf{g}^* = \arg \min_{\mathbf{g} \in \mathcal{P}} & -\frac{1}{2} \|\mathbf{v} - \tau \mathbf{L}^T \mathbf{g} - \text{proj}_B(\mathbf{v} - \tau \mathbf{L}^T \mathbf{g})\|_F^2 \\ & + \|\mathbf{v} - \tau \mathbf{L}^T \mathbf{g}\|_F^2, \end{aligned} \quad (\text{A.10})$$

where the set \mathcal{P} depends on the regularization term. For the anisotropic TV, we have $\mathcal{P} = \{\mathbf{g} \in \mathbb{R}^{N \times D} : \|[g_n]\|_\infty \leq 1, \forall n \in [1, \dots, N]\}$, and, for HS, we refer the reader to [126]. The iterates of FGP are summarized in Algorithm 9. In Step 4, the operator $\text{proj}_{\mathcal{P}}$ is the orthogonal projection onto \mathcal{P} . For the 3D anisotropic TV, the operator is given by

$$[\text{proj}_{\mathcal{P}}(\mathbf{g})]_n = \begin{pmatrix} \frac{g_{n,0}}{\max(|g_{n,0}|, 1)} \\ \frac{g_{n,1}}{\max(|g_{n,1}|, 1)} \\ \frac{g_{n,2}}{\max(|g_{n,2}|, 1)} \end{pmatrix}, \quad (\text{A.11})$$

for $n = 1, \dots, N$. Once (A.10) is solved, the primal solution is then given by

$$\mathbf{f}^* = \text{proj}_B(\mathbf{v} - \tau \mathbf{L}^T \mathbf{g}^*). \quad (\text{A.12})$$

Note that, in this thesis, FGP is embedded in one iteration of FBS. By using few iterations of FGP, we obtained an approximate solution of (A.10) at each iteration of FBS, but this was sufficient to converge in our experiments.

A.3 Proofs for Chapter 3

A.3.1 Preliminary Lemmas

Lemma A.3.1 (Smoothness of a function and decay of its Fourier transform in \mathbb{R}^3). *Let $v \in L_2(\mathbb{R}^3)$ have $(q-1)$ continuous derivatives in $L_2(\mathbb{R}^3)$ for some $q \geq 1$*

Algorithm 9 FGP for solving (A.10).

Require: $\mathbf{f}^0 \in \mathbb{R}^N$, $\tau > 0$, $\mathbf{g}^0 \in$
 1: $\mathbf{d}^0 = \mathbf{g}^0$, $\alpha^0 = 1$, $\gamma = 1/\|\mathbf{L}\|^2$
 2: $t = 0$
 3: **while** (not converged) **do**
 4: $\mathbf{g}^{t+1} = \text{proj}_{\mathcal{P}} (\mathbf{d}^t + \gamma \mathbf{L} (\text{proj}_B (\mathbf{v} - \tau \mathbf{L}^T \mathbf{d}^t)))$
 5: $\alpha^{t+1} = \frac{1 + \sqrt{1 + 4(\alpha^t)^2}}{2}$
 6: $\mathbf{d}^{t+1} = \mathbf{g}^t + \frac{\alpha^t - 1}{\alpha^{t+1}} (\mathbf{g}^{t+1} - \mathbf{g}^t)$
 7: $t = t + 1$
 8: **end while**
 9: **return** \mathbf{g}^t

and a q th derivative of bounded variations. Then,

$$|\hat{v}(\boldsymbol{\omega})| \leq \frac{C_1}{\|\boldsymbol{\omega}\|^{q+1}} \quad \forall \boldsymbol{\omega} \text{ s.t. } \|\boldsymbol{\omega}\| \geq C_2, \quad (\text{A.13})$$

where C_1 and C_2 are positive constants.

Proof. It is an extension of the well known result in one-dimension, see for instance [290, Theorems 6.1 and 6.2]. \square

Lemma A.3.2 (DFT aliasing for compactly supported functions in \mathbb{R}^3). *Let $v \in L_2([-L/2, L/2]^3)$ be compactly supported, have $(q - 1)$ continuous derivatives in $L_2(\mathbb{R}^3)$ for some $q \geq 3$, and a q th derivative of bounded variations. Let $\mathbf{v} \in \mathbb{R}^N$ ($N = n^3$) be a sampled version of v with sampling step $h = L/n$. Finally, denote by $\delta = 2\pi/(hn)$ the frequency sampling step of $\hat{\mathbf{v}}$, the DFT of \mathbf{v} . Then, for all $\mathbf{q} \in \llbracket \frac{-n}{2} + 1; \frac{n}{2} \rrbracket^3$*

$$|\hat{v}(\delta \mathbf{q}) - h^3 \hat{\mathbf{v}}[\mathbf{q}]| \leq Ch^{q+1} \quad (\text{A.14})$$

for a positive constant $C > 0$.

Proof. From Poisson's summation formula and the compact support of v , we have that

$$\sum_{\mathbf{k} \in \llbracket \frac{-n}{2} + 1; \frac{n}{2} \rrbracket^3} \mathbf{v}[\mathbf{k}] e^{-j h \mathbf{k}^T \boldsymbol{\omega}} = \frac{1}{h^3} \sum_{\mathbf{m} \in \mathbb{Z}^3} \hat{v}(\boldsymbol{\omega} + 2\pi \mathbf{m}/h). \quad (\text{A.15})$$

Setting $\boldsymbol{\omega} = \delta \mathbf{q} = 2\pi \mathbf{q}/(hn)$ in (A.15), one recognizes that the left-hand side is the DFT of \mathbf{v} . Hence, we obtain that

$$\hat{v}(\delta \mathbf{q}) = h^3 \hat{\mathbf{v}}[\mathbf{q}] - \sum_{\substack{\mathbf{m} \in \mathbb{Z}^3 \\ \mathbf{m} \neq \mathbf{0}}} \hat{v}(\delta \mathbf{q} + 2\pi \mathbf{m}/h). \quad (\text{A.16})$$

Then, from Lemma A.3.1, we obtain that there exists $C > 0$ such that

$$\begin{aligned} |\hat{v}(\delta \mathbf{q}) - h^3 \hat{\mathbf{v}}[\mathbf{q}]| &\leq \sum_{\substack{\mathbf{m} \in \mathbb{Z}^3 \\ \mathbf{m} \neq \mathbf{0}}} \frac{C}{\|\delta \mathbf{q} + 2\pi \mathbf{m}/h\|^{q+1}} \\ &\leq \frac{Ch^{q+1}}{(2\pi)^{q+1}} \sum_{\substack{\mathbf{m} \in \mathbb{Z}^3 \\ \mathbf{m} \neq \mathbf{0}}} \frac{1}{\|\mathbf{q}/n + \mathbf{m}\|^{q+1}} \end{aligned} \quad (\text{A.17})$$

Let us now study the convergence of the series in (A.17). Using the fact that $\|\cdot\|_2 \leq \|\cdot\|_1 \leq \sqrt{N} \|\cdot\|_2$, we obtain that

$$\sum_{\substack{\mathbf{m} \in \mathbb{Z}^3 \\ \mathbf{m} \neq \mathbf{0}}} \frac{1}{\|\mathbf{q}/n + \mathbf{m}\|_2^{q+1}} \leq \sum_{\substack{\mathbf{m} \in \mathbb{Z}^3 \\ \mathbf{m} \neq \mathbf{0}}} \frac{\sqrt{N}}{\|\mathbf{q}/n + \mathbf{m}\|_1^{q+1}}. \quad (\text{A.18})$$

Then, for $\mathbf{q} \in \left[\left[-\frac{n}{2} + 1; \frac{n}{2}\right]^3\right]$ and $m \in \mathbb{N}$ we introduce the set

$$S_{\mathbf{q}}^m = \{\mathbf{m} \in \mathbb{Z}^3 : m \leq \|\mathbf{q}/n + \mathbf{m}\|_1 < m + 1\}. \quad (\text{A.19})$$

Using the fact that $\mathbf{q} \in \left[\left[-\frac{n}{2} + 1; \frac{n}{2}\right]^3\right] \Rightarrow \mathbf{q}/n \in (-1/2, 1/2]^3$, we have that

$$\|\mathbf{m}\|_1 - 3/2 \leq \|\mathbf{q}/n + \mathbf{m}\|_1 \leq \|\mathbf{m}\|_1 + 3/2, \quad (\text{A.20})$$

which implies that

$$\begin{aligned} |S_{\mathbf{q}}^m| &\leq \sum_{m'=m-2}^{m+2} |S_{\mathbf{0}}^{m'}| \\ &\leq 5|S_{\mathbf{0}}^{m+2}| = 5(4(m+2)^2 + 2), \end{aligned} \quad (\text{A.21})$$

where $|\cdot|$ stands for the cardinality of the set. Using the inequality (A.21), we can bound the right-hand side of (A.18) as

$$\begin{aligned} \sum_{\substack{\mathbf{m} \in \mathbb{Z}^3 \\ \mathbf{m} \neq \mathbf{0}}} \frac{\sqrt{N}}{\|\mathbf{q}/n + \mathbf{m}\|_1^{q+1}} &\leq \sum_{m=1}^{+\infty} \frac{\sqrt{N}|S_{\mathbf{q}}^m|}{m^{q+1}} \\ &\leq \sum_{m=1}^{+\infty} \frac{5\sqrt{N}(4(m+2)^2+2)}{m^{q+1}}, \end{aligned} \quad (\text{A.22})$$

which is a convergent series when $q \geq 3$. This completes the proof. \square

A.3.2 Proof of Theorem 3.5.1

From the Fourier-convolution theorem, we have that

$$\begin{aligned} (g_t * v)(\mathbf{x}) &= \int_{\Omega} g_t(\mathbf{x} - \mathbf{z})v(\mathbf{z}) \, d\mathbf{z} \\ &= \frac{1}{(2\pi)^3} \int_{\mathbb{R}^3} \widehat{g}_t(\boldsymbol{\omega})\widehat{v}(\boldsymbol{\omega})e^{j\boldsymbol{\omega}^T \mathbf{x}} \, d\boldsymbol{\omega}. \end{aligned} \quad (\text{A.23})$$

Let $n \in 2\mathbb{N} \setminus \{0\}$ and $h = L/n$ be the spatial sampling step of the volume Ω in each dimension. It follows that the frequency domain that is associated to the DFT is $\widehat{\Omega} = [-\pi/h, \pi/h]^3$. Then, the padding factor $p \in \mathbb{N}_{>0}$ enlarges the spatial domain to $[-pL/2, pL/2]^3$, resulting in the frequency sampling step $\delta = 2\pi/(hnp) = 2\pi/(Lp)$, so that $\widehat{\Omega}$ is sampled using np equally spaced points in each dimension.

We are now equipped to discretize the integral in (A.23). To that end, we use a trapezoidal quadrature rule on $\widehat{\Omega}$ and write that

$$(g_t * v)(\mathbf{x}) \approx \frac{\delta^3}{(2\pi)^3} \sum_{\mathbf{q} \in [-\frac{np}{2}; \frac{np}{2}]^3} w_{\mathbf{q}} \widehat{g}_t(\delta\mathbf{q}) \widehat{v}(\delta\mathbf{q}) e^{j\delta\mathbf{q}^T \mathbf{x}}. \quad (\text{A.24})$$

There, the weights $w_{\mathbf{q}}$ are equal to 1, 1/2, 1/4, and 1/8 when \mathbf{q} belongs to the interior, the interior of the faces, the interior of the edges, and the corners of the cube $[-\frac{np}{2}; \frac{np}{2}]^3$, respectively.

The approximation we made in (A.24) generates two error terms.

1. The error ε^{tp} that is due to the trapezoidal quadrature rule used to approximate the integral over the domain $\widehat{\Omega}$. This error is well documented in the literature [291]. For integrand that are twice differentiable, such as $\boldsymbol{\omega} \mapsto \widehat{g}_t(\boldsymbol{\omega})\widehat{v}(\boldsymbol{\omega})e^{j\boldsymbol{\omega}^T \mathbf{x}}$, we have that

$$|\varepsilon^{\text{tp}}| \leq C\delta^2 = C \left(\frac{2\pi}{Lp} \right)^2 \quad (\text{A.25})$$

for a positive constant $C > 0$.

2. The error ε^{tr} that is due to the truncation of the integral in (A.23) to the domain $\widehat{\Omega}$, bounded as

$$\begin{aligned} |\varepsilon^{\text{tr}}| &= \frac{1}{(2\pi)^3} \left| \int_{\mathbb{R}^3 \setminus \widehat{\Omega}} \widehat{g}_t(\boldsymbol{\omega})\widehat{v}(\boldsymbol{\omega})e^{j\boldsymbol{\omega}^T \mathbf{x}} d\boldsymbol{\omega} \right| \\ &\leq \frac{1}{(2\pi)^3} \int_{\mathbb{R}^3 \setminus \widehat{\Omega}} \left| \widehat{g}_t(\boldsymbol{\omega})\widehat{v}(\boldsymbol{\omega})e^{j\boldsymbol{\omega}^T \mathbf{x}} \right| d\boldsymbol{\omega} \\ &\leq \frac{C}{(2\pi)^3} \int_{\mathbb{R}^3 \setminus \widehat{\Omega}} \frac{2}{(\|\boldsymbol{\omega}\| - k_b)\|\boldsymbol{\omega}\|^{q+2}} d\boldsymbol{\omega}, \end{aligned} \quad (\text{A.26})$$

for a constant $C > 0$.

The last inequality in (A.26) has been established in two steps. First, the assumption that $k_b < \pi/h$ implies that $\forall \boldsymbol{\omega} \in \mathbb{R}^3 \setminus \widehat{\Omega}$, $\|\boldsymbol{\omega}\| > k_b$. Then, one gets from (3.6) that, $\forall \boldsymbol{\omega} \in \mathbb{R}^3 \setminus \widehat{\Omega}$,

$$|\widehat{g}_t(\boldsymbol{\omega})| \leq \frac{2}{(\|\boldsymbol{\omega}\| - k_b)\|\boldsymbol{\omega}\|}. \quad (\text{A.27})$$

Second, Lemma A.3.1, along with the fact that v has $(q-1)$ continuous derivatives with a q th derivative of bounded variations, implies that its Fourier transform decays as

$$|\widehat{v}(\boldsymbol{\omega})| \leq \frac{C}{\|\boldsymbol{\omega}\|^{q+1}} \quad (\text{A.28})$$

for a constant $C > 0$. Combining these two bounds with $|e^{j\boldsymbol{\omega}^T \mathbf{x}}| = 1$ finally leads to (A.26).

A further refinement of the bound (A.26) is needed to recover the statement of Theorem 3.5.1. Denoting by $\mathcal{B}_{\pi/h}^2 = \{\boldsymbol{\omega} \in \mathbb{R}^3 : \|\boldsymbol{\omega}\| \leq \pi/h\}$ the ℓ_2 -ball of radius π/h , one sees that the integral in (A.26) is upper-bounded by the integration of the same integrand over the larger domain $\mathbb{R}^3 \setminus \mathcal{B}_{\pi/h}^2$. This bound is easier to evaluate using spherical coordinates, as in

$$\begin{aligned} |\varepsilon^{\text{tr}}| &\leq \frac{2C}{(2\pi)^3} \int_{\mathbb{R}^3 \setminus \mathcal{B}_{\pi/h}^2} \frac{1}{(\|\boldsymbol{\omega}\| - k_b)\|\boldsymbol{\omega}\|^{q+2}} d\boldsymbol{\omega} \\ &= \frac{2C}{(2\pi)^3} \int_0^{2\pi} \int_0^\pi \int_{\pi/h}^{+\infty} \frac{r^2 \sin(\theta)}{(r - k_b)r^{q+2}} dr d\theta d\phi \\ &= \frac{C}{\pi^2} \int_{\pi/h}^{+\infty} \frac{1}{(r - k_b)r^q} dr. \end{aligned} \tag{A.29}$$

To evaluate (A.29), we use the partial fraction decomposition

$$\frac{1}{(r - k_b)r^q} = \frac{1}{k_b^q(r - k_b)} - \sum_{m=0}^{q-1} \frac{1}{k_b^{q-m}r^{m+1}}. \tag{A.30}$$

Hence, we have that

$$\begin{aligned} |\varepsilon^{\text{tr}}| &\leq \frac{C}{\pi^2} \left(\frac{1}{k_b^q} \log(r - k_b) \Big|_{r=\frac{\pi}{h}}^{+\infty} - \frac{1}{k_b^q} \log(r) \Big|_{r=\frac{\pi}{h}}^{+\infty} \right. \\ &\quad \left. - \sum_{m=1}^{q-1} \frac{1}{k_b^{q-m}} \left(-\frac{1}{mr^m} \right) \Big|_{r=\frac{\pi}{h}}^{+\infty} \right) \\ &= \frac{-C}{k_b^q \pi^2} \left(\log \left(1 - \frac{k_b h}{\pi} \right) + \sum_{m=1}^{q-1} \frac{1}{m} \left(\frac{k_b h}{\pi} \right)^m \right) \end{aligned} \tag{A.31}$$

$$= \frac{C}{k_b^q \pi^2} \sum_{m=q}^{+\infty} \frac{1}{m} \left(\frac{k_b h}{\pi} \right)^m \tag{A.32}$$

$$= \frac{C}{k_b^q \pi^2} \left(\frac{k_b h}{\pi} \right)^q \sum_{m=0}^{+\infty} \left(\frac{k_b h}{\pi} \right)^m \frac{1}{m+q}. \tag{A.33}$$

To obtain (A.32) from (A.31), we used the fact that $k_b h/\pi < 1$ together with $\log(1-x) = (-\sum_{m=1}^{+\infty} x^m/m)$ for $|x| < 1$. Finally, we get the bound C^{tr}/n^q from the convergence of the series in (A.33) and $h = L/n$.

Let us focus on aliasing. As opposed to \widehat{g}_t for which we have access to an explicit expression in (3.6)–(3.7), the samples $\hat{v}(\delta\mathbf{q})$ in (A.24) have to be approximated by the DFT coefficients of a p -times zero-padded version of the sampled signal $\mathbf{v} \in \mathbb{C}^N$, denoted $\mathbf{v}_p \in \mathbb{C}^{Np^3}$, and defined by, $\forall \mathbf{k} \in \llbracket \frac{-np}{2} + 1; \frac{np}{2} \rrbracket^3$,

$$\mathbf{v}_p[\mathbf{k}] = \begin{cases} \mathbf{v}[\mathbf{k}] = v(h\mathbf{k}), & \mathbf{k} \in \llbracket \frac{-n}{2} + 1; \frac{n}{2} \rrbracket^3 \\ 0, & \text{otherwise.} \end{cases} \quad (\text{A.34})$$

We then replace $\hat{v}(\delta\mathbf{q})$ in (A.24) by $h^3 \widehat{\mathbf{v}}_p[\mathbf{q}]$ and obtain that

$$(g_t * v)(\mathbf{x}) \approx \frac{1}{(np)^3} \sum_{\mathbf{q} \in \llbracket \frac{-np}{2}; \frac{np}{2} \rrbracket^3} w_{\mathbf{q}} \widehat{g}_t(\delta\mathbf{q}) \widehat{\mathbf{v}}_p[\mathbf{q}] e^{j\delta\mathbf{q}^T \mathbf{x}}. \quad (\text{A.35})$$

This approximation introduces an error term ε^{al} that is due to aliasing. More precisely, we have that

$$\begin{aligned} |\varepsilon^{\text{al}}| &\leq \frac{\delta^3}{(2\pi)^3} \sum_{\mathbf{q} \in \llbracket \frac{-np}{2}; \frac{np}{2} \rrbracket^3} w_{\mathbf{q}} |\widehat{g}_t(\delta\mathbf{q})| |\hat{v}(\delta\mathbf{q}) - h^3 \widehat{\mathbf{v}}_p[\mathbf{q}]| \\ &\leq \frac{\delta^3}{(2\pi)^3} \sum_{\mathbf{q} \in \llbracket \frac{-np}{2}; \frac{np}{2} \rrbracket^3} w_{\mathbf{q}} |\widehat{g}_t(\delta\mathbf{q})| Ch^{q+1} \end{aligned} \quad (\text{A.36})$$

$$\begin{aligned} &\leq \frac{\delta^3 Ch^{q+1}}{(2\pi)^3} (np)^3 \|\widehat{g}_t\|_{\infty} \\ &= C \|\widehat{g}_t\|_{\infty} h^{q-2} = \frac{C \|\widehat{g}_t\|_{\infty} L^{q-2}}{n^{q-2}}, \end{aligned} \quad (\text{A.37})$$

where (A.36) comes from Lemma A.3.2.

To complete the proof, it remains to recognize an inverse DFT within (A.35). Let $\{\mathbf{q}_i\}_{i=1}^8$ denotes the eight corners of the cube $\llbracket \frac{-np}{2}; \frac{np}{2} \rrbracket^3$. Then, because \widehat{g}_t is radially symmetric (see (3.6) and (3.7)), and by periodicity of $\widehat{\mathbf{v}}_p$, we have that

$$\widehat{g}_t(\delta\mathbf{q}_i) \widehat{\mathbf{v}}_p[\mathbf{q}_i] = \widehat{g}_t(\delta\mathbf{q}_1) \widehat{\mathbf{v}}_p[\mathbf{q}_1], \quad \forall i \in \{2, \dots, 8\}. \quad (\text{A.38})$$

Hence we can factorize the corresponding terms in (A.35) as

$$\sum_{\mathbf{q} \in \{\mathbf{q}_i\}_{i=1}^8} \frac{1}{8} \widehat{g}_t(\delta \mathbf{q}_i) \widehat{\mathbf{v}}_p[\mathbf{q}_i] = \widehat{g}_t(\delta \mathbf{q}_1) \widehat{\mathbf{v}}_p[\mathbf{q}_1]. \quad (\text{A.39})$$

Finally, using the same arguments for points within the faces and edges of the cube $\llbracket \frac{-np}{2}; \frac{np}{2} \rrbracket^3$, and sampling (A.35) at points $h\mathbf{k}$, $\mathbf{k} \in \llbracket \frac{-n}{2} + 1; \frac{n}{2} \rrbracket^3$, we obtain that

$$(\mathbf{G}\mathbf{v})[\mathbf{k}] = \frac{1}{(np)^3} \sum_{\mathbf{q} \in \llbracket \frac{-np}{2} + 1; \frac{np}{2} \rrbracket^3} \widehat{\mathbf{g}}_t[\mathbf{q}] \widehat{\mathbf{v}}_p[\mathbf{q}] e^{\frac{2i\pi}{np} \mathbf{q}^T \mathbf{k}}, \quad (\text{A.40})$$

where $\widehat{\mathbf{g}}_t = (\widehat{g}_t(\delta \mathbf{q}))_{\mathbf{q} \in \llbracket \frac{-np}{2} + 1; \frac{np}{2} \rrbracket^3}$. We recognize an inverse DFT, which completes the proof.

A.3.3 Proof of Proposition 3.6.1

First, let us introduce the notation $\Omega_n = \llbracket \frac{-n}{2} + 1; \frac{n}{2} \rrbracket^3$. Then, we have that, for all $\mathbf{k} \in \Omega_n$,

$$\begin{aligned} & (\mathbf{F}^{-1}(\widehat{\mathbf{g}}_t \odot \widehat{\mathbf{v}}_p))[\mathbf{k}] \\ &= \frac{1}{(np)^3} \sum_{\mathbf{q} \in \Omega_{np}} \widehat{\mathbf{g}}_t[\mathbf{q}] \widehat{\mathbf{v}}_p[\mathbf{q}] e^{\frac{2i\pi}{np} \mathbf{q}^T \mathbf{k}} \\ &= \frac{1}{(np)^3} \sum_{\mathbf{q} \in \Omega_{np}} \widehat{\mathbf{g}}_t[\mathbf{q}] \sum_{\tilde{\mathbf{q}} \in \Omega_{np}} \mathbf{v}_p[\tilde{\mathbf{q}}] e^{\frac{-2i\pi}{np} \tilde{\mathbf{q}}^T \mathbf{q}} e^{\frac{2i\pi}{np} \mathbf{q}^T \mathbf{k}} \\ &= \frac{1}{(np)^3} \sum_{\tilde{\mathbf{q}} \in \Omega_{2n}} \mathbf{v}_2[\tilde{\mathbf{q}}] \sum_{\mathbf{q} \in \Omega_{np}} \widehat{\mathbf{g}}_t[\mathbf{q}] e^{\frac{2i\pi}{np} (\mathbf{k} - \tilde{\mathbf{q}})^T \mathbf{q}} \\ &= \frac{1}{(np)^3} \sum_{\tilde{\mathbf{q}} \in \Omega_{2n}} \mathbf{v}_2[\tilde{\mathbf{q}}] \sum_{\substack{\mathbf{s} \in \llbracket 0; \frac{p}{2} - 1 \rrbracket^3 \\ \mathbf{q} \in \Omega_{2n}}} \widehat{\mathbf{g}}_t[\frac{p}{2} \mathbf{q} - \mathbf{s}] e^{\frac{2i\pi}{np} (\mathbf{k} - \tilde{\mathbf{q}})^T (\frac{p}{2} \mathbf{q} - \mathbf{s})} \\ &= \frac{8}{p^3} \sum_{\tilde{\mathbf{q}} \in \Omega_{2n}} \mathbf{v}_2[\tilde{\mathbf{q}}] \sum_{\mathbf{s} \in \llbracket 0; \frac{p}{2} - 1 \rrbracket^3} \mathbf{F}^{-1}(\widehat{\mathbf{g}}_t[\frac{p}{2} \cdot - \mathbf{s}])[\mathbf{k} - \tilde{\mathbf{q}}] e^{\frac{-2i\pi}{np} (\mathbf{k} - \tilde{\mathbf{q}})^T \mathbf{s}} \end{aligned} \quad (\text{A.41})$$

where we have used the fact that $\text{supp}(\mathbf{v}_p) = \text{supp}(\mathbf{v}) \subseteq \Omega_n \subseteq \Omega_{2n}$. Hence, we have shown that $(\mathbf{F}^{-1}(\widehat{\mathbf{g}}_t \odot \widehat{\mathbf{v}}_p))|_{\Omega_n}$ can be obtained as the valid part of the

discrete convolution between \mathbf{v}_2 , defined as \mathbf{v} padded with $p = 2$, and a modified truncated Green function given by, $\forall \mathbf{k} \in \Omega_{2n}$,

$$\mathbf{g}_t^p[\mathbf{k}] = \frac{8}{p^3} \sum_{\mathbf{s} \in [0; \frac{p}{2} - 1]^3} \mathbf{F}^{-1}(\widehat{\mathbf{g}}_t[\frac{p}{2} \cdot - \mathbf{s}])[\mathbf{k}] e^{\frac{-2i\pi}{np} \mathbf{k}^T \mathbf{s}}, \quad (\text{A.42})$$

which completes the proof.

A.4 Experimental Setup

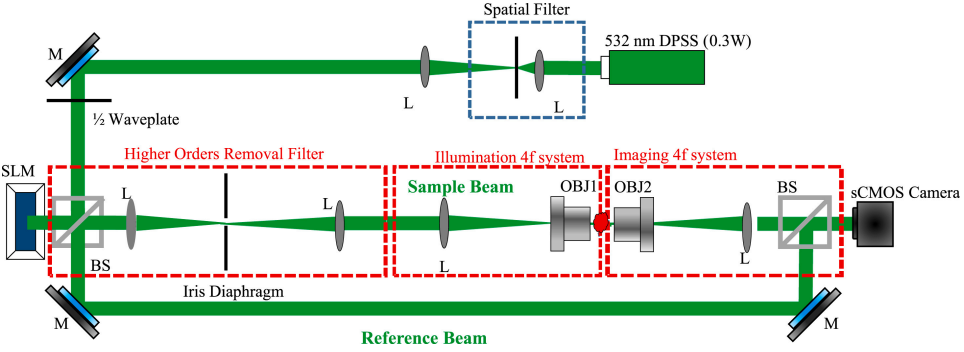


Figure A.1: Experimental tomographic setup. (M: Mirror, L: Lens, OBJ: Objective lens, BS: Beam splitter). Pinhole-based spatial filter cleans out the beam spatially. The higher-orders cleaning filter removes the unneeded higher orders, which prevents interference at the image plane on the sample and image deterioration.

The optical system shown in Fig. A.1 used a diode pumped solid state (DPSS) 532nm laser. The laser beam was first spatially filtered using a pinhole. A beam-splitter separated the input beam into a signal and a reference beam in an off-axis geometry. The signal beam was directed to the sample at different angles of incidence using a reflective liquid crystal on silicon (LCOS) SLM (Holoeye PLUTO VIS, pixel size: 8 μm , resolution: 1080 \times 1920 pixels) that modulates the phase of

the incident beam. Different illumination angles were obtained by displaying blazed gratings on the SLM. In the experiments presented here, a blazed grating with a period of 25 pixels ($200\ \mu\text{m}$) was rotated a full 360° with a resolution of 1 degree for a total of 361 projections, including normal incidence to be able to measure the shift of the k -vectors with respect to it. Two 4f systems between the SLM and the sample permitted filtering of higher orders reflected from the SLM (due to the pixilation of the device) as well as 240x angular magnification of the SLM projections onto the sample. Using a 100X oil immersion objective lens (OBJ1) with NA 1.4 (Olympus), the incident angle on the sample corresponding to the $200\ \mu\text{m}$ grating was about 37° . A third 4f system after the sample includes a 100X oil immersion objective lens (OBJ2) with NA 1.45 (Olympus). The sample and reference beams were collected on a second beam-splitter and projected onto a scientific complementary metal-oxide-semiconductor (sCMOS) camera (Andor Neo 5.5 sCMOS, pixel size: $6.5\ \mu\text{m}$, resolution: 2150×2650 pixels).

A.5 Supplementary Materials for Chapter 7

A.5.1 Architecture of the Generative Network

We choose a U-Net-like architecture based on the work of deep image prior [218] (Figure. A.2). It consists of repeated applications of four blocks of operations.

1. A (3×3) 2D convolutional layer with stride (2×2) for downsampling followed by a batch normalization (BN) [292] layer and a parametric rectified linear unit (PReLU) [225] layer.
2. A (3×3) 2D convolutional layer with stride (1×1) followed by a BN and a PReLU layer.
3. A (2×2) bilinear interpolation layer for upsampling followed by a BN layer.
4. A skip connection which contains a (1×1) 2D convolutional layer that concatenates the left-side encoder path to the right-side decoder path.

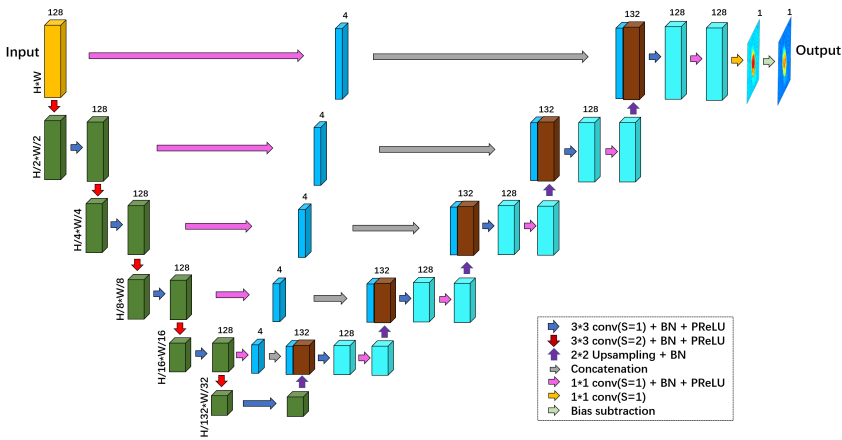


Figure A.2: Architecture of the network. Each box corresponds to a multichannel feature map. The number of channels is shown at the top of the cube. The height of the output is as same as that of the input. The size of the single-channel feature map is halved after the downsampling and doubled after the upsampling. The skip connections combine convolution and concatenation, which differs from a traditional U-Net [224].

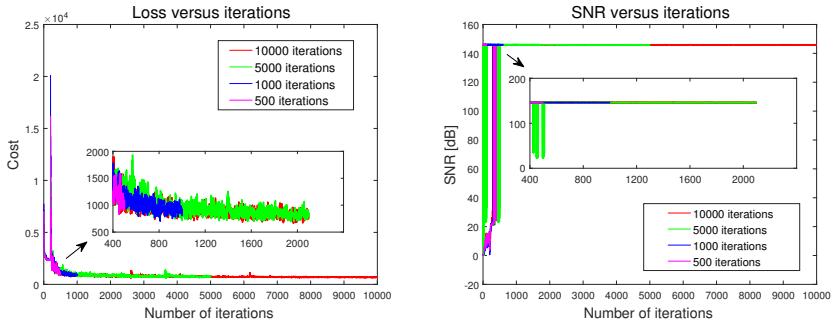


Figure A.3: Loss function (left) and SNR (right) with respect to iterations.

A.5.2 Stability of PUDIP

Deep image prior (DIP) is known to be unstable when a large number of iterations is used [218]. Our method can be seen as a sequence of DIPs with an adaptive loss. We then assessed whether our method suffers from such a destabilization. As shown in Fig. A.3, for the simulated data with 180° cropped angle, PUDIP shows a stable and converging cost and SNR with respect to the iterations. This allows us to set an arbitrary maximum number of iterations without risking any destabilization.

A.5.3 Training Dataset of PhaseNet

Samples of training data for PhaseNet [211] are shown in Figure. A.4.

A.5.4 Simulation Setup

Simulation of Phase Images of Organoid-like Sample

We simulated the acquisition of phase images of organoid-like samples. We first created 3D volumes made of overlapping ellipsoids of uniform RI n_1 , to which we added an external layer of RI n_2 . Then, we simulated the propagation of a plane wave through the sample by using BPM [43]. We propagated the wave with a square voxel of length $0.2\mu\text{m}$ in a square window of length $102.4\mu\text{m}$. We refocused the complex total field at the center of the volume (*i.e.*, free-space propagation). We

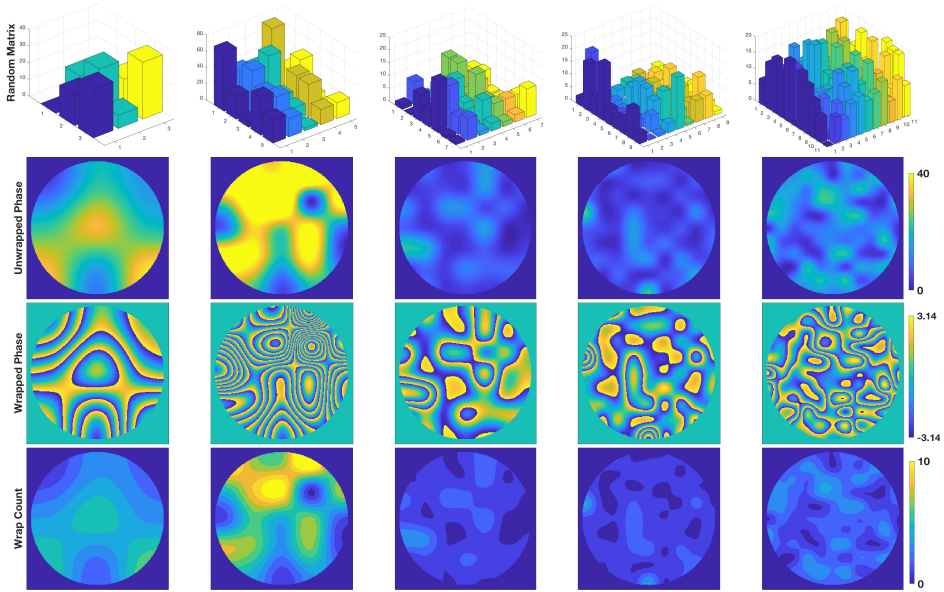


Figure A.4: Uniformly and Gaussian-distributed random square matrices (first row) and the corresponding unwrapped-phase images (second row), wrapped-phase images (third row), and the wrap-count images (last row). For training, the wrapped-phase images are the inputs and the wrap-count images are the ground-truths. From left to right, the size of the random matrix is (3×3) , (5×5) , (7×7) , (9×9) , and (11×11) . The unwrapped-phase images vary in the range 0 to 40π . The image size is (256×256) .

then downsampled the field to match the pixel size of the camera (*i.e.*, $0.645\mu\text{m}$). Finally, we extracted the (wrapped) phase from the ratio between the total field and the incident field. The straight-ray approximation Φ_{sr} the expected phase [35] as

$$\Phi_{\text{sr}} = \frac{2\pi}{\lambda} \int_{-\infty}^{\infty} (\eta(x_1, x_2, x_3) - \eta_b) dx_3, \quad (\text{A.43})$$

where $\eta(x_1, x_2, x_3) : \mathbb{R}^3 \rightarrow \mathbb{R}$ is the distribution of RI of the 3D volume, and $n_m > 0$ is the RI of the medium (*i.e.*, water).

Ellipses with Varying Cropping Angles

As shown in Figure. A.7, we first simulated one phase surface with the shape of an ellipse of radii 80 pixels and 110 pixels along the vertical and horizontal dimensions, respectively. The ellipse was filled with a Gaussian function whose maximum is 15 and standard deviation is randomly generated $\sigma \sim U(0.30, 0.65)$. The area outside the ellipse was set to 0. We select the horizontal left-to-right direction as the x-axis and set the coordinate axes to be left-handed. The ellipse was cropped with angles ranging from 0° to 270° with an increment of 45° . Similar to [188, 192], these croppings introduce a variety of discontinuities and shapes.

Ellipses with Varying Maximum Phase Values

For this numerical experiment (Figure. A.8), we generated elliptical phase surfaces with radii 102 pixels and 120 pixels along the vertical and horizontal dimensions, respectively. The cropped part was kept constant, with an angle set at 135° . We scaled the phase so that its maximum was in the range of 6 to 42 with an increment of 6. For this case, the high values induce several wrapping events. By controlling their number, we could tune the difficulty of the unwrapping task.

A.5.5 Phase Unwrapping of Simulated Data

Supplementary Reconstructions of Organoid-like Samples

We simulated supplementary organoid-like samples and unwrapped their corresponding wrapped phase. As shown in Figure. A.5 and A.6, similar behaviors are

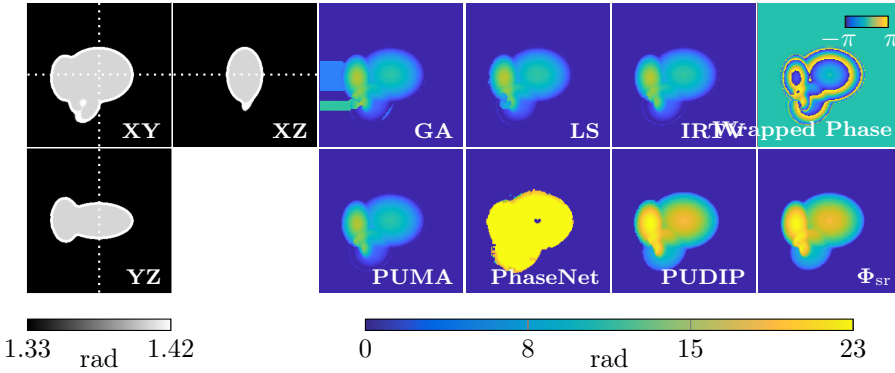


Figure A.5: Organoid-like reconstructions. The images were saturated for visualization purpose. The size of the unwrapped phase image is (159×159) . The first two columns are orthographic slices of the 3D distribution of RI. All slices include the center of the volume. From the third to fifth column, the text gives the method used to unwrap. The wrapped phase and the straight-ray approximation Φ_{sr} are displayed in the last column (from top to bottom).

observed. The slightly defocused parts are wrongly estimated by baseline methods, which impacts the whole unwrapping result. The phase unwrapped by PUDIP matches the straight-ray approximation Φ_{sr} .

Unwrapping of Ellipses with Varying Cropping Angles

The reconstructions obtained by different methods for the ellipses with varying cropping angles are shown in Figure. A.7. In this experiment, the cropping angle was gradually increased. All methods except PhaseNet are able to recover the correct unwrapped phase in the absence of cropping. When the phase image is cropped, all conventional methods lead to blocky errors, especially at large angles. For the 180° case only, PUMA [188] and the proposed method accurately unwrap the phase.

In general, CNN-based approaches perform better than the model-based meth-

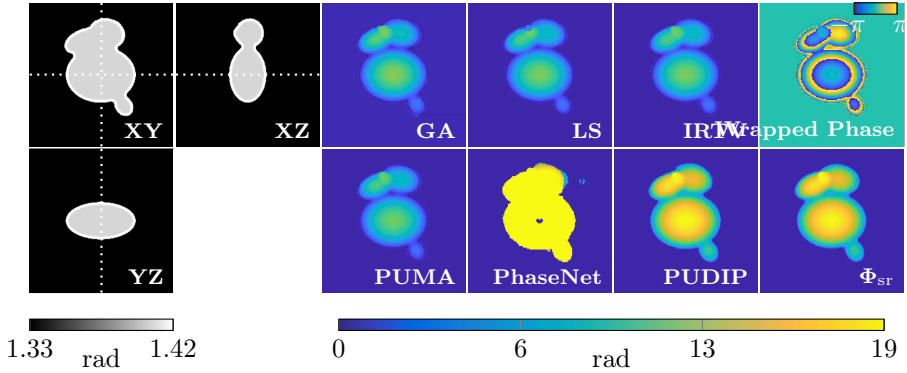


Figure A.6: Organoid-like reconstructions. The images were saturated for visualization purpose. The size of the unwrapped phase image is (159×159) . The first two columns are orthographic slices of the 3D distribution of RI. All slices include the center of the volume. From the third to fifth column, the text gives the method used to unwrap. The wrapped phase and the straight-ray approximation Φ_{sr} are displayed in the last column (from top to bottom).

ods. Both PhaseNet and PUDIP are able to reconstruct more accurate shapes and values, especially over the cropped region. For PhaseNet, we observe that the clustering-based postprocessing strongly improves the final results but still introduces undesirable values along the contours of clusters. By contrast, our method recovers well the samples in all cases, including the few over which PhaseNet fails.

Unwrapping of Ellipses with Varying Maximum Phase Values

We obtained similar results with the second experiment in which we increased the maximum value instead (Figure. A.8). When the height is low (first and second columns), IRTV [192] and PUMA perform well. When the height is higher, all the other baseline methods wrongly estimate large portions of the images.

PhaseNet always fails to recover the phase, which points out the sensitivity of this supervised-learning method to the mismatch between the training and testing

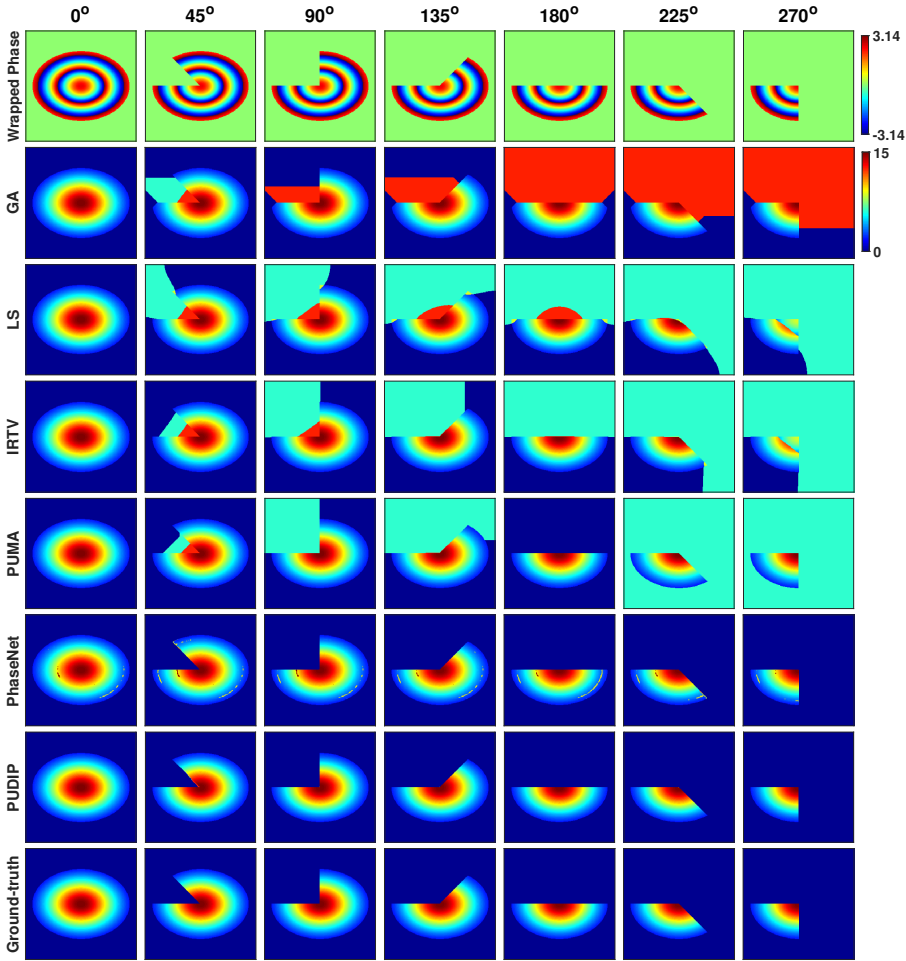


Figure A.7: Reconstructed unwrapped-phase images of simulated samples with diverse cropping angles. From top to bottom: wrapped phase, results obtained by GA, LS, IRTV, PUMA, PhaseNet, and our approach (PUDIP). The ground-truth images are presented in the last row.

set. On the contrary, our learning framework always unwraps the phase with few errors and without prior training.

Unwrapping of the Training Dataset of PhaseNet

As the samples are randomly generated, we simulated the samples from the training dataset of PhaseNet four times. In general, model-based methods fail to restore the correct background in most cases, as well as the inner structures for several samples (see second to fifth rows of Figures. A.9-A.12). By contrast, both PhaseNet and PUDIP yield better phase reconstructions for different configurations (see sixth to seventh rows of Figures. A.9-A.12).

A.5.6 Experimental Data

A.5.7 Reconstructions by Goldstein's Algorithm and PhaseNet

In Figure. A.13, GA [179] and PhaseNet failed to reconstruct the unwrapped phase for all real data. GA solutions exhibit several rectangular areas that cover both the background and the organoids. Their phase differs from their surrounding, which is inconsistent with the expected features of the sample. PhaseNet solutions similarly show jumps along vertical stripes and are likely to be artifacts of unwrapping. For PhaseNet, this behavior is expected since the network was trained on (mismatched) simulated data.

Supplementary Time-Lapse Measurements and Segmentations and Reconstructions by PhaseNet

We acquired other time-lapse measurements (Figures. A.14-A.16). We observe that the unwrapped phases exhibit similar artifacts at the borders of the organoids. The subsequent segmentation is also impacted, especially at the border, as pointed out by arrows. We provide the reconstructions by PhaseNet in Figure. A.17.

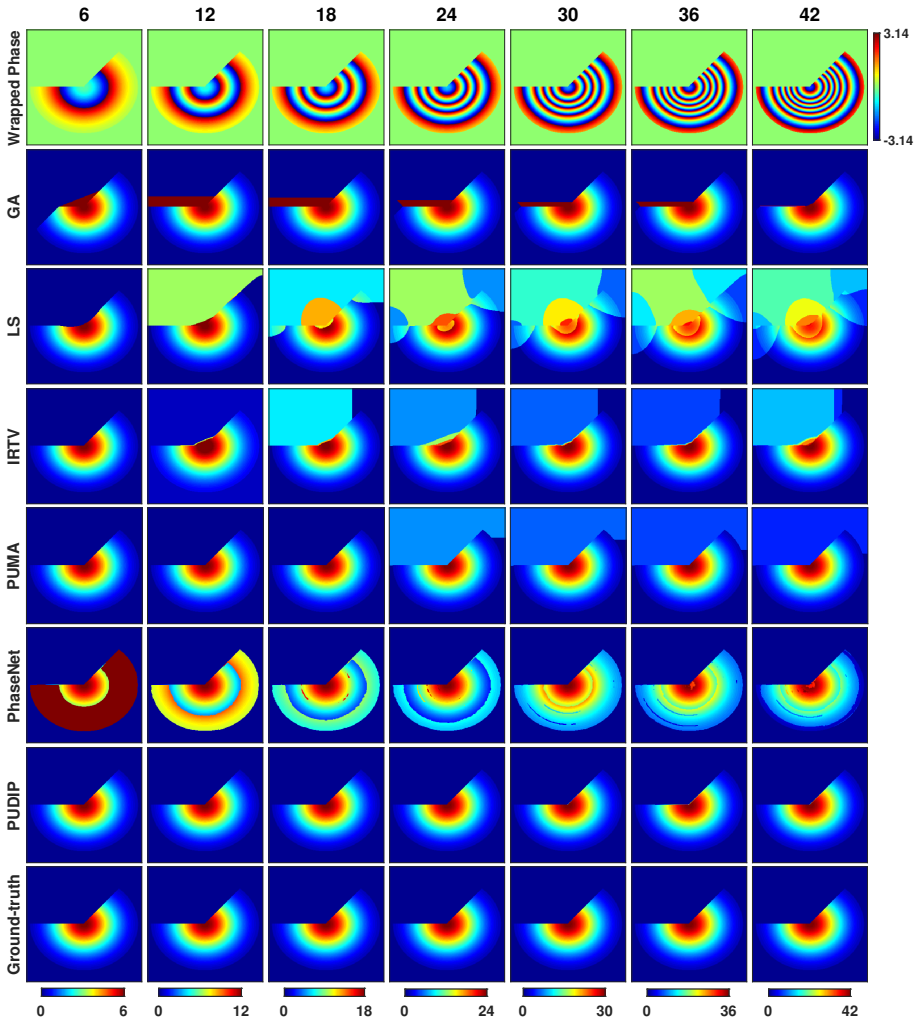


Figure A.8: Reconstructed unwrapped-phase images of simulated samples with diverse maximal values. From top to bottom: wrapped phase, results obtained by GA, LS, IRTV, PUMA, PhaseNet, and our approach (PUDIP). The ground-truth images are presented in the last row.

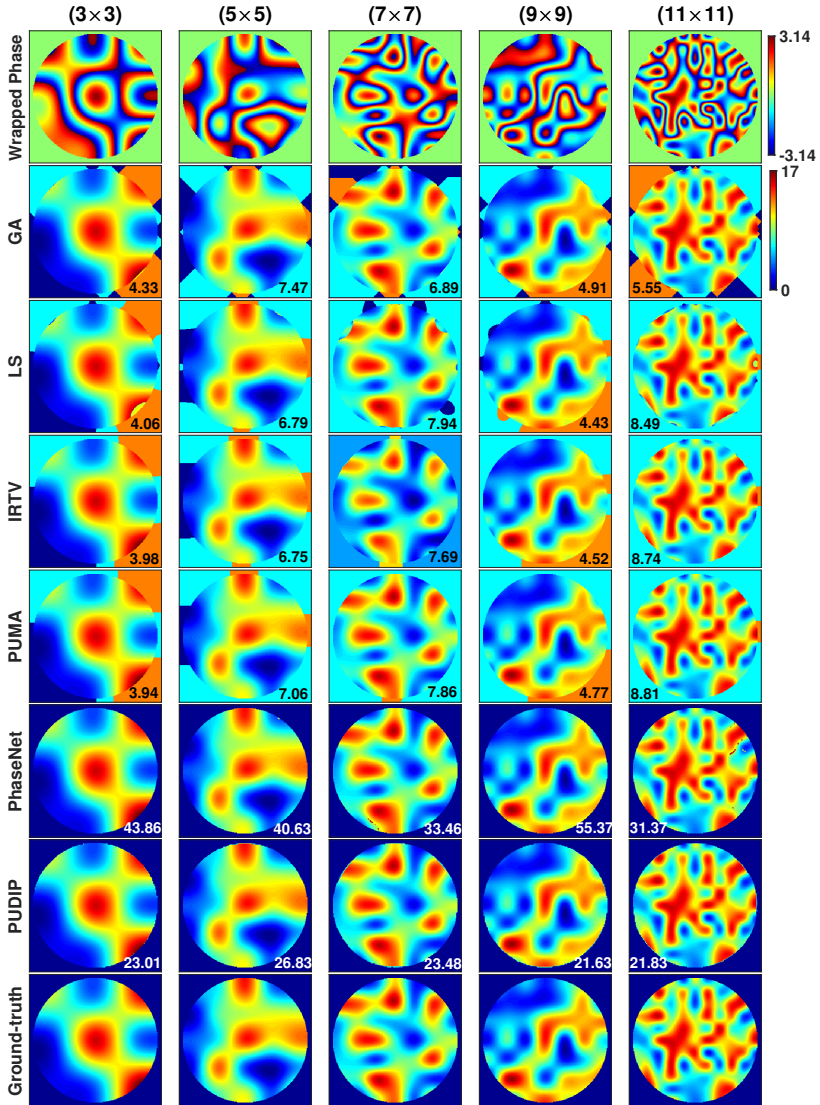


Figure A.9: Unwrapped-phase images of simulated samples with diverse random distributions (1st batch). From top to bottom: wrapped phase, results obtained by GA, LS, IRTV, PUMA, PhaseNet, and our approach (PUDIP). The ground-truth images are presented in the last row. The numbers give the corresponding RSNR [dB].

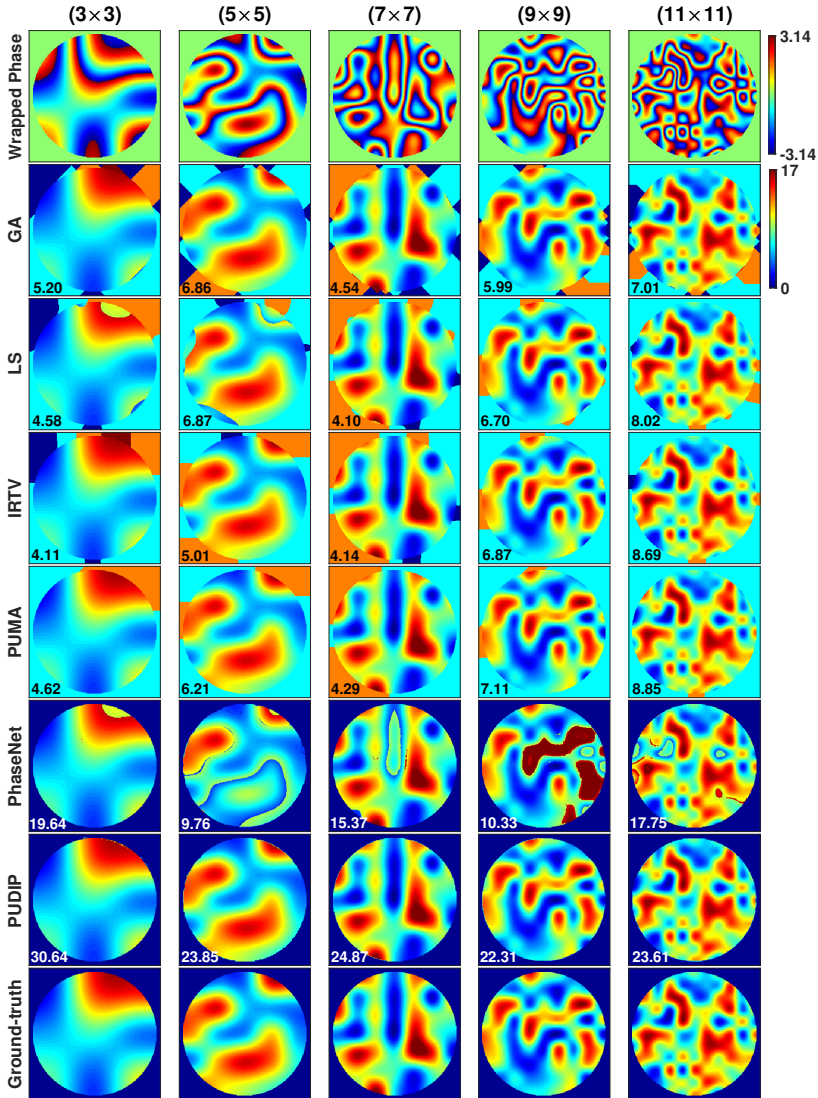


Figure A.10: Unwrapped-phase images of simulated samples with diverse random distributions (2nd batch). From top to bottom: wrapped phase, results obtained by GA, LS, IRTV, PUMA, PhaseNet, and our approach (PUDIP). The ground-truth images are presented in the last row. The numbers give the corresponding RSNR [dB].

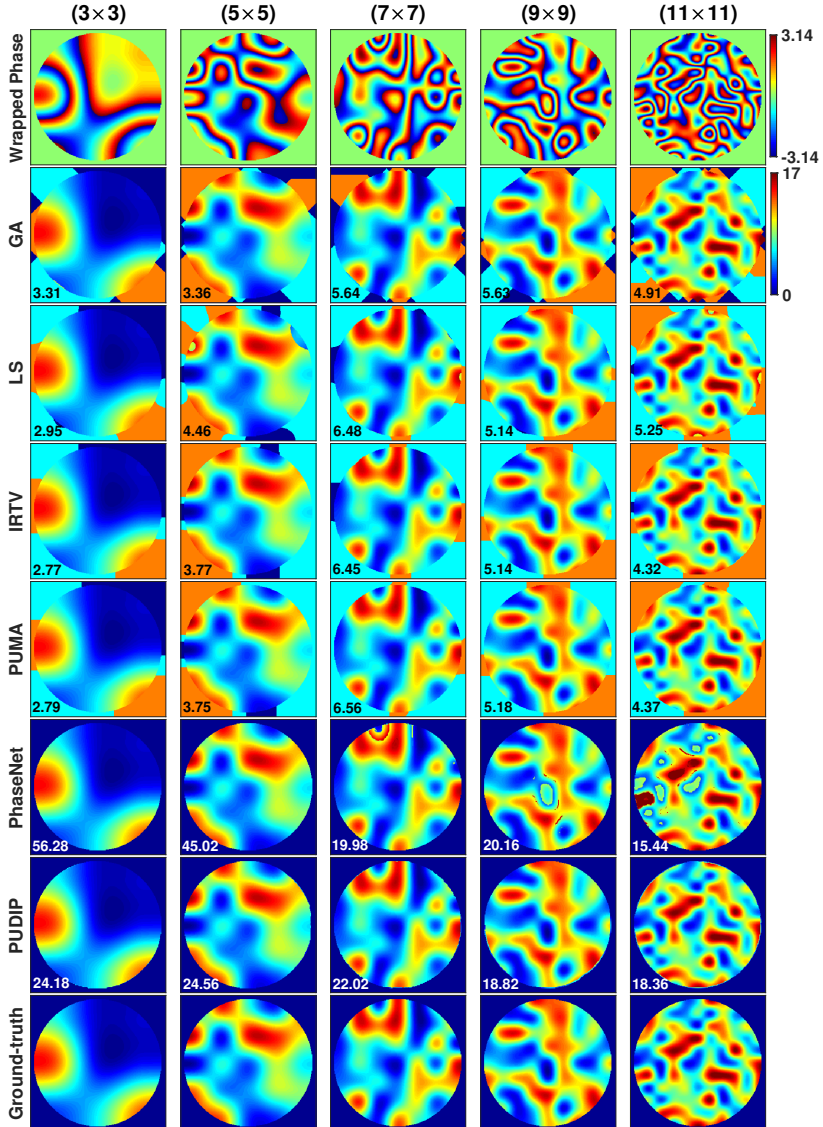


Figure A.11: Unwrapped-phase images of simulated samples with diverse random distributions (3rd batch). From top to bottom: wrapped phase, results obtained by GA, LS, IRTV, PUMA, PhaseNet, and our approach (PUDIP). The ground-truth images are presented in the last row. The numbers give the corresponding RSNR [dB].

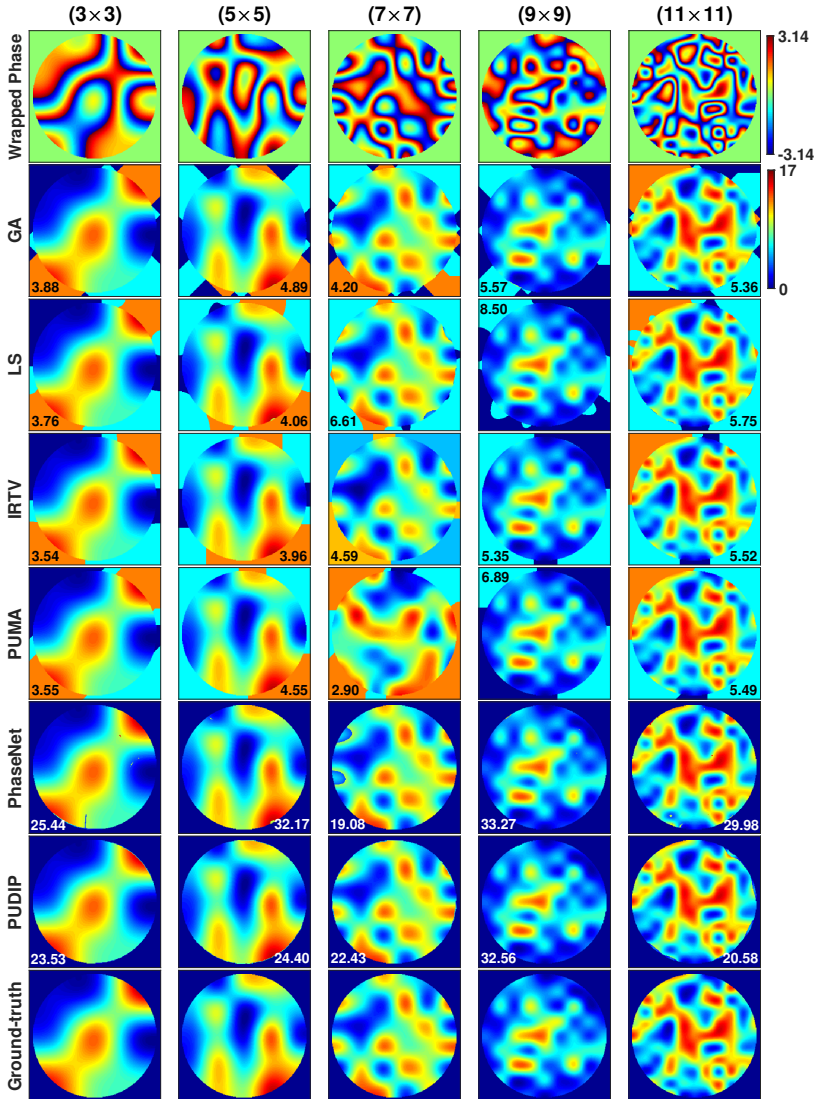


Figure A.12: Unwrapped-phase images of simulated samples with diverse random distributions (4th batch). From top to bottom: wrapped phase, results obtained by GA, LS, IRTV, PUMA, PhaseNet, and our approach (PUDIP). The ground-truth images are presented in the last row. The numbers give the corresponding RSNR [dB].

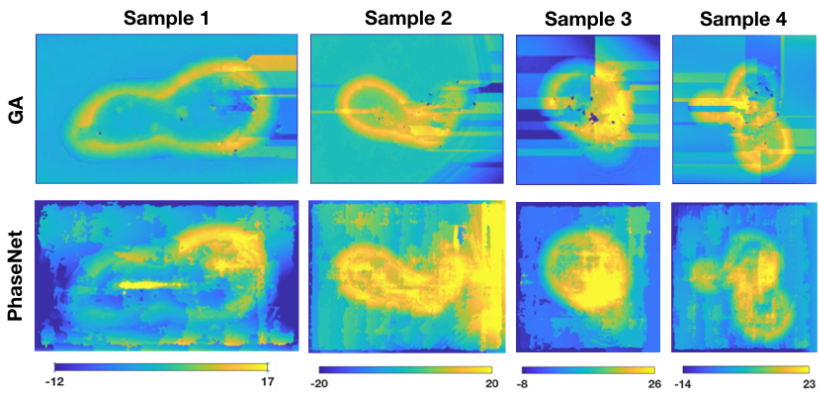


Figure A.13: Reconstructions of experimental data obtained by GA and PhaseNet.

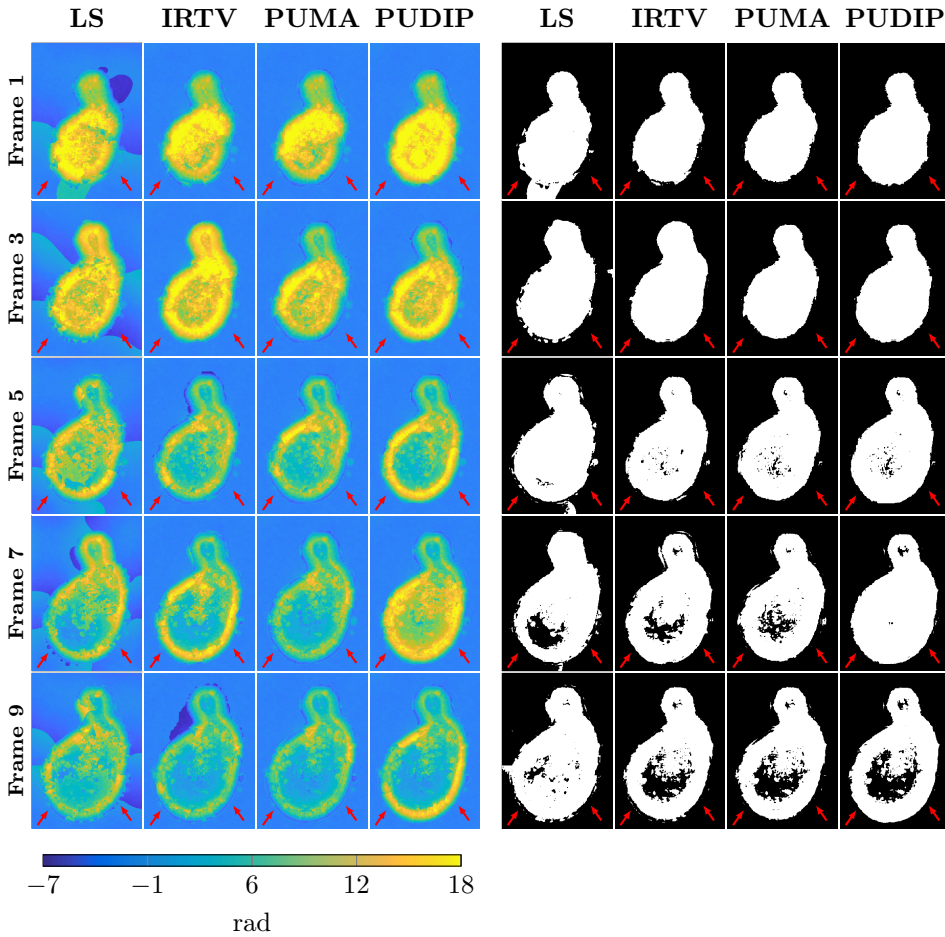


Figure A.14: Time-lapse reconstructions for supplementary real data of size (380×270) and their corresponding segmentation. Left: the images were saturated for visualization purpose. Right: segmentation of time-lapse reconstructions. We thresholded at 20% of the maximum value of the image.

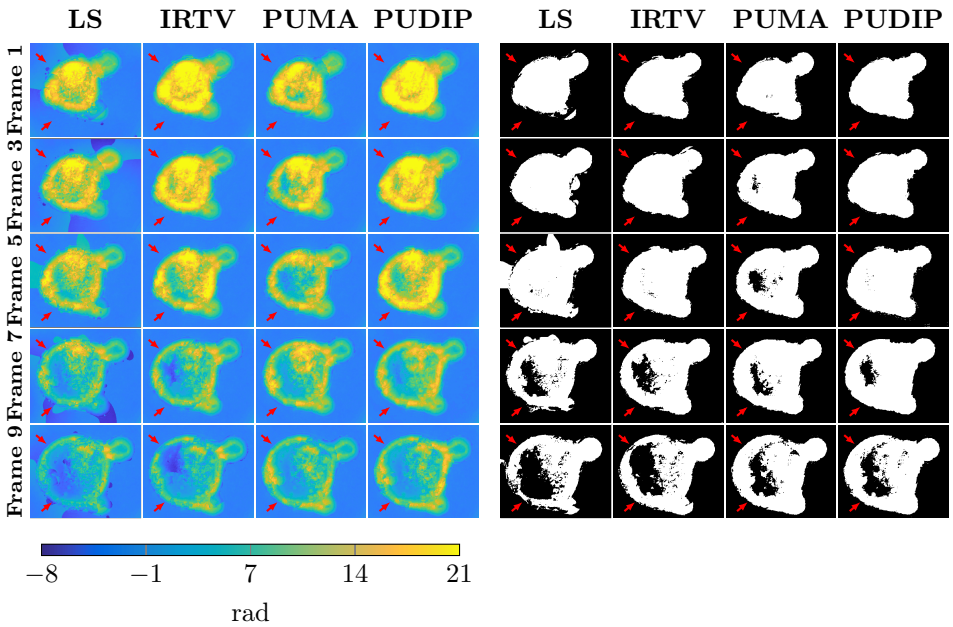


Figure A.15: Time-lapse reconstructions for supplementary real data of size (320×380) and their corresponding segmentation. Left: the images were saturated for visualization purpose. Right: segmentation of time-lapse reconstructions. We thresholded at 20% of the maximum value of the image.

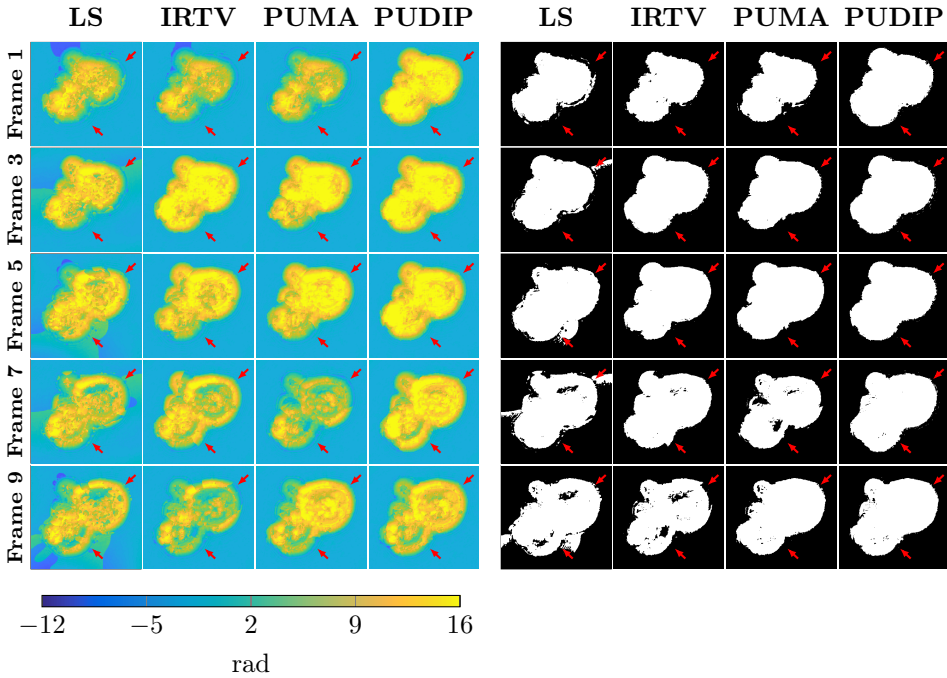


Figure A.16: Time-lapse reconstructions for supplementary real data of size (300×320) and their corresponding segmentation. Left: the images were saturated for visualization purpose. Right: segmentation of time-lapse reconstructions. We thresholded at 20% of the maximum value of the image.

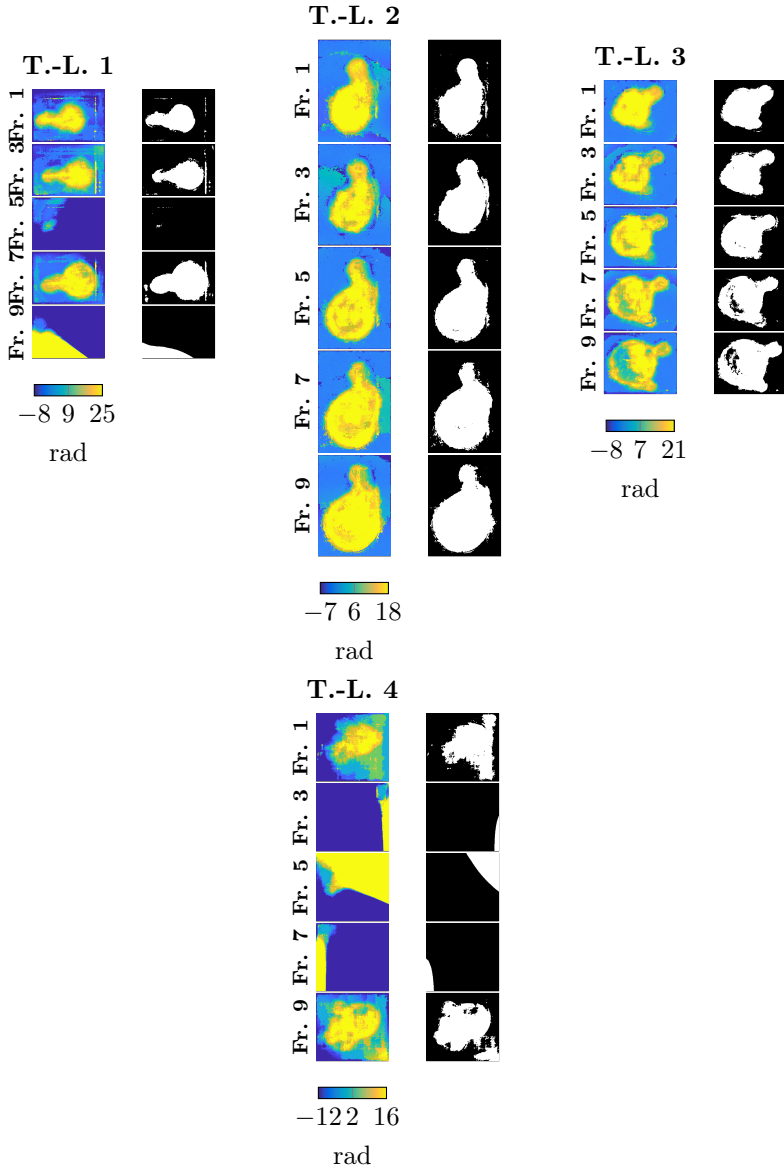


Figure A.17: Time-lapse reconstructions by PhaseNet for all real data and corresponding segmentation. For each panel of time-lapse measurements, Left: the images were saturated for visualization purpose. Right: segmentation of time-lapse reconstructions. We thresholded at 20% of the maximum value of the image. T.-L.: Time-Lapse; Fr.: Frame.

Bibliography

- [1] M. Zehni, L. Donati, E. Soubies, Z. Zhao, and M. Unser, “Joint angular refinement and reconstruction for single-particle cryo-em”, *IEEE transactions on image processing*, vol. 29, pp. 6151–6163, 2020. DOI: 10.1109/tip.2020.2984313.
- [2] C. Hu and G. Popescu, “Quantitative phase imaging (QPI) in neuroscience”, *IEEE journal of selected topics in quantum electronics*, vol. 25, no. 1, pp. 1–9, 2019. DOI: 10.1109/jstqe.2018.2869613.
- [3] F. Zernike, “Phase contrast, a new method for the microscopic observation of transparent objects”, *Physica*, vol. 9, no. 7, pp. 686–698, 1942. DOI: 10.1016/s0031-8914(42)80035-x.
- [4] Y. Park, C. Depeursinge, and G. Popescu, “Quantitative phase imaging in biomedicine”, *Nature photonics*, vol. 12, no. 10, pp. 578–589, 2018. DOI: 10.1038/s41566-018-0253-x.
- [5] C. Hu and G. Popescu, “Quantitative phase imaging: Principles and applications”, in *Label-free super-resolution microscopy*, V. Astratov, Ed., Cham: Springer International Publishing, 2019, pp. 1–24.
- [6] Y. Park, G. Popescu, K. Badizadegan, R. R. Dasari, and M. S. Feld, “Diffraction phase and fluorescence microscopy”, *Optics express*, vol. 14, no. 18, pp. 8263–8268, 2006. DOI: 10.1364/oe.14.008263.
- [7] L. Tian and L. Waller, “3D intensity and phase imaging from light field measurements in an LED array microscope”, *Optica*, vol. 2, no. 2, pp. 104–111, 2015. DOI: 10.1364/optica.2.000104.
- [8] R. Ling, W. Tahir, H.-Y. Lin, H. Lee, and L. Tian, “High-throughput intensity diffraction tomography with a computational microscope”, *Biomedical optics express*, vol. 9, no. 5, pp. 2130–2141, 2018. DOI: 10.1364/boe.9.002130.

-
- [9] S. Chowdhury, M. Chen, R. Eckert, D. Ren, F. Wu, N. Repina, and L. Waller, “High-resolution 3D refractive index microscopy of multiple-scattering samples from intensity images”, *Optica*, vol. 6, no. 9, pp. 1211–1219, 2019. DOI: 10.1364/optica.6.001211.
- [10] F. Charrière, A. Marian, F. Montfort, J. Kuehn, T. Colomb, E. Cuche, P. Marquet, and C. Depeursinge, “Cell refractive index tomography by digital holographic microscopy”, *Optics letters*, vol. 31, no. 2, pp. 178–180, 2006. DOI: 10.1364/ol.31.000178.
- [11] W. Choi, C. Fang-Yen, K. Badizadegan, S. Oh, N. Lue, R. R. Dasari, and M. S. Feld, “Tomographic phase microscopy”, *Nature methods*, vol. 4, no. 9, p. 717, 2007. DOI: 10.1038/nmeth1078.
- [12] E. Wolf, “Three-dimensional structure determination of semi-transparent objects from holographic data”, *Optics communications*, vol. 1, no. 4, pp. 153–156, 1969. DOI: 10.1016/0030-4018(69)90052-2.
- [13] A. Devaney, “Inverse-scattering theory within the Rytov approximation”, *Optics letters*, vol. 6, no. 8, pp. 374–376, 1981. DOI: 10.1364/ol.6.000374.
- [14] U. S. Kamilov, I. N. Papadopoulos, M. H. Shoreh, A. Goy, C. Vonesch, M. Unser, and D. Psaltis, “Optical tomographic image reconstruction based on beam propagation and sparse regularization”, *IEEE transactions on computational imaging*, vol. 2, no. 1, pp. 59–70, 2016. DOI: 10.1109/tci.2016.2519261.
- [15] U. S. Kamilov, D. Liu, H. Mansour, and P. T. Boufounos, “A recursive Born approach to nonlinear inverse scattering”, *IEEE signal processing letters*, vol. 23, no. 8, pp. 1052–1056, 2016. DOI: 10.1109/lsp.2016.2579647.
- [16] J. Lim, K. Lee, K. H. Jin, S. Shin, S. Lee, Y. Park, and J. C. Ye, “Comparative study of iterative reconstruction algorithms for missing cone problems in optical diffraction tomography”, *Optics express*, vol. 23, no. 13, pp. 16 933–16 948, 2015. DOI: 10.1364/oe.23.016933.
- [17] K. C. Zhou and R. Horstmeyer, “Diffraction tomography with a deep image prior”, *Optics express*, vol. 28, no. 9, pp. 12 872–12 896, 2020. DOI: 10.1364/oe.379200.
- [18] E. Soubies, T.-a. Pham, and M. Unser, “Efficient inversion of multiple-scattering model for optical diffraction tomography”, *Optics express*, vol. 25, no. 18, pp. 21 786–21 800, 2017. DOI: 10.1364/oe.25.021786.
- [19] T.-a. Pham, E. Soubies, A. Ayoub, J. Lim, D. Psaltis, and M. Unser, “Three-dimensional optical diffraction tomography with Lippmann-Schwinger model”, *IEEE transactions on computational imaging*, vol. 6, pp. 727–738, 2020. DOI: 10.1109/tci.2020.2969070.

- [20] T.-a. Pham, E. Soubies, A. Ayoub, D. Psaltis, and M. Unser, “Adaptive regularization for three-dimensional optical diffraction tomography”, in *Proceedings of the seventeenth IEEE international symposium on biomedical imaging (ISBI’20)*, Iowa City IA, USA, 2020, pp. 182–186.
- [21] F. Soulez, É. Thiébaud, A. Schutz, A. Ferrari, F. Courbin, and M. Unser, “Proximity operators for phase retrieval”, *Applied optics*, vol. 55, no. 26, pp. 7412–7421, 2016. DOI: 10.1364/ao.55.007412.
- [22] T.-a. Pham, E. Soubies, A. Goy, J. Lim, F. Soulez, D. Psaltis, and M. Unser, “Versatile reconstruction framework for diffraction tomography with intensity measurements and multiple scattering”, *Optics express*, vol. 26, no. 3, pp. 2749–2763, 2018. DOI: 10.1364/oe.26.002749.
- [23] T.-a. Pham, E. Soubies, J. Lim, A. Goy, F. Soulez, D. Psaltis, and M. Unser, “Phaseless diffraction tomography with regularized beam propagation”, in *Proceedings of the fifteenth IEEE international symposium on biomedical imaging: From nano to macro (ISBI’18)*, Washington DC, USA, 2018, pp. 1268–1271.
- [24] T.-a. Pham, E. Soubies, F. Soulez, and M. Unser, “Optical diffraction tomography from single-molecule localization microscopy”, *Optics communications*, vol. 499, p. 127 290, 2021. DOI: 10.1016/j.optcom.2021.127290.
- [25] —, “Diffraction tomography from single-molecule localization microscopy: Numerical feasibility”, *IEEE international symposium on biomedical imaging*, 2021.
- [26] F. Yang, T.-A. Pham, N. Brandenberg, M. P. Lutolf, J. Ma, and M. Unser, “Robust Phase Unwrapping via Deep Image Prior for Quantitative Phase Imaging”, *IEEE transactions on image processing*, vol. 30, pp. 7025–7037, 2021. DOI: 10.1109/tip.2021.3099956.
- [27] D. Sage, T.-a. Pham, H. Babcock, T. Lukes, T. Pengo, J. Chao, R. Velmurugan, A. Herbert, A. Agrawal, S. Colabrese, A. Wheeler, A. Archetti, B. Rieger, R. Ober, G. M. Hagen, J.-B. Sibarita, J. Ries, R. Henriques, M. Unser, and S. Holden, “Super-resolution fight club: Assessment of 2D and 3D single-molecule localization microscopy software”, *Nature methods—techniques for life scientists and chemists*, vol. 16, no. 5, pp. 387–395, 2019. DOI: 10.1038/s41592-019-0364-4.
- [28] A. B. Ayoub, T.-A. Pham, J. Lim, M. Unser, and D. Psaltis, “A method for assessing the fidelity of optical diffraction tomography reconstruction methods using structured illumination”, *Optics communications*, p. 124 486, 2019. DOI: 10.1016/j.optcom.2019.124486.

- [29] Q. Denoyelle, T.-a. Pham, P. del Aguila Pla, D. Sage, and M. Unser, “Optimal-transport-based metric for SMLM”, in *Proceedings of the eighteenth IEEE international symposium on biomedical imaging (ISBI’21)*, Nice, French Republic, 2021, pp. 797–801.
- [30] T.-a. Pham, E. Soubies, D. Sage, and M. Unser, “Closed-form expression of the Fourier ring-correlation for single-molecule localization microscopy”, in *Proceedings of the sixteenth IEEE international symposium on biomedical imaging: From nano to macro (ISBI’19)*, Venice, Italian Republic, 2019, pp. 321–324.
- [31] J. W. Goodman, *Introduction to Fourier Optics*. Roberts and Company Publishers, 2005.
- [32] K. Yee, “Numerical solution of initial boundary value problems involving Maxwell’s equations in isotropic media”, *IEEE transactions on antennas and propagation*, vol. 14, no. 3, pp. 302–307, 1966. DOI: 10.1109/tap.1966.1138693.
- [33] M. A. Yurkin and A. G. Hoekstra, “The discrete dipole approximation: An overview and recent developments”, *Journal of quantitative spectroscopy and radiative transfer*, vol. 106, no. 1, pp. 558–589, 2007. DOI: 10.1016/j.jqsrt.2007.01.034.
- [34] J. A. Schmalz, G. Schmalz, T. E. Gureyev, and K. M. Pavlov, “On the derivation of the Green’s function for the Helmholtz equation using generalized functions”, *American journal of physics*, vol. 78, no. 2, pp. 181–186, 2010. DOI: 10.1119/1.3253655.
- [35] A. C. Kak, M. Slaney, and G. Wang, “Principles of computerized tomographic imaging”, *Medical physics*, vol. 29, no. 1, pp. 107–107, 2002.
- [36] P. Müller, M. Schürmann, and J. Guck, “The theory of diffraction tomography”, 2015.
- [37] J. Lim, A. B. Ayoub, E. E. Antoine, and D. Psaltis, “High-fidelity optical diffraction tomography of multiple scattering samples”, *Light: Science & applications*, vol. 8, no. 1, p. 82, 2019. DOI: 10.1038/s41377-019-0195-1.
- [38] M. Chen, D. Ren, H.-Y. Liu, S. Chowdhury, and L. Waller, “Multi-layer Born multiple-scattering model for 3D phase microscopy”, *Optica*, vol. 7, no. 5, pp. 394–403, 2020. DOI: 10.1364/optica.383030.
- [39] S. Pang and G. Barbastathis, *Unified treatment of exact and approximate scalar electromagnetic wave scattering*, 2022. DOI: 10.48550/ARXIV.2202.08297.
- [40] B. E. Saleh and M. C. Teich, *Fundamentals of photonics*. John Wiley & sons, 2019.
- [41] F. Natterer, *The mathematics of computerized tomography*. SIAM, 2001.

- [42] M. Born, “Quantenmechanik der stoßvorgänge”, *Zeitschrift für physik*, vol. 38, no. 11, pp. 803–827, 1926. DOI: 10.1007/bf01397184.
- [43] M. Feit and J. Fleck, “Beam nonparaxiality, filament formation, and beam breakup in the self-focusing of optical beams”, *Josa b*, vol. 5, no. 3, pp. 633–640, 1988. DOI: 10.1364/josab.5.000633.
- [44] J. M. Cowley and A. F. Moodie, “The scattering of electrons by atoms and crystals. III. Single-crystal diffraction patterns”, *Acta crystallographica*, vol. 12, no. 5, pp. 360–367, 1959. DOI: 10.1107/s0365110x59001104.
- [45] A. M. Maiden, M. J. Humphry, and J. Rodenburg, “Ptychographic transmission microscopy in three dimensions using a multi-slice approach”, *Josa a*, vol. 29, no. 8, pp. 1606–1614, 2012. DOI: 10.1364/josaa.29.001606.
- [46] M. Born and E. Wolf, *Principles of optics: Electromagnetic theory of propagation, interference and diffraction of light*. Elsevier, 2013.
- [47] A. Sharma and A. Agrawal, “New method for nonparaxial beam propagation”, *Josa a*, vol. 21, no. 6, pp. 1082–1087, 2004. DOI: 10.1364/josaa.21.001082.
- [48] —, “Non-paraxial split-step finite-difference method for beam propagation”, *Optical and quantum electronics*, vol. 38, no. 1, pp. 19–34, 2006. DOI: 10.1007/s11082-006-0019-4.
- [49] G. Osnabrugge, S. Leedumrongwatthanakun, and I. M. Vellekoop, “A convergent Born series for solving the inhomogeneous Helmholtz equation in arbitrarily large media”, *Journal of computational physics*, vol. 322, pp. 113–124, 2016. DOI: 10.1016/j.jcp.2016.06.034.
- [50] B. Krüger, T. Brenner, and A. Kienle, “Solution of the inhomogeneous Maxwell’s equations using a Born series”, *Optics express*, vol. 25, no. 21, pp. 25 165–25 182, 2017. DOI: 10.1364/oe.25.025165.
- [51] M. Lee, H. Hugonnet, and Y. Park, “Inverse problem solver for multiple light scattering using modified Born series”, *Optica*, vol. 9, no. 2, pp. 177–182, 2022. DOI: 10.1364/optica.446511.
- [52] H.-Y. Liu, D. Liu, H. Mansour, P. T. Boufounos, L. Waller, and U. S. Kamilov, “SEAGLE: Sparsity-driven image reconstruction under multiple scattering”, *IEEE transactions on computational imaging*, vol. 4, no. 1, pp. 73–86, 2017. DOI: 10.1109/tci.2017.2764461.
- [53] S. Pang and G. Barbastathis, *Machine learning regularized solution of the Lippmann-Schwinger equation*, 2020. DOI: 10.48550/ARXIV.2010.15117.

- [54] E. CuChe, F. Bevilacqua, and C. Depeursinge, “Digital holography for quantitative phase-contrast imaging”, *Optics letters*, vol. 24, no. 5, pp. 291–293, 1999. DOI: 10.1364/ol.24.000291.
- [55] G. Zheng, C. Shen, S. Jiang, P. Song, and C. Yang, “Concept, implementations and applications of Fourier ptychography”, *Nature reviews physics*, vol. 3, no. 3, pp. 207–223, 2021. DOI: 10.1038/s42254-021-00280-y.
- [56] B. Javidi, A. Carnicer, A. Anand, G. Barbastathis, W. Chen, P. Ferraro, J. Goodman, R. Horisaki, K. Khare, M. Kujawinska, *et al.*, “Roadmap on digital holography”, *Optics express*, vol. 29, no. 22, pp. 35 078–35 118, 2021. DOI: 10.1364/oe.435915.
- [57] V. Balasubramani, M. Kujawińska, C. Allier, V. Anand, C.-J. Cheng, C. Depeursinge, N. Hai, S. Juodkazis, J. Kalkman, A. Kuś, M. Lee, P. J. Magistretti, P. Marquet, S. H. Ng, J. Rosen, Y. K. Park, and M. Ziemczonok, “Roadmap on digital holography-based quantitative phase imaging”, *Journal of imaging*, vol. 7, no. 12, p. 252, 2021. DOI: 10.3390/jimaging7120252.
- [58] M. Mir, B. Bhaduri, R. Wang, R. Zhu, and G. Popescu, “Quantitative phase imaging”, *Progress in optics*, vol. 57, pp. 133–217, 2012. DOI: 10.1016/b978-0-44-459422-8.00003-5.
- [59] D. Gabor, “A new microscopic principle”, *Nature*, vol. 161, pp. 777–778, 1948. DOI: 10.1038/161777a0.
- [60] M. K. Kim, “Principles and techniques of digital holographic microscopy”, *Spie reviews*, vol. 1, no. 1, pp. 1–51, 2010. DOI: 10.1117/6.0000006.
- [61] I. Yamaguchi and T. Zhang, “Phase-shifting digital holography”, *Optics letters*, vol. 22, no. 16, pp. 1268–1270, 1997. DOI: 10.1364/ol.22.001268.
- [62] M. Takeda, H. Ina, and S. Kobayashi, “Fourier-transform method of fringe-pattern analysis for computer-based topography and interferometry”, *Journal of the optical society of america*, vol. 72, no. 1, pp. 156–160, 1982. DOI: 10.1364/josa.72.000156.
- [63] G. Zheng, R. Horstmeyer, and C. Yang, “Wide-field, high-resolution Fourier ptychographic microscopy”, *Nature photonics*, vol. 7, no. 9, pp. 739–745, 2013. DOI: 10.1038/nphoton.2013.187.
- [64] L. Tian, X. Li, K. Ramchandran, and L. Waller, “Multiplexed coded illumination for Fourier ptychography with an LED array microscope”, *Biomedical optics express*, vol. 5, no. 7, pp. 2376–2389, 2014. DOI: 10.1364/boe.5.002376.

- [65] L.-H. Yeh, J. Dong, J. Zhong, L. Tian, M. Chen, G. Tang, M. Soltanolkotabi, and L. Waller, “Experimental robustness of Fourier ptychography phase retrieval algorithms”, *Optics express*, vol. 23, no. 26, pp. 33 214–33 240, 2015. DOI: 10.1364/oe.23.033214.
- [66] Y. Zhang, W. Jiang, L. Tian, L. Waller, and Q. Dai, “Self-learning based Fourier ptychographic microscopy”, *Optics express*, vol. 23, no. 14, pp. 18 471–18 486, 2015. DOI: 10.1364/oe.23.018471.
- [67] L. Bian, J. Suo, G. Zheng, K. Guo, F. Chen, and Q. Dai, “Fourier ptychographic reconstruction using Wirtinger flow optimization”, *Optics express*, vol. 23, no. 4, pp. 4856–4866, 2015. DOI: 10.1364/oe.23.004856.
- [68] D. Jin, R. Zhou, Z. Yaqoob, and P. T. So, “Tomographic phase microscopy: Principles and applications in bioimaging”, *Josa b*, vol. 34, no. 5, B64–B77, 2017. DOI: 10.1364/josab.34.000b64.
- [69] P. Y. Liu, L. K. Chin, W. Ser, H. F. Chen, C.-M. Hsieh, C.-H. Lee, K.-B. Sung, T. C. Ayi, P. H. Yap, B. Liedberg, K. Wang, T. Bourouina, and Y. Leprince-Wang, “Cell refractive index for cell biology and disease diagnosis: Past, present and future”, *Lab on a chip*, vol. 16, no. 4, pp. 634–644, 2016. DOI: 10.1039/c5lc01445j.
- [70] R. Eckert, Z. F. Phillips, and L. Waller, “Efficient illumination angle self-calibration in Fourier ptychography”, *Applied optics*, vol. 57, no. 19, pp. 5434–5442, 2018. DOI: 10.1364/ao.57.005434.
- [71] M. Debailleul, B. Simon, V. Georges, O. Haeberlé, and V. Lauer, “Holographic microscopy and diffractive microtomography of transparent samples”, *Measurement science and technology*, vol. 19, no. 7, p. 074 009, 2008. DOI: 10.1088/0957-0233/19/7/074009.
- [72] G. Gbur and E. Wolf, “The information content of the scattered intensity in diffraction tomography”, *Information sciences*, vol. 162, no. 1, pp. 3–20, 2004. DOI: 10.1016/j.ins.2003.01.001.
- [73] Y. Sung, W. Choi, C. Fang-Yen, K. Badizadegan, R. R. Dasari, and M. S. Feld, “Optical diffraction tomography for high resolution live cell imaging”, *Optics express*, vol. 17, no. 1, pp. 266–277, 2009. DOI: 10.1364/oe.17.000266.
- [74] M. H. Maleki, A. J. Devaney, and A. Schatzberg, “Tomographic reconstruction from optical scattered intensities”, *Josa a*, vol. 9, no. 8, pp. 1356–1363, 1992. DOI: 10.1364/josaa.9.001356.
- [75] M. H. Maleki and A. J. Devaney, “Phase-retrieval and intensity-only reconstruction algorithms for optical diffraction tomography”, *Josa a*, vol. 10, no. 5, pp. 1086–1092, 1993. DOI: 10.1364/josaa.10.001086.

- [76] D. Ren, E. Bostan, L.-H. Yeh, and L. Waller, “Total-variation regularized Fourier ptychographic microscopy with multiplexed coded illumination”, in *Mathematics in imaging*, Optical Society of America, 2017, pp. MM3C–5.
- [77] P. Li, D. J. Batey, T. B. Edo, and J. M. Rodenburg, “Separation of three-dimensional scattering effects in tilt-series Fourier ptychography”, *Ultramicroscopy*, vol. 158, pp. 1–7, 2015. DOI: 10.1016/j.ultramic.2015.06.010.
- [78] W. Van den Broek and C. T. Koch, “Method for retrieval of the three-dimensional object potential by inversion of dynamical electron scattering”, *Physical review letters*, vol. 109, no. 24, p. 245 502, 2012. DOI: 10.1103/physrevlett.109.245502.
- [79] P. C. Chaumet and K. Belkebir, “Three-dimensional reconstruction from real data using a conjugate gradient-coupled dipole method”, *Inverse problems. an international journal on the theory and practice of inverse problems, inverse methods and computerized inversion of data*, vol. 25, no. 2, p. 024 003, 2009.
- [80] K. Belkebir, P. Chaumet, and A. Sentenac, “Superresolution in total internal reflection tomography”, *Journal of the optical society of america a*, vol. 22, no. 9, pp. 1889–1897, 2005. DOI: 10.1364/josaa.22.001889.
- [81] T. Takenaka, D. J. Wall, H. Harada, and M. Tanaka, “Reconstruction algorithm of the refractive index of a cylindrical object from the intensity measurements of the total field”, *Microwave and optical technology letters*, vol. 14, no. 3, pp. 182–188, 1997. DOI: 10.1002/(sici)1098-2760(19970220)14:3<182::aid-mop15>3.0.co;2-a.
- [82] L. Crocco, M. D’Urso, and T. Isernia, “Inverse scattering from phaseless measurements of the total field on a closed curve”, *Journal of the optical society of america a*, vol. 21, no. 4, pp. 622–631, 2004. DOI: 10.1364/josaa.21.000622.
- [83] P. Lobel, L. Blanc-Féraud, C. Pichot, and M. Barlaud, “A new regularization scheme for inverse scattering”, *Inverse problems. an international journal on the theory and practice of inverse problems, inverse methods and computerized inversion of data*, vol. 13, no. 2, pp. 403–410, 1997. DOI: 10.1088/0266-5611/13/2/013.
- [84] T. Zhang, C. Godavarthi, P. C. Chaumet, G. Maire, H. Giovannini, A. Talneau, M. Allain, K. Belkebir, and A. Sentenac, “Far-field diffraction microscopy at $\lambda/10$ resolution”, *Optica*, vol. 3, no. 6, pp. 609–612, 2016. DOI: 10.1364/optica.3.000609.
- [85] M. Lambert and D. Lesselier, “Binary-constrained inversion of a buried cylindrical obstacle from complete and phaseless magnetic fields”, *Inverse problems. an international journal on the theory and practice of inverse problems, inverse methods and computerized inversion of data*, vol. 16, no. 3, p. 563, 2000.

- [86] A. Litman and K. Belkebir, “Two-dimensional inverse profiling problem using phaseless data”, *Journal of the optical society of america a*, vol. 23, no. 11, pp. 2737–2746, 2006. DOI: 10.1364/josaa.23.002737.
- [87] U. S. Kamilov, I. N. Papadopoulos, M. H. Shoreh, A. Goy, C. Vonesch, M. Unser, and D. Psaltis, “Learning approach to optical tomography”, *Optica*, vol. 2, no. 6, pp. 517–522, 2015. DOI: 10.1364/optica.2.000517.
- [88] A. C. Kak and M. Slaney, *Principles of computerized tomographic imaging*. SIAM, 2001.
- [89] S. Fan, S. Smith-Dryden, G. Li, and B. Saleh, “Optimization-based optical diffraction tomography using iODT initialization”, *Journal of the optical society of america a, optics and image science*, vol. 38, no. 7, pp. 947–953, 2021. DOI: 10.1364/josaa.419989.
- [90] O. Yasuhiko, K. Takeuchi, H. Yamada, and Y. Ueda, “Multiple-scattering suppressive refractive index tomography for the label-free quantitative assessment of multicellular spheroids”, *Biomedical optics express*, vol. 13, no. 2, pp. 962–979, 2022. DOI: 10.1364/boe.446622.
- [91] B. Chen and J. J. Stamnes, “Validity of diffraction tomography based on the first Born and the first Rytov approximations”, *Applied optics*, vol. 37, no. 14, pp. 2996–3006, 1998. DOI: 10.1364/ao.37.002996.
- [92] A. Abubakar and P. M. van den Berg, “The contrast source inversion method for location and shape reconstructions”, *Inverse problems. an international journal on the theory and practice of inverse problems, inverse methods and computerized inversion of data*, vol. 18, no. 2, p. 495, 2002.
- [93] P. M. van den Berg, A. Van Broekhoven, and A. Abubakar, “Extended contrast source inversion”, *Inverse problems. an international journal on the theory and practice of inverse problems, inverse methods and computerized inversion of data*, vol. 15, no. 5, p. 1325, 1999.
- [94] E. Mudry, P. Chaumet, K. Belkebir, and A. Sentenac, “Electromagnetic wave imaging of three-dimensional targets using a hybrid iterative inversion method”, *Inverse problems. an international journal on the theory and practice of inverse problems, inverse methods and computerized inversion of data*, vol. 28, no. 6, p. 065 007, 2012.
- [95] T. C. Wedberg and J. J. Stamnes, “Experimental examination of the quantitative imaging properties of optical diffraction tomography”, *Josa a*, vol. 12, no. 3, pp. 493–500, 1995. DOI: 10.1364/josaa.12.000493.

- [96] M. Holler, M. Guizar-Sicairos, E. H. Tsai, R. Dinapoli, E. Müller, O. Bunk, J. Raabe, and G. Aeppli, “High-resolution non-destructive three-dimensional imaging of integrated circuits”, *Nature*, vol. 543, no. 7645, pp. 402–406, 2017. DOI: 10.1038/nature21698.
- [97] R. Horstmeyer, J. Chung, X. Ou, G. Zheng, and C. Yang, “Diffraction tomography with Fourier ptychography”, *Optica*, vol. 3, no. 8, pp. 827–835, 2016. DOI: 10.1364/optica.3.000827.
- [98] R. W. Gerchberg and W. Saxton, “Phase determination from image and diffraction plane pictures in electron-microscope”, *Optik*, vol. 34, no. 3, pp. 275–+, 1971.
- [99] K. Guo, S. Dong, and G. Zheng, “Fourier ptychography for brightfield, phase, darkfield, reflective, multi-slice, and fluorescence imaging”, *IEEE journal of selected topics in quantum electronics*, vol. 22, no. 4, pp. 77–88, 2016. DOI: 10.1109/jstqe.2015.2504514.
- [100] F. Yang, T.-a. Pham, H. Gupta, M. Unser, and J. Ma, “Deep-learning projector for optical diffraction tomography”, *Optics express*, vol. 28, no. 3, pp. 3905–3921, 2020. DOI: 10.1364/oe.381413.
- [101] J. Lim, A. B. Ayoub, and D. Psaltis, “Three-dimensional tomography of red blood cells using deep learning”, *Advanced photonics*, vol. 2, no. 2, p. 026001, 2020. DOI: 10.1117/1.ap.2.2.026001.
- [102] H. Chung, J. Huh, G. Kim, Y. K. Park, and J. C. Ye, “Missing cone artifact removal in ODT using unsupervised deep learning in the projection domain”, *IEEE transactions on computational imaging*, vol. 7, pp. 747–758, 2021. DOI: 10.1109/tci.2021.3098937.
- [103] D. Ryu, D. Ryu, Y. Baek, H. Cho, G. Kim, Y. S. Kim, Y. Lee, Y. Kim, J. C. Ye, H.-S. Min, *et al.*, “DeepRegularizer: Rapid resolution enhancement of tomographic imaging using deep learning”, *IEEE transactions on medical imaging*, vol. 40, no. 5, pp. 1508–1518, 2021. DOI: 10.1109/tmi.2021.3058373.
- [104] B. Simon, M. Debailleul, M. Houkal, C. Ecoffet, J. Bailleul, J. Lambert, A. Spangenberg, H. Liu, O. Soppera, and O. Haeberlé, “Isotropic-resolution tomographic diffractive microscopy”, in *2018 20th international conference on transparent optical networks (ICTON)*, 2018, pp. 1–4. DOI: 10.1109/icton.2018.8473709.
- [105] B. Simon and O. Haeberlé, “Tomographic diffractive microscopy: Principles, implementations, and applications in biology”, in *Label-free super-resolution microscopy*, Springer, 2019, pp. 85–112.

- [106] A. M. Taddese, N. Verrier, M. Debailleul, J.-B. Courbot, and O. Haeberlé, “Optimizing sample illumination scanning for reflection and 4Pi tomographic diffractive microscopy”, *Applied optics*, vol. 60, no. 25, pp. 7745–7753, 2021. DOI: 10.1364/ao.435721.
- [107] H.-Y. Liu, U. S. Kamilov, D. Liu, H. Mansour, and P. T. Boufounos, “Compressive imaging with iterative forward models”, in *2017 IEEE international conference on acoustics, speech and signal processing (ICASSP)*, IEEE, 2017, pp. 6025–6029. DOI: 10.1109/icassp.2017.7953313.
- [108] H. van der Vorst, “Bi-CGSTAB: A fast and smoothly converging variant of bi-CG for the solution of nonsymmetric linear systems”, *SIAM journal on scientific and statistical computing*, vol. 13, no. 2, pp. 631–644, 1992. DOI: 10.1137/0913035.
- [109] G. Vainikko, “Fast solvers of the Lippmann-Schwinger equation”, *Helsinki university of technology, institute of mathematics research reports, a*, 1997. DOI: 10.1007/978-1-4757-3214-6_25.
- [110] F. Vico, L. Greengard, and M. Ferrando, “Fast convolution with free-space Green’s functions”, *Journal of computational physics*, vol. 323, pp. 191–203, 2016. DOI: 10.1016/j.jcp.2016.07.028.
- [111] A. J. Devaney, *Mathematical foundations of imaging, tomography and wavefield inversion*. Cambridge University Press, 2012.
- [112] A. Greenbaum, *Iterative methods for solving linear systems*. SIAM, 1997.
- [113] K. Belkebir and A. Sentenac, “High-resolution optical diffraction microscopy”, *Josa a*, vol. 20, no. 7, pp. 1223–1229, 2003. DOI: 10.1364/josaa.20.001223.
- [114] K. D. Unger, P. C. Chaumet, G. Maire, A. Sentenac, and K. Belkebir, “Versatile inversion tool for phaseless optical diffraction-tomography”, *Josa a*, vol. 36, no. 11, pp. C1–C8, 2019. DOI: 10.1364/josaa.36.0000c1.
- [115] M. R. Hestenes, E. Stiefel, *et al.*, *Methods of conjugate gradients for solving linear systems*, 1. NBS Washington, DC, 1952, vol. 49.
- [116] J. A. Stratton, *Electromagnetic theory*. John Wiley & Sons, 2007.
- [117] Y. Ma, H. Mansour, D. Liu, P. T. Boufounos, and U. S. Kamilov, “Accelerated image reconstruction for nonlinear diffractive imaging”, in *2018 IEEE international conference on acoustics, speech and signal processing (ICASSP)*, Calgary AB, Canada, 2018, pp. 6473–6477.
- [118] J. W. Goodman and R. W. Lawrence, “Digital image formation from electronically detected holograms”, *Applied physics letters*, vol. 11, no. 3, pp. 77–79, 1967. DOI: 10.1063/1.1755043.

- [119] A. Abubakar, T. M. Habashy, G. Pan, and M.-K. Li, “Application of the multiplicative regularized Gauss-Newton algorithm for three-dimensional microwave imaging”, *IEEE transactions on antennas and propagation*, vol. 60, no. 5, pp. 2431–2441, 2012. DOI: 10.1109/tap.2012.2189712.
- [120] G. Maire, Y. Ruan, T. Zhang, P. C. Chaumet, H. Giovannini, D. Sentenac, A. Talneau, K. Belkebir, and A. Sentenac, “High-resolution tomographic diffractive microscopy in reflection configuration”, *Josa a*, vol. 30, no. 10, pp. 2133–2139, 2013. DOI: 10.1364/josaa.30.002133.
- [121] A. Litman and L. Crocco, “Testing inversion algorithms against experimental data: 3D targets”, *Inverse problems. an international journal on the theory and practice of inverse problems, inverse methods and computerized inversion of data*, vol. 25, no. 2, p. 020201, 2009.
- [122] J. Girard, G. Maire, H. Giovannini, A. Talneau, K. Belkebir, P. C. Chaumet, and A. Sentenac, “Nanometric resolution using far-field optical tomographic microscopy in the multiple scattering regime”, *Physical review a*, vol. 82, no. 6, p. 061801, 2010. DOI: 10.1103/physreva.82.061801.
- [123] A. Ritter, “Modified shifted angular spectrum method for numerical propagation at reduced spatial sampling rates”, *Optics express*, vol. 22, no. 21, pp. 26265–26276, 2014. DOI: 10.1364/oe.22.026265.
- [124] C.-S. Guo, Y.-Y. Xie, and B. Sha, “Diffraction algorithm suitable for both near and far field with shifted destination window and oblique illumination”, *Optics letters*, vol. 39, no. 8, pp. 2338–2341, 2014. DOI: 10.1364/ol.39.002338.
- [125] L. I. Rudin, S. Osher, and E. Fatemi, “Nonlinear total variation based noise removal algorithms”, *Physica d: Nonlinear phenomena*, vol. 60, no. 1-4, pp. 259–268, 1992. DOI: 10.1016/0167-2789(92)90242-f.
- [126] S. Lefkimiatis, J. P. Ward, and M. Unser, “Hessian Schatten-Norm regularization for linear inverse problems”, *IEEE transactions on image processing*, vol. 22, no. 5, pp. 1873–1888, 2013. DOI: 10.1109/tip.2013.2237919.
- [127] A. Beck and M. Teboulle, “A fast iterative shrinkage-thresholding algorithm for linear inverse problems”, *SIAM journal on imaging sciences*, vol. 2, no. 1, pp. 183–202, 2009. DOI: 10.1137/080716542.
- [128] Y. Nesterov, “Gradient methods for minimizing composite functions”, *Mathematical programming*, vol. 140, no. 1, pp. 125–161, 2013. DOI: 10.1007/s10107-012-0629-5.

- [129] A. Beck and M. Teboulle, “Fast gradient-based algorithms for constrained total variation image denoising and deblurring problems”, *IEEE transactions on image processing*, vol. 18, no. 11, pp. 2419–2434, 2009. DOI: 10.1109/tip.2009.2028250.
- [130] D. P. Bertsekas, “Incremental proximal methods for large scale convex optimization”, *Mathematical programming*, vol. 129, no. 2, p. 163, 2011. DOI: 10.1007/s10107-011-0472-0.
- [131] E. Soubies, F. Soulez, M. T. McCann, T.-a. Pham, L. Donati, T. Debarre, D. Sage, and M. Unser, “Pocket guide to solve inverse problems with GlobalBioIm”, *Inverse problems. an international journal on the theory and practice of inverse problems, inverse methods and computerized inversion of data*, vol. 35, no. 10, pp. 1–20, 2019.
- [132] J.-M. Geffrin, P. Sabouroux, and C. Eyraud, “Free space experimental scattering database continuation: Experimental set-up and measurement precision”, *Inverse problems. an international journal on the theory and practice of inverse problems, inverse methods and computerized inversion of data*, vol. 21, no. 6, S117, 2005.
- [133] F. Soulez, “A “Learn 2D, apply 3D” method for 3D deconvolution microscopy”, in *2014 IEEE 11th international symposium on biomedical imaging (ISBI)*, Beijing, People’s Republic of China, 2014, pp. 1075–1078.
- [134] M. Elad and M. Aharon, “Image denoising via sparse and redundant representations over learned dictionaries”, *IEEE transactions on image processing*, vol. 15, no. 12, pp. 3736–3745, 2006. DOI: 10.1109/tip.2006.881969.
- [135] J. Mairal, F. Bach, J. Ponce, and G. Sapiro, “Online dictionary learning for sparse coding”, in *Proceedings of the 26th annual international conference on machine learning*, ACM, Montreal, QC, Canada, June 14 - 18 2009, pp. 689–696.
- [136] M. D. Zeiler, D. Krishnan, G. W. Taylor, and R. Fergus, “Deconvolutional networks”, in *2010 IEEE computer society conference on computer vision and pattern recognition*, San Francisco, CA, USA, 2010, pp. 2528–2535. DOI: 10.1109/cvpr.2010.5539957.
- [137] M. Mørup and M. N. Schmidt, “Transformation invariant sparse coding”, in *IEEE international workshop on machine learning for signal processing*, Beijing, People’s Republic of China, 2011, pp. 1–6.
- [138] C. Garcia-Cardona and B. Wohlberg, “Convolutional dictionary learning: A comparative review and new algorithms”, *IEEE transactions on computational imaging*, vol. 4, no. 3, pp. 366–381, 2018. DOI: 10.1109/tci.2018.2840334.
- [139] V. Pappayan, Y. Romano, M. Elad, and J. Sulam, “Convolutional dictionary learning via local processing”, in *International conference on computer vision*, Venice, Italy, 2017, pp. 5306–5314.

- [140] V. Pappyan, J. Sulam, and M. Elad, “Working locally thinking globally: Theoretical guarantees for convolutional sparse coding”, *IEEE transactions on signal processing*, vol. 65, no. 21, pp. 5687–5701, 2017. DOI: 10.1109/tsp.2017.2733447.
- [141] J. Mairal, F. Bach, and J. Ponce, “Sparse modeling for image and vision processing”, *Foundations and trends in computer graphics and vision*, vol. 8, no. 2-3, pp. 85–283, 2014. DOI: 10.1561/06000000058.
- [142] S. V. Venkatakrisnan, C. A. Bouman, and B. Wohlberg, “Plug-and-play priors for model based reconstruction”, in *2013 IEEE global conference on signal and information processing*, Austin, Texas, U.S.A., 2013, pp. 945–948.
- [143] S. Sreehari, S. V. Venkatakrisnan, B. Wohlberg, G. T. Buzzard, L. F. Drummy, J. P. Simmons, and C. A. Bouman, “Plug-and-play priors for bright field electron tomography and sparse interpolation”, *IEEE transactions on computational imaging*, vol. 2, no. 4, pp. 408–423, 2016.
- [144] U. S. Kamilov, H. Mansour, and B. Wohlberg, “A plug-and-play priors approach for solving nonlinear imaging inverse problems”, *IEEE signal processing letters*, vol. 24, no. 12, pp. 1872–1876, 2017. DOI: 10.1109/lsp.2017.2763583.
- [145] R. Tibshirani, “Regression shrinkage and selection via the LASSO”, *Journal of the royal statistical society: Series b (methodological)*, vol. 58, no. 1, pp. 267–288, 1996. DOI: 10.1111/j.2517-6161.1996.tb02080.x.
- [146] J. Van Roey, J. Van der Donk, and P. Lagasse, “Beam-propagation method: Analysis and assessment”, *Josa*, vol. 71, no. 7, pp. 803–810, 1981. DOI: 10.1364/josa.71.000803.
- [147] S. Boyd, N. Parikh, E. Chu, B. Peleato, and J. Eckstein, “Distributed optimization and statistical learning via the alternating direction method of multipliers”, *Foundations and trends in machine learning*, vol. 3, no. 1, pp. 1–122, 2011. DOI: 10.1561/22000000016.
- [148] P. L. Combettes and V. R. Wajs, “Signal recovery by proximal forward-backward splitting”, *Multiscale modeling & simulation*, vol. 4, no. 4, pp. 1168–1200, 2005. DOI: 10.1137/050626090.
- [149] G. Zheng, C. Kolner, and C. Yang, “Microscopy refocusing and dark-field imaging by using a simple LED array”, *Optics letters*, vol. 36, no. 20, pp. 3987–3989, 2011. DOI: 10.1364/ol.36.003987.
- [150] W. Wirtinger, “Zur formalen theorie der funktionen von mehr komplexen veränderlichen”, *Mathematische annalen*, vol. 97, no. 1, pp. 357–375, 1927. DOI: 10.1007/bf01447872.

- [151] T. Adali, P. J. Schreier, and L. L. Scharf, “Complex-valued signal processing: The proper way to deal with impropriety”, *IEEE transactions on signal processing*, vol. 59, no. 11, pp. 5101–5125, 2011. DOI: 10.1109/tsp.2011.2162954.
- [152] A. B. Ayoub, J. Lim, E. E. Antoine, and D. Psaltis, “3D reconstruction of weakly scattering objects from 2D intensity-only measurements using the Wolf transform”, *Optics express*, vol. 29, no. 3, pp. 3976–3984, 2021. DOI: 10.1364/oe.414543.
- [153] E. Betzig, G. H. Patterson, R. Sougrat, O. W. Lindwasser, S. Olenych, J. S. Bonifacino, M. W. Davidson, J. Lippincott-Schwartz, and H. F. Hess, “Imaging intracellular fluorescent proteins at nanometer resolution”, *Science (new york, n.y.)*, vol. 313, no. 5793, pp. 1642–1645, 2006. DOI: 10.1126/science.1127344.
- [154] S. T. Hess, T. P. Girirajan, and M. D. Mason, “Ultra-high resolution imaging by fluorescence photoactivation localization microscopy”, *Biophysical journal*, vol. 91, no. 11, pp. 4258–4272, 2006. DOI: 10.1529/biophysj.106.091116.
- [155] M. J. Rust, M. Bates, and X. Zhuang, “Sub-diffraction-limit imaging by stochastic optical reconstruction microscopy (STORM)”, *Nature methods*, vol. 3, 2006. DOI: 10.1038/nmeth929.
- [156] B. Huang, W. Wang, M. Bates, and X. Zhuang, “Three-dimensional super-resolution imaging by stochastic optical reconstruction microscopy”, *Science (new york, n.y.)*, vol. 319, no. 5864, pp. 810–813, 2008. DOI: 10.1126/science.1153529.
- [157] S. R. P. Pavani, M. A. Thompson, J. S. Biteen, S. J. Lord, N. Liu, R. J. Twieg, R. Piestun, and W. Moerner, “Three-dimensional, single-molecule fluorescence imaging beyond the diffraction limit by using a double-helix point spread function”, *Proceedings of the national academy of sciences*, vol. 106, no. 9, pp. 2995–2999, 2009. DOI: 10.1073/pnas.0900245106.
- [158] H. P. Babcock and X. Zhuang, “Analyzing single molecule localization microscopy data using cubic splines”, *Scientific reports*, vol. 7, no. 1, pp. 1–9, 2017. DOI: 10.1038/s41598-017-00622-w.
- [159] Y. Li, M. Mund, P. Hoess, J. Deschamps, U. Matti, B. Nijmeijer, V. J. Sabinina, J. Ellenberg, I. Schoen, and J. Ries, “Real-time 3D single-molecule localization using experimental point spread functions”, *Nature methods*, vol. 15, no. 5, pp. 367–369, 2018. DOI: 10.1038/nmeth.4661.
- [160] F. Xu, D. Ma, K. P. MacPherson, S. Liu, Y. Bu, Y. Wang, Y. Tang, C. Bi, T. Kwok, A. A. Chubykin, P. Yin, S. Calve, G. E. Landreth, and F. Huang, “Three-dimensional nanoscopy of whole cells and tissues with in situ point spread function retrieval”, *Nature methods*, vol. 17, no. 5, pp. 531–540, 2020. DOI: 10.1038/s41592-020-0816-x.

- [161] Y. Xue and L. Waller, *Computational hybrid imaging*, 2020.
- [162] A. C. Gilbert, H. W. Levinson, and J. C. Schotland, “Imaging from the inside out: Inverse scattering with photoactivated internal sources”, *Optics letters*, vol. 43, no. 12, pp. 3005–3008, 2018. DOI: 10.1364/ol.43.003005.
- [163] A. Cornea and P. M. Conn, *Fluorescence Microscopy: Super-Resolution and Other Novel Techniques*. Elsevier, 2014.
- [164] A. Aristov, B. Lelandais, E. Rensen, and C. Zimmer, “ZOLA-3D allows flexible 3D localization microscopy over an adjustable axial range”, *Nature communications*, vol. 9, no. 1, pp. 1–8, 2018. DOI: 10.1038/s41467-018-04709-4.
- [165] S. Liu, E. B. Kromann, W. D. Krueger, J. Bewersdorf, and K. A. Lidke, “Three dimensional single molecule localization using a phase retrieved pupil function”, *Optics express*, vol. 21, no. 24, pp. 29 462–29 487, 2013. DOI: 10.1364/oe.21.029462.
- [166] M. F. Juette, T. J. Gould, M. D. Lessard, M. J. Mlodzianoski, B. S. Nagpure, B. T. Bennett, S. T. Hess, and J. Bewersdorf, “Three-dimensional sub-100 nm resolution fluorescence microscopy of thick samples”, *Nature methods*, vol. 5, no. 6, pp. 527–529, 2008. DOI: 10.1038/nmeth.1211.
- [167] G. Ongie, A. Jalal, C. A. Metzler, R. G. Baraniuk, A. G. Dimakis, and R. Willett, “Deep learning techniques for inverse problems in imaging”, *IEEE journal on selected areas in information theory*, vol. 1, no. 1, pp. 39–56, 2020. DOI: 10.1109/jsait.2020.2991563.
- [168] H. Gupta, K. H. Jin, H. Q. Nguyen, M. T. McCann, and M. Unser, “CNN-Based projected gradient descent for consistent CT image reconstruction”, *IEEE transactions on medical imaging*, vol. 37, no. 6, pp. 1440–1453, 2018. DOI: 10.1109/tmi.2018.2832656.
- [169] A. Goy, G. Rughoobur, S. Li, K. Arthur, A. I. Akinwande, and G. Barbastathis, “High-resolution limited-angle phase tomography of dense layered objects using deep neural networks”, *Proceedings of the national academy of sciences*, vol. 116, no. 40, pp. 19 848–19 856, 2019. DOI: 10.1073/pnas.1821378116.
- [170] S. Kullback and R. A. Leibler, “On information and sufficiency”, *The annals of mathematical statistics*, vol. 22, no. 1, pp. 79–86, 1951. DOI: 10.1214/aoms/1177729694.
- [171] M. Xie, J. Liu, Y. Sun, W. Gan, B. Wohlberg, and U. S. Kamilov, “Joint reconstruction and calibration using regularization by denoising with application to computed tomography”, in *Proceedings of the IEEE/CVF international conference on computer vision (ICCV) workshops*, 2021, pp. 4028–4037.

- [172] P. Wolfe, “Convergence conditions for ascent methods”, *SIAM review*, vol. 11, no. 2, pp. 226–235, 1969. DOI: 10.1137/1011036.
- [173] L. Armijo, “Minimization of functions having Lipschitz continuous first partial derivatives”, *Pacific journal of mathematics*, vol. 16, no. 1, pp. 1–3, 1966. DOI: 10.2140/pjm.1966.16.1.
- [174] J. Min, S. J. Holden, L. Carlini, M. Unser, S. Manley, and J. C. Ye, “3D high-density localization microscopy using hybrid Astigmatic/Biplane imaging and sparse image reconstruction”, *Biomedical optics express*, vol. 5, no. 11, pp. 3935–3948, 2014. DOI: 10.1364/boe.5.003935.
- [175] Z. Wang, A. C. Bovik, H. R. Sheikh, and E. P. Simoncelli, “Image quality assessment: From error visibility to structural similarity”, *IEEE transactions on image processing*, vol. 13, no. 4, pp. 600–612, 2004. DOI: 10.1109/tip.2003.819861.
- [176] R. E. Thompson, D. R. Larson, and W. W. Webb, “Precise nanometer localization analysis for individual fluorescent probes”, *Biophysical journal*, vol. 82, no. 5, pp. 2775–2783, 2002. DOI: 10.1016/s0006-3495(02)75618-x.
- [177] J. Chao, E. S. Ward, and R. J. Ober, “Fisher information theory for parameter estimation in single molecule microscopy: Tutorial”, *Josa a*, vol. 33, no. 7, B36–B57, 2016. DOI: 10.1364/josaa.33.000b36.
- [178] D. C. Ghiglia and M. D. Pritt, *Two-Dimensional Phase Unwrapping: Theory, Algorithms, and Software*. Wiley New York, 1998, vol. 4.
- [179] R. M. Goldstein, H. A. Zebker, and C. L. Werner, “Satellite radar interferometry: Two-dimensional phase unwrapping”, *Radio science*, vol. 23, no. 4, pp. 713–720, 1988. DOI: 10.1029/rs023i004p00713.
- [180] X. Su and W. Chen, “Reliability-guided phase unwrapping algorithm: A review”, *Optics and lasers in engineering*, vol. 42, no. 3, pp. 245–261, 2004. DOI: 10.1016/j.optlaseng.2003.11.002.
- [181] D. C. Ghiglia and L. A. Romero, “Minimum L^p -Norm two-dimensional phase unwrapping”, *Journal of the optical society of america. a*, vol. 13, no. 10, pp. 1999–2013, 1996. DOI: 10/b2vjcg.
- [182] —, “Robust two-dimensional weighted and unweighted phase unwrapping that uses fast transforms and iterative methods”, *Journal of the optical society of america. a*, vol. 11, no. 1, pp. 107–117, 1994. DOI: 10.1364/josaa.11.000107.
- [183] W. He, L. Xia, and F. Liu, “Sparse-representation-based direct minimum L^p -Norm algorithm for MRI phase unwrapping”, *Computational and mathematical methods in medicine*, vol. 2014, pp. 1–11, 2014. DOI: 10/gb96xb.

- [184] G. Nico, G. Palubinskas, and M. Datcu, “Bayesian approaches to phase unwrapping: Theoretical study”, *IEEE transactions on signal processing*, vol. 48, no. 9, pp. 2545–2556, 2000. DOI: 10.1109/78.863057.
- [185] L. Ying, Z. P. Liang, D. C. Munson, R. Koetter, and B. J. Frey, “Unwrapping of MR phase images using a Markov random field model”, *IEEE transactions on medical imaging*, vol. 25, no. 1, pp. 128–136, 2005. DOI: 10.1109/tmi.2005.861021.
- [186] Z. P. Liang, “A model-based method for phase unwrapping”, *IEEE transactions on medical imaging*, vol. 15, no. 6, pp. 893–897, 1996. DOI: 10.1109/42.544507.
- [187] H. Takaajo and T. Takahashi, “Least-squares phase estimation from the phase difference”, *Journal of the optical society of america. a*, vol. 5, no. 3, pp. 416–425, 1988. DOI: 10.1364/josaa.5.000416.
- [188] J. M. Bioucas-Dias and G. Valadao, “Phase unwrapping via graph cuts”, *IEEE transactions on image processing*, vol. 16, no. 3, pp. 698–709, 2007. DOI: 10.1109/tip.2006.888351.
- [189] B. Zhang, L. Wei, S. Li, and Q. Hu, “Precise Markov random field model-based phase unwrapping method for airborne interferometric synthetic aperture radar imaging”, *Journal of applied remote sensing*, vol. 12, no. 3, p. 035 019, 2018. DOI: 10.1117/1.jrs.12.035019.
- [190] L. Zhou, D. Chai, Y. Xia, and C. Xie, “An extended PUMA algorithm for multi-baseline InSAR DEM reconstruction”, *International journal of remote sensing*, pp. 1–22, 2019. DOI: 10.1080/01431161.2019.1624868.
- [191] L. Condat, D. Kitahara, and A. Hirabayashi, “A convex lifting approach to image phase unwrapping”, in *ICASSP 2019-2019 IEEE international conference on acoustics, speech and signal processing (ICASSP)*, IEEE, 2019, pp. 1852–1856. DOI: 10.1109/icassp.2019.8682258.
- [192] U. S. Kamilov, I. N. Papadopoulos, M. H. Shoreh, D. Psaltis, and M. Unser, “Isotropic inverse-problem approach for two-dimensional phase unwrapping”, *Journal of the optical society of america. a*, vol. 32, no. 6, pp. 1092–1100, 2015. DOI: 10.1364/josaa.32.001092.
- [193] J. Besag, “On the statistical analysis of dirty pictures”, *Journal of the royal statistical society: Series b (methodological)*, vol. 48, no. 3, pp. 259–279, 1986. DOI: 10.1111/j.2517-6161.1986.tb01412.x.
- [194] K. Itoh, “Analysis of the phase unwrapping algorithm”, *Applied optics*, vol. 21, no. 14, pp. 2470–2470, 1982. DOI: 10.1364/ao.21.002470.

- [195] B. Bhaduri, H. Pham, M. Mir, and G. Popescu, “Diffraction phase microscopy with white light”, *Optics letters*, vol. 37, no. 6, pp. 1094–1096, 2012. DOI: 10.1364/ol.37.001094.
- [196] Z. Wang, L. Millet, M. Mir, H. Ding, S. Unarunotai, J. Rogers, M. U. Gillette, and G. Popescu, “Spatial light interference microscopy (SLIM)”, *Optics express*, vol. 19, no. 2, pp. 1016–1026, 2011. DOI: 10.1364/oe.19.001016.
- [197] C. J. Mann, P. R. Bingham, V. C. Paquit, and K. W. Tobin, “Quantitative phase imaging by three-wavelength digital holography”, *Optics express*, vol. 16, no. 13, pp. 9753–9764, 2008. DOI: 10.1364/oe.16.009753.
- [198] Y. Li, W. Xiao, and F. Pan, “Multiple-wavelength-scanning-based phase unwrapping method for digital holographic microscopy”, *Applied optics*, vol. 53, no. 5, pp. 979–987, 2014. DOI: 10.1364/ao.53.000979.
- [199] B. Zhu, J. Z. Liu, S. F. Cauley, B. R. Rosen, and M. S. Rosen, “Image reconstruction by domain-transform manifold learning”, *Nature*, vol. 555, no. 7697, pp. 487–493, 2018. DOI: 10.1038/nature25988.
- [200] M. T. McCann, K. H. Jin, and M. Unser, “Convolutional neural networks for inverse problems in imaging: A review”, *IEEE signal processing magazine*, vol. 34, no. 6, pp. 85–95, 2017. DOI: 10.1109/msp.2017.2739299.
- [201] H. Wang, Y. Rivenson, Y. Jin, Z. Wei, R. Gao, H. Günaydın, L. A. Bentolila, C. Kural, and A. Ozcan, “Deep learning enables cross-modality super-resolution in fluorescence microscopy”, *Nature methods*, vol. 16, no. 1, pp. 103–110, 2019. DOI: 10.1038/s41592-018-0239-0.
- [202] K. H. Jin, M. T. McCann, E. Froustey, and M. Unser, “Deep convolutional neural network for inverse problems in imaging”, *IEEE transactions on image processing*, vol. 26, no. 9, pp. 4509–4522, 2017. DOI: 10.1109/tip.2017.2713099.
- [203] C. Yan, B. Gong, Y. Wei, and Y. Gao, “Deep multi-view enhancement hashing for image retrieval”, *IEEE transactions on pattern analysis and machine intelligence*, 2020.
- [204] C. Yan, B. Shao, H. Zhao, R. Ning, Y. Zhang, and F. Xu, “3D room layout estimation from a single RGB image”, *IEEE transactions on multimedia*, 2020. DOI: 10.1109/TMM.2020.2967645.
- [205] C. Yan, Z. Li, Y. Zhang, Y. Liu, X. Ji, and Y. Zhang, “Depth image denoising using nuclear norm and learning graph model”, *Acm transactions on multimedia computing, communications, and applications (tomms)*, vol. 16, no. 4, pp. 1–17, 2020. DOI: 10.1145/3404374.

- [206] Y. Jo, H. Cho, S. Y. Lee, G. Choi, G. Kim, H.-s. Min, and Y. Park, “Quantitative phase imaging and artificial intelligence: A review”, *IEEE journal of selected topics in quantum electronics*, vol. 25, no. 1, pp. 1–14, 2018. DOI: 10.1109/jstqe.2018.2859234.
- [207] G. Barbastathis, A. Ozcan, and G. Situ, “On the use of deep learning for computational imaging”, *Optica*, vol. 6, no. 8, pp. 921–943, 2019. DOI: 10.1364/optica.6.000921.
- [208] W. Schwartzkopf, T. E. Milner, J. Ghosh, B. L. Evans, and A. C. Bovik, “Two-dimensional phase unwrapping using neural networks”, in *4th IEEE southwest symposium on image analysis and interpretation, austin, TX, USA, april 2-4, 2000*, pp. 274–277.
- [209] K. He, X. Zhang, S. Ren, and J. Sun, “Deep residual learning for image recognition”, in *IEEE conference on computer vision and pattern recognition (CVPR), las vegas, NV, june 27-30, 2016*, pp. 770–778.
- [210] G. Dardikman and N. T. Shaked, “Phase unwrapping using residual neural networks”, in *Computational optical sensing and imaging, orlando, FL, USA, june 25-28, 2018*, CW3B–5.
- [211] G. Spoorthi, S. Gorthi, and R. K. S. S. Gorthi, “PhaseNet: A deep convolutional neural network for two-dimensional phase unwrapping”, *IEEE signal processing letters*, vol. 26, no. 1, pp. 54–58, 2018. DOI: 10.1109/lsp.2018.2879184.
- [212] T. Zhang, S. Jiang, Z. Zhao, K. Dixit, X. Zhou, J. Hou, Y. Zhang, and C. Yan, “Rapid and robust two-dimensional phase unwrapping via deep learning”, *Optics express*, vol. 27, no. 16, pp. 23 173–23 185, 2019. DOI: 10.1364/oe.27.023173.
- [213] K. Wang, Y. Li, Q. Kemao, J. Di, and J. Zhao, “One-step robust deep learning phase unwrapping”, *Optics express*, vol. 27, no. 10, pp. 15 100–15 115, 2019. DOI: 10.1364/oe.27.015100.
- [214] J. Zhang, X. Tian, J. Shao, H. Luo, and R. Liang, “Phase unwrapping in optical metrology via denoised and convolutional segmentation networks”, *Optics express*, vol. 27, no. 10, pp. 14 903–14 912, 2019. DOI: 10.1364/oe.27.014903.
- [215] C. Li, Y. Tian, and J. Tian, “A method for single image phase unwrapping based on generative adversarial networks”, in *11th international conference on digital image processing (ICDIP), guangzhou, china, may 10-13, 2019*, pp. 272–278.
- [216] G. Dardikman-Yoffe, D. Roitshtain, S. K. Mirsky, N. A. Turko, M. Habaza, and N. T. Shaked, “PhUn-Net: Ready-to-use neural network for unwrapping quantitative phase images of biological cells”, *Biomedical optics express*, vol. 11, no. 2, pp. 1107–1121, 2020. DOI: 10.1364/boe.379533.

- [217] J. H. Rick Chang, C.-L. Li, B. Póczos, B. V. K. Vijaya Kumar, and A. C. Sankaranarayanan, “One network to solve them all—Solving linear inverse problems using deep projection models”, in *IEEE international conference on computer vision (ICCV), venice, italy, october 22-29, 2017*, pp. 5888–5897.
- [218] D. Ulyanov, A. Vedaldi, and V. Lempitsky, “Deep image prior”, in *Proceedings of the IEEE conference on computer vision and pattern recognition, salt lake city, UT, june 18-22, 2018*, pp. 9446–9454.
- [219] K. Gong, C. Catana, J. Qi, and Q. Li, “PET image reconstruction using deep image prior”, *IEEE transactions on medical imaging*, vol. 38, no. 7, pp. 1655–1665, 2018. DOI: 10.1109/tmi.2018.2888491.
- [220] L. Condat, “Discrete total variation: New definition and minimization”, *SIAM journal on imaging sciences*, vol. 10, no. 3, pp. 1258–1290, 2017. DOI: 10.1137/16m1075247.
- [221] M. D. Pritt, “Congruence in least-squares phase unwrapping”, in *Proceedings of the IEEE international geoscience and remote sensing symposium, singapore, singapore, august 3-8, 1997*, pp. 875–877.
- [222] E. Bostan, R. Heckel, M. Chen, M. Kellman, and L. Waller, “Deep phase decoder: Self-calibrating phase microscopy with an untrained deep neural network”, *Optica*, vol. 7, no. 6, pp. 559–562, 2020. DOI: 10.1364/optica.389314.
- [223] F. Wang, Y. Bian, H. Wang, M. Lyu, G. Pedrini, W. Osten, G. Barbastathis, and G. Situ, “Phase imaging with an untrained neural network”, *Light: Science & applications*, vol. 9, no. 1, pp. 1–7, 2020.
- [224] O. Ronneberger, P. Fischer, and T. Brox, “U-Net: Convolutional networks for biomedical image segmentation”, in *International conference on medical image computing and computer-assisted intervention, münchen, germany, october 5-9, 2015*, pp. 234–241.
- [225] K. He, X. Zhang, S. Ren, and J. Sun, “Delving deep into rectifiers: Surpassing human-level performance on ImageNet classification”, in *IEEE international conference on computer vision (ICCV), santiago, chile, december 13-16, 2015*, pp. 1026–1034.
- [226] D. P. Kingma and J. Ba, “Adam: A method for stochastic optimization”, in *3rd international conference on learning representations (ICLR), san diego, CA, USA, may 7-9, 2015*, 2015.
- [227] N. Ketkar, “Introduction to Pytorch”, in *Deep learning with pyThon*, Springer, 2017, pp. 195–208.

- [228] X. Li and M. T. Orchard, “New edge-directed interpolation”, *IEEE transactions on image processing*, vol. 10, no. 10, pp. 1521–1527, 2001. DOI: 10.1109/83.951537.
- [229] V. Bianco, P. Memmolo, M. Leo, S. Montresor, C. Distante, M. Paturzo, P. Piccart, B. Javidi, and P. Ferraro, “Strategies for reducing speckle noise in digital holography”, *Light: Science & applications*, vol. 7, no. 1, pp. 1–16, 2018. DOI: 10.1038/s41377-018-0050-9.
- [230] J. W. Goodman, *Speckle phenomena in optics: Theory and applications*. Roberts and Company Publishers, 2007.
- [231] T. Vicar, J. Balvan, J. Jaros, F. Jug, R. Kolar, M. Masarik, and J. Gumulec, “Cell segmentation methods for label-free contrast microscopy: Review and comprehensive comparison”, *Bmc bioinformatics*, vol. 20, no. 1, p. 360, 2019. DOI: 10.1186/s12859-019-2880-8.
- [232] N. Brandenburg, S. Hoehnel, F. Kuttler, K. Homicsko, C. Ceroni, T. Ringel, N. Gjorevski, G. Schwank, G. Coukos, G. Turcatti, *et al.*, “High-throughput automated organoid culture via stem-cell aggregation in microcavity arrays”, *Nature biomedical engineering*, pp. 1–12, 2020.
- [233] X. Yin, B. E. Mead, H. Safaei, R. Langer, J. M. Karp, and O. Levy, “Engineering stem cell organoids”, *Cell stem cell*, vol. 18, no. 1, pp. 25–38, 2016. DOI: 10.1016/j.stem.2015.12.005.
- [234] K. L. Fair, J. Colquhoun, and N. R. Hannan, “Intestinal organoids for modelling intestinal development and disease”, *Philosophical transactions of the royal society b: Biological sciences*, vol. 373, no. 1750, p. 20170217, 2018. DOI: 10.1098/rstb.2017.0217.
- [235] E. N. Leith and J. Upatnieks, “Holographic imagery through diffusing media”, *Journal of the optical society of america*, vol. 56, no. 4, pp. 523–523, 1966. DOI: 10.1364/josa.56.000523.
- [236] Z. Yaqoob, D. Psaltis, M. S. Feld, and C. Yang, “Optical phase conjugation for turbidity suppression in biological samples”, *Nature photonics*, vol. 2, no. 2, pp. 110–115, 2008. DOI: 10.1038/nphoton.2007.297.
- [237] M. Cui and C. Yang, “Implementation of a digital optical phase conjugation system and its application to study the robustness of turbidity suppression by phase conjugation”, *Optics express*, vol. 18, no. 4, pp. 3444–3455, 2010. DOI: 10.1364/oe.18.003444.

- [238] C.-L. Hsieh, Y. Pu, R. Grange, G. Laporte, and D. Psaltis, “Imaging through turbid layers by scanning the phase conjugated second harmonic radiation from a nanoparticle”, *Optics express*, vol. 18, no. 20, pp. 20 723–20 731, 2010. doi: 10.1364/oe.18.020723.
- [239] J. Radon, “Über die bestimmung von funktionen durch ihre integralwerte längs gewisser mannigfaltigkeiten”, *Classic papers in modern diagnostic radiology*, vol. 5, p. 21, 2005.
- [240] K. Lee, K. Kim, J. Jung, J. Heo, S. Cho, S. Lee, G. Chang, Y. Jo, H. Park, and Y. Park, “Quantitative phase imaging techniques for the study of cell pathophysiology: From principles to applications”, *Sensors*, vol. 13, no. 4, pp. 4170–4191, 2013. doi: 10.3390/s130404170.
- [241] F. Merola, P. Memmolo, L. Miccio, R. Savoia, M. Mugnano, A. Fontana, G. D’ippolito, A. Sardo, A. Iolascon, A. Gambale, *et al.*, “Tomographic flow cytometry by digital holography”, *Light: Science & applications*, vol. 6, no. 4, e16241–e16241, 2017. doi: 10.1038/lsa.2016.241.
- [242] D. Tajik, A. D. Pitcher, and N. K. Nikolova, “Comparative study of the Rytov and Born approximations in quantitative microwave holography”, *Progress in electromagnetic research b*, vol. 79, pp. 1–19, 2017. doi: 10.2528/pierb17081003.
- [243] D. Tajik, D. S. Shumakov, and N. K. Nikolova, “An experimental comparison between the Born and Rytov approximations in microwave tissue imaging”, in *2017 IEEE MTT-S international microwave symposium (IMS)*, IEEE, 2017, pp. 1391–1393. doi: 10.1109/mwsym.2017.8058875.
- [244] J. Kostencka, T. Kozacki, A. Kuś, B. Kemper, and M. Kujawińska, “Holographic tomography with scanning of illumination: Space-domain reconstruction for spatially invariant accuracy”, *Biomedical optics express*, vol. 7, no. 10, pp. 4086–4101, 2016. doi: 10.1364/boe.7.004086.
- [245] J. Yoon, K. Kim, H. Park, C. Choi, S. Jang, and Y. Park, “Label-free characterization of white blood cells by measuring 3D refractive index maps”, *Biomedical optics express*, vol. 6, no. 10, pp. 3865–3875, 2015. doi: 10.1364/boe.6.003865.
- [246] Y. Kim, H. Shim, K. Kim, H. Park, S. Jang, and Y. Park, “Profiling individual human red blood cells using common-path diffraction optical tomography”, *Scientific reports*, vol. 4, no. 1, pp. 1–7, 2014.
- [247] T. H. Nguyen, M. E. Kandel, M. Rubessa, M. B. Wheeler, and G. Popescu, “Gradient light interference microscopy for 3D imaging of unlabeled specimens”, *Nature communications*, vol. 8, no. 1, pp. 1–9, 2017. doi: 10.1038/s41467-017-00190-7.

- [248] J. Lim, A. Goy, M. H. Shoreh, M. Unser, and D. Psaltis, “Learning tomography assessed using Mie theory”, *Physical review applied*, vol. 9, no. 3, p. 034027, 2018. DOI: 10/gc9qqt.
- [249] J. Valkenburg and C. Woldringh, “Phase separation between nucleoid and cytoplasm in *Escherichia coli* as defined by immersive refractometry”, *Journal of bacteriology*, vol. 160, no. 3, pp. 1151–1157, 1984. DOI: 10.1128/jb.160.3.1151-1157.1984.
- [250] J. D. Wilson, W. J. Cottrell, and T. H. Foster, “Index-of-refraction-dependent subcellular light scattering observed with organelle-specific dyes”, *Journal of biomedical optics*, vol. 12, no. 1, p. 014010, 2007. DOI: 10.1117/1.2437765.
- [251] O. Haeberlé, K. Belkebir, H. Giovaninni, and A. Sentenac, “Tomographic diffractive microscopy: Basics, techniques and perspectives”, *Journal of modern optics*, vol. 57, no. 9, pp. 686–699, 2010. DOI: 10.1080/09500340.2010.493622.
- [252] K. Haseda, K. Kanematsu, K. Noguchi, H. Saito, N. Umeda, and Y. Ohta, “Significant correlation between refractive index and activity of mitochondria: Single mitochondrion study”, *Biomedical optics express*, vol. 6, no. 3, pp. 859–869, 2015. DOI: 10.1364/boe.6.000859.
- [253] R. P. Nieuwenhuizen, K. A. Lidke, M. Bates, D. L. Puig, D. Grünwald, S. Stallinga, and B. Rieger, “Measuring image resolution in optical nanoscopy”, *Nature methods*, vol. 10, no. 6, pp. 557–562, 2013. DOI: 10.1038/nmeth.2448.
- [254] N. Banterle, K. H. Bui, E. A. Lemke, and M. Beck, “Fourier ring correlation as a resolution criterion for super-resolution microscopy”, *Journal of structural biology*, vol. 183, no. 3, pp. 363–367, 2013. DOI: 10.1016/j.jsb.2013.05.004.
- [255] S. Culley, D. Albrecht, C. Jacobs, P. M. Pereira, C. Leterrier, J. Mercer, and R. Henriques, “Quantitative mapping and minimization of super-resolution optical imaging artifacts”, *Nature methods*, vol. 15, no. 4, p. 263, 2018. DOI: 10.1038/nmeth.4605.
- [256] A. C. Descloux, K. S. Grussmayer, and A. Radenovic, “Parameter-free image resolution estimation based on decorrelation analysis”, *Nature methods*, vol. 16, pp. 918–924, 2019. DOI: 10.1038/s41592-019-0515-7.
- [257] H. Mazidi, T. Ding, A. Nehorai, and M. D. Lew, “Quantifying accuracy and heterogeneity in single-molecule super-resolution microscopy”, *Nature communications*, vol. 11, no. 1, p. 6353, 2020. DOI: 10.1038/s41467-020-20056-9.
- [258] P. del Aguila Pla and J. Jaldén, “Cell detection by functional inverse diffusion and non-negative group sparsity—Part II: Proximal optimization and Performance evaluation”, *IEEE transactions on signal processing*, vol. 66, no. 20, pp. 5422–5437, 2018. DOI: 10.1109/tsp.2018.2868256.

- [259] ———, “Cell detection by functional inverse diffusion and non-negative group sparsity—Part I: Modeling and Inverse Problems”, *IEEE transactions on signal processing*, vol. 66, no. 20, pp. 5407–5421, 2018. DOI: 10.1109/tsp.2018.2868258.
- [260] Y. Sun, “Root mean square minimum distance as a quality metric for stochastic optical localization nanoscopy images”, *Scientific reports*, vol. 8, no. 1, pp. 1–11, 2018. DOI: 10.1038/s41598-018-35053-8.
- [261] H. Federer, *Geometric measure theory*. Springer, 2014.
- [262] G. Peyré and M. Cuturi, “Computational optimal transport”, *Foundations and trends in machine learning*, vol. 11 (5-6), pp. 355–602, 2019. DOI: 10.1561/22000000073.
- [263] L. G. Hanin, “Kantorovich-Rubinstein norm and its application in the theory of Lipschitz spaces”, *Proceedings of the american mathematical society*, vol. 115, no. 2, pp. 345–352, 1992. DOI: 10.1090/s0002-9939-1992-1097344-5.
- [264] J. Lellmann, D. A. Lorenz, C. Schonlieb, and T. Valkonen, “Imaging with Kantorovich-Rubinstein discrepancy”, *SIAM journal on imaging sciences*, vol. 7, no. 4, pp. 2833–2859, 2014. DOI: 10/gj3xcb.
- [265] P. Catala, V. Duval, and G. Peyré, “A low-rank approach to off-the-Grid sparse superresolution”, *SIAM journal on imaging sciences*, vol. 12, no. 3, pp. 1464–1500, 2019. DOI: 10.1137/19m124071x.
- [266] C. Villani, *Optimal Transport: Old and New*. Springer Science & Business Media, 2008, vol. 338.
- [267] F. Santambrogio, “Optimal transport for applied mathematicians”, *Birkhäuser, ny*, vol. 55, no. 58-63, p. 94, 2015.
- [268] B. Schmitzer and B. Wirth, *A framework for Wasserstein-1-type metrics*, 2017.
- [269] T. Pengo, S. J. Holden, and S. Manley, “PALMsiever: A tool to turn raw data into results for single-molecule localization microscopy”, *Bioinformatics (Oxford, England)*, vol. 31, no. 5, pp. 797–798, 2014. DOI: 10.1093/bioinformatics/btu720.
- [270] D. Baddeley, M. B. Cannell, and C. Soeller, “Visualization of localization microscopy data”, *Microscopy and microanalysis*, vol. 16, no. 1, pp. 64–72, 2010. DOI: 10.1017/s143192760999122x.
- [271] W. Saxton and W. Baumeister, “The correlation averaging of a regularly arranged bacterial cell envelope protein”, *Journal of microscopy*, vol. 127, no. 2, pp. 127–138, 1982. DOI: 10.1111/j.1365-2818.1982.tb00405.x.
- [272] M. Unser, B. L. Trus, and A. C. Steven, “A new resolution criterion based on spectral signal-to-noise ratios”, *Ultramicroscopy*, vol. 23, no. 1, pp. 39–51, 1987. DOI: 10.1016/0304-3991(87)90225-7.

- [273] H. Heydarian, F. Schueder, M. T. Strauss, B. Van Werkhoven, M. Fazel, K. A. Lidke, R. Jungmann, S. Stallinga, and B. Rieger, “Template-free 2D particle fusion in localization microscopy”, *Nature methods*, vol. 15, no. 10, p. 781, 2018. DOI: 10.1038/s41592-018-0136-6.
- [274] J. Schnitzbauer, Y. Wang, S. Zhao, M. Bakalar, T. Nuwal, B. Chen, and B. Huang, “Correlation analysis framework for localization-based superresolution microscopy”, *Proceedings of the national academy of sciences*, vol. 115, no. 13, pp. 3219–3224, 2018. DOI: 10.1073/pnas.1711314115.
- [275] D. Sage, H. Kirshner, T. Pengo, N. Stuurman, J. Min, S. Manley, and M. Unser, “Quantitative evaluation of software packages for single-molecule localization microscopy”, *Nature methods*, vol. 12, no. 8, p. 717, 2015. DOI: 10.1038/nmeth.3442.
- [276] R. J. Ober, S. Ram, and E. S. Ward, “Localization accuracy in single-molecule microscopy”, *Biophysical journal*, vol. 86, no. 2, pp. 1185–1200, 2004. DOI: 10.1016/s0006-3495(04)74193-4.
- [277] H. Deschout, F. C. Zanicchi, M. Mlodzianoski, A. Diaspro, J. Bewersdorf, S. T. Hess, and K. Braeckmans, “Precisely and accurately localizing single emitters in fluorescence microscopy”, *Nature methods*, vol. 11, no. 3, p. 253, 2014. DOI: 10.1038/nmeth.2843.
- [278] K. I. Mortensen, L. S. Churchman, J. A. Spudich, and H. Flyvbjerg, “Optimized localization analysis for single-molecule tracking and super-resolution microscopy”, *Nature methods*, vol. 7, no. 5, p. 377, 2010. DOI: 10.1038/nmeth.1447.
- [279] C. S. Smith, N. Joseph, B. Rieger, and K. A. Lidke, “Fast, single-molecule localization that achieves theoretically minimum uncertainty”, *Nature methods*, vol. 7, no. 5, p. 373, 2010. DOI: 10.1038/nmeth.1449.
- [280] S. Stallinga and B. Rieger, “The effect of background on localization uncertainty in single emitter imaging”, in *9th IEEE international symposium on biomedical imaging (ISBI)*, IEEE, Barcelona, Spain, 2012, pp. 988–991.
- [281] T. Chang, D. Ryu, Y. Jo, G. Choi, H.-S. Min, and Y. Park, “Calibration-free quantitative phase imaging using data-driven aberration modeling”, *Optics express*, vol. 28, no. 23, pp. 34 835–34 847, 2020. DOI: 10.1364/oe.412009.
- [282] A. Saba, J. Lim, A. B. Ayoub, E. E. Antoine, and D. Psaltis, “Polarization-sensitive optical diffraction tomography”, *Optica*, vol. 8, no. 3, pp. 402–408, 2021. DOI: 10.1364/optica.415343.
- [283] X. Dai, S. Xu, X. Yang, K. C. Zhou, C. Glass, P. C. Konda, and R. Horstmeyer, “Quantitative Jones matrix imaging using vectorial Fourier ptychography”, *Biomedical optics express*, vol. 13, no. 3, pp. 1457–1470, 2022. DOI: 10.1364/boe.448804.

-
- [284] J. Jung, K. Kim, J. Yoon, and Y. Park, “Hyperspectral optical diffraction tomography”, *Optics express*, vol. 24, no. 3, pp. 2006–2012, 2016. DOI: 10.1364/oe.24.002006.
- [285] J. Lim and D. Psaltis, “MaxwellNet: Physics-driven deep neural network training based on Maxwell’s equations”, *Apl photonics*, vol. 7, no. 1, p. 011 301, 2022. DOI: 10.1063/5.0071616.
- [286] I. Kang, A. Goy, and G. Barbastathis, “Dynamical machine learning volumetric reconstruction of objects’interiors from limited angular views”, *Light: Science & applications*, vol. 10, no. 1, p. 74, 2021. DOI: 10.1038/s41377-021-00512-x.
- [287] Y. Xue and L. Waller, “Computational hybrid imaging: Measure fluorescence and refractive index together”, in *Three-dimensional and multidimensional microscopy: Image acquisition and processing XXVIII*, T. G. Brown, T. Wilson, and L. Waller, Eds., International Society for Optics and Photonics, vol. 11649, SPIE, 2021. DOI: 10.1117/12.2579940.
- [288] J. J. MOREAU, “Fonctions convexes duales et points proximaux dans un espace hilbertien”, *C.r. acad. sci. paris ser. a math.*, vol. 255, pp. 2897–2899, 1962.
- [289] S. Boyd, “Alternating direction method of multipliers”, in *Talk at NIPS workshop on optimization and machine learning*, 2011.
- [290] W. L. Briggs and H. Van Emden, *The DFT: An owners’ manual for the discrete fourier transform*. SIAM, 1995, vol. 45.
- [291] A. Ralston and P. Rabinowitz, *A first course in numerical analysis*. Courier Corporation, 2001.
- [292] S. Ioffe and C. Szegedy, “Batch normalization: Accelerating deep network training by reducing internal covariate shift”, in *32th international conference on machine learning (ICML), lille, france, july 7-9, 2015*, vol. 37, 2015, pp. 448–456.

Personal Information	<p>Address: BM 4140, EPFL, CH-1015 Lausanne</p> <p>Date of birth: 2 April 1992</p> <p>E-mail: thanh-an.pham@epfl.ch</p> <p>Homepage: https://thanhanpham.github.io/</p> <p>Google Scholar ID: https://scholar.google.com/citations?user=_ZJ9X0QAAAAJ&hl=en</p> <p>Orcid ID: 0000-0001-6231-2569</p>	
Education	<p>EPFL, Biomedical Imaging Group</p> <ul style="list-style-type: none"> • PhD, Electrical engineering • Title: "Nonlinear Inverse Problems in Quantitative Phase Imaging" • Advisor: Prof. Michael Unser <p>EPFL</p> <ul style="list-style-type: none"> • MSc, Bioengineering <p>EPFL</p> <ul style="list-style-type: none"> • BSc, Life Science and Technologies 	<p>July 2017 - Apr. 2022 (expected date)</p> <p>Sept. 2013 - Apr. 2016</p> <p>Sept. 2010 - Aug. 2013</p>
Honors and Awards	<p>Best Student Paper Award, ISBI'21</p> <p>18th IEEE International Symposium on Biomedical Imaging, Nice, French Republic</p> <p>Best Student Paper Award, ISBI'19</p> <p>16th IEEE International Symposium on Biomedical Imaging, Venice, Italian Republic</p>	<p>Apr. 2021</p> <p>Apr. 2019</p>
Internships	<p>UNIL, Department of Fundamental Neurosciences</p> <ul style="list-style-type: none"> • Astrocyte-associated calcium imaging • Advisor: Prof. Andrea Volterra <p>EPFL, Laboratory of Geographic Information Systems</p> <ul style="list-style-type: none"> • Soundscape and health indicators • Advisor: Prof. François Golay <p>Advanced Digital Science Center (Singapore)</p> <ul style="list-style-type: none"> • Industry intern, monitoring mental fatigue with EEG signals 	<p>Aug. - Nov. 2018</p> <p>June - Dec. 2016</p> <p>June - July 2015</p>
Publications	<p>Journal (*: equal contributions)</p> <ol style="list-style-type: none"> 1. T. Hong*, T.-a. Pham*, E. Treister, and M. Unser, "Diffraction tomography with Helmholtz equation: Efficient and robust multigrid based solver," 2021, Under review. https://arxiv.org/pdf/2107.03679.pdf 2. J. Griffie, T.-a. Pham, C. Sieben, R. Lang, V. Cevher, S. Holden, M. Unser, S. Manley, and D. Sage, "Virtual-SMLM, a virtual environment for real-time interactive SMLM acquisition," 2020, Under review. https://www.biorxiv.org/content/10.1101/2020.03.05.967893v1.full.pdf 3. T.-a. Pham, E. Soubies, F. Soulez, and M. Unser, "Optical diffraction tomography from single-molecule localization microscopy," <i>Optics Communications</i>, vol. 499, p. 127290, November 15 2021, https://www.sciencedirect.com/science/article/pii/S0030401821005393 4. F. Yang, T.-a. Pham, N. Brandenberg, M. P. Lutolf, J. Ma, and M. Unser, "Robust Phase Unwrapping via Deep Image Prior for Quantitative Phase Imaging," <i>IEEE Transactions on Image Processing</i>, vol. 30, pp. 7025-7037, July 30 2021, https://ieeexplore.ieee.org/document/9502550 5. F. Yang, T.-a. Pham, H. Gupta, M. Unser, and J. Ma, "Deep-learning projector for optical diffraction tomography," <i>Optics Express</i>, vol. 28, no. 3, pp. 3905-3921, February 3, 2020, http://bigwww.epfl.ch/publications/yang2001.html 6. A. Ayoub, T.-a. Pham, J. Lim, M. Unser, and D. Psaltis, "A method for assessing the fidelity of optical diffraction tomography reconstruction methods using structured illumination," <i>Optics Communications</i>, vol. 454, no. 124486, pp. 1-6, January 1, 2020, http://bigwww.epfl.ch/publications/ayoub2001.html 	

Publications
(Cont'd)

7. **T.-a. Pham**, E. Soubies, A. Ayoub, J. Lim, D. Psaltis, and M. Unser, "Three-dimensional optical diffraction tomography with Lippmann-Schwinger model," *IEEE Transactions on Computational Imaging*, vol. 6, pp. 727–738, 2020, <http://bigwww.epfl.ch/publications/pham2002.html>
8. E. Soubies, F. Soulez, M. McCann, **T.-a. Pham**, L. Donati, T. Debarre, D. Sage, and M. Unser, "Pocket guide to solve inverse problems with GlobalBioIm," *Inverse Problems*, vol. 35, no. 10, pp. 1–20, October 2019, paper no. 104006 <http://bigwww.epfl.ch/publications/soubies1904.html>
9. D. Sage*, **T.-a. Pham***, H. Babcock, T. Lukes, T. Pengo, J. Chao, R. Velmurugan, A. Herbert, A. Agrawal, S. Colabrese, A. Wheeler, A. Archetti, B. Rieger, R. Ober, G. Hagen, J.-B. Sibarita, J. Ries, R. Henriques, M. Unser, and S. Holden*, "Super-resolution fight club: Assessment of 2D and 3D single-molecule localization microscopy software," *Nature Methods—Techniques for Life Scientists and Chemists*, vol. 16, no. 5, pp. 387–395, May 2019, <http://bigwww.epfl.ch/publications/sage1903.html>
10. **T.-a. Pham**, E. Soubies, A. Goy, J. Lim, F. Soulez, D. Psaltis, and M. Unser, "Versatile reconstruction framework for diffraction tomography with intensity measurements and multiple scattering," *Optics Express*, vol. 26, no. 3, pp. 2749–2763, February 5, 2018, <http://bigwww.epfl.ch/publications/pham1801.html>
11. E. Soubies*, **T.-a. Pham***, and M. Unser, "Efficient inversion of multiple-scattering model for optical diffraction tomography," *Optics Express*, vol. 25, no. 8, pp. 21 786–21 800, September 4, 2017, <http://bigwww.epfl.ch/publications/soubies1701.html>

Conference, symposium and workshops

1. **T.-a. Pham**, E. Soubies, F. Soulez, and M. Unser, "Diffraction tomography from single-molecule localization microscopy: Numerical feasibility," in *Proceedings of the Eighteenth IEEE International Symposium on Biomedical Imaging (ISBI'21)*, Nice, French Republic, April 13–16, 2021, pp. 854–857, **Best student paper award**
2. Q. Denoyelle, **T.-a. Pham**, P. del Aguila Pla, D. Sage, and M. Unser, "Optimal-transport-based metric for SMLM," in *Proceedings of the Eighteenth IEEE International Symposium on Biomedical Imaging (ISBI'21)*, Nice, French Republic, April 13–16, 2021, pp. 797–801
3. **T.-a. Pham**, E. Soubies, A. Ayoub, D. Psaltis, and M. Unser, "Adaptive regularization for three-dimensional optical diffraction tomography," in *Proceedings of the Seventeenth IEEE International Symposium on Biomedical Imaging (ISBI'20)*, Iowa City IA, USA, April 5–7, 2020, pp. 182–186, [nominated for best paper award.]
4. **T.-a. Pham**, E. Soubies, D. Sage, and M. Unser, "Closed-form expression of the Fourier ring-correlation for single-molecule localization microscopy," in *Proceedings of the Sixteenth IEEE International Symposium on Biomedical Imaging: From Nano to Macro (ISBI'19)*, Venice, Italian Republic, April 8–11, 2019, pp. 321–324, **Best student paper award**
5. **T.-a. Pham**, E. Soubies, J. Lim, A. Goy, F. Soulez, D. Psaltis, and M. Unser, "Phaseless diffraction tomography with regularized beam propagation," in *Proceedings of the Fifteenth IEEE International Symposium on Biomedical Imaging: From Nano to Macro (ISBI'18)*, Washington DC, USA, April 4–7, 2018, pp. 1268–1271
6. L. Donati, E. Soubies, **T.-a. Pham**, and M. Unser, "User-friendly building of reconstruction algorithms for solving inverse problems," in *Proceedings of the Seventeenth IEEE International Symposium on Biomedical Imaging (ISBI'20)*, Iowa City IA, USA, April 5–7, 2020, p. 1307
7. **T.-a. Pham**, N. Brandenberg, S. Hoelzel, B. Rappaz, M. Unser, M. Lütolf, and D. Sage, "Quantitative image-analysis of organoids with high-throughput digital holography microscopy," in *Proceedings of the 2020 Quantitative BioImaging Conference (QBI'20)*, Oxford, United Kingdom, January 6–9, 2020, paper no. 365
8. D. Sage, **T.-a. Pham**, and M. Unser, "3D single molecule localization microscopy: Key outcomes of the software benchmarking," in *Proceedings of the Sixteenth IEEE International Symposium on Biomedical Imaging: From Nano to Macro (ISBI'19)*, Venice, Italian Republic, April 8–11, 2019, p. 610
9. **T.-a. Pham**, D. Sage, and S. Holden, "Developments of the ongoing 3D SMLM software challenge," in *Seventh Single Molecule Localization Microscopy Symposium (SMLMS'17)*, London, United Kingdom, August 30–September 1, 2017

Teaching

Head Teaching Assistant

Sept. 2017 - Aug. 2021

- Image Processing I and II, EPFL

Teaching Assistant

Sept. 2012 - Aug. 2015

- Physics I, II and Analysis I, II & IV for Life Science and Technologies, EPFL
-

Supervised students	Master Thesis (full time, 4 months)	
	Yuxuan Long	Fall 2021
	Computational Methods for Dynamic Fourier Ptychography	
	Internship (full time, 6 months)	
	Paul Margain	Spring 2021
	High-resolution reconstruction in single-particle cryo-EM with a multiscale joint refinement scheme	
	Master Semester Project (16-24 hours per week, 4 months)	
	Mickael Gindroz	Spring 2021
	Differentiable Approximation of Hessian-Schatten Regularization for Image Reconstruction	
	Aiday Marlen	Spring 2021
	Using regularization to reduce the number of projection angles in optical projection tomography	
	Paul Margain	Fall 2020
	Deep learning for 3D particle field imaging	
	Louis-Nicolas Douce	Spring 2020
	Slice-based Dictionary Learning for Computed Tomography	
	Mohamed Bahroun	Spring 2020
	Image reconstruction for optical diffraction tomography	
	J�erome Savary	Fall 2019
	Phase Unwrapping with Deep Learning	
	Elias Gajo	Fall 2019
Off-the-grid algorithm in ImageJ for 3D single-molecule localization microscopy		
Amandine Evard	Spring 2019	
Off-the-grid algorithm in ImageJ for 3D single-molecule localization microscopy		
Luca Fetz	Spring 2019	
Timing correction for slow-scanning biomedical imaging devices		
Cl�elie De Witasse	Spring 2019	
Dictionary Learning for Limited Angle Computed Tomography		
C�edric Schumacher	Fall 2018	
Improving depth-of-field by deconvolution		
<hr/>		
Review Activities	Optica, Optics Express, Journal of the Optical Society of America A, Optics Letters, Transactions on Computational Imaging, Transactions on Microwave Theory and Techniques, Nature Methods, Nature Communications, International Symposium on Biomedical Imaging (ISBI)	
<hr/>		
Personal Skills	Languages	
	1. French: Native	
	2. English: Fluent	
	3. German: Intermediate	
	Digital Competences	
	1. Programming Language: C/C++, Python (including PyTorch), JAVA, MATLAB	
	2. Others: LaTeX, HTML, ImageJ	